Design and Non-Linear Frequency-Response Analysis of Smart Functionally Graded Plates using a 1-3 Piezoelectric Composite

A Thesis Submitted in
Partial Fulfillment of the Requirements
for the Degree of

DOCTOR OF PHILOSOPHY

by

M. S. Aravinda Kumar
(Roll No: 10610306)

DEPARTMENT OF MECHANICAL ENGINEERING
INDIAN INSTITUTE OF TECHNOLOGY GUWAHATI,
GUWAHATI-781039, INDIA

June, 2015

Department of Mechanical Engineering
Indian Institute of Technology Guwahati
Guwahati-781039 INDIA

CERTIFICATE

It is certified that the work contained in the thesis entitled "**Design and Non-Linear Frequency-Response Analysis of Smart Functionally Graded Plates using a 1-3 Piezoelectric Composite**" submitted by **Mr. M S Aravinda Kumar** to the Indian Institute of Technology Guwahati for the award of the degree of Doctor of Philosophy has been carried out under our supervision in the Department of Mechanical Engineering, Indian Institute of Technology Guwahati. This work has not been submitted elsewhere for the award of any other degree or diploma.

(Dr. Satyajit Panda)
Assistant Professor
Department of Mechanical Engineering
Indian Institute of Technology Guwahati
Guwahati-781039
INDIA

(Dr. Debabrata Chakraborty)
Professor
Department of Mechanical Engineering
Indian Institute of Technology Guwahati
Guwahati-781039
INDIA

Declaration

I M. S. Aravinda Kumar. (Roll no: 10610306) declare that the present written submission is my thoughts in my own words. I have adequately cited and referenced the original sources, where others ideas have been involved. I also declare that I have adhered to all principles of academic honesty and integrity and have neither fabricated nor falsified any idea/data/fact/source in my submission. I understand that any violation of the above will be cause for disciplinary action by the Institute and can also evoke penal action from the sources which have thus not been properly cited or from whom proper permission has not been taken when needed.

M.S. Aravinda Kumar

Date: (Roll No: 10610306)

Dedicated to

My parents, teachers,

Ashwin

and

Almighty

Acknowledgment

Over the course of four years at IIT Guwahati, I have been accompanied and supported by many people that have helped to make the undertaking of this magnitude possible. I would first like to express my deep appreciation and sincere gratitude to my thesis supervisors **Dr. Satyajit Panda** and **Dr. Debabrata Chakraborty** for their invaluable guidance. Their untiring guidance, demand for excellence, encouragement and technical expertise brought the best from me.

I would also like to acknowledge Prof. S. K. Dwivedy, Dr. Arbind Kumar Singh and Dr. Karuna Kalita for their valuable advice and suggestions on my work while serving in my doctoral committee.

I would like to acknowledge, Prof. Anoop K Dass, Head, Department of Mechanical Engineering, for providing an opportunity for higher learning in Department of Mechanical Engineering, IITG.

I would like to express my immense gratitude to my friends A. Srinivas Pavan Kumar, Dr. Bhaskar, Dr. Debjyoti Sahu, Dr. Prashanth Mishra, Samir Panda and Tamilarasan, Darshan for their help and suggestions in need.

I am grateful to my *parents* and *family* members for their love and support.

M. S. Aravinda kumar.

Abstract

This dissertation deals with the design and analysis of smart functionally graded (FG) plates using a 1-3 piezoelectric fiber-reinforced composite (PFRC). Two types of graded plates namely isotropic FG plate (ceramic-metal) and laminated FG composite plate are considered for the analysis. The PFRC acts as a material of actuator layer which is either directly attached to the surface of the host plate or attached to the same in the form of active constrained layer damping (ACLD). First, a geometrically nonlinear vibration analysis of smart isotropic FG plates (ceramic-metal) with a heated plate-surface is performed in the frequency-domain. The composition of ceramic and metal constituents in the isotropic FG plate is considered to vary from ceramic to metal across the thickness of the plate according to a simple power-law, and the ceramic-rich surface is exposed to a high temperature across the thickness of the plate. The PFRC-layer directly attached to the host plate-surface is utilized to induce smart damping in the overall FG plate, and the effects of plate-surface temperature on the nonlinear vibration characteristics of the smart FG plate in the frequency domain as well as on the corresponding control-performance of PFRC-actuator are investigated. The analysis is further extended for investigating the effect of FG plate-surface temperature on the control-performance of PFRC-actuator when it is used in the form of ACLD-layer. As a novel development, the Golla-Hughes-McTavish (GHM) method is implemented to model the constrained viscoelastic layer of ACLD arrangement for the analysis of nonlinear frequency responses of smart isotropic FG plates under the plate-surface temperature. An incremental finite element (FE) model of the overall smart heated FG plate is developed in the frequency-domain and the corresponding FE equations of motion are solved using an arc-length extrapolation solution technique in combination with a proposed strategy for determination of incremental arc-length. The numerical illustrations show a potential use of PFRC as a material for distributed actuator or active constraining layer of ACLD arrangement in control of nonlinear frequency responses of heated isotropic FG plates. The analysis reveals the significant effects of initial thermal bending of the overall smart FG plate on its nonlinear dynamic behavior in the frequency-domain. The effects of temperature, constituent-volume fractions in FG substrate, fiber volume fraction in PFRC and fiber orientation angle in PFRC on the active damping in the overall smart FG plate are presented. For the use of PFRC-actuator/ACLD layer in the form of a patch, a new numerical strategy for determining its effective size and location over the surface of host FG plate is also presented.

Next, the design and analysis of smart laminated FG composite plates are carried out considering one (ACLD) of the smart layers to induce active damping in the overall plate. The substrate laminated FG composite plate is constructed through the proposition of a new lamination scheme that involves the design of a graded orthotropic fiber-reinforced composite ply. The main objective in this design is to achieve

continuous variations of material properties and stresses along the thickness direction of laminated composite plates. The graded orthotropic composite ply is supposed to be a stack of uniformly oriented unidirectional fiber-reinforced composite layers. Every layer is comprised of one row of horizontally coplanar continuous fibers. The fiber-volume fraction (FVF) varies among the layers following a simple power-law that yields graded material properties of the composite ply across its thickness. Its effective graded elastic properties are predicted utilizing FE procedure in conjunction with an available concept of homogeneous model for FG composites. Utilizing this graded ply as well as conventional composite ply, the new lamination scheme is demonstrated through the conversion of a conventional laminated composite plate (CLCP) into a conventional-graded laminated composite plate (CGLCP). The suitability of this conversion/new lamination scheme is substantiated through the nonlinear bending analysis of both the plates (CLCP and CGLCP) and also, the nonlinear frequency response analysis of the same plates integrated with an ACLD layer. The bending responses of both the plates reveal ample changes of laminate-rigidity and maximum values of stresses for the conversion of a CLCP into a CGLCP while achieving the advantage of continuous variations of material properties in the thickness direction. Apart from this static result, the evaluated frequency responses of both the smart plates (CLCP and CGLCP) reveal close dynamic characteristics of a CGLCP to those of the corresponding CLCP. But, this similarity primarily depends on the way of utilization of graded orthotropic composite ply in the implementation of proposed lamination scheme. The change in the control-performance of ACLD-layer due to this conversion of CLCP is also numerically evaluated and presented in the dissertation.

TABLE OF CONTENTS

Abstract

NOTATION

LIST OF FIGURES

LIST OF TABLES

Chapter 1 **INTRODUCTION**

1.1 Introduction 1

1.2 Functionally graded materials(FGM) 2

1.2.1 Linear static analysis of FG plates 4

1.2.2 Nonlinear static analysis of FG plates 6

1.2.3 Linear dynamic analysis of FG plates 6

1.2.4 Nonlinear dynamic analysis of FG plates 7

1.3 Smart structures 8

1.3.1 Smart FG Structures 11

1.4 Piezoelectric composites 14

1.5 Active constrained layer damping (ACLD) 17

1.6 Graded fiber reinforced composites 19

1.7 Research motivation and objectives 22

1.8 Contributions 25

1.9 Dissertation Overview 26

Chapter 2 **HARMONICALLY EXCITED NONLINEAR VIBRATION OF HEATED FUNCTIONALLY GRADED PLATE INTEGRATED WITH PIEZOELECTRIC COMPOSITE ACTUATOR LAYER**

2.1 Introduction 29

2.2 Problem statement and incremental finite element formulation 30

2.2.1 Implementation of harmonic balance method 41

2.2.2 Smart damping 43

2.3 Solution methodology 46

2.4 Numerical results and discussions 49
2.4.1 Validation of the present incremental finite element model 51
2.4.2 Effect of fiber-volume fraction 53
2.4.3 Effect of fiber-orientation angle 54
2.4.4 PFRC layer on metal/ceramic rich surface of substrate FG plate 54
2.4.5 Effect of load-amplitude 55
2.4.6 Effect of control gain 56
2.4.7 Effect of ceramic rich temperature 57
2.4.8 Effect of volume fraction index 61
2.4.9 Effect of FG substrate plate-thickness 65
2.5 Conclusions 66

Chapter 3 **PIEZO-VISCOELASTICALLY DAMPED NONLINEAR FREQUENCY RESPONSE OF FUNCTIONALLY GRADED PLATES WITH A HEATED PLATE-SURFACE**

3.1 Introduction 69
3.2 Problem statement and incremental finite element formulation 70
3.2.1 Implementation of GHM model 81
3.2.2 Implementation of harmonic balance method(HBM) 82
3.2.3 Implementation of control strategy 83
3.3 Numerical results and discussions 86
3.3.1 Validation of the present incremental finite element model 87
3.3.2 Effect of control gain 88
3.3.3 Effect of plate-surface temperature 89
3.3.4 Effect of volume-fraction index 93
3.3.5 Effect of viscoelastic thickness 96
3.3.6 Effect of fiber volume fraction in constraining PFRC layer 97
3.3.7 Effect of fiber orientation angle 98
3.3.8 Effect of FG substrate plate thickness 98
3.4 Conclusions 99

Chapter 4 **SIZE AND LOCATION OF PFRC/ACLD PATCH FOR EFFECTIVE CONTROL OF NONLINEAR VIBRATION OF FG PLATS WITH A HEATED PLATE-SURFACE**

4.1 Introduction 101
4.2 Numerical procedure for effective size and location of PFRC/ACLD patch 101
4.3 Conclusions 108

Chapter 5 **DESIGN OF LAMINATED COMPOSITE PLATES USING GRADED ORTHOTROPIC FIBER-REINFORCED COMPOSITE PLIES**

5.1 Introduction 109
5.2 Present Graded Composite Lamina 110
5.3 Graded effective elastic properties 113
5.4 Finite Element Model of RV 119
5.5 Finite Element Formulation for Graded Laminated Composite Plate 122
5.6 Numerical results and discussions 127
5.6.1 Verification of present finite element model of RV 128
5.6.2 Effective properties of graded composite lamina 129
5.6.3 Graded laminated composite plates 141

5.6.3.1 Verification of FE model of laminated composite plate 143
5.6.3..2 Bending response of GLCPs 143
5.6.4 Conventional-graded laminated composite plates 146

5.7 Conclusions 153

Chapter 6 **NONLINEAR FREQUENCY RESPONSE ANALYSIS OF A SMART GRADED FIBER-REINFORCED COMPOSITE LAMINATED PLATE**

6.1 Introduction 155
6.2 Incremental finite element formulation 156
6.3 Numerical results and discussions 164

6.3.1 Verification of the present finite element formulation 165
6.3.2 Free vibration response of CLCP/CGLCP 166
6.3.3 Effect of load amplitude 168
6.3.4 Effect of power law-exponent 171
6.3.5 Effect of control gain 171
6.3.6 Effect of viscoelastic layer thickness in ACLD 171

arrangement
6.3.7 Effect of fiber orientation angle in PFRC layer 173
6.4 Conclusions 174

Chapter 7 **CONCLUSIONS**
7.1 General conclusions 176
7.2 Specific conclusions 177
7.3 Scope for future work 180

References 182

List of publications 203

LIST OF FIGURES

Fig. 1.1	Functionally graded material	3
Fig. 1.2	Schematic representation of smart structure	9
Fig. 1.3	Schematic diagram of (a) horizontally and (b) vertically reinforced 1-3 PZCs	15
Fig. 1.4	Working principle of active constrained layer damping treatment	17
Fig. 2.1	Schematic diagram of functionally graded (FG) plate integrated with a layer of PFRC	31
Fig. 2.2	Nonlinear frequency responses of the overall FG plate for different values of fiber volume fraction (v_f) in the PFRC actuator layer	53
Fig. 2.3	Variation of peak-point deflection (W^t_{peak}) of controlled nonlinear frequency response of the overall FG plate with the fiber orientation angle (ψ) in the PFRC actuator layer	53
Fig. 2.4	Nonlinear frequency responses of the overall FG plate when the PFRC layer is attached either to the ceramic rich (λ=2) or to the metal rich (λ=1) top surface of the FG substrate plate	54
Fig. 2.5	(a) Nonlinear frequency responses of the overall FG plate and (b) the corresponding variations of control voltage, variations of (c) the peak-point deflection (W^t_{peak}) and (d) the corresponding control voltage (V_{peak}) with the load amplitude	55
Fig. 2.6	(a) Nonlinear frequency responses of the overall FG plate for different values of control gain (k_d), (b) the corresponding variation of required control voltage	56
Fig. 2.7	Initial thermal bending deflections of the overall FG plate for different ceramic rich surface temperatures	57
Fig. 2.8	Linear and nonlinear frequency responses of the overall FG plate for different ceramic rich surface temperatures	57
Fig. 2.9	Variation of fundamental frequency (ω_0) of vibration with the ceramic rich surface temperature	58
Fig. 2.10	Difference between the frequencies ($\Delta\omega$) corresponding to the peak-points of linear and nonlinear frequency responses of the overall FG plate at each ceramic rich surface temperature	59
Fig. 2.11	(a) Variations of the peak point (W^t_{peak}) of frequency response and (b) the corresponding control voltage (V_{peak}) with ceramic rich surface temperature (T_c)	60
Fig. 2.12	Linear and nonlinear frequency responses of the overall FG plate for different values of volume fraction index (n)	62
Fig. 2.13	Initial thermal bending deflections ($W^s(a/2,b/2,0)$) of the overall FG plate for different values of volume fraction index (n) of the FG substrate plate at a constant temperature gradient	62
Fig. 2.14	Variation of fundamental frequency (ω_0) of vibration with the	63

volume fraction index (n) of the FG substrate plate in presence of temperature gradient

Fig. 2.15 Difference between the frequencies ($\Delta\omega$) corresponding to the peak-points of linear and nonlinear frequency responses for different volume fraction index (n) 64

Fig. 2.16 Variations of (a) peak-point deflection (W^t_{peak}) of nonlinear frequency response and (b) the corresponding required control voltage (V_{peak}) with the volume fraction index (n) 65

Fig. 2.17 Variations of (a) the peak-point deflection (W^t_{peak}) of frequency response and (b) the corresponding required control voltage (V_{peak}) of the overall FG plate with the substrate FG plate thickness (h) 66

Fig. 3.1 Schematic diagram of FG plate integrated with a layer of ACLD treatment 70

Fig. 3.2 Forced linear frequency responses of the overall FG plate 87

Fig. 3.3 Nonlinear frequency responses of the overall FG plate 88

Fig. 3.4 (a)Nonlinear frequency responses of the overall FG plate and (b) the corresponding variations of control voltage 89

Fig. 3.5 Variations of thermal bending deflections of the overall FG plate with increasing bottom ceramic rich substrate-plate-surface temperature (T_c) 90

Fig. 3.6 Linear and nonlinear frequency responses of the overall FG plate for different ceramic rich substrate-plate-surface temperatures 91

Fig. 3.7 Variation of fundamental frequency (ω_0) of the overall FG plate with the ceramic rich substrate-plate-surface temperature (T_c) 91

Fig. 3.8 Difference between the frequencies ($\Delta\omega_{peak}$) corresponding to the peak-points of linear and nonlinear frequency responses of the overall FG plate (Figure 3.6) at each ceramic rich surface temperature (T_c) 92

Fig. 3.9 Variations of (a) the peak-point deflection (W^t_{peak}) of frequency response curve and (b) the corresponding control voltage (V_{peak}) with the ceramic rich substrate-plate-surface temperature (T_c) 93

Fig. 3.10 Linear and nonlinear frequency responses of the overall FG plate for different values of volume fraction index (n) 94

Fig. 3.11 Initial thermal bending deflections of the overall FG plate for different volume fraction index (n) of the FG substrate plate 95

Fig. 3.12 Variation of linear fundamental frequency (ω_0) of overall FG plate with volume fraction index (n) of the FG substrate plate in presence of a temperature gradient 95

Fig. 3.13 Variations of (a) the peak point deflections (W^t_{peak}) of the nonlinear frequency response curve (Figure 10) and (b) the corresponding control voltage (V_{peak}) with the volume fraction index (n) of the FG 96

substrate plate

Fig. 3.14 Variations of peak-point deflection (W^t_{peak}) of nonlinear frequency response and (b) the corresponding required control voltage (V_{peak}) with the constrained viscoelastic layer thickness (h_v) 97

Fig. 3.15 Nonlinear frequency responses of the overall FG plate for different values of fiber volume fraction (v_f) in the PFRC constraining layers 97

Fig. 3.16 Variation of peak-point deflection (W^t_{peak}) of controlled nonlinear frequency response curve with the fiber orientation angle (ψ) in the PFRC constraining layer 98

Fig. 3.17 Variations of (a) peak-point deflection (W^t_{peak}) of the nonlinear frequency response curve and (b) the corresponding feedback control voltage (V_{peak}) with the FG substrate-plate-thickness (h) 99

Fig. 4.1 Schematic diagram of a FG plate integrated with a layer of PFRC 102

Fig. 4.2 Schematic diagram of a FG plate integrated with a layer of ACLD treatment 102

Fig. 4.3 Schematic diagram of a differential patch of PFRC removed surrounding a typical test point 103

Fig. 4.4 Schematic diagram of a differential patch of ACLD removed surrounding a typical test point 103

Fig. 4.5 (a) Surface plot for the variation of (W^t_{peak}) with the different test points on the top surface of FG substrate plate, (b) corresponding contour plot, (c)-(d) variations of W^t_{peak} with the different test points along x-direction ($y=b/2$) and $y-$direction ($x=a/2$)(PFRC patch , $T_c = T_m$ =300 K) 104

Fig. 4.6 (a) Surface plot for the variation of (W^t_{peak}) with the different test points on the top surface of FG substrate plate, (b) corresponding contour plot,(c)-(d) variations of W^t_{peak} with the different test points along x-direction ($y=b/2$) and $y-$direction ($x=a/2$) (PFRC patch, T_m = 300 K, T_c = 500 K). 105

Fig. 4.7 (a) Surface plot for the variation of (W^t_{peak}) with the test points on the top surface of FG substrate plate, (b) corresponding contour plot,(c)-(d) variations of W^t_{peak} with the test points along x-direction (y=b/2) and $y-$direction (x=a/2) (ACLD patch, $T_c = T_m$ =300 K). 106

Fig. 4.8 (a) Surface plot for the variation of (W^t_{peak}) with the test points on the top surface of FG substrate plate, (b) corresponding contour plot, (c)-(d) variations of W^t_{peak} with the test points along x-direction (y=b/2) 107

and $y-$ direction (x=a/2) (ACLD patch, $T_m = 300$ K, $T_c = 500$ K).

Fig. 5.1 Schematic diagram of (a) graded composite lamina, (b) a sectional view (yz-plane) and (c) variation of FVF according to power-law 111

Fig. 5.2 Schematic diagram of RV of the graded unidirectional continuous fiber-reinforced composite lamina (Fig. 5.1) 112

Fig. 5.3 Schematic diagram of a laminated graded composite plate 123

Fig. 5.4 Variations of FVF (v_f) across the thickness of composite lamina for different values of power-law exponent (n) 129

Fig. 5.5 Effective elastic coefficients $(c_{11}^{\ell}, c_{22}^{\ell}, c_{33}^{\ell})$ of different homogeneous layers in RV and the corresponding fitted curves 130

Fig. 5.6 Effective elastic coefficients $(c_{44}^{\ell}, c_{55}^{\ell}, c_{66}^{\ell})$ of different homogeneous layers in RV and the corresponding fitted curves 131

Fig. 5.7 Effective elastic coefficients $(c_{12}^{\ell}, c_{13}^{\ell}, c_{23}^{\ell})$ of different homogeneous layers in RV and the corresponding fitted curves 132

Fig. 5.8 Effective elastic coefficients $(c_{11}^{\ell}, c_{22}^{\ell}, c_{33}^{\ell})$ for different homogeneous layers in RV and the corresponding fitted curves for different values of power-law exponent 136

Fig. 5.9 Effective elastic coefficients $(c_{44}^{\ell}, c_{55}^{\ell}, c_{66}^{\ell})$ for different homogeneous layers in RV and the corresponding fitted curves for different values of power-law exponent 137

Fig. 5.10 Effective elastic coefficients $(c_{12}^{\ell}, c_{13}^{\ell}, c_{23}^{\ell})$ for different homogeneous layers in RV and the corresponding fitted curves for different values of power-law exponent 138

Fig. 5.11 Schematic diagrams of (a) graded fiber-reinforced composite lamina and (b) micro-structure of a typical yz-section of the graded fiber-reinforced composite lamina 139

Fig. 5.12 Schematic diagram of representative volume (RV) of the graded fiber-reinforced composite. 139

Fig. 5.13 Variations of elastic constants (C_{ij}) across the thickness of the graded composite lamina for different values of power-law exponent 140

Fig. 5.14 Comparison of dimensionless transverse deflections (W) at the middle point of a simply-supported conventional symmetric cross-ply ($0^o/90^o/0^o$) laminated plate 143

Fig. 5.15 Variations of dimensionless transverse deflection (W) at the middle point of (a) symmetric $(0^0/90^0/0^0)$ and (b) asymmetric $(90^0/0^0/90^0/0^0)$ cross-ply laminated composite plates with the 144

dimensionless transverse mechanical load (Q)

Fig. 5.16 Distributions of the dimensionless stresses $(\bar{\sigma}_x, \bar{\sigma}_y)$ across the thickness of the graded/conventional symmetric cross-ply $(0^0/90^0/0^0)$ laminated plate under the (a)-(b) linear (p = 10 N/m^2) and (c)-(d) nonlinear (p = 5 kN/m^2) bending deformations 145

Fig. 5.17 Distributions of the dimensionless stresses $(\bar{\sigma}_x, \bar{\sigma}_y)$ across the thickness of the graded /conventional asymmetric cross-ply $(90^0/0^0/90^0/0^0)$ laminated plate under the (a)-(b) linear (p = 10 N/m^2) and (c)-(d) nonlinear (p = 5 kN/m^2) bending deformations 146

Fig. 5.18 Modified stacking sequences for graded (a) symmetric and (b) asymmetric laminates 147

Fig. 5.19 Variations of elastic constants (C_{ij}) across the thickness of the symmetric conventional-graded laminated composite plate 148

Fig. 5.20 Variations of elastic constants (C_{ij}) across the thickness of the asymmetric conventional-graded laminated composite plate 150

Fig. 5.21 Variations of dimensionless transverse deflection (W) at the middle point of (a) symmetric and (b) asymmetric cross-ply laminated composite plates with the dimensionless transverse mechanical load (Q) 151

Fig. 5.22 Distributions of the dimensionless stresses $(\bar{\sigma}_x, \bar{\sigma}_y)$ across the thickness of the conventional-graded (Fig. 5.22(a))/conventional symmetric $(0^0/90^0/0^0)$ laminated plate under its (a)-(b) linear (p = 10 N/m^2) and (c)-(d) nonlinear (p = 5 kN/m^2) bending deformations 152

Fig. 5.23 Distributions of the dimensionless stresses $(\bar{\sigma}_x, \bar{\sigma}_y)$ across the thickness of the conventional-graded (Fig.5.23(a))/conventional asymmetric cross-ply $(90^0/0^0/90^0/0^0)$ laminated plate under its (a)-(b) linear (p = 10 N/m^2) and (c)-(d) nonlinear (p = 5 kN/m^2) bending deformations 153

Fig. 6.1 Schematic diagram of a graded laminated composite plate integrated with ACLD layer 156

Fig. 6.2 Linear frequency responses of asymmetric overall CLCP when the constrained viscoelastic layer is modeled using either GHM method 166

or complex stiffness method

Fig. 6.3 (a) Nonlinear frequency responses of the overall symmetric CGLCP (n = 1)/CLCP ($0^0/90^0/0^0$) and (b) the corresponding variations of control voltage ($k_d = 100$); variations of (c) peak-amplitude (W_{peak}) of frequency response curve and (d) the corresponding control voltage (V_{peak}) with the load-amplitude (p). 168

Fig. 6.4 (a) Nonlinear frequency responses of the overall asymmetric CGLCP (n = 1)/CLCP ($90^0/0^0/90^0/0^0$) and (b) the corresponding variations of control voltage ($k_d = 100$); variations of (c) peak-amplitude (W_{peak}) of frequency response curve and (d) the corresponding control voltage (V_{peak}) with the load-amplitude (p) 169

Fig. 6.5 Nonlinear frequency responses of the overall (a) symmetric and (b) asymmetric GLCPs for different values of power-law exponent 170

Fig. 6.6 Variations of peak-amplitude (W_{peak}) of frequency response curve and the corresponding control voltage (V_{peak}) with the control gain (k_d); (a)-(b) symmetric CGLCP/CLCP, (c)-(d) asymmetric C GLCP/CLCP 172

Fig. 6.7 Variation of peak-amplitude (W_{peak}) of frequency response curve with the thickness of the constrained viscoelastic layer, (a) symmetric CGLCP/CLCP, (b) asymmetric CGLCP/CLCP 173

Fig. 6.8 Variation of peak-amplitude (W_{peak}) of frequency response curve with the piezoelectric fiber orientation angle (ψ) of PFRC constraining layer; (a) symmetric CGLCP/CLCP, (b) asymmetric CGLCP/CLCP 174

LIST OF TABLES

Table 2.1	Convergence study for the present FE model of the overall smart plate	51
Table 2.2	Comparison of fundamental natural frequency (ω_o) parameter (Ω) of FG plate in the absence and in the presence of a temperature gradient across its thickness	52
Table 2.3	Comparison of frequency ratio (ω/ω_o) vs. W^t relation for nonlinear free vibration of FG plate with a temperature gradient	52
Table 3.1	GHM parameters	87
Table 5.1	Boundary conditions for determining elements of $\{\bar{\varepsilon}\}$	118
Table 5.2	Comparison of elastic constants obtained from present analysis for a lamina (AS4/3501-6 unidirectional continuous fiber reinforced composite, $v_f = 0.6$) with the similar published results	128
Table 5.3	$C_{ij}^{\max}, C_{ij}^{\min}$ and n_c corresponding to the fitted curves in Figs. 5.5-5.7 according to the power-law	133
Table 5.4	$C_{ij}^{\max}, C_{ij}^{\min}$ and n_c corresponding to the fitted curves in Figs. 5.8-5.10 according to the power-law	134
Table 5.5	C_{ij} predicted from coupled analysis (CA) and decoupled analysis (DCA) ($N_t = 3,\ n = 1$)	135
Table 5.6	C_{ij} predicted from coupled analysis (CA) and decoupled analysis (DCA) ($N_t = 5, n = 1$)	141
Table 5.7	C_{ij} predicted from coupled analysis (CA) and decoupled analysis (DCA) ($N_t = 7,\ n = 1$)	141
Table 6.1	Verification of fundamental natural frequency	165
Table 6.2	Comparison of nonlinear frequency ratio (ω/ω_0) for a fully clamped rectangular laminated composite plate analyzed in [157]	166
Table 6.3	Dimensionless natural frequencies ($\Omega = \omega a^2\sqrt{\rho/(E_m h^2)}$) for first four bending modes of symmetric and asymmetric GLCPs/CLCPs	167
Table 6.4	Dimensionless frequencies ($\Omega = \omega a^2\sqrt{\rho/(E_m h^2)}$) for different amplitudes of free vibration of symmetric and asymmetric GLCPs/CLCPs	167

NOTATIONS

Notations used throughout the thesis are listed. Notations less frequently used, or that have different meaning or different forms at different contexts, are defined where they are used.

a ,b	Dimensions of substrate plate
a_c	Cross-section of fiber matrix packs
$\{a_0\}$ / $\{a_{q0}\}$	Time-independent elemental nodal displacement vector
$\{a_r\}$ / $\{b_r\}$	Elemental nodal displacement vectors for the amplitudes in r-th harmonic term
$\{a_{qr}\}$ / $\{b_{qr}\}$	Elemental nodal auxillary dissipation coordination vectors
$[A_s]$	Area of the element in x-y plane
$[\bar{A}^{\ell}]$	Volume-average strain concentration matrix
C_{ij}^{k}	Effective elastic co-efficient for different layers
$[\bar{C}^{k}]$	Transformed elastic coefficient matrix of PFRC
$[C^{k}]$	Transformed elastic coefficient matrix of host structure
$[C_f]$	Elastic stiffness for fiber
$[C_m]$	Elastic stiffness for matrix phase
$[\bar{C}_b^k(z)]$, $[\bar{C}_s^k(z)]$	Transformed stiffness matrices of k^{th}-ply
$\{d\}$	Globalised general displacement field
$\{\tilde{d}\}$	Displacement vector
$\{\tilde{d}^e\}$	Elemental nodal displacement vector
$\{d_i\}$	Neighboring state of deformation corresponding to a given state
$\{d^e\}$	Elemental nodal displacement field
$\{D\}$	Electrical displacement field vector
$[\bar{e}]$	Transformed piezoelectric coefficient matrix for bending
$E(z)$	Young's modulus
$\{\bar{E}\}$	Electric field vector
G^{∞}	Equilibrium value of dynamic elastic modulus
$G(t)$	Modulus of elasticity for viscoelastic material
$s\tilde{G}(s)$	Material modulus function in Laplace domain
h	Thickness of substrate plate
h_p	PFRC layer thickness
h_v	Viscoelastic layer thickness
$[I]$	Identity matrix

k	Number of layers
k_d	Feed back control gain
$[K]$	Stiffness matrix
$[L]$	Linear and nonlinear Operator matrices
$\Delta l_1, \Delta l_2$	Least displacement
$[\bar{m}]$	Mass per unit area
$[M]$	Mass matrix
n	Power law exponent or volume fraction index
n_c	Power-law exponent that determines the shape of the fitted curve
N_s	Number of layers within the graded laminated plate
N_t	Number of fiber matrix packs
$[N]$	Shape function matrix
$\left[N_s\right]$	Transformation matrix
p	Mechanical load
P	Material properties of the substrate FG plate
$\left\{P_M^e\right\}$	Element mechanical load vector
R	Number of mini-oscillator terms
s	Laplace coordinate
Δs	Arc length
$[S]$	Harmonic terms represented in matrix form
T_c	Ceramic rich surface temperature of the FG plate
T_m	Metal rich surface temperature of FG plate
δT_k	Variation of total kinetic energy
δT_p	Variation of total potential energy
u, v, w	Displacements components in coordinate directions
v_f	Fiber volume fraction
V	Applied voltage
V_{peak}	control voltage at peak point
w^s	Equilibrium position corresponding to time dependent displacement
$\dot{w}$	Transverse velocity at a point of the plate
$w^t(t)$	Time dependent displacement
$\left\{w_{si}^v\right\}$	Displacement vectors corresponding to the sensing point velocity
W^s	Equilibrium position corresponding to the maximum value within a time period
W^t	Maximum value within a time period at a particular frequency
W_{peak}^t	Peak point of the response curve
$\{X^e\}$	Global nodal displacement vector

$\{X_i\}$	Global displacement vector
x, y, z	Cartesian coordinates
$\{z_q^e\}$	Auxillary coordinate or dissipation degree of freedom
$\alpha(z)$	Coefficient of thermal expansion
α_q, $\tilde{\xi}_q$ and $\tilde{\omega}_q$	Shape of modulus function in s-plane
$\nu(z)$	Poisson's ratio
γ_x / γ_y	Rotations of PFRC layer normals to the reference plane
ρ	Mass density
$\{\varepsilon\}$	Strain vector
$\{\bar{\varepsilon}\}$	Volume-average strain vector
$\{\sigma\}$	Stress vector
$\{\bar{\sigma}\}$	Volume-average stress vetor
$[\in]$	Transformed dielectric coefficient matrix
θ_x , θ_y	Rotations of substrate plate normals to the reference plane
ϕ_x, ϕ_y	Rotations of viscoelastic layer normals to the reference plane
$\{\kappa\}$	Bending strain vector
$k(z)$	Thermal conductivity
λ	Positive integer
Δ	Increment
ψ	Fiber orientation angle
ω	Circular frequency
ω_i	Neighboring state corresponding to a given state of vibration
ω_0	Fundamental frequency of vibration
$\{\Lambda\}$	Solution points of arc length
$[0]$	Null matrix
ℓ	Layer

Superscript:

e	Element
E	Electrical load
i	A State of deformation
s	Sensing point
T	Temperature
v	Velocity
$\mathbf{T}$	Transpose

Subscript:

b	Bending
L	Linear
N	Nonlinear
p	Predicted
ref	Reference
s	Shear
f	Fiber
m	Matrix

Abbreviations:

ACLD: Active constrained layer damping
CLCP: Conventional laminated composite plate
CGLCP: Conventional graded laminated composite
FGM: Functionally graded material
GFRC: Graded fiber reinforced composite
GHM : Golla-Hughes-McTavish
HBM: Harmonic balance method
PFRC: Piezoelectric fiber-reinforced composite

Chapter 1

INTRODUCTION

1.1 Introduction

Composite materials are being widely used in aerospace, automobile industries and other structural applications due to their advantages of light weight, high strength-to-weight ratio, high stiffness-to-weight ratio, good fatigue resistant properties, good corrosion resistance properties etc. The major drawback of composite laminates is the mismatch of material properties at the interface of two adjacent laminae which eventually causes the delamination under high thermal and/or mechanical stresses. In order to overcome this drawback, a new class of composite materials are developed which are comprised of two or more constituent materials with continuously varying composition of constituents particularly along the thickness direction. These materials are generally referred as functionally graded materials (FGMs) (Koizumi 1993). In the recent years, there has been large number of research works reported in the broad area of FGMs and in the dynamic responses of structures made of such materials in particular. In the direction of control of flexible structures made of such FGMs, smart FGM structures emerged as one of the important area of research where in smart materials are embedded in or mounted on FGM structures to achieve their self-sensing and self-controlling capabilities. However, researchers reported the problems associated with the deployment of commonly used monolithic piezoelectric layer/patches as distributed actuators in such smart structures mainly because of their low control authority. While exploring the enhancement of control authority of such actuators, a new class of composites known as piezoelectric composites (PZCs) were developed which could be used as materials for distributed actuators having higher control authority associated with other advantages over the conventional monolithic piezoelectric actuators. Among all the PZCs proposed till the date, piezoelectric fiber-reinforced composite (PFRC) is a promising PZC particularly in control of bending deformation of structures (Ray and Mallik 2004, 2005; Ray and Sachade 2006). In order to achieve more effective use

of monolithic piezoelectric or PZC actuators in control of vibration of structural components, researchers proposed to use a viscoelastic layer embedded between the host structure and the piezoelectric constraining actuator leading to what is known as active constrained layer damping (ACLD) (Baz 1993; Baz and Ro 1995a; Baz and Ro 1995b; Baz and Poh 1996). Analogous to the concept of FGMs, researchers have tried to develop graded fiber-reinforced composite (GFRCs) where the fiber volume fraction (FVF) and/or fiber orientation angle are supposed to be varied within a fiber-reinforced composite lamina. This concept of GFRC provides graded material properties within a fiber-reinforced composite lamina which certainly improve the performance of composite structures in various aspects like reduction of thermal stresses, reduction of stress concentration etc. Employing the same concept of GFRC, the problem of delamination of composite laminates due to high stress concentration at the inter-laminar interfaces could also be alleviated through the reduction of mismatch of material properties at such surfaces.

The current research direction is to combine all or some of the aforesaid concepts for further development of smart FG (ceramic-metal) structures and smart graded fiber-reinforced composite (GFRC) structures. In order to do so, first review of literature on the linear and the nonlinear analyses of FG structures, smart structures, smart FG structures, GFRC structures and smart GFRC structures is performed. A brief review on the use of piezoelectric fiber-reinforced composite (PFRC) and the active constrained layer damping (ACLD) of smart structures is also done. Next, based on the review of literature, the scope of research for this thesis is identified and the objectives of this dissertation are defined. Subsequently, the contributions in the field of smart FG structures made towards the preparation of this dissertation are delineated. In the end, organization of the chapters is outlined.

1.2 Functionally graded materials (FGMs)

Functionally graded materials (FGMs) are the advanced class of microscopically inhomogeneous composite materials which have been used in various engineering applications. In the quest of developing high temperature-barrier-materials, the concept of FGMs was first proposed by material scientists in Japan in 1984. Later in the year 1987, a project to develop advanced high thermal resistant materials for

space programme began under the auspices of STA (Agency of Science and Technology). In this project, FGM (SiC-C FGM) was developed as the super heat resistant materials for base of fuselage of space planes, hemi-spherical bowls for nose cones etc. However, the concept of FGM became available in the literature in 1993 (Koizumi 1993). The ceramic-metal FGM (Koizumi 1993) is basically a particulate composite in which single composition gradient is created along the thickness direction through exponential or power-law distributions of ceramic and metal particles. These graded materials are microscopically heterogeneous and, attributed by the smooth and continuous variations of material properties along any/all of the reference coordinate directions. The graded material properties of such FGMs are usually computed utilizing three homogenization methods namely power-law distribution, exponential distribution and Mori-Tanaka scheme (Belabed et al. 2014).

Fig. 1.1 Schematic diagram of functionally graded material (FGM) (Markworth et al. 1995**).**

Figure 1.1 shows the microstructure of a FGM (Markworth et al. 1995). This FGM consists of ceramic and metal constituents which are varied from one surface to the other surface along the thickness direction. The smooth and continuous variations of composition of constituents along the thickness direction of the FG component yield continuous variations of effective material properties which in turn result continuous stresses in the same direction. The ceramic phase increases the temperature resistant

properties of the material while the metallic phase provides sufficient strength and stiffness. The continuous variations of stresses remove the chance of delamination that usually occurs in the equivalent laminate of ceramic and metallic layers. This concept of FGM is not only of interest in developing temperature barrier-materials but also in developing new functional materials. The graded properties of these materials can be tailored according to the design requirements and also have the advantage to alleviate the effect of delamination present in conventional laminated composites. Functionally graded materials can be broadly divided into two groups namely *thin* and *bulk* FGMs. Thin FGMs are basically surface coatings which are produced by physical or chemical vapour deposition (PVD/CVD), plasma spraying, self-propagating high temperature synthesis (SHS) etc. Bulk FGMs are volume of materials which require more labour intensive processes. Bulk FGMs are manufactured using powder metallurgy technique, centrifugal casting method, solid freeform technology etc. Even though FGMs were initially used for few structural components in aircraft, but the same also have lot of potentials in other high temperature structural applications such as turbine components, nozzles, cutting tools and scaffolds for tissue engineering (Wolfe and Singh 1998; Pompe et al. 2003; Cooley 2005). Since the time of reporting of FGMs, it has been an important area of research due to its potential usefulness in different fields of applications. Some of these researches which are especially relevant to this thesis work in the study of dynamic behaviour are described in the following sections.

1.2.1 Linear static analysis of FG plates

Lot of studies on the linear thermo-elastic behaviour of FG plates have been reported in the literature. These studies are basically on the development of analytical and numerical models of FG plates under the thermal and mechanical loads. Abbasi and Meguid (2000) studied the thermo-elastic behaviour of functionally graded beams, plates and shells. This study reveals the effects of volume fractions of the constituent materials on the thermo-elastic responses of the FG structures. Reddy and Cheng (2001) presented three-dimensional thermo-mechanical deformation characteristics of simply-supported FG rectangular plates using asymptotic method. The temperature, displacements and stresses of the plate are computed for different

volume fractions of the ceramic and metallic constituents, and they could serve as benchmark results to assess similar results using two-dimensional approximate plate theories. Kashtalyan (2004) presented three-dimensional elasticity solutions for a simply-supported FG plate subjected to transverse loading. Dependence of stress and displacement fields on the inhomogeneity ratio, geometry and loading is examined and discussed. Lanhe (2004) derived equilibrium and stability equations for a moderately thick rectangular FG plate under thermal loads, and reported the influences of the plate aspect ratio, the relative thickness, the gradient index and the transverse shear. Ferreira et al. (2005) developed collocation multi-quadric radial basis functions to analyze static deformations of a simply-supported FG plate using third-order shear deformation theory. The computed results are found to agree well with the solution of the problem by an alternative meshless method. Chi and Chung (2006a, 2006b) developed closed-form solutions for a simply-supported rectangular FG plate subjected to transverse loading. The analytical solutions of P-, S- and E-FGM plates are compared with the similar finite element results. This comparison reveals that the formulations for the solutions of FGM plates and homogeneous plates are similar, except for the bending stiffness of plates. Zhang and Wang (2007) used the Navier analytic method to study the thermo-elastic deformations or quasi-static thermo-viscoelastic deformations of functionally graded thin plates under mechanical or thermal load. Matsunaga (2009) presented a two-dimensional higher order shear deformation theory for the evaluation of displacements and stresses in FG plates subjected to mechanical and thermal loads. It was reported that the present 2D higher-order approximate theories could accurately predict the stresses and displacements of simply supported FG plates. Zhao et al. (2009) presented mechanical and thermal buckling analyses of FG ceramic–metal plates with arbitrary geometry including square and circular holes at the centre of the plates. This study exhibits the influences of volume fraction exponent, boundary conditions, hole geometry and hole size on the buckling strengths of these plates. Alibeigloo (2010) presented analytical solutions for the three-dimensional thermo-elastic behaviour of simply-supported rectangular FG plates. This study examined the effects of temperature change, applied mechanical load, gradient index, aspect ratio and thickness-to-length ratio on the deformation characteristics of the FG plate.

Fereidoon et al. (2011) presented a bending analysis of FG plates under transverse loading using the polynomial differential quadrature (PDQ) and the harmonic differential quadrature (HDQ) methods. It was shown that the formulation for thin FG plates was similar to that for homogeneous plates, except that the plane strain components of the middle surface in FG plates were not zero.

1.2.2 Nonlinear static analysis of FG plates

Thin and flexible FG plates under thermo-mechanical loads are susceptible to undergo large/nonlinear deformations. So, the nonlinear thermo-elastic analysis of thin FG plates is an important issue that has been addressed by many researchers. Praveen and Reddy (1998) developed a nonlinear finite element model of a FG plate for investigating its static nonlinear behaviour under thermo-mechanical loads. Yang (1999) developed an analytical model for the calculation of stresses in FG plates and showed that the corresponding solutions could also be used to study the time and temperature dependence of the stresses in a structure. Woo and Meguid (2001) presented analytical solutions for large deflection of FG plates and shallow FG shells under the combined action of mechanical and thermal loads. In this study, the effects of material properties and geometry of the plate on the stress field were addressed. Shen (2002) presented the nonlinear bending analysis of functionally graded plates subjected to uniform/sinusoidal transverse loads in thermal environment and reported the influence of temperature-rise on nonlinear bending of FG plates. Yang and Shen (2003) studied large deflection and postbuckling behaviour of rectangular FG plates under transverse as well as in-plane loads using a semi analytical method. Tsunglinwu et al. (2006) studied the effects of volume fractions of constituents of an FG plate on its nonlinear static as well as dynamic responses.

1.2.3 Linear dynamic analysis of FG plates

Yang and Shen (2001) studied the linear dynamic response of initially stressed thin FG plate subjected to distributed impulsive loads. Yang and Shen (2002) have also investigated free and transient vibration of initially stressed FG plates in thermal environment. Vel and Batra (2004) presented three-dimensional exact solutions for free and forced vibrations of simply-supported FG plates. Park and Kim (2006)

investigated thermal postbuckling and vibration responses of FG plates. Li et al. (2009) studied free vibration characteristics of FG plates in thermal environment using three-dimensional linear theory of elasticity. Hashemi et al. (2010) presented analytical solutions for free vibration of moderately thick rectangular FG plates. Akbarzadeh et al. (2011) presented analytical solutions for dynamic behaviour of a simply-supported FG plate subjected to thermo-mechanical loads. Based on a higher order shear deformation theory, Nguyen et al. (2014) performed isogeometric finite element analysis of FG plates for investigating their static, free vibration and buckling responses.

1.2.4 Nonlinear dynamic analysis of FG plates

Besides the linear dynamic analyses of FG plates, their nonlinear dynamic analyses have also been reported by many researchers. Reddy (2000) developed both analytical and finite element models of FG plates, and analysed the effects of varying material properties on the stresses and transverse deflection. Huang and Shen (2004) investigated the significant effects of temperature field and phase-volume-fraction distribution on the nonlinear dynamic responses of FG plates in the thermal environment. Chen (2005) presented the effects of the amplitude of vibration, initial conditions and volume fractions of constituents on the nonlinear vibration characteristics of a FG plate. Sundararajan et al. (2005) presented a finite element model of FG plates to study their nonlinear free vibration characteristics under thermal environment. Woo et al. (2006) performed nonlinear free vibration analysis of FG plates and showed that the nonlinear coupling effects could play a major role in dictating the fundamental frequency of FG plates. Chen et al. (2006) derived nonlinear partial differential equations for the vibration of an initially stressed FG plate based on classical plate theory. It was concluded that the nonlinear frequency responses of FG plates are sensitive to the state of initial stress, the amplitude of vibration and the volume fractions of constituents. Chen and Tan (2007) studied the effects of initial stress, geometrical imperfection and phase-volume fractions on the nonlinear dynamic responses of FG plates. Allahverdizadeh et al. (2008) derived semi-analytical solutions for nonlinear free and forced axisymmetric vibration of a thin circular FG plate. The results illustrate the nature of variation of

free-vibration frequency of a axisymmetric circular FG plate with respect to its vibration-amplitude and phase-volume fractions. Tornabene et al. (2009) derived 2D quadrature solutions for vibration analysis of FG conical, cylindrical and annular plates. Ke et al. (2010) studied nonlinear vibration of FG beams, and observed the corresponding vibration responses at positive and negative amplitudes due to the presence of quadratic nonlinear terms arising from bending-stretching coupling. Alijani et al. (2011) studied the nonlinear vibration of FG rectangular plates. The Pseudo arc-length and collocation technique are utilized in this study to obtain correct natural frequencies of the plate under thermal environment. Zhang et al. (2011) studied nonlinear oscillations and chaotic dynamics of a simply-supported rectangular plate based on asymptotic perturbation method. Hao et al. (2011) presented an analysis on nonlinear dynamic characteristics of a simply-supported FG rectangular plate subjected to transverse and in-plane excitations in the presence of time-dependent temperature. Mohammad and Singh (2011) investigated the large amplitude free and forced vibration characteristics of shear deformable FG plates using higher order shear deformation theory. This study presents the nature of variation of nonlinear frequency-ratio with the amplitude-ratio for different values of parameters like plate-aspect-ratio and phase-volume fractions. Upadhyay and Shukla (2013) investigated the nonlinear static and dynamic responses of FG skew plates under different types of mechanical load. This study addresses the effects of phase-volume fractions, skew angle and boundary conditions on the nonlinear displacement as well as moment responses of FG skew plates.

1.3 Smart structures

Design of lightweight and flexible structures is becoming an important issue for increasing space activities. These structures are susceptible to undergo large vibrations with long decay time because of their flexibility and low internal damping. This often leads to the structural fatigue and instability which result in serious deterioration on the performance of the structures under operation. Such possibilities of failure can be mitigated by integration of an active control system onto the host structure and the performance of the overall structure under operation can be enhanced. In the quest for developing high performing lightweight flexible

structures, a concept was emerged to develop the structures with self-controlling and/or self-monitoring capabilities. Utilizing the coupled interaction between electric and elastic fields in a piezoelectric material Tiersten (1969) and Forward (1981) introduced the feasibility of the effectiveness of the piezoelectric actuators to damp out two closely spaced orthogonal bending modes of a cylindrical fiber glass mast employing a simple control law. Next, Chirappa and Claysmith (1981) demonstrated the effectiveness of the use of distributed piezoelectric actuator for controlling the deformable mirror surface. Subsequently, the design and analysis of an active control of thin cantilever beam using piezoelectric materials was presented by Bailey and Hubbard (1985); Crawley and Luis (1987); Bruke and Hubbard (1987) and Im and Atluri (1989). Miller and Hubbard (1987) introduced the use of piezoelectric materials as distributed sensors. After this, Tzou and Panditha (1987) used these materials for tactile sensors of robot manipulators. Crawley et al. (1988) demonstrated the use of piezoelectric technology for control of intelligent structures. However, flexible structures integrated with distributed actuators and/or sensors made of piezoelectric materials are able to achieve self-controlling and self-sensing capabilities. Such structure is customarily known as "Smart structures" (Crawley et al. 1988) and a typical smart structure is schematically illustrated in Fig. 1.2.

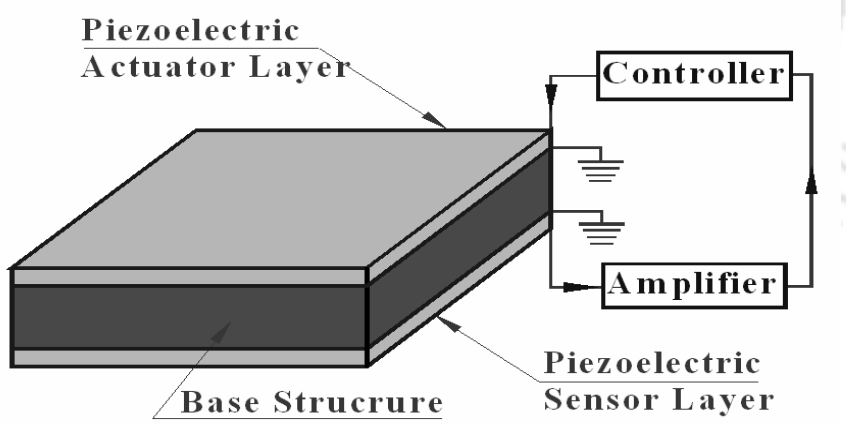

Fig. 1.2 Schematic representation of smart structure.

Such a structure is capable of adapting or taking corrective action to changing operating conditions. The passive material part of a smart structure (Fig. 1.2) is the load bearing part i.e. the host structure and the active material parts of the same are the layers/patches of piezoelectric materials which perform the operations of sensing

and actuation. Piezoelectric materials can easily be integrated with the load bearing structures by surface bonding or embedding into it and do not significantly alter the passive stiffness characteristics of the host structures (Crawley et al. 1988). The load bearing part or the passive part of the smart structure is generally called as substrate which can be beams, plates or shells.

A great deal of research on smart structures has already been reported on the exact solutions (Ray et al. 1993; Heyliger et al. 1995; Chen et al. 1996; Heyliger 1997; He 1998; Batra et al. 1996; Ray et al. 1998; Luo and Tong 2003; Kumari et al. 2003; Vel and Batra 2001) , analytical solutions (Tzou and Gadre 1989; Crawley and Lazarus 1991; Dimitriads et al. 1991a; Tauchert 1992; Clark et al. 1993), finite element (FE) analysis (Robbins and Reddy 1991; Wang and Rogers 1991; Ha et al. 1992; Rao and Sunar 1993; Hwang and Park 1993; Samantha et al. 1993; Robbins Jr and Reddy 1996; Sze and Yao 2000; Lee and Saravonos 2000; Tian and Shen 2002; Görnandt and Gabbert 2002; Cho and Oh 2004;Thornburgh et al. 2004; Mannini and Gaudenzi 2004; Hamed and Negm 2004; Giannopoulos and Vantomme 2005; Cotoni et al. 2006; Giannopoulos and Vantomme 2006; Zemčik et al. 2007; Maiti and Sinha 2011; Kapuria , Yasin and Hagedorn 2014) and active vibration control analysis (Baz and Poh 1988, 1990; Lee and Moon 1990; Tzou and Gadre 1990; Tzou and Tseng 1990, 1991; Tzou 1991; Lee et al. 1991; Baz et al. 1992; Hanagud et al. 1992; Chaudhury and Rogers 1993; Birman 1993; Devasia et al. 1993; Gu et al. 1994; Baz and Poh 1996; Varadan et al.1997; Ray 1998; Koko et al. 1998; Agarwal and Treanor 1999; Stöbener and Gaul 2000; Dong and Tong 2001; Balamurugan and Narayanan 2001, Sun et al. 2002; Narayanan and Balamurugan 2003; Ray 2003; Nguyen and Tong 2004; Kusculuoglu and Royston 2005; Gabbert et al. 2006; Nejhad et al. 2006; Gupta et al. 2006; Nguyen and Tong 2007; Balamurugan et al. 2007; Sateesh and Maiti 2009, Kapuria and Yasin 2014; Kapuria and Yasin 2014; Kapuria and Yasin 2013). The concept of smart structures has also been implemented for active control of rotor dynamic systems (Lin et al. 1993), aerospace structures (Song et al. 1992; Crawley 1994; Zhou et al. 1995) international space station (Scioscio et al. 2005), sound radiated from vibrating structures (Fuller et al. 1989; Dimitriads and Fuller 1991b; Fuller et al. 1992; Steven et al. 2001). Further more this concept has been used for structural health monitoring as a non-destructive evaluation technique (Liu and

Chang 2002; Goshal et al. 2003; Mook et al. 2003; Sastry et al. 2004; Johnson et al. 2004; Giurgiutiu et al. 2004; Zayas et al. 2007).

1.3.1 Smart FG structures

The FG materials have several advantages over the convectional composites and hence find their wide applications especially for aerospace structures. The aerospace structures are generally lightweight flexible structures and always require advanced structural design that could be achieved through the use of the concept of smart structure. So, the concept of smart structure is extensively employed for designing similar flexible FG structural components. If an FG structure is integrated with piezoelectric sensor and/or actuator patches for achieving its self-sensing and/or self-controlling capabilities, then the overall FG structure may be called as smart FG structure. A great deal of research has already been carried out on this topic and also reported in the literature. Wang and Noda (2001) presented an analysis of a smart FG structure using piezoelectric distributed actuator and found that the smart actuator could control both the stress and thermal deformation effectively. Ootao and Tanigawa (2001) studied the performance of a piezoelectric actuator for controlling the transient thermo-elastic displacements of FG plates. Chen et al. (2002) developed a three-dimensional theory for free vibration analysis of smart FG rectangular plates. Liew et al. (2003) performed the static and dynamic analyses of smart FG plates under a temperature gradient, and determined the optimum configurations of the piezoelectric sensor/actuator pairs for effective control of FG plates under various thermal as well as mechanical loads. Zhong and Shang (2003) derived three-dimensional exact solutions for a simply-supported smart FG plate, and studied the influences of the different FG material properties on the structural response of the plate to the mechanical and electric stimuli. Liew et al. (2003) developed a finite element model for the static and dynamic pizeo-thermo-elastic analyses of smart FG plates under thermal environment. This work presents the effects of the constituent-volume fractions and the influence of feedback control gain on the static and dynamic responses of the FG plates. Liew et al. (2004) presented numerical results for shape control of FG plates under a temperature gradient by optimizing the voltage distribution for the open-loop control and the displacement control-gain values for

the closed-loop feedback control. They also carried out similar study of optimal control of FG plates using genetic algorithm (Liew et al. 2004). Altay and Kmeci (2005) derived two-dimensional approximate equations for vibration of FG piezo-electro-magnetic plate. Shen (2005) presented post-buckling analysis for a simply-supported shear deformable FG plate integrated with piezoelectric distributed actuators, where the smart FG plate was considered to be subjected to a combined load of mechanical, electrical and thermal loads. In this study, the effects of temperature-rise, constituent-volume fractions, applied voltage, the character of in-plane boundary conditions as well as initial geometric imperfections on the post-buckling responses of the smart FG plate are studied. Ebrahimi and co-workers (2008, 2009) carried out an analytical investigation on the free vibration behaviour of thin/moderately thick circular FG plates integrated with two uniformly distributed actuator layers made of piezoelectric material (PZT4). This study exhibits effect of variation of the gradient index of FG plate on its free vibration characteristics. Shakeri and Mirzaeifar (2009) presented a finite element formulation based on layer-wise theory for analysing the quasi-static and free vibration response of smart FG plates to impulse loads. The authors (Shakeri and Mirzaeifar, 2009) showed that the non-linear distribution of electric potential in thick piezoelectric layers could be captured using the proposed model. Xiang and Shi (2009) studied FG-piezoelectric sandwich cantilever plates under an applied electric field and/or a thermal load for finding out the influences of electro-mechanical coupling, FG index and temperature change on the bending behaviour of piezoelectric actuators or sensors. Mehrabadi et al. (2009) presented free vibration analysis of a smart FG circular plate using classical plate theory (CPT). In this work, the phase-volume fractions were varied for different boundary conditions and their effects on the resonant frequencies were studied.

The smart FG structures are usually thin-walled flexible structures embedded with piezoelectric distributed actuators. Since such thin-walled and flexible smart FG structures are prone to undergo large/nonlinear deformations, researchers have already carried out nonlinear static and dynamic analyses of smart FG structures for the purpose of understanding more realistic structural behaviour of the same under thermo-mechanical loads. Yang et al. (2003) presented semi-analytical solutions for large amplitude vibration of rectangular FG laminated plates integrated with

piezoelectric sensors and actuators. Results of this study illustrate that the normalized frequency of the FG laminated plate is very sensitive to vibration amplitude, out-of-plane boundary support, temperature change, in-plane compression and the side-to-thickness ratio. The same study (Yang et al. 2003) also shows that FG laminated plates change the inherent "hard-spring" characteristic to "soft-spring" behaviour at large vibration amplitudes. Huang and Shen (2004) analyzed the nonlinear vibration responses of a smart FG plate under the thermal environment. The host FG plate is integrated with piezoelectric layers and the corresponding analysis reveals significant effects of temperature field and constituent-volume fractions of FG substrate on the nonlinear dynamic response of overall smart FG plate. Yang et al. (2004) carried out a nonlinear bending analysis of smart FG plates in the thermal environment using a differential quadrature method. This analysis addresses nonlinear bending characteristics of smart heated FG plates in regard to the applied actuator-voltage, the constituent-volume fractions and the temperature gradient. Ebrahimi and Rastgoo (2009) presented nonlinear analytical solutions for a circular FG plate coupled with piezoelectric layers. These analytical solutions reveal controlled dynamic characteristics of the smart circular FG plate with respect to the applied actuator-voltage, thermal environment and constituent-volume fractions in FG substrate plate. Ebrahimi and Rastgoo (2009) also carried out similar nonlinear analysis of thin smart circular pre-stressed FG plate to illustrate the control of nonlinear deflections and natural frequencies using high control voltages. Yiqi and Fuming (2010) analysed the actively controlled/uncontrolled nonlinear dynamic response of a FG plate integrated with piezoelectric layers and demonstrated corresponding influences of mechanical load, electric load, constituent-volume fraction in FG substrate and geometric parameters. Fakhari et al. (2011) developed a finite element model of smart FG plate for investigating its nonlinear free and forced transient vibration characteristics under thermo-electro-mechanical load. The numerical results in this study illustrate the effects of FG volume fraction exponent, applied voltage to piezoelectric layers, thermal load and vibration amplitude on the nonlinear free/forced vibration characteristics of the smart FG plate. Behjat and Khoshravan (2012) carried out nonlinear static and free vibration analyses of smart FG plates under different sets of mechanical and

electrical loads. The corresponding numerical results illustrate the effects of material composition and boundary conditions on nonlinear responses of smart FG plates.

1.4 Piezoelectric composites

In the development of smart structures, the monolithic piezoelectric materials are extensively utilized because of their commercial availability. However, there are some limitations in the use of monolithic piezoelectric actuators. These actuators are vulnerable to accidental breakage during handling and bonding procedures due to their inherent brittle nature especially to conform to curved surfaces of host structure. Apart from this brittle nature, these actuators provide low control-force because of the small magnitudes of their stress/strain coefficients. It is also difficult to achieve the control-force in a particular direction using such actuators. These drawbacks in the use of monolithic piezoelectric actuators lead to the development of a new class of composite materials named as piezoelectric composites (PZCs). In PZC materials, the reinforcements are made of the existing monolithic piezoelectric materials while the matrix is the conventional polymer material. The use of polymer-matrix causes enhanced flexibility and conformability of PZCs while tailoring of piezoelectric reinforcement within the polymer matrix provides wide range of material properties as compared to the existing monolithic piezoelectric materials. Being a composite material, such PZCs have the ability to cause anisotropic actuations those are useful to have control-force in the desired directions. Research on tailoring of piezoelectric stress/strain coefficients through the proposition of different PZCs started in 1980s. Chan and Unsworth (1989) derived a simple micromechanics model for the analysis of piezoelectric ceramic/polymer 1-3 composites. Smith and Auld (1991) predicted the effective properties of vertically reinforced 1-3 piezoelectric composites using the strength of material approach of micromechanics. These materials have improved mechanical performance and electro-mechanical coupling, and are useful for studying the thickness mode oscillations of structures. In order to attain the in-plane actuation by the piezoelectric composites, Bent et al. (1995) developed piezoelectric fiber composites. But, since the control authority of these piezoelectric composite materials is very low, Bent and Hagood (1997) extended this work for intensifying the control authority of these

materials using interdigitated electrodes which create the electric field along the length of the piezoelectric fibers. These composites are known as Active Fiber Composites (AFCs). Zhang and Shen (2007) investigated the usefulness of AFCs for vibration control of flexible structures. Macro-fiber composites were developed by National Aeronautical Space Agency (NASA) to improve control authority of smart composite actuators (Wilkie et al. 2000). Mallik and Ray (2003) proposed the concept of horizontally reinforced 1-3 piezoelectric composite (PFRC) and predicted the effective electro-elastic properties of this composite. Kumar and Chakraborty (2008) presented a micromechanics model to predict the thermal, mechanical and electrical properties of the horizontally reinforced 1-3 piezoelectric composite. Kapuria S, Kumari (2011) presented three dimensional micromechanics model based on isofield method for predicting the effective properties of PFRC material. The constructional features of the lamina made of the horizontally (Mallik and Ray 2003) and vertically (Smith and Auld 1991) reinforced 1-3 piezoelectric composite materials are schematically illustrated in Figs. 1.3 (a) and (b), respectively. It is to be noted that the designation "1-3" represents the connectivity pattern of these composite materials. Of the connectivity pattern, 1-3, the first digit refers to the number of connectivity of the fiber reinforcement while the second indicates the number of connectivity of the matrix phase (Newnham et al. 1978).

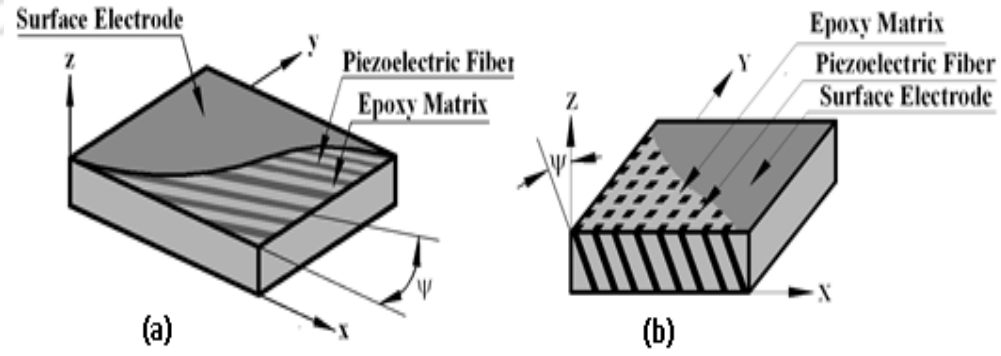

Fig. 1.3 Schematic diagram of (a) horizontally and (b) vertically reinforced 1-3 piezoelectric composites.

The piezoelectric fibers in the lamina of the horizontally reinforced 1-3 piezoelectric composite material (Mallik and Ray 2003) are aligned horizontally such that they are parallel to each other and coplanar with the top and bottom surfaces of

the lamina. The fiber orientation angle with respect to the x-axis is denoted by ψ. In case of the lamina of the vertically reinforced 1-3 piezoelectric composite material (Smith and Auld 1991), the piezoelectric fibers are aligned in the vertical plane such that they are coplanar with either the xz plane or the yz plane while they may be inclined in the vertical plane making an angle ψ with the vertical direction (z).

The effective piezoelectric coefficient (e_{31}) of the horizontally reinforced 1-3 piezoelectric composite (Mallik and Ray 2003) has improved magnitude as compared to the similar magnitude of corresponding monolithic piezoelectric fiber. Since this piezoelectric coefficient (e_{31}) quantifies the in-plane actuation force due to the applied electric field in the thickness direction, the improved magnitude of e_{31} results greater in-plane actuation force. For this advantage, horizontally reinforced 1-3 piezoelectric composite (PFRC) has been utilized widely as a material for distributed actuator especially in control of bending deformations of thin-walled flexible structures. As per the present direction of research, some of the researches on the use of PFRC for controlling static and dynamic responses of FG plates are furnished here. Ray and Sachade (2006) derived exact solutions for the static analysis of FG plates integrated with a layer of piezoelectric fiber reinforced composite (PFRC) material. The numerical results in this study reveal that the coupling of bending and extension takes place in the FG plates even if the PFRC layer is not subjected to the applied voltage. Reddy and Ray (2007) derived the closed form solutions for optimal control of vibration of smart FG plate and demonstrated the change in the controlled response of smart FG plate for the placement of PFRC actuator on the softest side of FG substrate instead of the stiffest side of the same. A similar bidirectional flexure analysis of smart FG plate has also been reported by Shiyekar and Kant (2010).

Although the actuation-capability of PFRC actuators is higher than that of monolithic piezoelectric actuators (Ray and Sachade 2006; Reddy and Ray 2007), but its (PFRC) applications are limited to thin-walled flexible structures which normally undergo large/nonlinear deformations. So, in the use of PFRC actuators for thin flexible FG plates, the large/nonlinear deflection analysis of such smart FG plates has been addressed in the literature. Panda and Ray (2008) presented a nonlinear static finite element analysis of simply-supported smart FG plates in the presence/absence

of the thermal environment. This study presents the effect of variation of piezoelectric fiber orientation angle in the PFRC patches on their actuation-capability for counteracting the large deflections of FG plates. Xia and Shen (2009) presented the nonlinear vibration responses of a shear deformable FG plate integrated with PFRC actuators in thermal environment. This analysis reveals that the effect of control voltage on the natural frequency of an FG plate with PFRC actuators is larger than that of the same FG plate with monolithic piezoelectric actuators.

1.5 Active constrained layer damping

Although the smart composite materials are developed in order to have better performance of smart structures, but still they are unable to provide good enough control authority. This is due to the fact that there is a huge difference between the electrically and mechanically induced stresses in the smart structure which makes them incompatible with the host structure. Thus, the quest for further improvement in the performance of the smart structures led to the concept of active constrained layer damping (ACLD) treatment (Nostrand et al. 1994; Baz and Ro 1995a,995b; Azvine et al. 1995; Varadan et al. 1996; Kumar and Singh 2012).

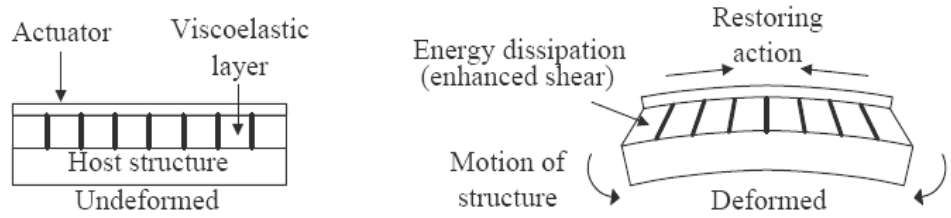

Fig. 1.4 Working principle of active constrained layer damping treatment (Illaire and Kropp, 2005).

Figure 1.4 shows the ACLD arrangement consisting of a layer of viscoelastic material constrained between the host structure and an active constraining layer made of piezoelectric material. When the host structure undergoes bending deformation, the active constraining layer not only restrains the constrained soft viscoelastic layer to undergo transverse shear deformation but also enhances its transverse shear deformation to cause improved damping characteristics of the overall structure over the passive constrained layer damping (PCLD). If the constraining layer is not subjected to applied voltage, the treatment turns out to be

the conventional passive constrained layer damping (PCLD) treatment. Thus, the ACLD treatment provides the attributes of both active and passive damping acting in unison because of the fact that the passive damping mechanism is integral to this treatment. Also, the task of controlling the transverse shear deformations of soft viscoelastic layer is compatible with the low control authority of the piezoelectric actuators. Hence, the ACLD treatment has earned wide acceptability for efficient and reliable active control of flexible structures (Shen 1994 1997; Yellin and Shen 1996; Ray and Baz 1997; Shi et al. 2004; Illaire and Kropp 2005; Koma and Mehrabian 2011). Since stiffness and damping of the viscoelastic materials have to be considered while developing the structural dynamic model, the GHM (Golla-Hughes-McTavish) technique (Golla et al. 1985) is one of the useful tool for modelling these materials in the time-domain.

Some of the available studies for active constrained layer damping of plates using monolithic piezoelectric or piezoelectric composite actuators are furnished here. Zhang and Zhang (1998) presented the active control and passive control of thin plates using LQR control strategy. The numerical results show that the hybrid control technique used is better for vibration control of plates. Park and Baz (1999) investigated the active control of plates theoretically as well as experimentally using proportional and derivative control laws. The results obtained indicate the potential advantage of ACLD treatments for damping of structural vibration in comparison to passive constrained layer damping (PCLD). Sung and Sze (2000) studied the vibration responses of composite laminates integrated with a smart constrained layer damping using finite element method. Chantalakhana and Stanway (2001) presented numerical as well as experimental studies of active constrained layer damping of clamped-clamped plates and showed the suppression of different modes of vibration of plates within certain frequency range. Sheng and Zhao (2004) presented active control of structural vibration and acoustic radiation of a fluid loaded composite plate using finite element approach, and demonstrated the usefulness of ACLD treatment to induce more effective damping in the overall smart plate. Ray and Reddy (2004) presented active structural acoustic control of laminated composite plates using PFRC as the constraining layer. The significant effect of variation of

piezoelectric fiber orientation angle in the PFRC layer on controlling the structure-borne sound radiated from thin laminated plates has been studied.

For better utilization of monolithic piezoelectric as well as piezoelectric composite distributed actuators in control of vibration of FG structures, the idea of ACLD treatment has also been utilized by many researchers. Lim et al. (2002) developed a three-dimensional closed-loop finite element model to study actively and passively damped vibration characteristics of a FG structure. The results obtained showed that ACLD is somewhat better for vibration suppression than either the purely passive or the active system and provides higher structural damping with less control gain when compared to the purely active system. Ray (2006) investigated the performance of PFRC as a material of the constraining layer of ACLD treatment for active control of FG plates. The analysis revealed that the activated patches of the ACLD treatment are more effective in controlling the vibration of FG plates when the patches are attached to the surface of the FG plates with minimum stiffness than when they are attached to the surface of the same with maximum stiffness. Panda and Ray (2008) studied geometrically nonlinear vibration of FG laminated composite plates integrated with a patch of active constrained layer damping. Panda and Ray (2009) presented the geometrically nonlinear dynamic analysis of FG plates integrated with a patch of active constrained layer damping (ACLD) treatment. The analysis suggests the potential use of the ACLD treatment with its constraining layer made of the PFRC material for active control of geometrically nonlinear forced vibrations of FG laminated composite plates. They also studied the effect of piezoelectric fiber orientation angle in the active constraining PFRC layer on the damping characteristics of the overall FG plates. Inman and Yang (2013) investigated the frequency dependent viscoelastic dynamics of a multifunctional composite structure using finite element analysis. The authors (Inman and Yang 2013) also conducted experiments for verification of numerical results obtained through finite element analysis.

1.6 Graded fiber-reinforced composites

In recent years, the concept of FGM has been further utilized by many researchers to develop light weight, high strength functionally graded fiber-reinforced composites

for alleviating several structural discrepancies in the use of traditional fiber-reinforced composite laminates. These FG composites are a new class of fiber-reinforced composite materials and generally known as graded fiber-reinforced composites (GFRCs) or functionally graded fiber-reinforced composites (FGFRCs). Generally, a GFRC/FGFRC has varying fiber volume fraction (FVF) and/or fiber orientation angle (FOA) which create the graded material properties within the domain of the material. Since these parameters (FVF and FOA) could easily be tailored to meet specific requirement in the design of a structural component, GFRCs/FGFRCs have found wide applications especially for reducing thermal deflection of composite laminates, stress concentration near a cut-out within a composite laminate and inter-laminar stress concentration in composite laminates. A considerable number of reports are available in the literature for the design and analysis of graded fiber-reinforced composite (GFRC) lamina with varying fiber volume fraction (FVF) along its in-plane directions. Martin and Leissa (1990) first proposed a GFRC lamina by varying the FVF along one of the in-plane directions and derived exact solutions of a plane stress problem under different boundary conditions. Subsequently, the work was extended to investigate the effects of graded material properties of a GFRC plate on its critical buckling loads and resonant frequencies (Leissa and Martin 1990). The variation of fiber spacing or FVF along in-plane direction of GFRC lamina was also utilized for mitigating some of the structural problems like high stress concentration, reinforcement of shear walls etc. (Shiau and Cheu 1991; Siau and Lee 1993; Meftah et al. 2007,2008). The variation of FVF along the thickness direction of a GFRC lamina was introduced by Wetherhold et al. (1996) for eliminating or controlling thermal deflections of composite laminates. In this study, a FG symmetric laminated fiber-reinforced composite beam with varying FVF along the thickness direction is analysed to demonstrate the advantage of creating graded material properties for controlling the thermal deflection of the laminated beam. Kubiak (2005) considered variable FVF across the width of a thin-walled rectangular composite plate and investigated its dynamic response under the in-plane pulse loading. Benatta et al. (2008) considered continuous variation of FVF along the thickness direction of a short FG fiber-reinforced composite beam for demonstrating the effects of different distributions of FVF on the bending response

of the beam. Bedjilili et al. (2009) presented free vibration characteristics of a symmetric composite beam with the variable FVF along the thickness direction and reported the effect of varying FVF on the natural frequencies. Kuo and Shiau (2009) presented the effect of variation of FVF along the thickness direction of a laminated composite plate on its critical buckling loads and natural frequencies. Oyekoya et al. (2009) developed a finite element model of a composite plate having functionally variable FVF along any of the axes of reference coordinate system. The study showed enhancement of structural integrity and strength maximization of composite structures through gradation of material properties. Bouremana et al. (2009) performed a thermo-elastic analysis of a symmetric laminated composite beam in order to minimize the thermal deformation of the beam by varying its FVF along the thickness direction. Fu et al. (2010) proposed various gradient-designs across the thickness of the fiber-reinforced composite plates including non-uniform distributions of fiber-orientation and FVF. This three-dimensional analysis demonstrated exact stresses in the proposed kinds of laminated composite plates. This study also demonstrated the methods for reduction of inter-laminar stress-concentration problem in the composite laminates. Kargarnovin and Hashemi (2012) presented buckling analysis of multilayered cylindrical shell with variable FVF along longitudinal direction. Tahouneh et al. (2013) considered a thick annular graded fiber-reinforced composite plate of variable FVF along the thickness direction and analyzed its free vibration characteristics.

Similar to FVF, the fiber-orientation angle is another important parameter for creating graded material properties along the thickness direction of a fiber-reinforced composite lamina. Batra and Jin (2005) analyzed a graded composite plate of variable fiber-orientation angle along the thickness direction and investigated the effect of the variation of fiber-orientation angle in the plate on its resonant frequencies. Han et al. (2009) presented linear and nonlinear analyses of composite plates/shells those have variable fiber-orientation angle along the thickness direction according to a sigmoid distribution. This analysis revealed the effect of the varying fiber orientation on the mechanical responses of the structures. Cho and Rowlands (2009) presented an optimized local fiber-orientation angle near the holes or notches of composite structure in order to reduce associated tensile stress concentration. Panda and Ray

(2009) presented the controlled nonlinear transient responses of laminated composite plates of variable fiber-orientation angle along the thickness direction. Yas and Aragh (2010, 2011) analyzed the free vibration characteristics of cylindrical panels with continuous variations of FVF and fiber-orientation angle along the radial direction. The same authors (Yas and Aragh 2010, 2011) also presented free vibration characteristics of fiber-reinforced plates/panels resting on elastic foundations considering continuous variation of fiber-reinforcement in the thickness direction. The study indicates the advantages of graded composite laminated plates/panels over the traditional composite laminated plates/panels.

In the aforesaid available studies on the design and analysis of structural behavior of graded fiber-reinforced composite lamina/laminate, the graded material properties are estimated using standard micromechanics theories. Since the implementation of standard micromechanics theories in a straight forward manner may not provide good enough estimation of graded material properties of a GFRC lamina (Aboudi et al. 1995), new micromechanics models have been developed by several researchers particularly for particulate and fiber-reinforced FG composites. Aboudi et al. (1995,1999) proposed a coupled higher-order theory for functionally graded composites with partial homogenization. Although this higher-order theory provides good estimations of material properties of FG solids, but the requirement of this theory could be justified through a parallel work of Reiter and Dvorak (1997,1998). Reiter and Dvorak (1997, 1998) proposed a micromechanics model for graded composite materials using standard micromechanics theories. This micromechanics model does not support the requirement of higher-order theory in evaluation of graded material properties of FG solid but, it is addressed that the higher-order theory is required only for the locations of low field averages and high gradients within the domain of a FG solid (Dvorak and Zuiker, 1994).

1.7 Research motivation and objectives

Literature review was performed with an objective of understanding the state-of-art research in the broad area of smart FGM structures with a particular interest in control of vibration of such structures. The literature review reveals that a substantial number of research-works have been reported on the linear vibration analysis of

smart FG (metal-ceramic) plates under the thermal environment. However, the analyses on the nonlinear vibration of the same are still less in number. Moreover, these analyses address the time-domain responses of FG plates integrated either with the monolithic piezoelectric/piezoelectric composite actuators or the layer/patches of ACLD treatment. Similar to these nonlinear time-domain analyses, the nonlinear frequency-domain analysis of smart FG plates under the thermal environment is an equally important issue with reference to the control authorities of monolithic piezoelectric/piezoelectric composite actuators and ACLD treatment. Since this issue has not yet been addressed in the literature, an investigation on the nonlinear vibration characteristics of smart FG (metal-ceramic) plates in the frequency-domain deserves a thorough investigation. These time-domain responses of heated smart FG plates exhibit the variations of its nonlinear vibration characteristics and corresponding control-performance of piezoelectric actuators with time for standard transient loads. Similar to the transient loads, the same plate may be utilized under harmonic mechanical excitations which appear in many engineering structural applications. In this case of harmonic mechanical excitations, the variations of its vibration characteristics as well as the control-performance of piezoelectric actuators with frequency of operation are the main concerns those are not yet available in the literature. In view of this, one of the objectives of the present research is decided as the frequency-domain analysis of non-linear vibration of smart FGM (metal-ceramic) plates under the thermal environment. Specially, the effect of temperature on the nonlinear vibration characteristics of smart FG plates and, also on the corresponding control authorities of piezoelectric composite (PFRC) actuator and ACLD treatment has been investigated.

A considerable number of studies on the graded fiber-reinforced composite (GFRC) laminas/laminates with varying fiber-volume fraction (FVF) and/or fiber-orientation angle along the thickness direction are reported in the literature. These studies are carried out mainly for improved structural characteristics of laminated composite structures. The applications of GFRC for attaining continuous variations of stresses/material properties across the thickness of a composite laminate are also addressed in limited literatures in which the graded material properties are created through the variation of fiber-orientation angle. The variation of fiber-orientation

angle within an FRC lamina yields a GFRC lamina but, the orthotropic material properties of FRC switch to anisotropic material properties to reach GFRC. This alteration of material properties may not be acceptable in general. So, the FVF becomes an important parameter in creating an orthotropic GFRC lamina. However, the use of orthotropic GFRC lamina in attaining continuous variations of stresses/material properties across the thickness of a composite laminate has been demonstrated in only one literature (Fu et al. 2010) till the date. Although this study (Fu et al. 2010) shows continuous variations of stresses by the use of orthotropic GFRC laminas, but the stress-concentration for every in-plane normal stress arises at the top/bottom surface of the laminate. Moreover, the use of GFRC lamina for all layers of laminate and the consideration of low FVF at interlaminar surfaces of plies may significantly affect the rigidity of the laminate. This issue of the change of laminate-rigidity is not addressed in the same study (Fu et al. 2010) while achieving continuous variations of stresses/material properties in the thickness direction. So, further research is needed on the design and analysis of graded laminated composite structures especially by the use of graded orthotropic composite laminas. Thus, another objective of present research is decided to design a graded laminated composite plate through the proposition of a microstructure of orthotropic GFRC laminas in such a manner that the stresses/material properties vary continuously retaining sufficient laminate-rigidity and stresses within their permissible values. This objective is decided with the aim of developing advanced composite structures. However, an associated issue in the design of such advanced composite structures is the suppression of their vibration that is often carried out using piezoelectric actuators or the same in advanced form of active constrained layer damping (ACLD). So, the analysis of vibration characteristics of graded laminated fiber-reinforced composite plate integrated with a layer of ACLD is chosen as an additional objective in the present research.

In order to fulfil the aforesaid objectives in the present research, the following theoretical analyses are carried out,

(a) Harmonically excited nonlinear vibration of heated FG (metal-ceramic) plates integrated with PFRC distributed actuator layer.

(b) Piezo-viscoelastically damped (ACLD) nonlinear frequency response analysis of FG (metal-ceramic) plates with a heated plate-surface.

(c) Determination of size and location of PFRC/ACLD patch over the surface of FG (metal-ceramic) substrate plate for effective control of nonlinear frequency responses of the overall smart FG plate with/without a heated plate-surface.

(d) Design and evaluation of effective elastic properties of a graded orthotropic fiber-reinforced composite lamina.

(e) Design and analysis of graded laminated fiber-reinforced composite plates with an objective of continuous variations of stresses/material properties in the thickness direction.

(f) Nonlinear frequency response analysis of graded laminated fiber-reinforced composite plates integrated with an ACLD layer.

1.8 Contributions

The following contributions in the field of smart FG structures have been made towards the preparation of the dissertation,

(a) A geometrically nonlinear incremental finite element model of FG (metal-ceramic) plate integrated with PFRC-actuator layer is developed for investigating the effect of host-plate-surface temperature on the nonlinear dynamic behaviour of the overall smart FG plate in the frequency-domain. The effect of temperature on the smart damping in the overall FG plate caused by PFRC-actuator layer is presented.

(b) A three-dimensional incremental finite element model of FG plates (metal-ceramic) integrated with an ACLD layer is developed for the geometrically nonlinear frequency response analysis of the overall FG plate under a host-plate-surface temperature. A time-domain model (GHM model) of material modulus function of constrained viscoelastic layer in ACLD arrangement is implemented for the analysis of overall FG plate in the frequency-domain. The effect of host-plate-surface temperature on the control authority of ACLD layer is investigated.

(c) An arc-length extrapolation technique (Lau et al. 1990) is implemented for numerical solutions of nonlinear incremental finite element equations of motion

of smart FG plates. In this implementation of the solution procedure (Lau et al. 1990), a new strategy for selecting the arc-length in each incremental step is proposed in order to reduce the difficulties in the convergence of solutions.

(d) A new numerical strategy for determination of size and location of PFRC/ACLD patch over the host-plate-surface for effective control of vibration of overall smart FG plate is presented.

(e) A microstructure for graded orthotropic fiber-reinforced composite lamina with varying fiber-volume fraction (FVF) in the thickness direction is designed and its (lamina) effective graded elastic properties are estimated using finite element procedure in conjunction with an available micromechanics model for FG composites (Reiter and Dvorak 1997,1998).

(f) A novel lamination scheme is proposed in the design of composite laminates using conventional as well as graded orthotropic fiber-reinforced composite plies. The objective in this proposed lamination scheme is to attain continuous variations of stresses/material properties in the thickness direction retaining sufficient laminate-rigidity and stresses within their permissible values.

(g) The conversion of a conventional laminated composite plate into a graded laminated composite plate according to the proposed lamination scheme is demonstrated and its (conversion) suitability is justified through the static as well as dynamic analyses of both (conventional and graded) the plates. The effect of this conversion as per the proposed lamination scheme on the control authority of ACLD layer is also investigated.

1.9 Dissertation overview

A brief introduction and review of literature on the linear/nonlinear analysis of FG structures, smart structures, piezoelectric composite materials, and graded fiber-reinforced composite laminas/laminates are presented in Chapter 1. Subsequently, the scope and objectives of the present research are outlined.

Chapter 2 deals with the nonlinear frequency response analysis of smart FG (metal-ceramic) plates under a host-plate-surface temperature. The host FG plate is

integrated with a PFRC-actuator layer. First, a geometrically nonlinear incremental finite element model of the smart FG plate is derived for the analysis in the frequency-domain. Next, the implementation of an incremental arc-length solution methodology is presented along with a new strategy for selecting the arc-length in each incremental step. Finally, the numerical results are presented for investigating the effect of temperature in substrate FG plate on the nonlinear vibration characteristics of the overall smart FG plate in the frequency-domain and, also on the corresponding control authority of PFRC-actuator layer.

In Chapter 3, the nonlinear frequency responses of FG plates integrated with an ACLD layer are presented through the derivation of a nonlinear incremental finite element model of overall FG plates. The implementation of time-domain model (GHM method) of material modulus function of viscoelastic layer for the analysis of overall FG plate in the frequency-domain is presented. The numerical results in this chapter present the effect of temperature at host-plate-surface on the nonlinear frequency responses of overall smart FG plates. The effect of the same (temperature) on the performance of ACLD layer in control of nonlinear frequency responses of FG plates is also presented.

A new numerical strategy for determination of size and location of PFRC-actuator/ACLD patch over the surface of FG substrate plate for effective control of frequency responses of overall FG plates is presented in Chapter 4. The numerical results in this chapter present the effective size and location of PFRC-actuator/ACLD patch in the absence as well as the presence of host-plate-surface temperature.

A microstructure for graded orthotropic fiber-reinforced composite laminas with varying fiber-volume fraction along the thickness direction is presented in Chapter 5. First, the constructional features of microstructure are illustrated and then, a formulation for estimating graded material properties is presented. Subsequently, a three-dimensional finite element model of corresponding representative volume (RV) is derived for numerical evaluation of effective graded material properties. A new lamination scheme in the design of graded laminated composite plates is proposed in this chapter. The new lamination scheme is demonstrated through the conversion of a conventional laminated composite plate into a graded laminated composite plate. A finite element model of conventional/graded laminated

composite plate is derived for bending analyses of both (conventional and graded) the laminated composite plates. Finally, the suitability of proposed lamination scheme is substantiated through the comparison between the bending responses of both the laminated composite plates.

The suitability of new lamination scheme proposed in Chapter 5 is again substantiated in Chapter 6 through the evaluation of nonlinear frequency responses of both (conventional and graded) the laminated composite plates. Every (conventional/graded) laminated composite plate is considered to be integrated with an ACLD layer and a corresponding incremental finite element model is derived for the analysis of overall smart laminated composite plate in the frequency-domain. The numerical results present the vibration characteristics of both the laminated composite plates in the frequency-domain, which also indicate the changes in dynamic characteristics of conventional laminated composite plate when it is converted to graded laminated composite plate. The changes in control authority of ACLD layer due the conversion of substrate composite plate are also presented.

Finally, the major conclusions from the work carried out and the scopes for further work are outlined in Chapter 7. The list of references is provided at the end of the dissertation.

Chapter 2

HARMONICALLY EXCITED NONLINEAR VIBRATION OF HEATED FUNCTIONALLY GRADED PLATE INTEGRATED WITH PIEZOELECTRIC COMPOSITE ACTUATOR LAYER

This chapter deals with the nonlinear frequency-response analysis of a smart FG plate with a heated plate-surface. The substrate FG plate is integrated with a PFRC actuator-layer and the effect of temperature on the performance of this smart actuator layer in control of nonlinear frequency-response of smart FG plate is investigated. The analysis also reveals the effect of temperature on the non-linear vibration characteristics of the smart FG plate in the frequency domain. An incremental closed-loop finite element model of the smart FG plate is developed for the analysis. The numerical results are evaluated by implementing an arc-length extrapolation (Lau et al. 1990) solution strategy along with the proposition of a new strategy for selecting incremental arc-length.

2.1 Introduction

The literature review in the previous chapter (Chapter 1) shows limited studies (Ebrahimi and Rastgoo, 2009a, 2009b; Xia and Shen 2009; Yiqi and FuYiming 2010; Fakhari et al. 2011; Behjat and Khoshravan 2012) on the geometrically nonlinear vibration analysis of smart FG (ceramic-metal) plates under thermal environment. Moreover, these studies were carried out mainly for investigating the performance of monolithic piezoelectric or PFRC actuators (Mallik and Ray 2003) for nonlinear vibration control of FG plates under transient mechanical loads. The nonlinear vibration analysis of smart heated FG plates under the harmonic mechanical load is an equally important issue that is not yet reported in the literature. Therefore, a nonlinear frequency-response analysis of FG plates integrated with a PFRC actuator layer is carried out in this chapter. The temperature-dependent material properties of FG substrate plate are assumed to be graded along the thickness direction according to a power-law distribution in terms of volume fractions of its ceramic and metal constituents (Praveen and Reddy 1998; Woo

and Meguid 2001). The ceramic-rich surface of the FG plate is considered to be exposed to a high temperature while the metal-rich surface of the same is in the room temperature. The smart actuator layer is attached to the metal-rich surface in order to keep it (actuator) out of thermal effect. The analysis is mainly for investigating the effect of high substrate-plate-surface temperature on the harmonically excited nonlinear vibration characteristics of smart FG plates and also, on the corresponding actuation-capability of PFRC actuator layer. A negative velocity feedback control strategy is utilized so as to achieve smart damping in the overall plate. Based on the von Karman nonlinear strain-displacement relations, an incremental closed-loop finite element model of the overall smart FG plate is derived by assuming its (plate) periodic motion. An arc-length extrapolation technique with a new strategy for determining the arc-length is used for numerical solutions. The numerical results are presented according to the aforesaid objectives of the present analysis.

2.2 Problem statement and incremental finite element formulation

Figure 2.1 shows a FG plate integrated with a PFRC layer. The FG substrate plate is made of two homogeneous and isotropic constituent materials such as ceramic and metal. The middle plane of the substrate FG plate is considered as the reference plane and one corner (Fig. 2.1) of the reference plane is considered as the origin of the reference coordinate system such that $x = 0, a$ and $y = 0, b$ represent the boundaries of the overall laminated FG plate. The thickness of the FG substrate plate is denoted by h and that of the PFRC layer is symbolized by h_p. One of the top and bottom surfaces of the substrate FG plate is ceramic rich surface while the other surface is the metal rich surface. The ceramic rich surface is considered to be exposed to a high temperature (T_c) and the metal rich surface is always exposed to the room temperature (T_m = 300 K). The planes parallel to the reference plane are assumed to be isothermal planes and the temperature varies only across the thickness of the substrate FG plate. The PFRC layer is always attached to the metal surface of the FG substrate that is exposed to the room

temperature. This attachment removes the effect of temperature on the PFRC layer. The piezoelectric fibers in the PFRC layer are longitudinally aligned in the plane parallel to the xy-plane and oriented at angle ψ with respect to the x-axis.

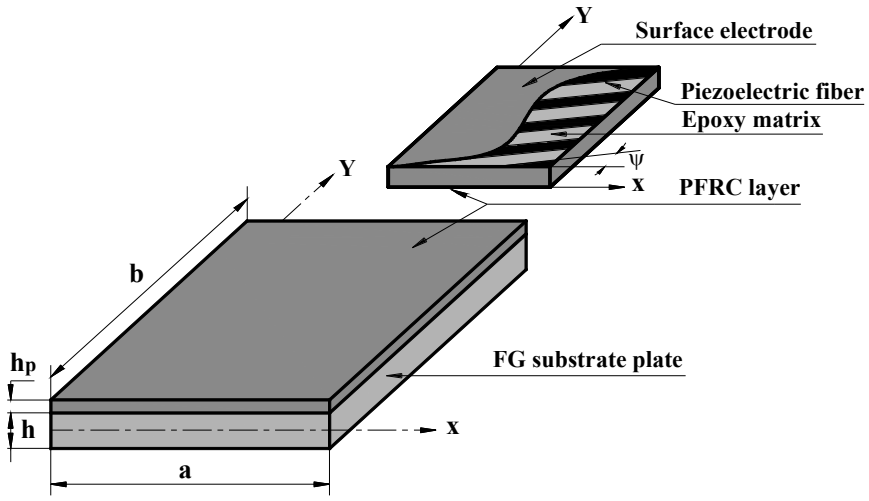

Fig. 2.1 Schematic diagram of FG plate integrated with a layer of piezoelectric fiber reinforced composite (PFRC).

The state of strain and the state of stress at a point in the overall laminated plate can be expressed as,

$$\{\varepsilon_b\}=\{\varepsilon_x \quad \varepsilon_y \quad \varepsilon_{xy}\}^{\mathrm{T}} \text{ and } \{\varepsilon_s\}=\{\varepsilon_{yz} \quad \varepsilon_{xz}\}^{\mathrm{T}} \tag{2.1}$$

$$\{\sigma_b\}=\{\sigma_x \quad \sigma_y \quad \sigma_{xy}\}^{\mathrm{T}} \text{ and } \{\sigma_s\}=\{\sigma_{yz} \quad \sigma_{xz}\}^{\mathrm{T}} \tag{2.2}$$

where ε_x and ε_y are the normal strains along x and y directions, ε_{xy} is the in-plane shear strain in the xy-plane; ε_{yz} and ε_{xz} are the transverse shear strains in the yz and xz-planes, respectively. σ_x and σ_y are the normal stresses along x and y-directions, respectively; σ_{xy} is the in-plane shear stress in the xy-plane; σ_{yz} and σ_{xz} are the transverse shear stresses in the yz and the xz-planes, respectively. In Eqs. (2.1) and (2.2), b and s subscripts represent the bending and the transverse shear counterparts of the strain/stress vector, respectively. The graded material properties of FGMs are usually

computed utilizing three homogenization methods namely power-law distribution, exponential distribution and Mori-Tanaka scheme (Belabed et al. 2014). Among these three schemes, power-law distribution scheme based on the rule of mixture is employed in the present work. This scheme for modeling the FG material is chosen at present in view of its extensive utilization in many available research papers. According to the rule of mixture, the effective material properties of the FG plate made of ceramic and metal constituent materials can be expressed as (Reddy and Chin 1998),

$$P(z,T) = P_c(T)\times V_c(z) + P_m(T)\times V_m(z) \tag{2.3a}$$

where, $P_c(T)$ and $P_m(T)$ are the temperature dependent material properties of ceramic and metal constituents, respectively; $V_c(z)$ and $V_m(z)$ are the corresponding volume fractions which vary along the thickness direction of the plate according to a simple power-law as,

$$V_c = \left(0.5 + (-1)^{\lambda}\left\langle z/h\right\rangle\right)^n,\ V_m = (1 - V_c) \tag{2.3b}$$

where, n $(0 \le n \le \infty)$ is the volume fraction index and it determines the variations of volume fractions of two constituent materials along the thickness direction of the plate; λ is a positive integer. The top surface of the plate can be modeled as either ceramic rich or metal rich according to the value of λ as 1 or 2, respectively. Inserting Eq. (2.3b) in Eq. (2.3a), the following expression can be obtained that defines all material properties like Young's modulus $(E(r,T)$, Poisson's ratio $(\nu(r,T))$, coefficient of thermal expansion $(\alpha(r,T)$, thermal conductivity $(\kappa(r,T)$ etc.,

$$P(z,T) = \left\langle P_c(T) - P_m(T)\right\rangle\left(0.5 + (-1)^{\lambda}\left\langle z/h\right\rangle\right)^n + P_m(T) \tag{2.3c}$$

The constitutive relations of the FG substrate plate can be written as,

$$\left\{\sigma_b^k\right\} = [C_b^k]\left(\{\varepsilon_b^k\} - \{\alpha^k\}\Delta T\right),\ \{\sigma_s^k\} = [C_s^k]\{\varepsilon_s^k\},\ k = 1$$

$$\{\alpha^k\} = \{\alpha_x(z) \quad \alpha_y(z) \quad 0\}^{\mathrm{T}},\ \Delta T = T(z) - T_0\ ,$$

$$[C_s^k]=\frac{E(z)}{2(1+\nu(z))}\begin{bmatrix}1 & 0\\ 0 & 1\end{bmatrix},\ [C_b^k]=\frac{E(z)}{1-\nu^2(z)}\begin{bmatrix}1 & \nu(z) & 0\\ \nu(z) & 1 & 0\\ 0 & 0 & \frac{1-\nu(z)}{2}\end{bmatrix} \tag{2.4}$$

where, $\alpha_x(z)$ and $\alpha_y(z)$ are the coefficients of thermal expansion along x and y-directions respectively. $T(z)$ is the temperature at any point in the FG plate and T_0 is the reference temperature that is considered as equal to the room temperature ($T_0=T_m=300$ K). The temperature distribution ($T(z)$) across the thickness of the FG plate can be determined by the solution of the following one-dimensional steady state heat conduction equation,

$$-\frac{d}{dz}\left[k(z)\frac{dT(z)}{dz}\right]=0$$

$$T(z)\big|_{z=h/2}=T_c \text{ and } T(z)\big|_{z=-h/2}=T_m \text{ when } \lambda=2$$
$$T(z)\big|_{z=h/2}=T_m \text{ and } T(z)\big|_{z=-h/2}=T_c \text{ when } \lambda=1 \tag{2.5}$$

The solution of in Eq. (2.5) can be written as (Woo and Meguid, 2001),

$$k(z)=(k_c-k_m)\times((mul\times z\times 2+h)/(2\times h))^n+k_m \tag{2.5a}$$

The constitutive relations of the PFRC material at stress-free reference temperature can be written as (Mallik and Ray 2003),

$\{\sigma_b^k\}=[\bar{C}_b^k]\{\varepsilon_b^k\}-[\bar{e}_b]\{\bar{E}\}$, $\{\sigma_s^k\}=[\bar{C}_s^k]\{\varepsilon_s^k\}-[\bar{e}_s]\{\bar{E}\}$, $\{D\}=[\bar{e}_b]^{\mathrm{T}}\{\varepsilon_b^k\}+[\bar{e}_s]^{\mathrm{T}}\{\varepsilon_s^k\}+[\bar{\in}]\{\bar{E}\}$,

$k=2$

$$[\bar{C}_b^k]=\begin{bmatrix}\bar{C}_{11}^k & \bar{C}_{12}^k & \bar{C}_{16}^k\\ \bar{C}_{12}^k & \bar{C}_{22}^k & \bar{C}_{26}^k\\ \bar{C}_{16}^k & \bar{C}_{26}^k & \bar{C}_{66}^k\end{bmatrix},\ [\bar{C}_s^k]=\begin{bmatrix}\bar{C}_{44}^k & \bar{C}_{45}^k\\ \bar{C}_{45}^k & \bar{C}_{55}^k\end{bmatrix},\ [\bar{\in}]=\begin{bmatrix}\bar{\in}_{11} & 0 & 0\\ 0 & \bar{\in}_{22} & 0\\ 0 & 0 & \bar{\in}_{33}\end{bmatrix},$$

$$[\bar{e}_b]=\begin{bmatrix}0 & 0 & \bar{e}_{31}\\ 0 & 0 & \bar{e}_{32}\\ 0 & 0 & \bar{e}_{36}\end{bmatrix},\ [\bar{e}_s]=\begin{bmatrix}\bar{e}_{15} & \bar{e}_{25} & 0\\ \bar{e}_{14} & \bar{e}_{24} & 0\end{bmatrix} \tag{2.6}$$

In Eqs. (2.4) and (2.6), the superscript k denotes FG substrate plate or PFRC layer according to its value as 1 or 2, respectively. $[\bar{C}_b^k]$ and $[\bar{C}_s^k]$ are the transformed elastic coefficient matrices;$[\bar{e}_b]$ and $[\bar{e}_s]$ are the transformed piezoelectric coefficient matrices and $[\bar{\in}]$ is the transformed dielectric constant matrix with respect to the reference co-ordinate system (xyz).

The electric field vector $\{\bar{E}\}$ and the electric displacement vector $\{D\}$ appearing in Eq. (2.6) are given by,

$$\{\bar{E}\}=\{E_x \quad E_y \quad E_z\}^{\mathrm{T}} \text{ and } \{D\}=\{D_x \quad D_y \quad D_z\}^{\mathrm{T}} \tag{2.7}$$

where, E_x, E_y and E_z are the electric fields along x, y and z-directions, respectively; D_x, D_y and D_z are the corresponding electric displacements. The top and bottom surfaces of the PFRC layer are considered to be fully electroded isopotential surfaces. Since its thickness is considered as very small, the electric fields can be assumed as: $E_x \approx 0$, $E_y \approx 0$ and $E_z = -V/h_p$, V being the applied voltage across the top and the bottom electrode- surfaces of the PFRC layer. Since a thin laminated plate is considered in the present analysis, the kinematics of deformation of the overall laminated plate is defined according to the first order shear deformation theory (FSDT) as,

$$u(x,y,z,t)=u_0(x,y,t)+z\theta_x(x,y,t),$$

$$v(x,y,z,t)=v_0(x,y,t)+z\theta_y(x,y,t),$$

$$w(x,y,z,t)=w_0(x,y,t) \tag{2.8}$$

where, u, v and w are the displacements at any point of the overall plate along x, y and z-directions, respectively; u_0, v_0 and w_0 are the translational displacements at any point on the reference plane along x, y and z directions, respectively; θ_x and θ_y are

the rotations of the normal to the reference plane with respect to y and x-axes, respectively. A state of deformation of the overall plate can be defined in terms of the generalized displacements (u_0, v_0, w_0, θ_x and θ_y) which can also be expressed in the form of a generalized displacement vector as follows,

$$\{d\} = [u_0 \quad v_0 \quad w_0 \quad \theta_x \quad \theta_y]^{\mathrm{T}} \tag{2.9}$$

In accordance with the kinematics of deformation given by Eq. (2.8), the von Karman nonlinear strain displacement relations can be expressed as,

$$\{\varepsilon_b\} = \{\varepsilon_{bL}\} + \{\varepsilon_{bN}\} + z\{\kappa\}$$

$$\{\varepsilon_{bL}\} = \left[\frac{\partial u_0}{\partial x} \quad \frac{\partial v_0}{\partial y} \quad \frac{\partial u_0}{\partial y} + \frac{\partial v_0}{\partial x}\right]^{\mathrm{T}},$$

$$\{\varepsilon_{bN}\} = \left[\frac{1}{2}\left(\frac{\partial w_0}{\partial x}\right)^2 \quad \frac{1}{2}\left(\frac{\partial w_0}{\partial y}\right)^2 \quad \frac{\partial w_0}{\partial x}\frac{\partial w_0}{\partial y}\right]^{\mathrm{T}},$$

$$\{\varepsilon_s\} = \left[\frac{\partial w_0}{\partial y} + \theta_y \quad \frac{\partial w_0}{\partial x} + \theta_x\right]^{\mathrm{T}}, \quad \{\kappa\} = \left[\frac{\partial \theta_x}{\partial x} \quad \frac{\partial \theta_y}{\partial y} \quad \frac{\partial \theta_y}{\partial x} + \frac{\partial \theta_x}{\partial y}\right]^{\mathrm{T}} \tag{2.10}$$

For an applied uniformly distributed transverse mechanical load of intensity p, the first variation of the total potential energy (δT_p) of the overall smart FG plate can be written as (Tierstien, 1969),

$$\delta T_p = \int_0^a \int_0^b \left[\sum_{k=1}^{2} \int_{h_k}^{h_{k+1}} \left(\left\{\delta\varepsilon_b^k\right\}^{\mathrm{T}} \{\sigma_b^k\} + \left\{\delta\varepsilon_s^k\right\}^{\mathrm{T}} \{\sigma_s^k\}\right) dz - \int_{h_k}^{h_{k+1}} \{\delta\bar{E}\}^{\mathrm{T}} \{D\}\,|_{k=2}\, dz - (\delta w \times p)\right] dy dx \tag{2.11}$$

where, δ is an operator for first variation. Substituting Eqs. (2.4), (2.6) and (2.10) in Eq. (2.11), the following expression for δT_p can be obtained,

$$\delta T_p = \int_0^a \int_0^b \begin{bmatrix} \left\langle \{\delta\varepsilon_{bL}\}^{\mathrm{T}} + \{\delta\varepsilon_{bN}\}^{\mathrm{T}} \right\rangle [A_b] \left\langle \{\varepsilon_{bL}\} + \{\varepsilon_{bN}\} \right\rangle + \{\delta\kappa\}^{\mathrm{T}} [B_b] \left\langle \{\varepsilon_{bL}\} + \{\varepsilon_{bN}\} \right\rangle + \\ \left\langle \{\delta\varepsilon_{bL}\}^{\mathrm{T}} + \{\delta\varepsilon_{bN}\}^{\mathrm{T}} \right\rangle [B_b]\{\kappa\} + \{\delta\kappa\}^{\mathrm{T}} [D_b]\{\kappa\} + \{\delta\varepsilon_s\}^{\mathrm{T}} [A_s]\{\varepsilon_s\} - \\ \left\langle \{\delta\varepsilon_{bL}\}^{\mathrm{T}} + \{\delta\varepsilon_{bN}\}^{\mathrm{T}} \right\rangle \{A_{be}\} \times V - \{\delta\kappa\}^{\mathrm{T}} \{B_{be}\} \times V - \{\delta\varepsilon_s\}^{\mathrm{T}} \{A_{se}\} \times V - \\ \left\langle \{\delta\varepsilon_{bL}\}^{\mathrm{T}} + \{\delta\varepsilon_{bN}\}^{\mathrm{T}} \right\rangle \{A_T\} - \{\delta\kappa\}^{\mathrm{T}} \{B_T\} - \left\langle \delta w \times p \right\rangle \end{bmatrix} dydx \tag{2.12}$$

In Eq. (2.12), $[A_b]$ is the extensional stiffness, $[A_s]$ is shear stiffness, $[B_b]$ is the bending-extension coupling stiffness, $[D_b]$ is the bending stiffness matrices are as follows,

$$[A_b] = \int_{h_k}^{h_{k+1}} [C_b^k]|_{k=1}\, dz + \int_{h_k}^{h_{k+1}} [\bar{C}_b^k]|_{k=2}\, dz, [A_s] = \int_{h_k}^{h_{k+1}} [C_s^k]|_{k=1}\, dz + \int_{h_k}^{h_{k+1}} [\bar{C}_s^k]|_{k=2}\, dz,$$

$$[B_b] = \int_{h_k}^{h_{k+1}} [C_b^k]|_{k=1}\, zdz + \int_{h_k}^{h_{k+1}} [\bar{C}_b^k]|_{k=2}\, zdz,\ [D_b] = \int_{h_k}^{h_{k+1}} [C_b^k]|_{k=1}\, z^2 dz + \int_{h_k}^{h_{k+1}} [\bar{C}_b^k]|_{k=2}\, z^2 dz$$

The closed form integrations in the stiffness and thermo-elastic constants are performed utilizing the symbolic integral function in MATLAB. Thermo-elastic coupling vectors ($\{A_T\}, \{B_T\}$) are as follows,

$$\{A_T\} = \int_{h_k}^{h_{k+1}} [1 \quad 1 \quad 0]^{\mathrm{T}} \frac{E(z)}{1-\nu(z)} \alpha(z)\Delta T(z)|_{k=1}\, dz,$$

$$\{B_T\} = \int_{h_k}^{h_{k+1}} [1 \quad 1 \quad 0]^{\mathrm{T}} \frac{E(z)}{1-\nu(z)} \alpha(z)\Delta T(z)|_{k=1}\, zdz,$$

The electro-elastic coupling vectors ($\{A_{be}\}, \{B_{be}\}, \{A_{se}\}$) are as follows,

$$\{B_{be}\} = \int_{h_k}^{h_{k+1}} [\bar{e}_b][0 \quad 0 \quad -1/h_p]^{\mathrm{T}}|_{k=2}\, zdz, \{A_{be}\} = \int_{h_k}^{h_{k+1}} [\bar{e}_b][0 \quad 0 \quad -1/h_p]^{\mathrm{T}}|_{k=2}\, dz,$$

$$\{A_{se}\} = \int_{h_k}^{h_{k+1}} [\bar{e}_s][0 \quad 0 \quad -1/h_p]^{\mathrm{T}}|_{k=2}\, dz \tag{2.13}$$

For the vibration of the overall plate, the first variation of its total kinetic energy (δT_k) can be written as follows,

$$\delta T_K = \int_0^a \int_0^b \left[\sum_{k=1}^{2} \int_{h_k}^{h_{k+1}} \left\langle [\delta \dot{u} \quad \delta \dot{v} \quad \delta \dot{w}] \rho^k [\dot{u} \quad \dot{v} \quad \dot{w}]^{\mathrm{T}} \right\rangle dz \right] dy dx = \int_0^a \int_0^b \left(\{\delta \dot{d}\}^{\mathrm{T}} [\bar{m}] \{\dot{d}\} \right) dy dx \tag{2.14}$$

where, ρ^k is the mass density of the k-th layer and $[\bar{m}]$ is given by,

$$[\bar{m}] = \sum_{k=1}^{2} \int_{h_k}^{h_{k+1}} \left\langle \left([N_{mt}]^{\mathrm{T}} + z[N_{mr}]^{\mathrm{T}} \right) \rho^k \left([N_{mt}] + z[N_{mr}] \right) \right\rangle dz$$

$$[N_{mt}] = \begin{bmatrix} 1 & 0 & 0 & 0 & 0 \\ 0 & 1 & 0 & 0 & 0 \\ 0 & 0 & 1 & 0 & 0 \end{bmatrix}, \; [N_{mr}] = \begin{bmatrix} 0 & 0 & 0 & 1 & 0 \\ 0 & 0 & 0 & 0 & 1 \\ 0 & 0 & 0 & 0 & 0 \end{bmatrix} \tag{2.15}$$

The governing equations of motion of the overall smart FG plate for its vibration can be derived employing the Hamilton's principle as follows,

$$\int_{t_1}^{t_2} \left(\delta T_K - \delta T_p \right) dt = 0 \tag{2.16}$$

Substituting Eqs. (2.12) and (2.14) in Eq. (2.16), the following simplified equation can be obtained,

$$\int_{t_1}^{t_2} \int_0^a \int_0^b \begin{bmatrix} \{\delta d\}^{\mathrm{T}} [\bar{m}] \{\ddot{d}\} + \left\langle \{\delta \varepsilon_{bL}\}^{\mathrm{T}} + \{\delta \varepsilon_{bN}\}^{\mathrm{T}} \right\rangle [A_b] \left\langle \{\varepsilon_{bL}\} + \{\varepsilon_{bN}\} \right\rangle \\ + \{\delta \kappa\}^{\mathrm{T}} [B_b] \left\langle \{\varepsilon_{bL}\} + \{\varepsilon_{bN}\} \right\rangle + \left\langle \{\delta \varepsilon_{bL}\}^{\mathrm{T}} + \{\delta \varepsilon_{bN}\}^{\mathrm{T}} \right\rangle [B_b] \{\kappa\} + \\ \{\delta \kappa\}^{\mathrm{T}} [D_b] \{\kappa\} + \{\delta \varepsilon_s\}^{\mathrm{T}} [A_s] \{\varepsilon_s\} - \left\langle \{\delta \varepsilon_{bL}\}^{\mathrm{T}} + \{\delta \varepsilon_{bN}\}^{\mathrm{T}} \right\rangle \{A_T\} \\ - \{\delta \kappa\}^{\mathrm{T}} \{B_T\} - \left\langle \{\delta \varepsilon_{bL}\}^{\mathrm{T}} + \{\delta \varepsilon_{bN}\}^{\mathrm{T}} \right\rangle \{A_{be}\} \times V - \{\delta \kappa\}^{\mathrm{T}} \{B_{be}\} \times V \\ - \{\delta \varepsilon_s\}^{\mathrm{T}} \{A_{se}\} \times V - (\delta w \times p \times \cos(\omega t)) \end{bmatrix} dy dx dt = 0 \tag{2.17}$$

For the steady state vibration of the overall FG plate with the circular frequency as ω, a state of vibration can be defined by specifying $\{d\}$ and ω. A neighboring state corresponding to a given state of vibration ($\{d_i\}$, ω_i) can be expressed in addition of corresponding increments ($\{\Delta d\}$ and $\Delta\omega$),

$$\{d\} = \{d_i\} + \{\Delta d\}\,,\ \omega = (\omega_i + \Delta\omega) \tag{2.18a}$$

$$\{d_i\} = [u_{0i} \quad v_{0i} \quad w_{0i} \quad \theta_{xi} \quad \theta_{yi}]^{\mathrm{T}}, \{\Delta d\} = [\Delta u_0 \quad \Delta v_0 \quad \Delta w_0 \quad \Delta\theta_x \quad \Delta\theta_y]^{\mathrm{T}} \tag{2.18b}$$

Also, the incremental form of strain vectors can be expressed as,

$$\{\varepsilon_{bL}\} = \{\varepsilon_{bL}^i\} + \{\Delta\varepsilon_{bL}\}, \{\varepsilon_{bN}\} = \{\varepsilon_{bN}^i\} + \{\Delta\varepsilon_{bN}\},$$
$$\{\kappa\} = \{\kappa^i\} + \{\Delta\kappa\}, \{\varepsilon_s\} = \{\varepsilon_s^i\} + \{\Delta\varepsilon_s\} \tag{2.19}$$

where, $\{\varepsilon_{bL}^i\}$, $\{\varepsilon_{bN}^i\}$, $\{\kappa^i\}$ and $\{\varepsilon_s^i\}$ are the strain vectors for the given state of deformation $\{d_i\}$ while $\{\Delta\varepsilon_{bL}\}$, $\{\Delta\varepsilon_{bN}\}$, $\{\Delta\kappa\}$ and $\{\Delta\varepsilon_s\}$ are the corresponding increments as follows,

$$\{\Delta\varepsilon_{bL}\} = \begin{Bmatrix} \dfrac{\partial\Delta u_0}{\partial x} \\ \dfrac{\partial\Delta v_0}{\partial y} \\ \dfrac{\partial\Delta u_0}{\partial y} + \dfrac{\partial\Delta v_0}{\partial x} \end{Bmatrix}, \{\Delta\kappa\} = \begin{Bmatrix} \dfrac{\partial\Delta\theta_x}{\partial x} \\ \dfrac{\partial\Delta\theta_y}{\partial y} \\ \dfrac{\partial\Delta\theta_y}{\partial x} + \dfrac{\partial\Delta\theta_x}{\partial y} \end{Bmatrix},$$

$$\{\Delta\varepsilon_s\} = \begin{Bmatrix} \dfrac{\partial\Delta w_0}{\partial y} + \Delta\theta_y \\ \dfrac{\partial\Delta w_0}{\partial x} + \Delta\theta_x \end{Bmatrix}, \{\Delta\varepsilon_{bN}\} = \begin{Bmatrix} \dfrac{\partial w_{0i}}{\partial x}\dfrac{\partial\Delta w_0}{\partial x} + \dfrac{1}{2}\left(\dfrac{\partial\Delta w_0}{\partial x}\right)^2 \\ \dfrac{\partial w_{0i}}{\partial y}\dfrac{\partial\Delta w_0}{\partial y} + \dfrac{1}{2}\left(\dfrac{\partial\Delta w_0}{\partial y}\right)^2 \\ \dfrac{\partial w_{0i}}{\partial x}\dfrac{\partial\Delta w_0}{\partial y} + \dfrac{\partial w_{0i}}{\partial y}\dfrac{\partial\Delta w_0}{\partial x} + \left(\dfrac{\partial\Delta w_0}{\partial x}\dfrac{\partial\Delta w_0}{\partial y}\right) \end{Bmatrix} \tag{2.20}$$

The isoparametric elements based on FSDT suffer from shear-locking in case of the analysis of thin plates. In order to eliminate this discrepancy, the selective integration strategy is to be performed (Cook RD, John Wiley and Sons 2002). This integration strategy is followed in the present use of isoparametric element. The accuracy in the present results is verified as illustrated in Tables 2.1 of the thesis. The side to thickness

ratio of the present plate is considered as 66.67 and the shear locking phenomena is not observed in the corresponding results. The overall plate is discretized by 9-node isoparametric quadrilateral elements. Thus, the displacement field within a typical element can be expressed as $\{d\} = [N]\{d^e\}$ (2.21)

where, $\{d^e\}$ is the elemental nodal displacement vector and $[N]$ is the shape function matrix. Substituting Eqs. (2.18a) and (2.19) in Eq. (2.17) and then using Eq. (2.21), the following simplified equation for a typical element can be obtained,

$$\int_{t_1}^{t_2} \delta\left\{\Delta d^e\right\}^{\mathrm{T}} \begin{bmatrix} [M^e]\{\ddot{d}_i^e\} + [\dot{M}^e]\{\Delta\ddot{d}^e\} + [K_L^e]\{d_i^e\} + [K_L^e]\{\Delta d^e\} + \\ [K_{Ni}^e]\{d_i^e\} + [K_N^e]\{\Delta d^e\} + [K_{NNi}^e]\{d_i^e\} + [K_{NN}^e]\{\Delta d^e\} \\ -\{P_L^{Te}\} - \{P_N^{Te}\} - \{P_L^{Ee}\}V - \{P_N^{Ee}\}V - \left\{P_M^e\right\} cos(\omega t) \end{bmatrix} dt = 0 \tag{2.22}$$

In Eq. (2.22) the expressions of elemental linear stiffness matrix ($[K_L^e]$) ; non-linear stiffness matrices ($[K_{Ni}^e],[K_N^e],[K_{NNi}^e],[K_{NN}^e]$) ,linear thermal load ($\{P_L^{Te}\}$) and nonlinear thermal load ($\{P_N^{Te}\}$) vector, linear electrical load vector ($\{P_L^{Ee}\}$)and nonlinear electrical load , mechanical load vector ($\{P_M^e\}$), Mass matrix ($[M^e]$) are,

$$[K_L^e] = \int_{A_e} ([B_b^L]^{\mathrm{T}} \left\langle [A_b][B_b^L] + [B_b][B_\kappa] \right\rangle + [B_\kappa]^{\mathrm{T}} \left\langle [B_b][B_b^L] + [D_b][B_\kappa] \right\rangle + [B_s]^{\mathrm{T}}[A_s][B_s]) dA_e ,$$

$$[K_{Ni}^e] = \int_{A_e} (\left\langle [B_b^L]^{\mathrm{T}}[A_b] + [B_\kappa]^{\mathrm{T}}[B_b] \right\rangle [B_{Ni}] + [B_N^d]^{\mathrm{T}} \left\langle [A_b][B_b^L] + [B_b][B_\kappa] \right\rangle) dA_e ,$$

$$[K_N^e] = \int_{A_e} (\left\langle [B_b^L]^{\mathrm{T}}[A_b] + [B_\kappa]^{\mathrm{T}}[B_b] \right\rangle [B_N] + [B_N^d]^{\mathrm{T}} \left\langle [A_b][B_b^L] + [B_b][B_\kappa] \right\rangle) dA_e ,$$

$$[K_{NNi}^e] = \int_{A_e} ([B_N^d]^{\mathrm{T}}[A_b][B_{Ni}]) dA_e , [K_{NN}^e] = \int_{A_e} ([B_N^d]^{\mathrm{T}}[A_b][B_N]) dA_e ,$$

$$\{P_L^{Te}\} = \int_{A_e} ([B_b^L]^{\mathrm{T}}\{A_T\} + [B_\kappa]^{\mathrm{T}}\{B_T\}) dA_e , \{P_N^{Te}\} = \int_{A_e} ([B_N^d]^{\mathrm{T}}\{A_T\}) dA_e ,$$

$$\{P_L^{Ee}\} = \int_{A_e} ([B_b^L]^{\mathrm{T}}\{A_{be}\} + [B_\kappa]^{\mathrm{T}}\{B_{be}\} + [B_s]^{\mathrm{T}}\{A_{se}\})dA_e \ ,$$

$$\{P_N^{Ee}\} = \int_{A_e} ([B_N^d]^{\mathrm{T}}\{A_{be}\})dA_e \ , \ \{P_M^e\} = \int_{A_e} ([N]^{\mathrm{T}}[0 \quad 0 \quad p \quad 0 \quad 0]^{\mathrm{T}})dA_e$$

$$[M^e] = \int_{A_e} ([N]^{\mathrm{T}}[\bar{m}][N])dA_e \tag{2.22a}$$

where, A_e is the area of a typical element in the xy-plane. The different strain-displacement matrices appearing in Eq. (2.22a) are given by,

$$[B_b^L] = [L_b^L][N], \ [B_{Ni}] = [L_{Ni}][N], \ [B_s] = [L_s][N],$$
$$[B_\kappa] = [L_\kappa][N], \ [B_N^d] = [L_N^d][N], \ [B_N] = [L_N][N]$$

$$[L_b^L] = \begin{bmatrix} \frac{\partial}{\partial x} & 0 & 0 & 0 & 0 \\ 0 & \frac{\partial}{\partial y} & 0 & 0 & 0 \\ \frac{\partial}{\partial y} & \frac{\partial}{\partial x} & 0 & 0 & 0 \end{bmatrix}, [L_\kappa] = \begin{bmatrix} 0 & 0 & 0 & \frac{\partial}{\partial x} & 0 \\ 0 & 0 & 0 & 0 & \frac{\partial}{\partial y} \\ 0 & 0 & 0 & \frac{\partial}{\partial y} & \frac{\partial}{\partial x} \end{bmatrix},$$

$$[L_s] = \begin{bmatrix} 0 & 0 & \frac{\partial}{\partial y} & 0 & 1 \\ 0 & 0 & \frac{\partial}{\partial x} & 1 & 0 \end{bmatrix}, [L_{Ni}] = \begin{bmatrix} 0 & 0 & \frac{1}{2}\frac{\partial w_{oi}}{\partial x}\frac{\partial}{\partial x} & 0 & 0 \\ 0 & 0 & \frac{1}{2}\frac{\partial w_{oi}}{\partial y}\frac{\partial}{\partial y} & 0 & 0 \\ 0 & 0 & \frac{\partial w_{oi}}{\partial x}\frac{\partial}{\partial y} & 0 & 0 \end{bmatrix},$$

$$[L_N] = \begin{bmatrix} 0 & 0 & \frac{\partial w_{0i}}{\partial x}\frac{\partial}{\partial x} + \frac{1}{2}\frac{\partial \Delta w_0}{\partial x}\frac{\partial}{\partial x} & 0 & 0 \\ 0 & 0 & \frac{\partial w_{0i}}{\partial y}\frac{\partial}{\partial y} + \frac{1}{2}\frac{\partial \Delta w_0}{\partial y}\frac{\partial}{\partial y} & 0 & 0 \\ 0 & 0 & \frac{\partial w_{0i}}{\partial x}\frac{\partial}{\partial y} + \frac{\partial w_{0i}}{\partial y}\frac{\partial}{\partial x} + \frac{\partial \Delta w_0}{\partial x}\frac{\partial}{\partial y} & 0 & 0 \end{bmatrix},$$

$$[L_N^d]=\begin{bmatrix} 0 & 0 & \dfrac{\partial w_{0i}}{\partial x}\dfrac{\partial}{\partial x}+\dfrac{\partial \Delta w_0}{\partial x}\dfrac{\partial}{\partial x} & 0 & 0 \\ 0 & 0 & \dfrac{\partial w_{0i}}{\partial y}\dfrac{\partial}{\partial y}+\dfrac{\partial \Delta w_0}{\partial y}\dfrac{\partial}{\partial y} & 0 & 0 \\ 0 & 0 & \left(\dfrac{\partial w_{0i}}{\partial x}+\dfrac{\partial \Delta w_0}{\partial x}\right)\dfrac{\partial}{\partial y}+\left(\dfrac{\partial w_{0i}}{\partial y}+\dfrac{\partial \Delta w_0}{\partial y}\right)\dfrac{\partial}{\partial x} & 0 & 0 \end{bmatrix} \tag{2.23}$$

In Eq. (2.22), the bending and shear counterparts of the total stiffness matrix are formulated separately and the selective integration can be applied in a straight forward manner.

2.2.1 Implementation of harmonic balance method (HBM)

An approximate periodic solution of Eq. (2.22) for the nonlinear vibration of overall smart FG laminated plates can be obtained by harmonic balance method (HBM) (Von and Ewins, 2001). According to this method, multiple harmonics are anticipated in the periodic solution. Therefore, the periodic solution can be expanded following the Fourier series as follows,

$$\{d^e\}=\{a_0\}+\sum_{r=1}^{F}\left\langle\{a_r\}\cos(r\omega t)+\{b_r\}\sin(r\omega t)\right\rangle \tag{2.24}$$

where, $\{a_0\}$ is the time-independent elemental nodal displacement vector; $\{a_r\}$ and $\{b_r\}$ are the elemental nodal displacement vectors for the amplitudes in r-th harmonic term. q is the number of harmonic terms . In order to ease the formulation, Eq. (2.24) and its time derivatives are written as follows,

$$\{d^e\}=[S^e]\{X^e\},\ \{\dot{d}^e\}=\omega\times[S_1^e]\{X^e\},\ \{\ddot{d}^e\}=-\omega^2\times[S_2^e]\{X^e\}$$

$$[S^e]=\begin{bmatrix}[I] & [I]\cos\theta & [I]\sin\theta & \ldots & [I]\cos(F\theta) & [I]\sin(F\theta)\end{bmatrix}$$

$$[S_1^e]=\begin{bmatrix}[0] & -[I]\sin\theta & [I]\cos\theta & \ldots & -q\times[I]\sin(F\theta) & q\times[I]\cos(F\theta)\end{bmatrix}$$

$$[S_2^e]=\Big[[0] \quad [I]\cos\theta \quad [I]\sin\theta \quad . \quad . \quad . \quad q^2\times[I]\cos(F\theta) \quad q^2\times[I]\sin(F\theta)\Big]$$

$$\{X^e\}=\Big[\{a_0\}^{\mathrm{T}} \quad \{a_1\}^{\mathrm{T}} \quad \{b_1\}^{\mathrm{T}} \quad . \quad . \quad . \quad \{a_F\}^{\mathrm{T}} \quad \{b_F\}^{\mathrm{T}}\Big]^{\mathrm{T}} \tag{2.25}$$

In Eq. (2.25), $\theta=\omega\times t$; $[I]$ and $[0]$ are the unit and null matrices, respectively. Using Eq. (2.18), the corresponding incremental vectors ($\{\Delta d^e\}$, $\{\Delta\dot{d}^e\}$ and $\{\Delta\ddot{d}^e\}$) can be obtained as,

$$\{\Delta d^e\}=[S^e]\left\{\Delta X^e\right\},\ \{\Delta\dot{d}^e\}=\omega_i[S_1^e]\left\{\Delta X^e\right\}+\Delta\omega[S_1^e]\left\{X_i^e\right\},$$

$$\{\Delta\ddot{d}^e\}=\omega_i^2[S_2^e]\left\{\Delta X^e\right\}+2\omega_i\Delta\omega[S_2^e]\left\{X_i^e\right\} \tag{2.26}$$

The expressions in Eq. (2.26) are obtained considering small increment over a given state that assumes, $\Delta\omega[S_1^e]\Delta X^e\approx 0$ and $\Delta\omega[S_2^e]\Delta X^e\approx 0$. For the present form of solution (Eqs. (2.24)-(2.26)), the nonlinear strain-displacement matrices (Eq. (2.23)) can be modified as follows,

$$|B_{Ni}|=\Big\langle\big[|B_{Ni}^0| \ |B_{Ni}^{1a}| \ |B_{Ni}^{1b}|.....|B_{Ni}^{Fa}| \ |B_{Ni}^{Fb}|\big]\Big\rangle|S^e|^{\mathrm{T}}=|B_{Ni}^t||S^e|^{\mathrm{T}},$$

$$|B_N|=\Big\langle\big[|B_N^0| \ |B_N^{1a}| \ |B_N^{1b}|.....|B_N^{Fa}| \ |B_N^{Fb}|\big]\Big\rangle|S^e|^{\mathrm{T}}=|B_N^t||S^e|^{\mathrm{T}},$$

$$|B_N^d|=\Big\langle\big[|B_N^{d0}| \ |B_N^{d1a}| \ |B_N^{d1b}|.....|B_N^{dFa}| \ |B_N^{dFb}|\big]\Big\rangle|S^e|^{\mathrm{T}}=|B_N^{dt}||S^e|^{\mathrm{T}} \tag{2.27}$$

where, $[\mathrm{B}_{Ni}^0]/[\mathrm{B}_{Ni}^{ra}]/[\mathrm{B}_{Ni}^{rb}]$, $[\mathrm{B}_N^0]/[\mathrm{B}_N^{ra}]/[\mathrm{B}_N^{rb}]$, $[\mathrm{B}_N^{d0}]/[\mathrm{B}_N^{dra}]/[\mathrm{B}_N^{drb}]$ are in similar form of $[\mathrm{B}_{Ni}]$, $[\mathrm{B}_N]$,$[\mathrm{B}_N^d]$, respectively and are given in Eq. (2.27a). These matrices are the functions of $\{a_0\}$ and/or $\{\Delta a_0\}$, $\{a_r\}$ and/or $\{\Delta a_r\}$, $\{b_r\}$ and/or $\{\Delta b_r\}$ according to their superscripts 0, ra, rb ($r=1,2,3,\ldots\ldots F$), respectively.

$$[B_{Ni}^i]=[L_{Ni}^i][N],\ [B_N^{di}]=[L_N^{di}][N],\ [B_N^i]=[L_N^i][N]$$

$$[L_{Ni}^{i}]=\begin{bmatrix} 0 & 0 & \frac{1}{2}\frac{\partial w_{oi}^{i}}{\partial x}\frac{\partial}{\partial x} & 0 & 0 \\ 0 & 0 & \frac{1}{2}\frac{\partial w_{oi}^{i}}{\partial y}\frac{\partial}{\partial y} & 0 & 0 \\ 0 & 0 & \frac{\partial w_{oi}^{i}}{\partial x}\frac{\partial}{\partial y} & 0 & 0 \end{bmatrix}, [L_{N}^{i}]=\begin{bmatrix} 0 & 0 & \frac{\partial w_{0i}^{i}}{\partial x}\frac{\partial}{\partial x}+\frac{1}{2}\frac{\partial \Delta w_0}{\partial x}\frac{\partial}{\partial x} & 0 & 0 \\ 0 & 0 & \frac{\partial w_{0i}^{i}}{\partial y}\frac{\partial}{\partial y}+\frac{1}{2}\frac{\partial \Delta w_0}{\partial y}\frac{\partial}{\partial y} & 0 & 0 \\ 0 & 0 & \frac{\partial w_{0i}^{i}}{\partial x}\frac{\partial}{\partial y}+\frac{\partial w_{0i}^{i}}{\partial y}\frac{\partial}{\partial x}+\frac{\partial \Delta w_0}{\partial x}\frac{\partial}{\partial y} & 0 & 0 \end{bmatrix},$$

$$[L_{N}^{di}]=\begin{bmatrix} 0 & 0 & \frac{\partial w_{0i}^{i}}{\partial x}\frac{\partial}{\partial x}+\frac{\partial \Delta w_0}{\partial x}\frac{\partial}{\partial x} & 0 & 0 \\ 0 & 0 & \frac{\partial w_{0i}^{i}}{\partial y}\frac{\partial}{\partial y}+\frac{\partial \Delta w_0}{\partial y}\frac{\partial}{\partial y} & 0 & 0 \\ 0 & 0 & \left(\frac{\partial w_{0i}^{i}}{\partial x}+\frac{\partial \Delta w_0}{\partial x}\right)\frac{\partial}{\partial y}+\left(\frac{\partial w_{0i}^{i}}{\partial y}+\frac{\partial \Delta w_0}{\partial y}\right)\frac{\partial}{\partial x} & 0 & 0 \end{bmatrix} \quad (2.27a)$$

2.2.2 Smart damping

The velocity feedback control strategy is utilized in the present model in order to utilize the PFRC actuator in the form of smart dampers. The transverse velocity ($\dot{w}$) at the middle point on the top surface of the actuator layer is measured by locating a velocity sensor at the same location. This transverse velocity is feed back in the form of voltage across the electrodes of actuator layer by means of a feedback control-gain as follows,

$$V=-k_d\dot{w}_s=-k_d\left(\dot{w}_{si}+\Delta\dot{w}_s\right) \quad (2.28)$$

where, $\dot{w}_s$ is the velocity of sensing point in the form of an increment $\Delta\dot{w}_s$ over $\dot{w}_{si}$; k_d is the feed-back control gain. The form of solutions (Eqs. (2.25) and (2.26)), $\dot{w}_{si}$ and $\Delta\dot{w}_s$ appearing in Eq. (2.28) can be written as,

$$\dot{w}_{si}=\omega_i\times\left[S_1^s\right]\left\{w_{si}\right\},$$

$$\Delta\dot{w}_s=\omega_i\times\left[S_1^s\right]\left\{\Delta w_s\right\}+\Delta\omega\times\left[S_1^s\right]\left\{w_{si}\right\}, \left\{w_{si}\right\}=\left[w_{si}^{1a} \quad w_{si}^{1b} \quad . \quad . \quad . \quad . \quad w_{si}^{Fa} \quad w_{si}^{Fb}\right]^{\mathrm{T}},$$

$$\left\{\Delta w_s\right\}=\left[\Delta w_s^{1a} \quad \Delta w_s^{1b} \quad . \quad . \quad . \quad . \quad \Delta w_s^{Fa} \quad \Delta w_s^{Fb}\right]^{\mathrm{T}},$$

$$\left[S_1^s\right]=\left[-sin(\omega t)\quad cos(\omega t)\quad .\quad .\quad .\quad .\quad -q\times sin(F\omega t)\quad q\times cos(F\omega t)\right] \quad (2.29)$$

In Eq. (2.29), $w_{si}^{ra}/\Delta w_s^{ra}$ and $w_{si}^{rb}/\Delta w_s^{rb}$ ($r=1,\ 2,\ 3,\ \ldots\ldots F$) are the amplitudes corresponding to *cosine* and *sine* terms in r^{th}-harmonic. Introducing Eq. (2.29) in Eq. (2.28), the following expression of V can be obtained,

$$V=-k_d\left[S_1^s\right]\left\langle \omega_i\left\{w_{si}\right\}+\omega_i\left\{\Delta w_s\right\}+\Delta\omega\left\{w_{si}\right\}\right\rangle \quad (2.30)$$

Substituting Eqs. (2.25), (2.26) ,(2.27) and (2.30) in Eq. (2.22), the simplified equation can be written as follows,

$$\left[K_t^e\right]\left\{\Delta X^e\right\}+\Delta\omega\left[K_i^e\right]\left\{X_i^e\right\}=-\left\{f_t^{ie}\right\}+\left\{f_t^{Te}\right\}+\left\{f_t^{Pe}\right\}-(\omega_i+\Delta\omega)\left[C_s^e\right]\left\{w_{si}\right\}-\omega_i\left[C_s^e\right]\left\{\Delta w_s\right\} \quad (2.31)$$

In Eq. (2.31), the different matrices are as follows,

$$\left[K_t^e\right]=\left\langle -\omega_i^2\left[M_t^e\right]+\left[K_{Lt}^e\right]+\left[K_{Nt}^e\right]+\left[K_{NNt}^e\right]\right\rangle,\ \left[K_i^e\right]=\left\langle -2\omega_i\left[M_t^e\right]\right\rangle,$$

$$\{f_t^{ie}\}=\left\langle -\omega_i^2\left[M_t^e\right]+\left[K_{Lt}^e\right]+\left[K_{Nit}^e\right]+\left[K_{NNit}^e\right]\right\rangle\{X_i^e\},\ \{f_t^{Te}\}=\left\langle\{P_{Lt}^{Te}\}+\{P_{Nt}^{Te}\}\right\rangle,\ \{f_t^{Pe}\}=\{P_t^{Me}\},$$

$$[M_t^e]=\int_{\theta_1}^{\theta_2}\left[[S^e]^{\mathrm{T}}[M^e][S_2^e]\right]\mathrm{d}\theta,\ \left[K_{Lt}^e\right]=\int_{\theta_1}^{\theta_2}\left[\left[S^e\right]^{\mathrm{T}}\left[K_L^e\right]\left[S^e\right]\right]\mathrm{d}\theta,$$

$$\left[K_{Nt}^e\right]=\int_{\theta_1}^{\theta_2}\left[\left[S^e\right]^{\mathrm{T}}\left\langle\int_{A_e}\left(\left[B_b^L\right]^{\mathrm{T}}\left[A_b\right]+\left[B_\kappa\right]^{\mathrm{T}}\left[B_b\right]\right)\left[B_N^t\right]\mathrm{d}A_e\right\rangle\left[S^e\right]^{\mathrm{T}}+\left[S^e\right]^{\mathrm{T}}\left[S^e\right]\left\langle\int_{A_e}\left[B_N^{dt}\right]^{\mathrm{T}}\left(\left[A_b\right]\left[B_b^L\right]+\left[B_b\right]\left[B_\kappa\right]\right)\mathrm{d}A_e\right\rangle\right]\left[S^e\right]\mathrm{d}\theta$$

$$\left[K_{Nit}^e\right]=\int_{\theta_1}^{\theta_2}\left[\left[S^e\right]^{\mathrm{T}}\left\langle\int_{A_e}\left(\left[B_b^L\right]^{\mathrm{T}}\left[A_b\right]+\left[B_\kappa\right]^{\mathrm{T}}\left[B_b\right]\right)\left[B_{Ni}^t\right]dA_e\right\rangle\left[S^e\right]^{\mathrm{T}}+\left[S^e\right]^{\mathrm{T}}\left[S^e\right]\left\langle\int_{A_e}\left[B_N^{dt}\right]^{\mathrm{T}}\left(\left[A_b\right]\left[B_b^L\right]+\left[B_b\right]\left[B_\kappa\right]\right)dA_e\right\rangle\right]\left[S^e\right]d\theta$$

$$\left[K_{NNt}^e\right]=\int_{\theta_1}^{\theta_2}\left[\left[S^e\right]^{\mathrm{T}}\left[S^e\right]\left\langle\int_{A_e}\left[B_N^{dt}\right]^{\mathrm{T}}\left[A_b\right]\left[B_N^t\right]dA_e\right\rangle\left[S^e\right]^{\mathrm{T}}\left[S^e\right]\right]d\theta,$$

$$\left[K_{NNit}^e\right]=\int_{\theta_1}^{\theta_2}\left[\left[S^e\right]^{\mathrm{T}}\left[S^e\right]\left\langle\int_{A_e}\left[B_N^{dt}\right]^{\mathrm{T}}\left[A_b\right]\left[B_{Ni}^t\right]dA_e\right\rangle\left[S^e\right]^{\mathrm{T}}\left[S^e\right]\right]d\theta,\ \{P_{Lt}^{Te}\}=\int_{\theta_1}^{\theta_2}\left\langle\left[S^e\right]^{\mathrm{T}}\{P_L^{Te}\}\right\rangle d\theta,$$

$$\{P_{Nt}^{Te}\}=\int_{\theta_1}^{\theta_2}\left[\left[S^e\right]^{\mathrm{T}}\left[S^e\right]\left\langle\int_{A_e}\left[B_N^{dt}\right]^{\mathrm{T}}\{A_T\}dA_e\right\rangle\right]d\theta,\ \{P_t^{Me}\}=\int_{\theta_1}^{\theta_2}\left\langle\left[S^e\right]^{\mathrm{T}}\{P_M^e\}\right\rangle d\theta,$$

$$\left[C_s^e\right] = k_d \int_{\theta_1}^{\theta_2} \left\langle \left[S^e\right]^{\mathrm{T}} \left\{P_L^{Ee}\right\} + \left[S^e\right]^{\mathrm{T}} \left[S^e\right] \int_{A_e} \left(\left[B_N^{dt}\right]^{\mathrm{T}} \left\{A_{be}\right\} \right) dA_e \right\rangle \left[S_1^s\right] d\theta \tag{2.32}$$

Since the response of the overall plate is assumed as periodic, the angle limits (i.e. θ_1 and θ_2) are considered for one cycle/period (i.e. 0 to 2π). Assembling the elemental equations (Eq. (2.31)) in the whole domain of the overall plate, the following global equation can be obtained,

$$\left[K_t\right]\{\Delta X\} + \Delta\omega\left[K_i\right]\{X_i\} = -\{f_t^i\} + \{f_t^T\} + \{f_t^P\} - (\omega_i + \Delta\omega)[C_s]\{w_{si}\} - \omega_i[C_s]\{\Delta w_s\} \tag{2.33}$$

Now, the displacement vectors ($\{w_{si}\}$, $\{\Delta w_s\}$) corresponding to the sensing point velocity ($\dot{w}_s$) can be expressed in terms of the global displacement vectors ($\{X_i\}$, $\{\Delta X\}$) using a transformation matrix ($[N_s]$) as follows,

$$\{w_{si}\} = [N_s]\{X_i\} \text{ and } \{\Delta w_s\} = [N_s]\{\Delta X\} \tag{2.34}$$

Introducing Eq. (2.34) in Eq. (2.33), the simplified equation can be written as,

$$|K_c|\{\Delta X\} + \Delta\omega|K_{ic}|\{X_i\} = \{f_c^{TP}\} - \{f_c^i\},$$

$$|C| = |C_s||N_s|, |K_c| = \langle |K_t| + \omega_i|C| \rangle, |K_{ic}| = \langle |K_i| + |C| \rangle, \{f_c^{TP}\} = \langle \{f_t^T\} + \{f_t^P\} \rangle,$$

$$\{f_c^i\} = \langle \{f_t^i\} + \omega_i|C|\{X_i\} \rangle \tag{2.35}$$

Equation (2.35) can also be expressed in the following form,

$$\{\Delta X\} = \{f_1\} - \Delta\Phi\{f_2\}, \tag{2.36}$$

where $\{f_1\} = \{K_c\}^{-1}(\{f_t^{TP}\} - \{f_{tc}^0\}), \{f_2\} = [K_c]^{-1}[K_{ic}]\{X_i\}$ (2.36a)

in which, the relations $\omega_i = \omega_0 \times \Phi_i$ and $\Delta\omega = \omega_0 \times \Delta\Phi$ are introduced utilizing the fundamental frequency (ω_0) of vibration.

2.3 Solution methodology

In the present solution methodology (Cheung et al. 1990; Hellwig and Crisfield 1995), the increment over a state of vibration is constrained by an arc-length (Δs) and the solutions for an assigned arc-length (Δs) in an incremental step are evaluated using direct iteration method. The arc-length (Δs) in each incremental step yields a constrained equation as follows,

$$\{\Delta X\}^{\mathrm{T}}\{\Delta X\} + \Delta\Phi^2 = \Delta s^2 \tag{2.37}$$

Introducing Eq. (2.36) in the constrained Eq. (2.37), the following quadratic equation can be obtained,

$$C_1\Delta\Phi^2 + C_2\Delta\Phi + C_3 = 0$$

$$C_1 = (f_2{}^{\mathrm{T}} f_2 + 1),\ C_2 = (f_1{}^{\mathrm{T}} f_2 + f_2{}^{\mathrm{T}} f_1),\ C_3 = (f_1{}^{\mathrm{T}} f_1 - \Delta s^2) \tag{2.38}$$

The incremental solutions over a state of vibration corresponding to an assigned arc-length (Δs) can be predicted utilizing an arc-length extrapolation technique (Cheung et al., 1990). Let a state of vibration is defined as: $\{\Lambda\} = [X^T \quad \Phi]$ and $\{\Lambda_1\}$, $\{\Lambda_2\}$, $\{\Lambda_3\}$,.....$\{\Lambda_m\}$ are the m number of solution points. Then the next solution point (Λ_{m+1}) for arc-length (Δs) can be obtained as,

$$\{\Lambda_{m+1}\} = \sum_{i=1}^{m}\left\langle \prod_{\substack{j=0 \\ j\neq i}}^{m}\left(\frac{t_{m+1}-t_j}{t_i-t_j}\right)\right\rangle\{\Lambda_i\}$$

$$t_0 = 0,\ t_1 = (t_0 + s_1),\ t_2 = (t_1 + s_2),\ldots\ldots\ldots\ldots,t_{m+1} = (t_m + \Delta s)$$

$$S_i = \sqrt{\sum_{j=1}^{N_t}\left\langle \Lambda_i(j) - \Lambda_{i-1}(j)\right\rangle^2} \tag{2.39}$$

where, N_t is the number of elements in $\{\Lambda\}$. The predicted solutions ($\{\Lambda_p\}=[\{X_p\}^T \quad \Phi_p]$) yield the predicted increments: $\{\Delta\Lambda_p\}=[\{\Delta X_p\}^T \quad \Delta\Phi_p]$ and those are taken as the initial solutions for the iteration within an incremental step. In each iteration within an arc-length incremental step, the coefficient vectors $\{f_1\}$ and $\{f_2\}$ are updated using either the predicted solution (for first iteration) or the solution of previous iteration. Then, these coefficient vectors are used to obtain two roots ($\Delta\Phi_1$ and $\Delta\Phi_2$) from Eq. (2.38) along with the corresponding solutions ($\{\Delta X_1\},\{\Delta X_2\}$) from Eq. (2.36). If the roots ($\Delta\Phi_1$ and $\Delta\Phi_2$) are imaginary, then recalculation is required by assigning a new value of Δs. Otherwise, for two real roots, the correct one can be determined by the least distance from the predicted solution (for first iteration) or the previous iterative solution as follows,

$$\Delta l_1=\sqrt{\sum_{j=1}^{N_t}\left\langle\Delta\Lambda_1(j)-\Lambda_0(j)\right\rangle^2}\ ,\ \Delta l_2=\sqrt{\sum_{j=1}^{N_t}\left\langle\Delta\Lambda_2(j)-\Lambda_0(j)\right\rangle^2}\ ,$$

$$\{\Delta\Lambda_1\}=[\Delta X_1^T \quad \Delta\Phi_1],\{\Delta\Lambda_2\}=[\Delta X_2^T \quad \Delta\Phi_2]$$

$$\text{for}\ \ \Delta l_1<\Delta l_2,\ \Delta\Phi=\Delta\Phi_1 \text{ and } \{\Delta X\}=\{\Delta X_1\}$$

$$\text{or}$$

$$\text{for}\ \Delta l_2<\Delta l_1,\ \Delta\Phi=\Delta\Phi_2 \text{ and } \{\Delta X\}=\{\Delta X_2\} \qquad (2.40)$$

where, $\{\Lambda_0\}$ is the predicted solution or the previous iterative solution. The new solutions ($\Delta\Phi,\{\Delta X\}$) along with the converged solutions (Φ_i, $\{X_i\}$) of previous incremental step are again used to form the coefficient vectors $\{f_1\}$ and $\{f_2\}$ in the subsequent iteration and the process goes on till the convergence of solutions.

For a particular arc-length incremental step, the required number of iteration for the convergence of solution depends on the corresponding assigned value of Δs. For an assigned value of Δs, the number of iteration may rise or the difficulty in the convergence of solution may arise in case where the response curve takes sharp turn. In

order to ease this difficulty, the Δs in an incremental step is determined based on the corresponding magnitudes of the largest component of $\{\Delta X\}$ and $\Delta\Phi$. The allowable increments for the largest component of $\{\Delta X\}$ and $\Delta\Phi$ are first decided from experience and those are taken as the reference values (ΔX_{ref}, $\Delta\Phi_{ref}$). Following these reference increments, the value of Δs is decided by executing the following routine:

1. Take an initial large value of Δs.
2. Determine the extrapolated point $(\Phi_p, \{X_p\})$ using Eq. (2.39) and also the corresponding increments $(\Delta\Phi_p, \{\Delta X_p\})$.
3. Compare the magnitudes of largest component of $\{\Delta X_p\}$ and $\Delta\omega_p$ with the corresponding reference values (ΔX_{ref}, $\Delta\Phi_{ref}$).
4. If the magnitudes of both the increments are less than the corresponding reference values (ΔX_{ref}, $\Delta\Phi_{ref}$), take the value of Δs for the current incremental step.
5. Otherwise, if any one or both the increments are greater than the corresponding reference values (ΔX_{ref}, $\Delta\Phi_{ref}$), decrease the current Δs and recalculate from step 2.

In this process, the solution in an incremental step is controlled by the incremental displacement and/or incremental frequency while the involvement of arc-length (Δs) procedure reduces the number of iteration for the convergence of solution. In the present solutions, constant values of ΔX_{ref} and $\Delta\Phi_{ref}$ are considered for evaluating the whole response curve. But, these reference increments may be varied in different incremental steps depending on the difficulty in the convergence of solution. For the prediction of initial solution utilizing arc-length extrapolation technique, the number of previously converged solution points i.e. the value of m (Eq. (2.39)) is an important factor. For higher value of m, the error in the predicted solution will be more. However, in the present solutions, three previously converged solution points

($m=3$) are considered i.e. the quadratic arc-length extrapolation is considered for prediction of initial solution.

2.4 Numerical results and discussion

In this section, the numerical results for investigating the nonlinear dynamic behavior of the smart heated FG plates in the frequency-domain are presented. The numerical results also asses the performance of PFRC distributed actuator for controlling the harmonically excited nonlinear vibration of heated FG plates. A square FG substrate plate ($a=b=400$ mm, $h=6$ mm) is considered and the PFRC layer attached to the top surface of the substrate plate is considered to have a thickness (h_p) of, 250 μm. Unless otherwise mentioned, the piezoelectric fiber orientation angle (ψ) and the piezoelectric fiber volume fraction (v_f) in the PFRC actuator layer are considered as 0^o and 40%, respectively. The substrate FG plate is considered to be composed of zirconium (ceramic) and aluminum (metal). The temperature dependent material properties of these constituent materials are given by (Noda, 1999),

Aluminium alloy:

$$E(T)=(74+23\times10^{-3}T-11\times10^{-5}T^2+51\times10^{-9}T^3)\ \text{GPa},$$

$$\alpha(T)=(1.6\times10^{-5}+3.45\times10^{-8}T-3.3\times10^{-11}T^2+2.4\times10^{-14}T^3)\ \text{K}^{-1},$$

$$k(T)=218\ \text{WmK}^{-1} \tag{2.41}$$

Zirconium:

$$E(T)=(225-20\times10^{-2}T-90\times10^{-6}T^2+4\times10^{-9}T^3)\ \text{GPa},$$

$$\alpha(T)=(1.48\times10^{-5}-2.2\times10^{-8}T+1.15\times10^{-11}T^2+4\times10^{-15}T^3)\ \text{K}^{-1},$$

$$k(T)=(11\times10^{-1}+1.6\times10^{-5}T+19\times10^{-7}T^2-97\times10^{-11}T^3)\ \text{WmK}^{-1} \tag{2.42}$$

Since the thermal conductivity (k(T)) of the ceramic constituent material is weakly dependent on the temperature variation, it is assumed as a constant having a value of

1.5 W mK^{-1}. The Poisson's ratio is assumed to be constant having a value of 0.33 over the domain of the substrate FG plate. For a given temperature gradient, the temperature distribution in the FG plate can be determined from Eq. 2.5. Subsequently, the effective material properties at any point in the substrate FG plate can be computed using Eqs. (2.41), (2.42) and (2.3). The effective material properties of the PFRC actuator layer corresponding to the fiber orientation angle as 0^0 ($\psi = 0^0$) are given by (Mallik and Ray 2003),

$$[\bar{C}_b^k] = \begin{bmatrix} 32.6 & 4.3 & 0 \\ 4.3 & 7.2 & 0 \\ 0 & 0 & 1.29 \end{bmatrix} \text{GPa}, \quad [\bar{C}_s^k] = \begin{bmatrix} 1.05 & 0 \\ 0 & 1.29 \end{bmatrix} \text{GPa},$$

$$e_{31} = -6.76 \text{ C/m}^2 \quad \text{and} \quad e_{32} = -0.076 \text{ C/m}^2 \tag{2.43}$$

The circular frequency (ω) of the applied uniformly distributed transverse harmonic mechanical load ($p \times cos(\omega t)$) is considered near the fundamental frequency of the overall plate. The boundaries of the overall plate are considered to be simply supported ($\boldsymbol{v_0 = w_0 = \theta_y = 0}$ at $\boldsymbol{x = 0, a}$ and $\boldsymbol{u_0 = w_0 = \theta_x = 0}$ at $\boldsymbol{y = 0, b}$).

Since the periodic response of the overall smart FG plate is anticipated in combination of different harmonics, the number of harmonic terms in the Fourier series is an important consideration for correct frequency repose. It is observed that one term ($F = 1$, Eq. (2.24)) of the Fourier series can give the accurate response up to an amplitude of $0.8 \times h$ (Ribeiro and Petyt 2000). In the present analysis, the maximum transverse deflection of the overall plate during its vibration is considered to be limited to h and that is evaluated considering three harmonic terms ($F = 3$, Eq. (2.24)). According to the form of the solution (Eq. (2.24)), the transverse deflection at the middle point of the overall plate during its vibration can be written as: $w^s + w^t(t)$, where, $w^t(t)$ is the time-dependent displacement with respect to the equilibrium position w^s. For presenting the frequency response of the overall plate, the maximum value of $w^t(t)$ within a time-period at a

frequency is calculated and represented as: $W^t = w^t_{max} / h$, while the corresponding equilibrium position is represented as: $W^s = w^s / h$. The value of W^t corresponding to a frequency of vibration of the overall plate changes as the PFRC actuator layer electrically induces the damping in the overall plate. It is observed from the frequency response of the overall plate that the maximum change in the value of W^t due to the induced damping by the PFRC layer occurs at the peak-point of a frequency response. Thus, in the present work, the performance of the PFRC actuator layer for inducing smart damping in the overall plate is measured in terms of the change in time-dependent deflection (W^t_{peak}) at the peak-point of the frequency response curve.

In the present FE model, the elements are considered in square shape. A convergence study for the present FE model is carried out through the computation of peak point-deflection near fundamental frequency for different meshes of the overall plate and it is illustrated in Table 2.1. It may be observed from this table that a 8×8 mesh could provide sufficient numerical accuracy and hence the present results are evaluated considering the same FE mesh of the smart plate.

Table 2.1 Convergence study for the present FE model of the overall smart plate.

Mesh size	2×2	4×4	6×6	8×8
W_{peak}	0.2147	0.2088	0.2067	0.2066

2.4.1 Validation of the present incremental finite element model

In order to verify the present incremental nonlinear dynamic finite element formulation, implementation of HBM and solution methodology, first the fundamental natural frequency of the FG plate ($h_p \approx 0$, $k_d = 0$) is computed in the absence/presence of a temperature gradient across the thickness of the substrate plate.

Table 2.2 Comparison of fundamental natural frequency (ω_o) parameter ($\Omega = \omega_o(a^2/h)\sqrt{\rho_m(1-\nu^2)/E_m}$) of FG plate in the absence and in the presence of a temperature gradient across its thickness

Description	Ω (Huang and Shen, 2004)	Ω (present)
$n=$ 1, T_c = 300 K, T_m = 300 K	7.555	7.553
$n=$ 1, T_c = 400 K, T_m = 300 K	7.514	7.512
$n=$ 2, T_c = 300 K, T_m = 300 K	6.777	6.774
$n=$ 2, T_c = 400 K, T_m = 300 K	6.728	6.724

Table 2.3 Comparison of frequency ratio (ω/ω_o) vs. W^t relation for nonlinear free vibration of FG plate with a temperature gradient (T_c = 400 K, T_m = 300 K, n =2)

W^t	0.2	0.4	0.6	0.8	1.0
ω/ω_o (Huang and Shen, 2004)	1.021	1.082	1.175	1.255	1.437
ω/ω_o (present)	1.020	1.083	1.177	1.258	1.440

It may be observed from Table 2.1 that the present results are in good agreement with the similar results given in Huang and Shen (2004).This comparison validates the present finite element formulation. The relationship in between the amplitude (W^t) and the frequency (ω) for the nonlinear free vibration of the plate is evaluated and presented in Table 2.2 along with the published results Huang and Shen (2004). Table 2.2 shows an excellent agreement of the present results with those reported in Huang and Shen (2004) and this comparison verifies the implementation of HBM as well as present solution methodology.

2.4.2 Effect of fiber-volume fraction (v_f) of PFRC actuator layer

In the absence of temperature gradient ($T_c = T_m =$ 300 K), Fig. 2.2 illustrates the controlled nonlinear frequency responses of the overall FG plate for different values of fiber volume fraction (v_f) of the PFRC actuator layer while the values of control gain (k_d) and mechanical load-amplitude (p) remain constant. It could be noted that the responses corresponding to 60% and 100% fiber volume fractions (v_f) are identical. Figure 2.2 also demonstrates significant variation in the control authority of the PFRC actuator layer as its fiber volume fraction (v_f) varies. However, in the present analysis, the performance of the PFRC actuator for controlling the harmonically excited nonlinear vibration of the heated FG plate is investigated considering a fiber volume fraction (v_f) of 40%.

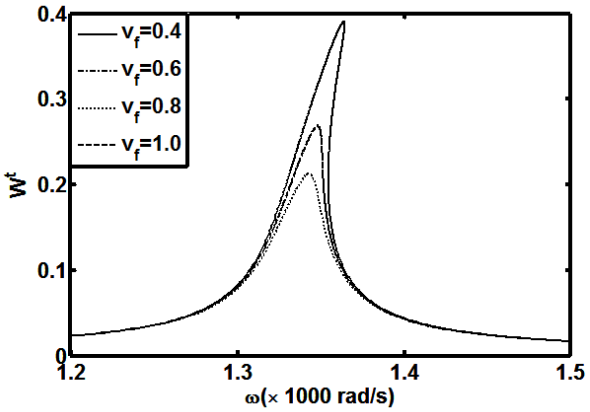

Fig. 2.2 Nonlinear frequency responses of the overall FG plate for different values of fiber volume fraction (v_f) of the PFRC actuator layer (p= 400 N/m^2, λ=1, k_d=100, $T_c = T_m$ = 300 K, n=1).

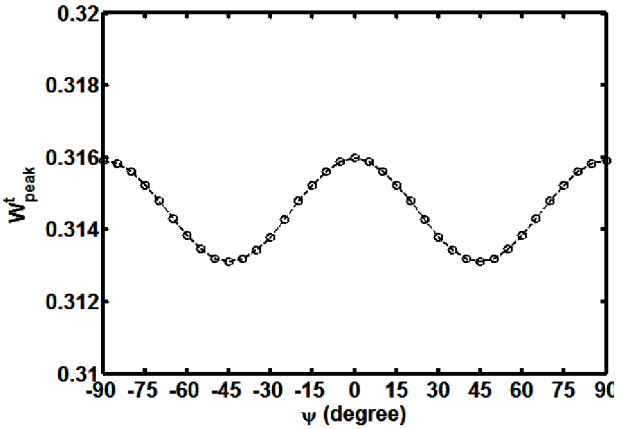

Fig. 2.3 Variation of peak-point deflection (W^t_{peak}) of controlled nonlinear frequency response of the overall FG plate with the fiber orientation angle (ψ) in the PFRC actuator layer (p= 400 N/m^2, λ=1, k_d=100, $T_c = T_m$ =300 K, n=2).

2.4.3 Effect of fiber-orientation angle (ψ) of PFRC actuator layer

Figure 2.3 shows the variation of peak-point deflection (W^t_{peak}) of controlled nonlinear frequency response of the overall FG plate for different values of piezoelectric fiber orientation angle (ψ) in the PFRC actuator layer. This figure suggests a better use the PFRC actuator layer when its piezoelectric fiber orientation angle is, $\pm 45^o$. But, the negligibly small variation in the magnitude of W^t_{peak} (Fig. 2.3) indicates insignificant effect of ψ on the control authority of PFRC actuator layer. Thus, the present investigations are carried out considering the piezoelectric fiber orientation angle in the PFRC actuator layer as, 0^o.

2.4.4 PFRC layer on metal/ceramic rich surface of substrate FG plate

Figure 2.4 illustrates the controlled nonlinear frequency responses of the overall smart FG plate when the PFRC actuator layer is attached either to the ceramic rich top surface ($\lambda = 2$) or to the metal rich top surface ($\lambda = 1$) of the substrate FG plate. This figure demonstrates a better control authority of the PFRC actuator layer when it is attached to the metal rich surface of the host FG plate. Following this observation, further results are evaluated considering the PFRC actuator layer on the metal rich top surface of the FG substrate plate.

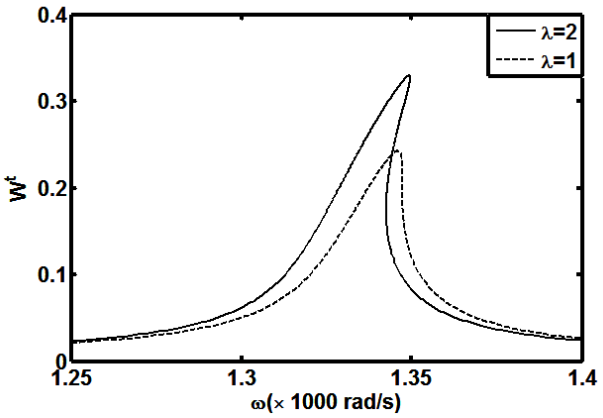

Fig. 2.4 Nonlinear frequency responses of the overall FG plate when the PFRC layer is attached either to the ceramic rich (λ=2) or to the metal rich (λ=1) top surface of the FG substrate plate ($T_c = T_m$=300 K, n=2, p = 300 N/m^2, k_d=100).

2.4.5 Effect of load-amplitude (p)

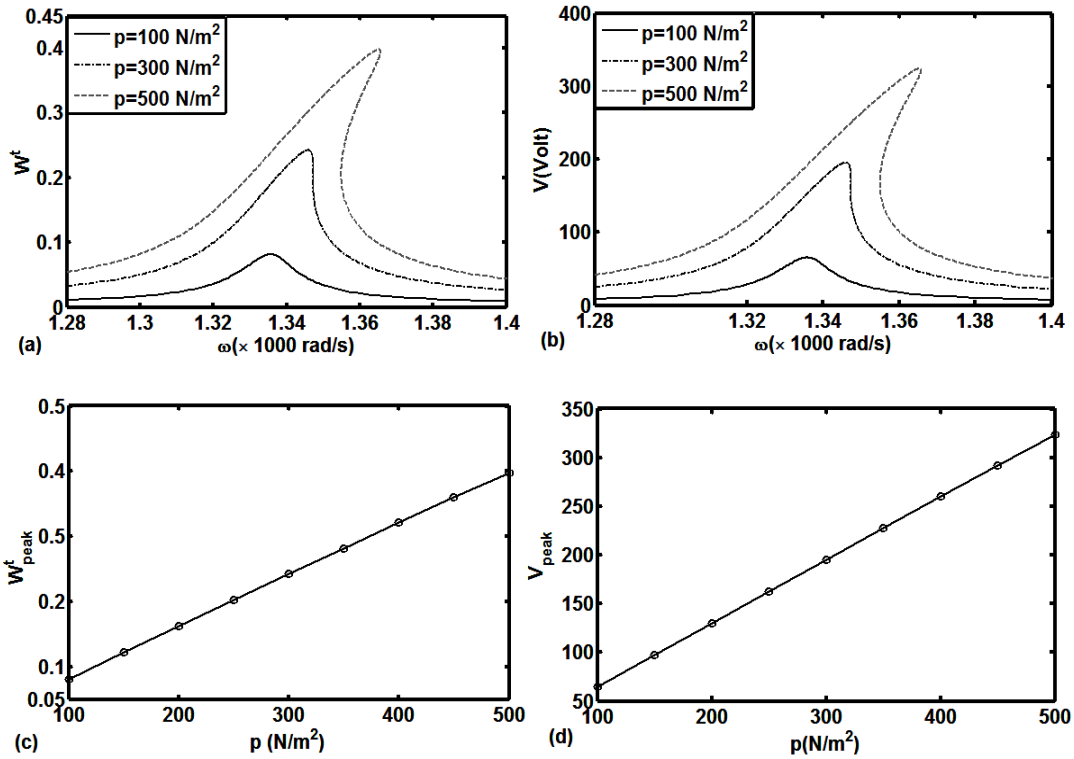

Fig. 2.5 (a) Nonlinear frequency responses of the overall FG plate and (b) the corresponding variations of control voltage, variations of (c) the peak-point deflection (W^t_{peak}) and (d) the corresponding control voltage (V_{peak}) with the load amplitude (300K, k_d=100, n=2, λ=1).

Figure 2.5(a) represents the nonlinear frequency responses of the overall FG plate for different values of load-amplitude (p) when the control gain (k_d) remains constant in room temperature ($T_c = T_m = 300$ K). The corresponding variations in the required control voltage across the thickness of the PFRC actuator layer are also illustrated in Fig. 2.5(b). These figures indicate that a significant damping in the overall FG plate can be achieved in expense of feasible applied control voltage across the thickness of PFRC actuator layer. The peak-point deflections (W^t_{peak}) of frequency responses and the corresponding required control voltages (V_{peak}) are plotted against load-amplitude (p) in Figs. 2.5(c) and 2.5(d), respectively. These figures demonstrate an important fact that a

higher value of load-amplitude (p) causes more nonlinearity in the frequency response (Fig. 2.5(a)), but the corresponding variations in W^t_{peak} and V_{peak} (Figs. 2.5(c)-(d)) are linear.

2.4.6 Effect of control gain (k_d)

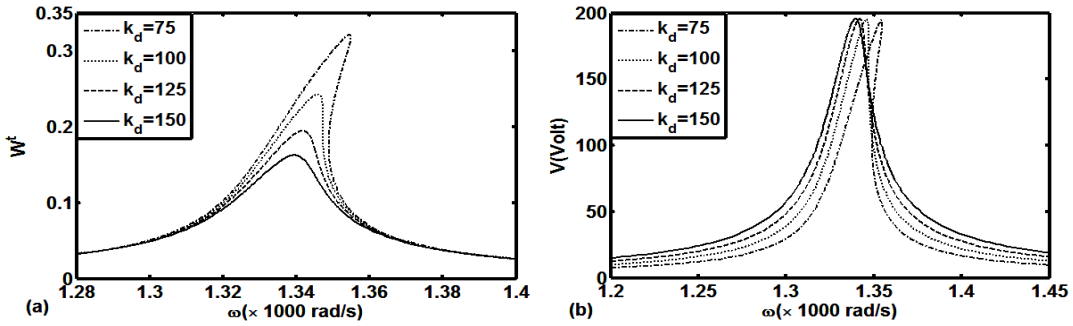

Fig. 2.6 (a) Nonlinear frequency responses of the overall FG plate for different values of control gain (k_d), (b) the corresponding variation of required control voltage ($T_c = T_m$ =300 K, n =2, λ =1, p = 300 N/m^2).

Figure 2.6(a) demonstrates the nonlinear frequency responses of the overall FG plate for different values of the feedback control gain (k_d) while the load-amplitude (p) and the temperature gradient ($T_c = T_m =$ 300 K) remain constant. Figure 2.6(a) shows that the PFRC actuator layer is capable to induce more damping in the overall FG plate when a higher value of control gain (k_d) are assigned. From Fig. 2.6(b), it is also observed that when the mechanical load-amplitude remains constant, higher values of control gain (k_d) do not cause the increase in the maximum value of required control voltage (V_{peak}). An important aspect in the present analysis is to investigate the effect of temperature gradient ($T_c >$ 300 K, $T_m =$ 300 K) across the thickness of the substrate FG plate on its nonlinear dynamic behavior in the frequency-domain and also on the control authority of PFRC actuator layer.

2.4.7 Effect of ceramic rich surface temperature (T_c)

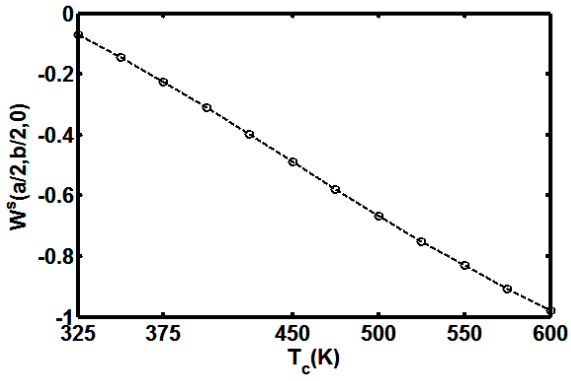

Fig. 2.7 Initial thermal bending deflections of the overall FG plate for different ceramic rich surface temperatures (n=1, λ=1, T_m=300 K).

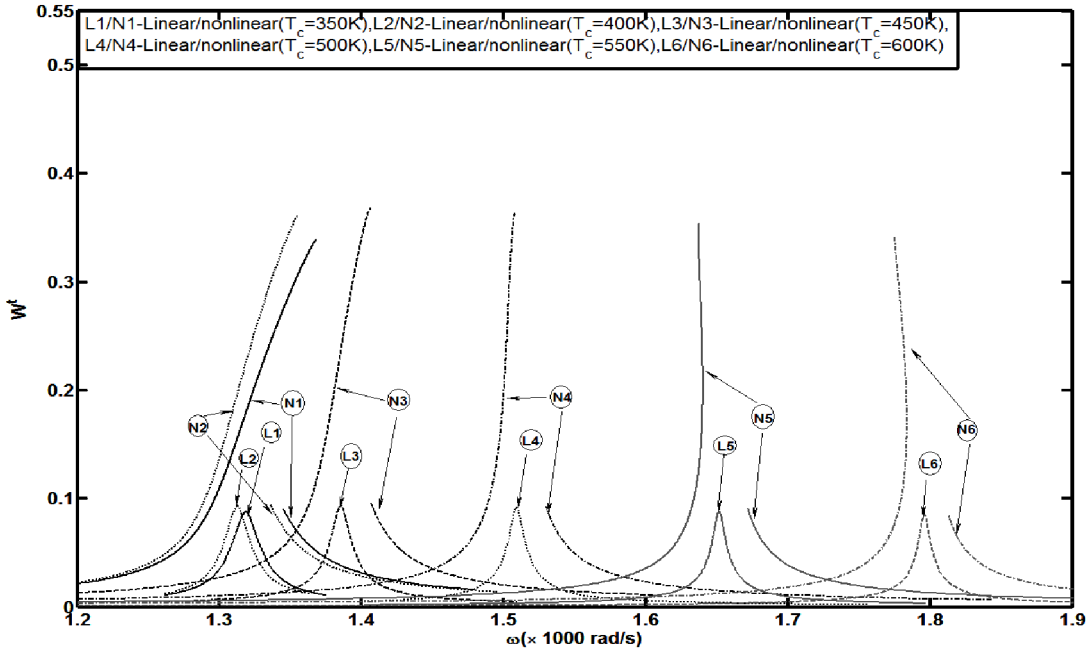

Fig. 2.8 Linear and nonlinear frequency responses of the overall FG plate for different ceramic rich surface temperatures (n=1, λ=1, k_d =100, T_m=300 K, p = 100 N/m^2 for linear responses and p = 400 N/m^2 for nonlinear responses).

The temperature of the bottom ceramic rich surface of the FG plate causes an initial bending deformation of the overall FG plate along the negative z-direction. It is observed that due to an applied harmonic mechanical load, the variation of this initial bending deflection with the frequency of vibration is negligibly small. Therefore, at a temperature gradient, it is reasonable to assume that the equilibrium position (W^s) of the overall FG plate is constant to its initial thermal bending deflection at all frequencies of vibration. Figure 2.7 illustrates the initial thermal bending deflections of the overall FG plate for different ceramic rich surface temperatures. The linear and the nonlinear frequency responses of the overall FG plate corresponding to different ceramic rich surface temperatures are shown in Fig. 2.8. The linear and the nonlinear frequency responses at a particular temperature gradient are achieved by applying a lower ($p = 100\ N/\text{m}^2$) and a higher ($p = 400\ N/\text{m}^2$) values of mechanical load-amplitude. It should be noted that although the difficulty in the convergence of

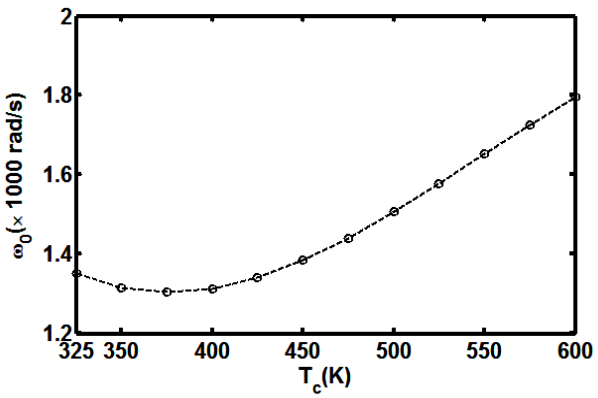

Fig. 2.9 Variation of fundamental frequency (ω_0) of vibration with the ceramic rich surface temperature (T_c) (p = 100 N/m^2, λ =1, k_d =100, n =1, T_m =300 K).

solutions arises in evaluation of the nonlinear frequency responses under a temperature

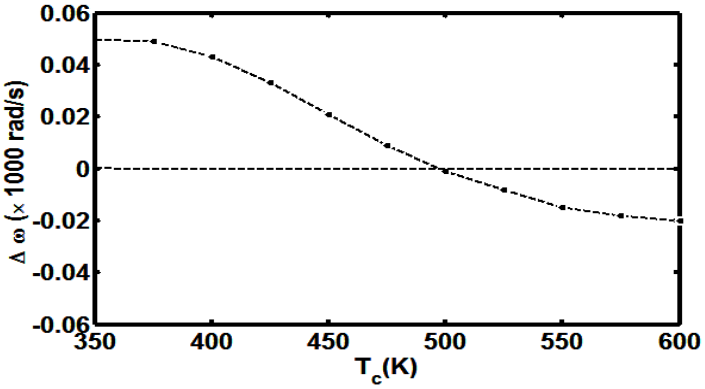

Fig. 2.10 Difference between the frequencies ($\Delta\omega$) corresponding to the peak-points of linear and nonlinear frequency responses of the overall FG plate at each ceramic rich surface temperature (n=1, λ=1, k_d=100, T_m=300 K, p=100 N/m^2 for linear responses and p=400 N/m^2 for nonlinear responses).

gradient, but the peak points of the response curves are distinctly obtained as shown in the results. It may be observed from Fig. 2.8 that the fundamental frequency (ω_o) of vibration of the overall FG plate decreases up to a certain value of increasing ceramic rich surface temperature ($T_c = 375$ K). After that, it (ω_o) increases with further increase of temperature (T_c). It should be noted here that while the initial decrease in the fundamental frequency (ω_o) with the increase in T_c is a known fact, the increase in the same (ω_o) for further increase in temperature ($T_c > 375$ K) is due to the significant effect of initial thermal bending of the overall FG plate at high temperature (T_c). In Fig. 2.9 the fact of initial thermal bending seen in Fig. 2.8 is also demonstrated by plotting the variation of fundamental frequency (ω_o) with the ceramic rich surface temperature (T_c). Another important effect of initial thermal bending of the overall FG plate on its nonlinear dynamic behavior in the frequency-domain can also be observed from Fig. 2.8 that the hardening structural behavior of the overall FG plate switches from to softening

one as the ceramic rich surface temperature increases from room temperature to a higher temperature. In Fig. 2.10, the difference between the frequencies, ($\Delta\omega = \left(\omega|_{nonlinear} - \omega|_{linear}\right)$) corresponding to the peak-points of linear and nonlinear responses at each ceramic rich surface temperature is plotted in order to show the switching of the structural behavior in a clear manner. It is known that the positive/negative value of this frequency difference indicates hardening/softening structural behavior of the plates. Thus, as demonstrated in Fig. 2.10, the overall FG plate turns to behave as a softening structure when the ceramic rich surface temperature (T_c) exceeds a value about 500 K. Figure 2.11(a) shows the peak-points (W^t_{peak}) of nonlinear frequency responses for different ceramic rich surface temperatures (T_c). The effect of ceramic rich surface temperature on the performance of PFRC actuator layer for controlling the harmonically excited nonlinear vibration of the overall FG plate is also significant as can be noticed from Fig. 2.8.

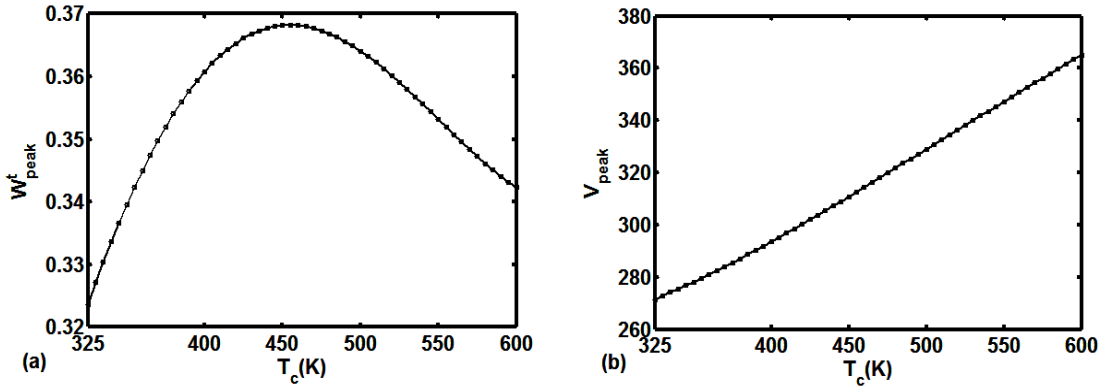

Fig. 2.11 (a) Variations of the peak point (W^t_{peak}) of frequency response and (b) the corresponding control voltage (V_{peak}) with ceramic rich surface temperature (T_c) (p = 400 N/m^2, λ=1, k_d=100, n=1, T_m=300 K).

It may be observed from Fig. 2.11(a) that for constant values of control gain (k_d) and mechanical load-amplitude (p), the magnitude of W^t_{peak} increases with the increasing ceramic rich surface temperature (T_c). But, the same again decreases after a certain value

of ceramic rich surface temperature (i.e. about 450 K (Fig. 2.11(a)). Although this result shows more control authority of PFRC actuator layer at very high temperature (T_c), but the corresponding maximum value of required control voltage (V_{peak}) (at a constant gain value) significantly increases as can be noticed from Fig. 2.11(b). In fact, since it happens at a high frequency (Fig. 2.8), the corresponding required control voltage reaches to a higher value. Therefore, Fig. 2.11(b) suggests a lesser value of control gain (k_d) at higher temperature in view of the permissible applied voltage across the thickness of the PFRC actuator layer.

2.4.8 Effect of volume fraction index (n) of FG substrate plate

In the presence of a temperature gradient ($T_c = 500$ K, $T_m = 300$ K) across the thickness of the FG substrate plate, the frequency responses (linear and nonlinear) and the corresponding equilibrium positions (W^s) for different values of volume fraction index (n) of the FG substrate are shown Figs. 2.12 and 2.13 respectively.

As the value of n increases, the amount of metal in the FG substrate plate increases resulting in more temperature in the substrate plate at a constant temperature gradient. Thus, the initial thermal bending deflection of the overall FG plate increases as the value of n increases at a constant temperature gradient. Since the higher value of n causes a softer overall FG plate, the fundamental frequency of vibration decreases with the increasing value of n as demonstrated in Fig. 2.12 (from linear responses). But, when the initial bending deflection corresponding to this increase of n becomes too large, this characteristic may change i.e. the fundamental frequency of vibration increases with the increasing value of n. Figure 2.13 illustrates this fact as the value of n increases from 0.2 to 5.0 in the presence of a temperature gradient ($T_c = 500$ K, $T_m = 300$ K).

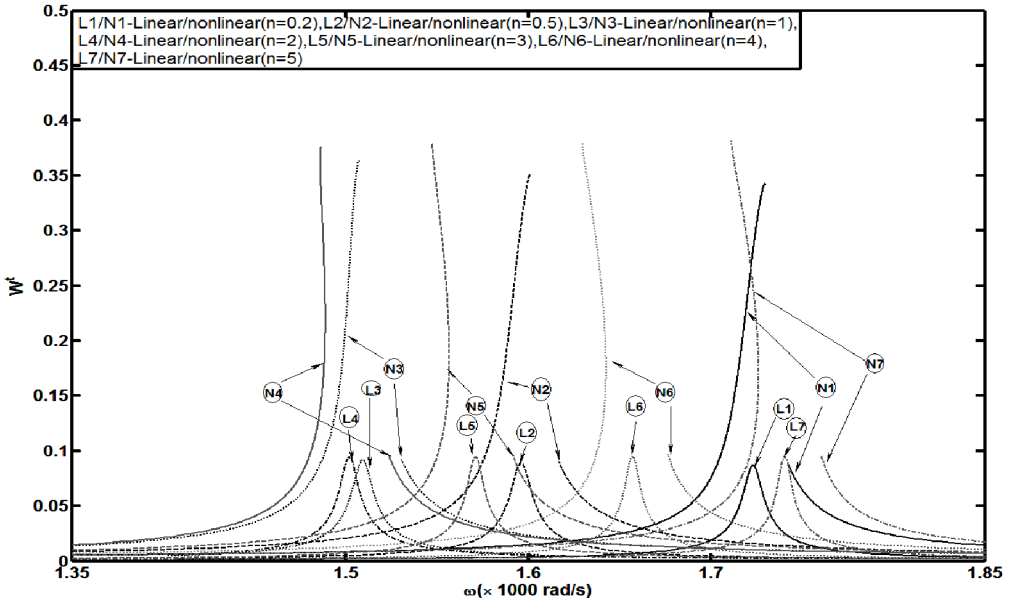

Fig. 2.12 Linear and nonlinear frequency responses of the overall FG plate for different values of volume fraction index (n) (λ=1, k_d=100, T_m=300 K, T_c=500K, p=100 N/m^2 for linear responses and p = 400 N/m^2 for nonlinear responses).

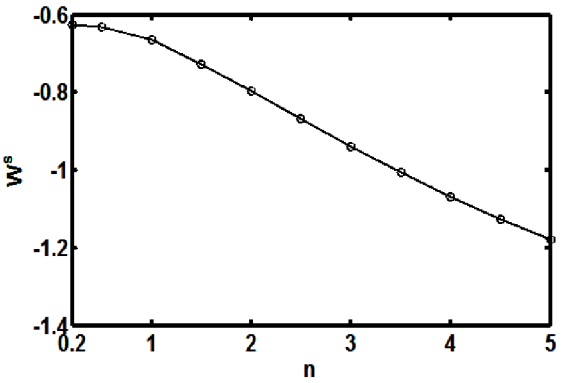

Fig. 2.13 Initial thermal bending deflections ($W^s(a/2,b/2,0)$) of the overall FG plate for different values of volume fraction index (n) of the FG substrate plate at a constant temperature gradient (T_c =500 K, T_m =300K, λ=1).

Figure 2.14 shows the variation of fundamental frequency (ω_o) with n for the temperature gradient T_c = 500 K and T_m = 300 K. It may be observed that although the fundamental frequency (ω_o) decreases with the increasing value of n, but it (ω_o) again increases beyond $n = 1.5$. The earlier results demonstrate an alteration of structural behavior of the overall plate for increase in temperature gradient from a lower value to a higher value. At a constant temperature gradient, this observation may also appear if the value of n increases to a high value.

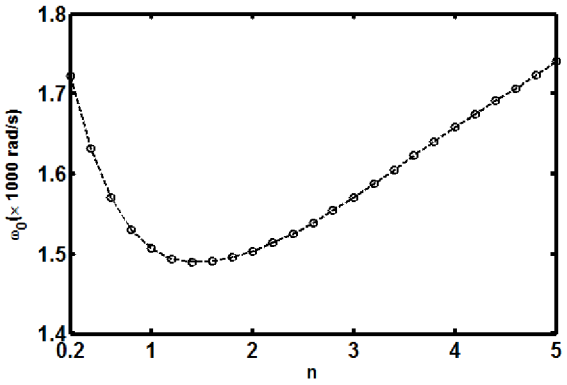

Fig. 2.14 Variation of fundamental frequency (ω_0) of vibration with the volume fraction index (n) of the FG substrate plate in presence of temperature gradient (T_c =500K, T_m = 300 K, p =100 N/m^2, λ =1, k_d =100).

Figure 2.15 illustrates this fact by plotting the difference between the frequencies $\Delta\omega = \left(\omega|_{nonlinear} - \omega|_{linear}\right)$) corresponding to the peak-points of linear and nonlinear responses (Fig. 2.12) for different values of n. This figure shows a change of structural behavior of the overall FG plate when the value of n exceeds a value about 0.8 in the presence of a temperature gradient (T_c = 500 K, T_m = 300 K). The variation in the control authority of PFRC actuator with the volume fraction index (n) of FG substrate plate is demonstrated in Fig. 2.16. For constant values of control gain (k_d) and load-amplitude (p). Figure 2.16(a) illustrates the peak-points (W^t_{peak}) of nonlinear

frequency responses for different values of n in the presence/absence of temperature gradient.

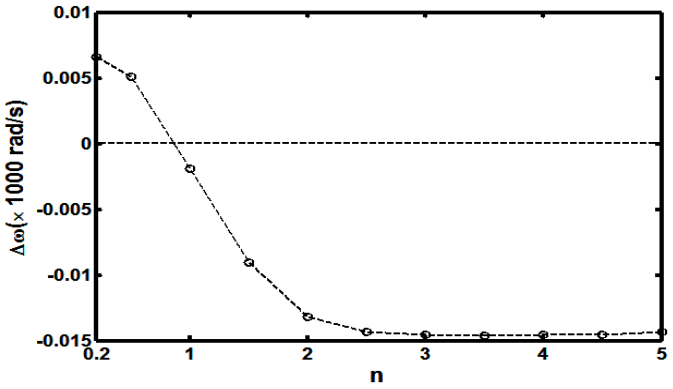

Fig. 2.15 Difference between the frequencies ($\Delta\omega$) corresponding to the peak-points of linear and nonlinear frequency responses for different volume fraction index (n) (T_c = 500 K, T_m = 300 K, λ =1, k_d =100, p = 100 N/m^2 for linear response and p =400 N/m^2 for nonlinear

The variation in the corresponding required control voltage (V_{peak}) is also illustrated in Fig. 2.16(b). Since an increased value of W^t_{peak} indicates lesser damping in the overall FG plate, Fig. 2.16(a) demonstrates a decrease in the control authority of the PFRC actuator layer at a higher value of n. The figure (Fig. 2.16(b)) for the corresponding control voltage shows a relatively higher rate of increase of required control voltage (V_{peak}) with the increasing value of n when there is a temperature gradient (T_c = 500 K, T_m = 300 K). Thus, in order to limit the applied voltage across the thickness of the PFRC layer to its (voltage) permissible value, this result suggests a lower value of control gain (k_d) for the higher value of n in the presence of a temperature gradient.

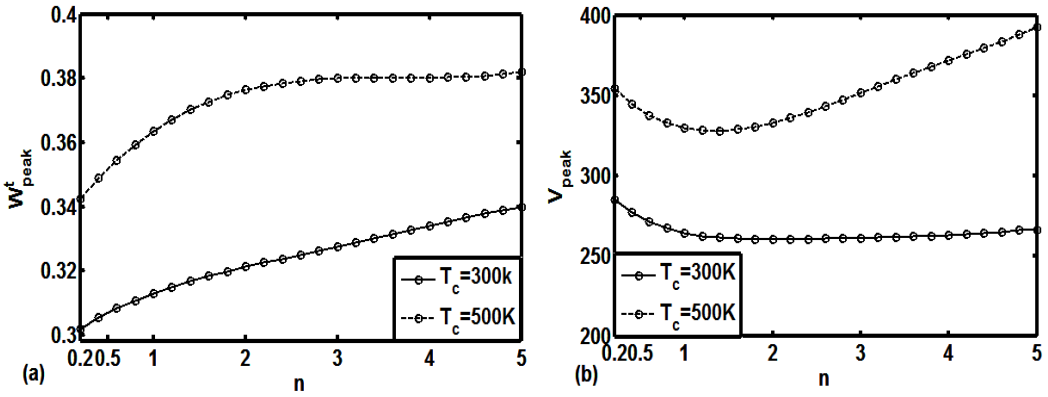

Fig. 2.16 Variations of (a) peak-point deflection (W^t_{peak}) of nonlinear frequency response and (b) the corresponding required control voltage (V_{peak}) with the volume fraction index (n) (p = 400 N/m^2, λ=1, k_d=100, T_m = 300 K).

2.4.9 Effect of FG substrate plate-thickness (h)

In Fig. 2.17 the effect of FG substrate plate thickness on the control authority of PFRC actuator layer is demonstrated. For constant values of control gain (k_d), load-amplitude (p) and temperature gradient (T_c = 500 K, T_m = 300 K), Fig. 2.17(a) illustrates the peak-point deflections (W^t_{peak}) of frequency responses of the overall plate for different values of substrate FG plate thickness. The corresponding required control voltages (V_{peak}) are also illustrated in Fig. 2.17(b). In these figures, W^t_{peak} and the corresponding V_{peak} both decrease with the increasing FG substrate plate thickness. This result indicates a better control authority of the PFRC actuator layer with lesser amount of required control voltage in case of thicker FG substrate plates.

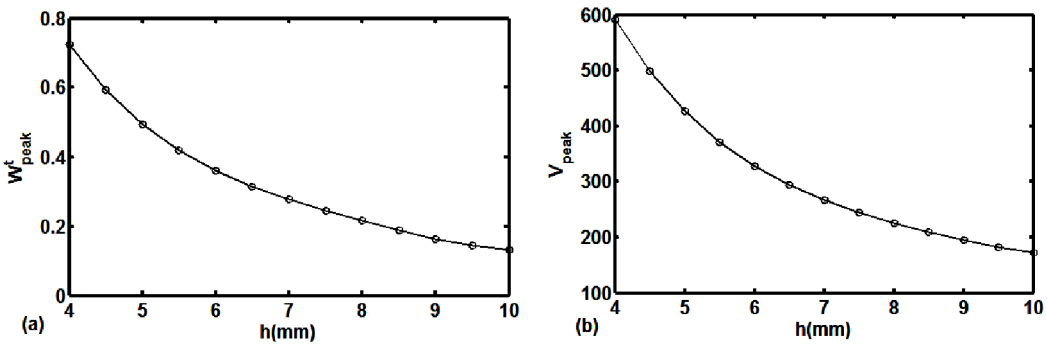

Fig. 2.17 Variations of (a) the peak-point deflection (W^t_{peak}) of frequency response and (b) the corresponding required control voltage (V_{peak}) of the overall FG plate with the substrate FG plate thickness (h) (p =400 N/m^2, λ =1, k_d =100, T_m =300 K, T_c =500 K, n =1).

2.5 Conclusions

A nonlinear dynamic incremental finite element model of smart FG plates with a heated plate-surface is developed for analyzing its nonlinear dynamic characteristics in the frequency-domain. The substrate FG plates are integrated with a smart PFRC layer. The PFRC layer induces smart damping in the overall FG plate as it is activated by external voltage supplied according to the negative velocity feedback control strategy. The temperature in the substrate FG plate is spatially distributed and assumed to be varied only in the thickness direction. The temperature-dependent material properties of the FG plates are graded in the thickness direction according to a simple power law and expressed in terms of the volume fractions of ceramic and metal constituent materials. Based on the von Karman nonlinear strain displacement relations and the first order shear deformation theory, the nonlinear incremental finite element equations of motion in the time-domain are derived employing the Hamilton's principle. The motion of the overall smart heated FG plate is assumed as periodic and modeled following the Fourier series representation in order to express the nonlinear incremental equations of motion in the frequency-domain. For the numerical solutions of these incremental equations of motion in the frequency-domain, an arc-length extrapolation technique is utilized and

also a new strategy for selecting the arc-length in each incremental step is described in the present work.

The numerical results from this chapter reveal the following important observations:

1. The initial flexural deformation of the overall FG plate due to the ceramic rich surface temperature remains almost constant during its vibration under the harmonic mechanical load of any frequency.

2. Normally, the fundamental frequency of vibration of the overall FG plate decreases as its temperature increases. But, because of the corresponding increase of initial bending deformation, the fundamental frequency of vibration of the overall FG plate increases beyond a certain value of increasing temperature.

3. The overall FG plate usually exhibits hardening structural behavior. But in the presence of a high temperature, the same may behave as a softening structure due to the effect of its initial thermal bending deformations.

4. The increase in temperature of the substrate FG plate significantly affects the control authority of the PFRC actuator layer and also causes higher value of required control voltage at a constant value of feedback control gain.

5. The fundamental frequency of vibration of the overall FG plate decreases with the increase of metal-volume fraction in the FG substrate. However, in the presence of a temperature gradient across the thickness of the FG substrate plate, the fundamental frequency of vibration may increase when the increasing metal-volume fraction exceeds a certain value.

6. In the presence of a temperature gradient across the thickness of the FG substrate plate, the overall plate may alter its hardening structural behavior to softening one as the metal-volume fraction in the substrate plate increases.

7. The control authority of PFRC layer decreases for increase of metal-volume fraction with constant values of control gain, load amplitude and temperature gradient.

8. Use of a higher metal-volume fraction in the presence of a temperature gradient across the substrate plate-thickness needs a lower value of control gain to keep the maximum value of applied voltage within its (voltage) permissible value for PFRC actuator.

9. A better control authority of PFRC actuator with lesser control voltage is observed for thicker substrate FG plates.

Chapter 3

PIEZO-VISCOELASTICALLY DAMPED NONLINEAR FREQUENCY-RESPONSE OF FUNCTIONALLY GRADED PLATES WITH A HEATED PLATE-SURFACE

This chapter presents the control of variation of smart FG plates incorporating a constrained viscoelastic layer between the host FG plate-surface and the PFRC layer with an objective of enhanced damping especially at high temperature applications. Incremental finite element formulation along with GHM method for modeling the viscoelastic layer is described in details along with the solution strategy for solution of active vibration of such smart structures. Based on the formulations, numerical results are presented to substantiate the efficacy of ACLD in enhancing the effective damping. In addition effects of important parameters such as initial thermal deflection, temperature, volume fraction on the controlled non-linear dynamic response are also presented in this Chapter.

3.1 Introduction

For high temperature of a surface of substrate FG plate, the control-capability of the PFRC actuator layer decreases resulting in lesser active damping within the overall smart FG plate. Meaningful damping in the overall FG plate at high temperature, could still be enhanced to some extent through its (PFRC actuator layer) utilization in the form of ACLD layer (Baz 1993; Baz and Poh 1995) and this issue is not yet addressed in the literature especially for the vibration of FG plates under harmonic mechanical load. Thus, it is important to study the use of an ACLD layer instead of PFRC actuator layer, with an aim of achieving increased damping. The PFRC actuator layer is considered as the active constraining layer of ACLD layer and the negative velocity feedback control strategy is utilized for activating the actuator layer. The nonlinear vibration characteristics of the overall FG plate need to be evaluated in the frequency-domain to investigate the effect of substrate-plate-surface temperature on the actuation-capability of ACLD layer. The

constrained viscoelastic layer (ACLD) is modeled in the time-domain utilizing Golla-Hughes-McTavish (GHM) method. First, the incremental closed-loop finite element equations of motion of the overall plate are derived in the time-domain. Next, these equations are expressed in the frequency-domain assuming periodic motion of the overall plate. The solution methodology as discussed in Section 2.3,(Chapter 2) is utilized for numerical evaluation of nonlinear frequency responses of the overall plate. The analysis reveals a potential use of PFRC actuator layer in the form of ACLD layer. The analysis also reveals the significant effect of initial thermal bending of the overall smart FG plate on its nonlinear dynamic characteristics in the frequency-domain. The effects of temperature, metal-volume fraction in FG substrate, fiber volume fraction in PFRC and fiber orientation angle in PFRC on the actuation-capability of ACLD layer are also presented.

3.2 Problem Statement and Incremental Finite Element Formulation

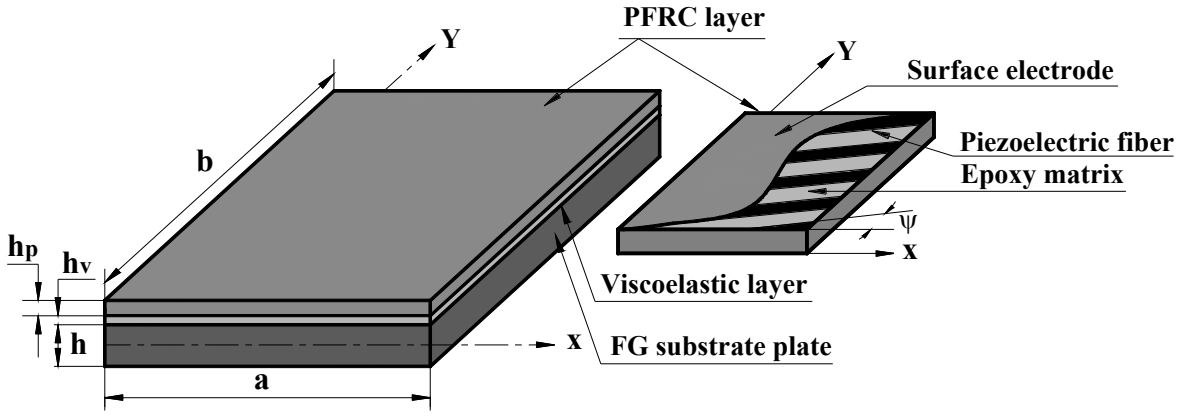

Fig. 3.1 Schematic diagram of FG plate integrated with a layer of ACLD treatment.

Figure 3.1 shows a FG plate integrated with a layer of ACLD treatment. It is a modified form of the previous smart FG plate (Fig. 3.1) in which an ACLD layer is attached to the top surface of the FG substrate plate instead of PFRC layer. The constraining layer of ACLD is made of PFRC. The thickness of the constrained viscoelastic layer is denoted by, h_v while other geometrical parameters are denoted by the same symbols as those are in Fig. 2.1. The substrate FG plate is made of two homogeneous and isotropic constituent

materials such as ceramic and metal. The bottom ceramic rich surface of the substrate is considered to be exposed to a high temperature while the metal rich top surface of the same is always exposed to the room temperature (T_m = 300 K). Material properties (P) of the substrate FG plate are assumed to vary along the thickness direction as the functions of volume fractions and material properties of the constituent materials according to a simple power law (Praveen and Reddy 1998, Woo and Meguid 2001). The planes parallel to the reference plane ($z = 0$) are assumed to be isothermal planes and the temperature varies only across the thickness of the substrate FG plate. The ACLD layer is attached to the metal rich surface of FG substrate in order to keep it apart from the thermal effect. The piezoelectric fiber alignment remains the same as those illustrated in Fig 2.1. The state of strain and the state of stress at a point in the overall laminated plate are defined by Eq. (2.1) and Eq. (2.2) respectively,

$$\{\varepsilon_b\}=\{\varepsilon_x \quad \varepsilon_y \quad \varepsilon_{xy}\}^{\mathrm{T}} \text{ and } \{\varepsilon_s\}=\{\varepsilon_{yz} \quad \varepsilon_{xz}\}^{\mathrm{T}} \tag{2.1}$$

$$\{\sigma_b\}=\{\sigma_x \quad \sigma_y \quad \sigma_{xy}\}^{\mathrm{T}} \text{ and } \{\sigma_s\}=\{\sigma_{yz} \quad \sigma_{xz}\}^{\mathrm{T}} \tag{2.2}$$

The substrate FG plate, viscoelastic layer and PFRC layer within the overall plate are denoted by the symbol k according to its value as 1, 2 and 3, respectively. The constitutive relations for substrate FG plate and PFRC layer are illustrated in Eq. (2.4) and Eq. (2.6), respectively in which the value of k for PFRC layer is taken as 3 for the present overall analysis. According to the material properties of FG plate (Eq.(2.3)) and present thermal environment , the temperature-distribution within the FG plate can readily be obtained from (Eq. 2.5a). The uni-axial, isothermal stress-strain relation for an isotropic linear viscoelastic material is given by (Christensen, 1982),

$$\sigma(t) = E(t)\varepsilon(0) + \int_0^t E(t-\tau)\frac{\partial}{\partial\tau}\varepsilon(\tau)d\tau \tag{3.1}$$

where, $E(t)$ is the time dependent relaxation modulus and $\varepsilon(t)$ is restricted to be zero for $t \in (-\infty, 0)$. The constitutive relations for this linear isotropic viscoelastic material can be written as,

$$\{\sigma_b^k\} = [C_b^k]E(t)\{\varepsilon_b^k(0)\} + \int_0^t [C_b^k]E(t-\tau)\frac{\partial}{\partial\tau}\{\varepsilon_b^k(\tau)\}d\tau\,,$$

$$\{\sigma_s^k\} = [C_s^k]G(t)\{\varepsilon_s^k(0)\} + \int_0^t [C_s^k]G(t-\tau)\frac{\partial}{\partial\tau}\{\varepsilon_s^k(\tau)\}d\tau \tag{3.2}$$

where,

$$[C_b^k] = \frac{1}{1-\nu^2}\begin{bmatrix} 1 & \nu & 0 \\ \nu & 1 & 0 \\ 0 & 0 & (1-\nu)/2 \end{bmatrix}, \quad [C_s^k] = \begin{bmatrix} 1 & 0 \\ 0 & 1 \end{bmatrix},$$

$$G(t) = E(t)/2(1+\nu), \; k=2 \tag{3.2a}$$

The superscript k in Eq. (3.2) denotes constrained viscoelastic layer as per its value as 2. The constraining PFRC layer is activated by applying external voltage (V) across its top and bottom electrode-surfaces. Moreover, since a thin constraining PFRC layer is considered, the electric field components are assumed as, $E_x \approx 0, E_y \approx 0$ and $E_z = -V/h_p$. Since a thin overall laminated FG plate is considered in the present analysis, the kinematics of deformation of the overall laminated plate is defined according to the layer-wise FSDT as follows,

$$u^k(x,y,z,t) = u_0(x,y,t) + z_1^k\theta_x(x,y,t) + z_2^k\phi_x(x,y,t) + z_3^k\gamma_x(x,y,t) \;,$$

$$v^k(x,y,z,t) = v_0(x,y,t) + z_1^k\theta_y(x,y,t) + z_2^k\phi_y(x,y,t) + z_3^k\gamma_y(x,y,t) \,,$$

$$w^k(x,y,z,t) = w_0(x,y,t) \tag{3.3}$$

where,

$$z_1^k = z, z_2^k = z_3^k = 0 \;\text{ for }\; k=1,$$

$$z_1^k = h/2, z_2^k = (z-h/2), z_3^k = 0 \;\text{ for } k=2 \,,$$

$$z_1^k = h/2, z_2^k = h_v, z_3^k = (z-h/2-h_v) \;\text{ for } k=3 \tag{3.3a}$$

where, u^k, v^k and w^k are the displacements at any point of the k^{th} layer along x, y and z-directions, respectively; u_0, v_0 and w_0 are the translational displacements at any point on the reference plane along x, y and z directions, respectively; θ_x / θ_y, ϕ_x / ϕ_y and γ_x / γ_y are the rotations of the normal to the middle plane of substrate FG plate,

viscoelastic layer and PFRC layer, respectively with respect to y/x axis. According to the displacement field given in Eq. (3.3), the state of deformation of the overall plate can be defined in terms of the generalized displacements (u_0, v_0, w_0, θ_x, θ_y, ϕ_x, ϕ_y, γ_x, γ_y) which can also be expressed in the form of a generalized displacement vector as follows,

$$\{d\} = [u_0 \quad v_0 \quad w_0 \quad \theta_x \quad \phi_x \quad \gamma_x \quad \theta_y \quad \phi_y \quad \gamma_y]^{\mathrm{T}} \tag{3.4}$$

Following the displacement field given by Eq. (3.3), the von Karman nonlinear strain displacement relations can be written as,

$$\{\varepsilon_b^k\} = \{\varepsilon_{bL}\} + \{\varepsilon_{bN}\} + [z_b^k]\{\kappa_b\},$$

$$\{\varepsilon_s^k\} = \{\varepsilon_s\} + [z_s^k]\{\kappa_s\} \tag{3.5}$$

where, the generalized strain vectors ($\{\varepsilon_{bL}\}, \{\varepsilon_{bN}\}, \{\kappa_b\}, \{\varepsilon_s\}, \{\kappa_s\}$) and the z-coordinate matrices ($[z_b^k], [z_s^k]$) are as follows,

$$\{\varepsilon_{bL}\} = \left\{\frac{\partial u_o}{\partial x} \quad \frac{\partial v_o}{\partial y} \quad \frac{\partial u_o}{\partial x} + \frac{\partial v_o}{\partial y}\right\}^{\mathrm{T}},$$

$$\{\varepsilon_{bN}\} = \left\{\frac{1}{2}\left(\frac{\partial w_o}{\partial x}\right)^2 \quad \frac{1}{2}\left(\frac{\partial w_o}{\partial y}\right)^2 \quad \left(\frac{\partial w_o}{\partial x}\frac{\partial w_o}{\partial y}\right)\right\}^{\mathrm{T}},$$

$$\{\kappa_b\} = \left\{\frac{\partial \theta_x}{\partial x} \quad \frac{\partial \phi_x}{\partial x} \quad \frac{\partial \gamma_x}{\partial x} \quad \frac{\partial \theta_y}{\partial y} \quad \frac{\partial \phi_y}{\partial y} \quad \frac{\partial \gamma_y}{\partial y} \quad \frac{\partial \theta_x}{\partial y} + \frac{\partial \theta_y}{\partial x} \quad \frac{\partial \phi_x}{\partial y} + \frac{\partial \phi_y}{\partial x} \quad \frac{\partial \gamma_x}{\partial y} + \frac{\partial \gamma_y}{\partial x}\right\}^{\mathrm{T}},$$

$$\{\varepsilon_s\} = \left\{\frac{\partial w_0}{\partial y} \quad \frac{\partial w_0}{\partial x}\right\}^{\mathrm{T}},$$

$$\{\kappa_s\} = \{\theta_x \quad \phi_x \quad \gamma_x \quad \theta_y \quad \phi_y \quad \gamma_y\}^{\mathrm{T}},$$

$$[z_b^k]=\begin{bmatrix} z_1^k & z_2^k & z_3^k & 0 & 0 & 0 & 0 & 0 & 0 \\ 0 & 0 & 0 & z_1^k & z_2^k & z_3^k & 0 & 0 & 0 \\ 0 & 0 & 0 & 0 & 0 & 0 & z_1^k & z_2^k & z_3^k \end{bmatrix},$$

$$[z_s^k]=\begin{bmatrix} 0 & 0 & 0 & \frac{\partial z_1^k}{\partial z} & \frac{\partial z_2^k}{\partial z} & \frac{\partial z_3^k}{\partial z} \\ \frac{\partial z_1^k}{\partial z} & \frac{\partial z_2^k}{\partial z} & \frac{\partial z_3^k}{\partial z} & 0 & 0 & 0 \end{bmatrix} \tag{3.6}$$

For an applied uniformly distributed harmonic transverse mechanical load of intensity, $p(x,y,t)$, the first variations of total potential energy (δT_p) and total kinetic energy (δT_K) of the overall FG plate at any time t can be written as (Tiersten, 1982),

$$\delta T_p=\int_0^a\int_0^b\left[\sum_{k=1}^{3}\int_{h_k}^{h_{k+1}}\left(\left\{\delta\varepsilon_b^k\right\}^{\mathrm{T}}\{\sigma_b^k\}+\left\{\delta\varepsilon_s^k\right\}^{\mathrm{T}}\{\sigma_s^k\}\right)dz-\int_{h_k}^{h_{k+1}}\{\delta\bar{E}\}^{\mathrm{T}}\{D\}\,|_{k=3}\,dz-(\delta w\times p)\right]dydx \tag{3.7}$$

$$\delta T_K=\int_0^a\int_0^b\left[\sum_{k=1}^{3}\int_{h_k}^{h_{k+1}}\left\langle[\delta\dot{u}^k \quad \delta\dot{v}^k \quad \delta\dot{w}^k]\rho^k[\dot{u}^k \quad \dot{v}^k \quad \dot{w}^k]^{\mathrm{T}}\right\rangle dz\right]dydx \tag{3.8}$$

where , δ is an operator for first variation and ρ^k is the mass density of the k-th layer. The values of h_k / h_{k+1} for $k=1,2$ and 3 are, $h_1=-h/2$, $h_2=h/2$, $h_3=(h/2+h_v)$ and $h_4=(h/2+h_v+h_p)$. Substituting Eqs. (2.4), (2.6), (3.2), (3.3), (3.4) and (3.5) in Eqs. (3.7) and (3.8), the following simplified equations can be obtained,

$$\delta T_p=\int_0^a\int_0^b\begin{bmatrix} \left\langle\{\delta\varepsilon_{bL}\}^{\mathrm{T}}+\{\delta\varepsilon_{bN}\}^{\mathrm{T}}\right\rangle[A_b^{13}]\left\langle\{\varepsilon_{bL}\}+\{\varepsilon_{bN}\}\right\rangle+\{\delta\kappa_b\}^{\mathrm{T}}[B_{b1}^{13}]\left\langle\{\varepsilon_{bL}\}+\{\varepsilon_{bN}\}\right\rangle+\left\langle\{\delta\varepsilon_{bL}\}^{\mathrm{T}}+\{\delta\varepsilon_{bN}\}^{\mathrm{T}}\right\rangle[B_{b2}^{13}]\{\kappa_b\} \\ +\{\delta\kappa_b\}^{\mathrm{T}}[D_b^{13}]\{\kappa_b\}+\{\delta\varepsilon_s\}^{\mathrm{T}}[A_s^{13}]\{\varepsilon_s\}+\{\delta\kappa_s\}^{\mathrm{T}}[B_{s1}^{13}]\{\varepsilon_s\}+\{\delta\varepsilon_s\}^{\mathrm{T}}[B_{s2}^{13}]\{\kappa_s\}+\{\delta\kappa_s\}^{\mathrm{T}}[D_s^{13}]\{\kappa_s\} \\ -\left\langle\{\delta\varepsilon_{bL}\}^{\mathrm{T}}+\{\delta\varepsilon_{bN}\}^{\mathrm{T}}\right\rangle\{A_T\}-\{\delta\kappa_b\}^{\mathrm{T}}\{B_T\}-\left\langle\{\delta\varepsilon_{bL}\}^{\mathrm{T}}+\{\delta\varepsilon_{bN}\}^{\mathrm{T}}\right\rangle\{A_{be}\}V-\{\delta\kappa_b\}^{\mathrm{T}}\{B_{be}\}V-\{\delta\varepsilon_s\}^{\mathrm{T}}\{A_{se}\}V \\ -\{\delta\kappa_s\}^{\mathrm{T}}\{B_{se}\}V-(\delta w\times p)+\{\delta\varepsilon_s\}^{\mathrm{T}}G(t)\left\langle[A_s^2]\{\varepsilon_s(0)\}+[B_{s2}^2]\{\kappa_s(0)\}\right\rangle+\{\delta\kappa_s\}^{\mathrm{T}}G(t)\left\langle[B_{s1}^2]\{\varepsilon_s(0)\}+[D_s^2]\{\kappa_s(0)\}\right\rangle+ \\ \{\delta\varepsilon_s\}^{\mathrm{T}}\int_0^t G(t-\tau)\left\langle[A_s^2]\frac{\partial}{\partial\tau}\{\varepsilon_s(\tau)\}+[B_{s2}^2]\frac{\partial}{\partial\tau}\{\kappa_s(\tau)\}\right\rangle\partial\tau+\{\delta\kappa_s\}^{\mathrm{T}}\int_0^t G(t-\tau)\left\langle[B_{s1}^2]\frac{\partial}{\partial\tau}\{\varepsilon_s(\tau)\}+[D_s^2]\frac{\partial}{\partial\tau}\{\kappa_s(\tau)\}\right\rangle\partial\tau \end{bmatrix}dydx \tag{3.9}$$

$$\delta T_k = \int_0^a \int_0^b \left\langle \{\delta \dot{d}\}^{\mathrm{T}} [\bar{m}] \{\dot{d}\} \right\rangle dy dx \tag{3.10}$$

In Eqs. (3.9) and (3.10), the rigidity matrices ($[A_b^{13}]$, $[A_s^{13}]$, $[B_{b1}^{13}]$, $[B_{b2}^{13}]$, $[D_b^{13}]$, $[B_{s1}^{13}]$, $[B_{s2}^{13}]$, $[D_s^{13}]$, $[A_s^2]$, $[B_{s1}^2]$, $[B_{s2}^2]$, $[D_s^2]$), thermo-elastic coupling vectors ($\{A_T\}$, $\{B_T\}$), electro-elastic coupling vectors ($\{A_{be}\}$, $\{B_{be}\}$, $\{A_{se}\}$, $\{B_{se}\}$) and the mass matrix ($[\bar{m}]$) per unit area are as follows,

$$[A_b^{13}] = \int_{h_k}^{h_{k+1}} [C_b^k]|_{k=1}\, dz + \int_{h_k}^{h_{k+1}} [\bar{C}_b^k]|_{k=3}\, dz,$$

$$[A_s^{13}] = \int_{h_k}^{h_{k+1}} [C_s^k]|_{k=1}\, dz + \int_{h_k}^{h_{k+1}} [\bar{C}_s^k]|_{k=3}\, dz,$$

$$[B_{b2}^{13}] = \int_{h_k}^{h_{k+1}} [C_b^k][z_b^k]|_{k=1}\, dz + \int_{h_k}^{h_{k+1}} [\bar{C}_b^k][z_b^k]|_{k=3}\, dz,$$

$$[B_{b1}^{13}] = \int_{h_k}^{h_{k+1}} [z_b^k]^{\mathrm{T}}[C_b^k]|_{k=1}\, dz + \int_{h_k}^{h_{k+1}} [z_b^k]^{\mathrm{T}}[\bar{C}_b^k]|_{k=3}\, dz,$$

$$[D_b^{13}] = \int_{h_k}^{h_{k+1}} [z_b^k]^{\mathrm{T}}[C_b^k][z_b^k]|_{k=1}\, dz + \int_{h_k}^{h_{k+1}} [z_b^k]^{\mathrm{T}}[\bar{C}_b^k][z_b^k]|_{k=3}\, dz,$$

$$[B_{s2}^{13}] = \int_{h_k}^{h_{k+1}} [C_s^k][z_s^k]|_{k=1}\, dz + \int_{h_k}^{h_{k+1}} [\bar{C}_s^k][z_s^k]|_{k=3}\, dz,$$

$$[B_{s1}^{13}] = \int_{h_k}^{h_{k+1}} [z_s^k]^{\mathrm{T}}[C_b^k]|_{k=1}\, dz + \int_{h_k}^{h_{k+1}} [z_s^k]^{\mathrm{T}}[\bar{C}_b^k]|_{k=3}\, dz,$$

$$[D_s^{13}] = \int_{h_k}^{h_{k+1}} [z_s^k]^{\mathrm{T}}[C_s^k][z_s^k]|_{k=1}\, dz + \int_{h_k}^{h_{k+1}} [z_s^k]^{\mathrm{T}}[\bar{C}_s^k][z_s^k]|_{k=3}\, dz,$$

$$\{A_T\} = \int_{h_k}^{h_{k+1}} [1 \quad 1 \quad 0]^{\mathrm{T}} \frac{E(z)}{1-\nu(z)} \alpha(z) \Delta T|_{k=1}\, dz,$$

$$\{B_T\} = \int_{h_k}^{h_{k+1}} [z_b^k]^{\mathrm{T}} [1 \quad 1 \quad 0]^{\mathrm{T}} \frac{E(z)}{1-\nu(z)} \alpha(z) \Delta T|_{k=1}\, dz,$$

$$\{B_{be}\} = \int_{h_k}^{h_{k+1}} [z_b^k]^{\mathrm{T}} [\bar{e}_b] [0 \quad 0 \quad -1/h_p]^{\mathrm{T}}|_{k=3}\, dz,$$

$$\{B_{se}\} = \int_{h_k}^{h_{k+1}} [z_s^k]^{\mathrm{T}} [\overline{e}_s][0 \quad 0 \quad -1/h_p]^{\mathrm{T}}|_{k=3}\, dz\,,$$

$$[A_s^2] = \int_{h_k}^{h_{k+1}} [C_s^k]|_{k=2}\, dz\,,\ [B_{s1}^2] = \int_{h_k}^{h_{k+1}} [z_s^k]^{\mathrm{T}} [C_s^k]|_{k=2}\, dz\,,$$

$$\{A_{be}\} = \int_{h_k}^{h_{k+1}} [\overline{e}_b][0 \quad 0 \quad -1/h_p]^{\mathrm{T}}|_{k=3}\, dz\,,$$

$$\{A_{se}\} = \int_{h_k}^{h_{k+1}} [\overline{e}_s][0 \quad 0 \quad -1/h_p]^{\mathrm{T}}|_{k=3}\, dz\,,$$

$$[B_{s2}^2] = \int_{h_k}^{h_{k+1}} [C_s^k][z_s^k]|_{k=2}\, dz\,,$$

$$[\mathrm{D}_s^2] = \int_{h_k}^{h_{k+1}} [z_s^k]^{\mathrm{T}} [C_s^k][z_s^k]|_{k=2}\, dz\,,$$

$$[\overline{m}] = \sum_{k=1}^{3} \int_{h_k}^{h_{k+1}} \left\langle \left([Z_{mt}]^{\mathrm{T}} + [Z_{mr}^k]^{\mathrm{T}}\right) \rho^k \left([Z_{mt}] + [Z_{mr}^k]\right) \right\rangle dz\,,$$

$$|Z_{mt}| = \begin{bmatrix} 1 & 0 & 0 & 0 & 0 & 0 & 0 & 0 & 0 \\ 0 & 1 & 0 & 0 & 0 & 0 & 0 & 0 & 0 \\ 0 & 0 & 1 & 0 & 0 & 0 & 0 & 0 & 0 \end{bmatrix},$$

$$|Z_{mr}^k| = \begin{bmatrix} 0 & 0 & 0 & z_1^k & z_2^k & z_3^k & 0 & 0 & 0 \\ 0 & 0 & 0 & 0 & 0 & 0 & z_1^k & z_3^k & z_3^k \\ 0 & 0 & 0 & 0 & 0 & 0 & 0 & 0 & 0 \end{bmatrix} \tag{3.11}$$

The constrained layer damping of vibration of the overall FG plate is mainly achieved by the transverse shear deformation of the constrained viscoelastic layer (Baz 1993). Moreover, since the extensional stiffness of the viscoelastic layer is very small as compared to that of the substrate plate, the extensional stiffness of the viscoelastic layer is not considered in the expression of total potential energy (Eq. (3.9)). A state of steady-state vibration of the overall FG plate with a circular frequency (ω) is defined in similar incremental form as given in Eq. (2.18a). So, the given displacement vector ($\{d_i\}$) and corresponding increment vector for the present problem can be written as,

$$\{d_i\} = [u_{0i} \quad v_{0i} \quad w_{0i} \quad \theta_{xi} \quad \phi_{xi} \quad \gamma_{xi} \quad \theta_{yi} \quad \phi_{yi} \quad \gamma_{yi}]^{\mathrm{T}},$$

$$\{\Delta d\} = [\Delta u_0 \quad \Delta v_0 \quad \Delta w_0 \quad \Delta\theta_x \quad \Delta\phi_x \quad \Delta\gamma_x \quad \Delta\theta_y \quad \Delta\phi_y \quad \Delta\gamma_y]^{\mathrm{T}} \quad (3.12)$$

Corresponding to the incremental displacement vector, the generalized strain vectors (Eq.(3.5)) can be expressed as,

$$\{\varepsilon_{bL}\} = \{\varepsilon_{bL}^i\} + \{\Delta\varepsilon_{bL}\},$$

$$\{\varepsilon_{bN}\} = \{\varepsilon_{bN}^i\} + \{\Delta\varepsilon_{bN}\},$$

$$\{\kappa_b\} = \{\kappa_b^i\} + \{\Delta\kappa_b\},$$

$$\{\varepsilon_s\} = \{\varepsilon_s^i\} + \{\Delta\varepsilon_s\},$$

$$\{\kappa_s\} = \{\kappa_s^i\} + \{\Delta\kappa_s\} \quad (3.13)$$

where, $\{\varepsilon_{bL}^i\}$, $\{\varepsilon_{bN}^i\}$, $\{\kappa_b^i\}$, $\{\varepsilon_s^i\}$ and $\{\kappa_s^i\}$ are the strain vectors for the given sate of deformation $\{d_i\}$ while $\{\Delta\varepsilon_{bL}\}$, $\{\Delta\varepsilon_{bN}\}$, $\{\Delta\kappa_b\}$, $\{\Delta\kappa_s\}$ and $\{\Delta\varepsilon_s\}$ are the corresponding increments as follows,

$$\{\Delta\varepsilon_{bL}\} = \left\{\frac{\partial\Delta u_0}{\partial x} \quad \frac{\partial\Delta v_0}{\partial y} \quad \frac{\partial\Delta u_0}{\partial y} + \frac{\partial\Delta v_0}{\partial x}\right\}^{\mathrm{T}},$$

$$\{\Delta\varepsilon_s\} = \left\{\frac{\partial\Delta w_0}{\partial y} \quad \frac{\partial\Delta w_0}{\partial x}\right\}^{\mathrm{T}},$$

$$\{\Delta\kappa_b\} = \left\{\frac{\partial\Delta\theta_x}{\partial x} \quad \frac{\partial\Delta\phi_x}{\partial x} \quad \frac{\partial\Delta\gamma_x}{\partial x} \quad \frac{\partial\Delta\theta_y}{\partial y} \quad \frac{\partial\Delta\phi_y}{\partial y} \quad \frac{\partial\Delta\gamma_y}{\partial y} \quad \frac{\partial\Delta\theta_x}{\partial y} + \frac{\partial\Delta\theta_y}{\partial x} \quad \frac{\partial\Delta\phi_x}{\partial y} + \frac{\partial\Delta\phi_y}{\partial x} \quad \frac{\partial\Delta\gamma_x}{\partial y} + \frac{\partial\Delta\gamma_y}{\partial x}\right\}^{\mathrm{T}},$$

$$\{\Delta\varepsilon_{bN}\} = \left\{\frac{\partial w_{0i}}{\partial x}\frac{\partial\Delta w_0}{\partial x} + \frac{1}{2}\left(\frac{\partial\Delta w_0}{\partial x}\right)^2 \quad \frac{\partial w_{0i}}{\partial y}\frac{\partial\Delta w_0}{\partial y} + \frac{1}{2}\left(\frac{\partial\Delta w_0}{\partial y}\right)^2 \quad \frac{\partial w_{0i}}{\partial x}\frac{\partial\Delta w_0}{\partial y} + \frac{\partial w_{0i}}{\partial y}\frac{\partial\Delta w_0}{\partial x} + \left(\frac{\partial\Delta w_0}{\partial x}\frac{\partial\Delta w_0}{\partial y}\right)\right\}^{\mathrm{T}},$$

$$\{\Delta\kappa_s\} = [\Delta\theta_x \quad \Delta\phi_x \quad \Delta\gamma_x \quad \Delta\theta_y \quad \Delta\phi_y \quad \Delta\gamma_y]^{\mathrm{T}} \quad (3.14)$$

For deriving the finite element model of the overall FG plate, it is discretized by 9-node isoparametric quadrilateral elements. Accordingly, the generalized displacements within typical element can be expressed in terms of its (element) nodal displacement vector as illustrated in Eq. (2.21) $\{d\}=[N]\{d^e\}$. Substituting Eqs. (3.12) and (3.13) in Eqs. (3.9) and (3.10) and then using Eq. (2.21), the following simplified equations for a typical element can be obtained,

$$\delta T_p^e=\delta\left\{\Delta d^e\right\}^{\mathrm{T}}\begin{bmatrix}[K_L^e]\{d_i^e\}+[K_L^e]\{\Delta d^e\}+[K_{Ni}^e]\{d_i^e\}+[K_N^e]\{\Delta d^e\}+[K_{NNi}^e]\{d_i^e\}\\+[K_{NN}^e]\{\Delta d^e\}-\{P_L^{Te}\}-\{P_N^{Te}\}-\{P_L^{Ee}\}V-\{P_N^{Ee}\}V-\left\{P_M^e(t)\right\}\\+[K_v^e]G(t)\{d^e(0)\}+[K_v^e]\int_0^t G(t-\tau)\left\langle\frac{\partial}{\partial\tau}\{d_i^e(\tau)\}+\frac{\partial}{\partial\tau}\{\Delta d^e(\tau)\}\right\rangle\partial\tau\end{bmatrix}$$

$$\delta T_k^e=\delta\{\Delta\dot{d}^e\}^{\mathrm{T}}\left\langle[M^e]\{\dot{d}_i^e\}+[M^e]\{\Delta\dot{d}^e\}\right\rangle \tag{3.15}$$

where,

$$[K_L^e]=\int_{A_e}\begin{bmatrix}[B_b^L]^{\mathrm{T}}\left\langle[A_b^{13}][B_b^L]+[B_{b2}^{13}][B_{b\kappa}]\right\rangle+[B_{b\kappa}]^{\mathrm{T}}\left\langle[B_{b1}^{13}][B_b^L]+[D_b^{13}][B_{b\kappa}]\right\rangle\\+[B_s]^{\mathrm{T}}\left\langle[A_s^{13}][B_s]+[B_{s2}^{13}][B_{s\kappa}]\right\rangle+[B_{s\kappa}]^{\mathrm{T}}\left\langle[B_{s1}^{13}][B_s]+[D_s^{13}][B_{s\kappa}]\right\rangle\end{bmatrix}dA_e,$$

$$[K_{Ni}^e]=\int_{A_e}(\left\langle[B_b^L]^{\mathrm{T}}[A_b^{13}]+[B_{b\kappa}]^{\mathrm{T}}[B_{b1}^{13}]\right\rangle[B_{Ni}]+[B_N^d]^{\mathrm{T}}\left\langle[A_b^{13}][B_b^L]+[B_{b2}^{13}][B_{b\kappa}]\right\rangle)dA_e,$$

$$[K_N^e]=\int_{A_e}(\left\langle[B_b^L]^{\mathrm{T}}[A_b^{13}]+[B_{b\kappa}]^{\mathrm{T}}[B_{b1}^{13}]\right\rangle[B_N]+[B_N^d]^{\mathrm{T}}\left\langle[A_b^{13}][B_b^L]+[B_{b2}^{13}][B_{b\kappa}]\right\rangle)dA_e,$$

$$[K_{NNi}^e]=\int_{A_e}([B_N^d]^{\mathrm{T}}[A_b^{13}][B_{Ni}])dA_e,$$

$$[K_{NN}^e]=\int_{A_e}([B_N^d]^{\mathrm{T}}[A_b^{13}][B_N])dA_e,$$

$$\{P_L^{Te}\}=\int_{A_e}([B_b^L]^{\mathrm{T}}\{A_T\}+[B_{b\kappa}]^{\mathrm{T}}\{B_T\})dA_e,$$

$$\{P_N^{Te}\}=\int_{A_e}([B_N^d]^{\mathrm{T}}\{A_T\})dA_e,$$

$$\{P_N^{Ee}\} = \int_{A_e} ([B_N^d]^{\mathrm{T}} \{A_{be}\}) dA_e \,,$$

$$\{P_L^{Ee}\} = \int_{A_e} ([B_b^L]^{\mathrm{T}} \{A_{be}\} + [B_{b\kappa}]^{\mathrm{T}} \{B_{be}\} + [B_s]^{\mathrm{T}} \{A_{se}\} + [B_{s\kappa}]^{\mathrm{T}} \{B_{se}\}) dA_e \,,$$

$$\{P_M^e\} = \int_{A_e} ([N]^{\mathrm{T}} [0 \quad 0 \quad p \quad 0 \quad 0]^{\mathrm{T}}) dA_e \,,\ [M^e] = \int_{A_e} ([N]^{\mathrm{T}} [\bar{m}][N]) dA_e \,,$$

$$[K_v^e] = \int_{A_e} [B_s]^{\mathrm{T}} \left\langle [A_s^2][B_s] + [B_{s2}^2][B_{s\kappa}] \right\rangle + [B_{s\kappa}]^{\mathrm{T}} \left\langle [B_{s1}^2][B_s] + [D_s^2][B_{s\kappa}] \right\rangle dA_e \qquad (3.15a)$$

In Eq. (3.15a), A_e is the area of a typical element in the xy-plane. The different strain-displacement matrices appearing in Eq. (3.15a) are as follows,

$$[B_b^L] = [L_b^L][N],\ [B_{Ni}] = [L_{Ni}][N],$$

$$[B_s] = [L_s][N],\ [B_{b\kappa}] = [L_{b\kappa}][N],$$

$$[B_N^d] = [L_N^d][N],\ [B_{s\kappa}] = [L_{s\kappa}][N], [B_N] = [L_N][N],$$

$$[L_{Ni}] = \begin{bmatrix} 0 & 0 & \frac{1}{2}\frac{\partial w_{oi}}{\partial x}\frac{\partial}{\partial x} & 0 & 0 & 0 & 0 & 0 & 0 \\ 0 & 0 & \frac{1}{2}\frac{\partial w_{oi}}{\partial y}\frac{\partial}{\partial y} & 0 & 0 & 0 & 0 & 0 & 0 \\ 0 & 0 & \frac{\partial w_{oi}}{\partial x}\frac{\partial}{\partial y} & 0 & 0 & 0 & 0 & 0 & 0 \end{bmatrix},$$

$$[L_s] = \begin{bmatrix} 0 & 0 & \frac{\partial}{\partial y} & 0 & 0 & 0 & 0 & 0 & 0 \\ 0 & 0 & \frac{\partial}{\partial x} & 0 & 0 & 0 & 0 & 0 & 0 \end{bmatrix},$$

$$[L_N] = \begin{bmatrix} 0 & 0 & \frac{\partial w_{0i}}{\partial x}\frac{\partial}{\partial x} + \frac{1}{2}\frac{\partial \Delta w_0}{\partial x}\frac{\partial}{\partial x} & 0 & 0 & 0 & 0 & 0 & 0 \\ 0 & 0 & \frac{\partial w_{0i}}{\partial y}\frac{\partial}{\partial y} + \frac{1}{2}\frac{\partial \Delta w_0}{\partial y}\frac{\partial}{\partial y} & 0 & 0 & 0 & 0 & 0 & 0 \\ 0 & 0 & \frac{\partial w_{0i}}{\partial x}\frac{\partial}{\partial y} + \frac{\partial w_{0i}}{\partial y}\frac{\partial}{\partial x} + \frac{\partial \Delta w_0}{\partial x}\frac{\partial}{\partial y} & 0 & 0 & 0 & 0 & 0 & 0 \end{bmatrix},$$

$$[L_N^d]=\begin{bmatrix} 0 & 0 & \dfrac{\partial w_{0i}}{\partial x}\dfrac{\partial}{\partial x}+\dfrac{\partial \Delta w_0}{\partial x}\dfrac{\partial}{\partial x} & 0 & 0 & 0 & 0 & 0 & 0 \\ 0 & 0 & \dfrac{\partial w_{0i}}{\partial y}\dfrac{\partial}{\partial y}+\dfrac{\partial \Delta w_0}{\partial y}\dfrac{\partial}{\partial y} & 0 & 0 & 0 & 0 & 0 & 0 \\ 0 & 0 & \left(\dfrac{\partial w_{0i}}{\partial x}+\dfrac{\partial \Delta w_0}{\partial x}\right)\dfrac{\partial}{\partial y}+\left(\dfrac{\partial w_{0i}}{\partial y}+\dfrac{\partial \Delta w_0}{\partial y}\right)\dfrac{\partial}{\partial x} & 0 & 0 & 0 & 0 & 0 & 0 \end{bmatrix},$$

$$,\qquad [L_{b\kappa}]=\begin{bmatrix} 0 & 0 & 0 & \dfrac{\partial}{\partial x} & 0 & 0 & 0 & 0 & 0 \\ 0 & 0 & 0 & 0 & \dfrac{\partial}{\partial x} & 0 & 0 & 0 & 0 \\ 0 & 0 & 0 & 0 & 0 & \dfrac{\partial}{\partial x} & 0 & 0 & 0 \\ 0 & 0 & 0 & 0 & 0 & 0 & \dfrac{\partial}{\partial y} & 0 & 0 \\ 0 & 0 & 0 & 0 & 0 & 0 & 0 & \dfrac{\partial}{\partial y} & 0 \\ 0 & 0 & 0 & 0 & 0 & 0 & 0 & 0 & \dfrac{\partial}{\partial y} \\ 0 & 0 & 0 & \dfrac{\partial}{\partial y} & \dfrac{\partial}{\partial x} & 0 & 0 & 0 & 0 \\ 0 & 0 & 0 & 0 & 0 & \dfrac{\partial}{\partial y} & \dfrac{\partial}{\partial x} & 0 & 0 \\ 0 & 0 & 0 & 0 & 0 & 0 & 0 & \dfrac{\partial}{\partial y} & \dfrac{\partial}{\partial x} \end{bmatrix},$$

$$[L_b^L]=\begin{bmatrix} \dfrac{\partial}{\partial x} & 0 & 0 & 0 & 0 & 0 & 0 & 0 & 0 \\ 0 & \dfrac{\partial}{\partial y} & 0 & 0 & 0 & 0 & 0 & 0 & 0 \\ \dfrac{\partial}{\partial y} & \dfrac{\partial}{\partial x} & 0 & 0 & 0 & 0 & 0 & 0 & 0 \end{bmatrix},$$

$$[L_{s\kappa}]=\begin{bmatrix} 0 & 0 & 0 & 1 & 0 & 0 & 0 & 0 & 0 \\ 0 & 0 & 0 & 0 & 1 & 0 & 0 & 0 & 0 \\ 0 & 0 & 0 & 0 & 0 & 1 & 0 & 0 & 0 \\ 0 & 0 & 0 & 0 & 0 & 0 & 1 & 0 & 0 \\ 0 & 0 & 0 & 0 & 0 & 0 & 0 & 1 & 0 \\ 0 & 0 & 0 & 0 & 0 & 0 & 0 & 0 & 1 \end{bmatrix} \tag{3.16}$$

In Eq. (3.15), the bending and shear counterparts of the total stiffness matrix are formulated separately so as to implement the selective integration in a straight forward

manner. The governing equation of motion of the overall FG plate are derived by employing the extended Hamilton's principle (Eq. (2.16)). Substituting Eq. (3.15) in Eq. (2.16), the following simplified elemental governing equations of motion of a typical element can be obtained,

$$\begin{bmatrix} [M]\{\ddot{d}_i^e\}+[M]\{\Delta\ddot{d}^e\}+[K_L^e]\{d_i^e\}+[K_L^e]\{\Delta d^e\}+[K_{Ni}^e]\{d_i^e\}+[K_N^e]\{\Delta d^e\} \\ +[K_{NNi}^e]\{d_i^e\}+[K_{NN}^e]\{\Delta d^e\}-\{P_L^{Te}\}-\{P_N^{Te}\}-\{P_L^{Ee}\}\times V-\{P_N^{Ee}\}\times V \\ -\left\{P_M^e(t)\right\}+[K_v^e]G(t)\{d^e(0)\}+[K_v^e]\int_0^t G(t-\tau)\left\langle\frac{\partial}{\partial\tau}\{d_i^e(\tau)\}+\frac{\partial}{\partial\tau}\{\Delta d^e(\tau)\}\right\rangle\partial\tau \end{bmatrix}=0 \qquad (3.17)$$

3.2.1 Implementation of GHM model

The viscoelastic materials are usually characterized by frequency and temperature dependent complex modulus. Use of this complex modulus model of viscoelastic layer in the nonlinear frequency response analysis decreases the computational speed for convergence of solutions. In order to avoid this discrepancy, the material is first modeled in the time-domain using GHM method (Golla and Hughes, 1985). Subsequently, it is transferred to the frequency-domain. According to the GHM model of viscoelastic material, the complex modulus is represented as a series of mini-oscillator terms in the Laplace-domain as follows,

$$s\tilde{G}(s)=G^{\infty}\left[1+\sum_{q=1}^{R}\alpha_q\frac{s^2+2\tilde{\xi}_q\tilde{\omega}_q s}{s^2+2\tilde{\xi}_q\tilde{\omega}_q s+\tilde{\omega}_q^2}\right] \qquad (3.18)$$

The factor G^{∞} is the value of the modulus in equilibrium and R represents the number of mini-oscillator terms. The constants, α_q, $\tilde{\xi}_q$ and $\tilde{\omega}_q$ govern the shape of the modulus function in the complex S-plane and those can be obtained by curve fitting the experimental data. The form of the complex modulus ($s\tilde{G}(s)$) is introduced in Eq. (3.17) by taking its (Eq. 3.17) Laplace transform. Subsequently, the inverse Laplace transform of the resulting equation gives the following equations of motion in the time-domain,

$$\begin{aligned}&[M^e]\{\ddot{d}_i^e\}+[M^e]\{\Delta\ddot{d}^e\}+[K_{Lc}^e]\{d_i^e\}+[K_{Lc}^e]\{\Delta d^e\}+[K_{Ni}^e]\{d_i^e\}+[K_N^e]\{\Delta d^e\}+[K_{NNi}^e]\{d_i^e\} \\ &+[K_{NN}^e]\{\Delta d^e\}-\sum_{q=1}^{R}[K_{Lq}^e]\left\langle\{z_{iq}^e\}+\{\Delta z_q^e\}\right\rangle=\{P_L^{Te}\}+\{P_N^{Te}\}+\{P_L^{Ee}\}\times V+\{P_N^{Ee}\}\times V+\left\{P_M^e\right\}\end{aligned} \qquad (3.19)$$

$$\left\langle \{\ddot{z}_{iq}^e\} + \{\Delta\ddot{z}_q^e\} \right\rangle + 2\tilde{\xi}_q\tilde{\omega}_q \left\langle \{\dot{z}_{iq}^e\} + \{\Delta\dot{z}_q^e\} \right\rangle + \tilde{\omega}_q^2 \left\langle \{z_{iq}^e\} + \{\Delta z_q^e\} \right\rangle = \tilde{\omega}_q^2 \left\langle \{d_i^e\} + \{\Delta d^e\} \right\rangle \quad (3.20)$$

where, $q = (1, 2, ..., R)$; $\{z_{iq}^e\}$ and $\{\Delta z_q^e\}$ are the elemental nodal auxiliary dissipation coordinate vector and the corresponding increment vector, respectively. The matrices ($\lfloor K_{Lc}^e \rfloor$, $\lfloor K_{Lq}^e \rfloor$) appearing in Eq. (3.19) are as follows,

$$[K_{Lc}^e] = \left\langle [K_L^e] + [K_v^e] \mathrm{G}^\infty (1 + \sum_{q=1}^{R} \alpha_q) \right\rangle, \; [K_{Lq}^e] = [K_v^e] G^\infty \alpha_q \quad (3.21)$$

3.2.2 Implementation of harmonic balance method (HBM)

In order to express the equations of motion in the frequency-domain, the harmonic balance method (HBM) is utilized by assuming periodic motion of the overall FG plate. According to this method, the expression of elemental nodal displacement vector ($\{d^e\}$) is given in Eq. (2.24). Following the same form of solution for auxiliary dissipation coordinates, the corresponding vector ($\{z_q^e\}$) could be expressed as,

$$\{z_q^e\} = \{a_{q0}\} + \sum_{r=1}^{F} \left\langle \{a_{qr}\} \cos(r\omega t) + \{b_{qr}\} \sin(r\omega t) \right\rangle \quad (3.22)$$

where, $\{a_{q0}\}$ is the time-independent elemental nodal auxiliary dissipation coordinate vector; $\{a_{qr}\}$ and $\{b_{qr}\}$ are the elemental nodal auxiliary dissipation coordinate vectors for the amplitudes in r-th harmonic term. For the sake of simplicity in the present formulation, the vectors ($\{d^e\}, \{\dot{d}^e\}, \{\ddot{d}^e\}, \{\Delta d^e\}, \{\Delta\dot{d}^e\}, \{\Delta\ddot{d}^e\}$) in Eq. (3.19) and the nonlinear strain displacement matrices ($\lfloor B_{Ni} \rfloor, \lfloor B_N \rfloor, \lfloor B_N^d \rfloor$) in Eq. (3.16) are expressed in similar forms as presented in Eqs. (2.25), (2.26) and (2.27). The same strategy is also implemented for elemental nodal auxiliary dissipation coordinate vector that yields the following expressions,

$$\{z_q^e\} = [S^e]\left\{X_q^e\right\}, \{\dot{z}_q^e\} = \omega \times [S_1^e]\left\{X_q^e\right\}, \{\ddot{z}_q^e\} = -\omega^2 \times [S_2^e]\left\{X_q^e\right\},$$

$$\{\Delta z_q^e\} = [S^e]\left\{\Delta X_q^e\right\},$$

$$\{\Delta\dot{z}_q^e\} = \omega_i [S_1^e]\left\{\Delta X_q^e\right\} + \Delta\omega [S_1^e]\left\{X_{iq}^e\right\},$$

$$\{\Delta\ddot{z}_q^e\} = -\omega_i^2[S_2^e]\left\{\Delta X_q^e\right\} - 2\omega_i\Delta\omega[S_2^e]\left\{X_{iq}^e\right\}$$

$$\{X_q^e\} = \left[\{a_{q0}\}^{\mathrm{T}} \quad \{a_{q1}\}^{\mathrm{T}} \quad \{b_{q1}\}^{\mathrm{T}} \quad . \quad . \quad . \quad \{a_{qF}\}^{\mathrm{T}} \quad \{b_{qF}\}^{\mathrm{T}}\right]^{\mathrm{T}}$$

$$\{\Delta X_q^e\} = \left[\{\Delta a_{q0}\}^{\mathrm{T}} \quad \{\Delta a_{q1}\}^{\mathrm{T}} \quad \{\Delta b_{q1}\}^{\mathrm{T}} \quad . \quad . \quad . \quad \{\Delta a_{qF}\}^{\mathrm{T}} \quad \{\Delta b_{qF}\}^{\mathrm{T}}\right]^{\mathrm{T}} \tag{3.23}$$

3.2.3 Implementation of control strategy

The external voltage across the thickness of PFRC constraining layer is supplied according to the negative velocity feedback control-strategy (Eq. (2.28)). According to this control-strategy and present form of solutions, the supplied voltage (V) could be expressed in term of the sensing point displacement as it is derived in the previous chapter (Eq. (2. 30)). Substituting Eqs. (2.26), (3.23), (2.27) and (2.30) in Eq. (3.19)-(3.20) and then using Galerkin procedure, the simplified equation can be written as,

$$[K_t^e]\{\Delta X^e\} - \sum_{q=1}^{R}[K_{Lqt}^e]\{\Delta X_q^e\} = \{f_{it}^e\} + \{f_t^{Te}\} + \{f_t^{Pe}\} - (\omega_i + \Delta\omega)[C_s^e]\{w_{si}\} - \omega_i[C_s^e]\{\Delta w_s\} + \{f_w^e\}\Delta\omega \tag{3.24}$$

$$[K_{tq}^e]\{\Delta X^e\} - [K_{dtq}^e]\{\Delta X_q^e\} = \{f_{itq}^e\} + \{f_{wq}^e\}\Delta\omega\,,\ q = 1,2,.....R. \tag{3.25}$$

In Eqs. (3.24) and (3.25), the different vectors and matrices are as follows,

$$[K_t^e] = \left\langle -\omega_i^2[M_t^e] + [K_{Lct}^e] + [K_{Nt}^e] + [K_{NNt}^e]\right\rangle,$$

$$\{f_{it}^e\} = \left\langle \omega_i^2[M_t^e] - [K_{Lct}^e] - [K_{Nit}^e] - [K_{NNit}^e]\right\rangle\{X_i^e\} + \sum_{q=1}^{R}[K_{Lqt}]\{X_{iq}^e\}\,,\ \{f_t^{Te}\} = \left\langle\{P_{Lt}^{Te}\} + \{P_{Nt}^{Te}\}\right\rangle,$$

$$\{f_w^e\} = 2\omega_i[M_t^e]\{X_i^e\}\,,$$

$$[K_{Lqt}^e] = \int_{\theta_1}^{\theta_2}\left\langle[S^e]^{\mathrm{T}}[K_{Lq}^e][S^e]\right\rangle d\theta\,,$$

$$[M_t^e] = \int_{\theta_1}^{\theta_2}\left\langle[S^e]^{\mathrm{T}}[M^e][S_2^e]\right\rangle d\theta\,,$$

$$[K_{Lct}^e] = \int_{\theta_1}^{\theta_2}\left\langle[S^e]^{\mathrm{T}}[K_{Lc}^e][S^e]\right\rangle d\theta\,,$$

$$[K_{tq}^{e}]=\int_{\theta_1}^{\theta_2}\left\langle [S^e]^{\mathrm{T}}\tilde{\omega}_q^2[S^e]\right\rangle d\theta\,,$$

$$[K_{dtq}^{e}]=\int_{\theta_1}^{\theta_2}[S^e]^{\mathrm{T}}\left\langle -\omega_i^2[S_2^e]+2\tilde{\xi}_q\tilde{\omega}_q\omega_i[S_1^e]+\tilde{\omega}_q^2[S^e]\right\rangle d\theta\,,$$

$$\{f_{itq}^{e}]=\int_{\theta_1}^{\theta_2}[S^e]^{\mathrm{T}}\left\langle -\tilde{\omega}_q^2[S^e]\right\rangle d\theta\{X_i^e\}+\int_{\theta_1}^{\theta_2}[S^e]^{\mathrm{T}}\left\langle -\omega_i^2[S_2^e]+2\tilde{\xi}_q\tilde{\omega}_q\omega_i[S_1^e]+\tilde{\omega}_q^2[S^e]\right\rangle d\theta\{X_{iq}^e\}\,,$$

$$\{f_{\omega q}^{e}]=\int_{\theta_1}^{\theta_2}[S^e]^{\mathrm{T}}\left\langle -2\omega_i[S_2^e]+2\tilde{\xi}_q\tilde{\omega}_q[S_1^e]\right\rangle d\theta\{X_{iq}^e\}\,,$$

$$[K_{Nt}^{e}]=\int_{\theta_1}^{\theta_2}\begin{bmatrix}[S^e]^{\mathrm{T}}\left\langle\int_{A_e}\left([B_b^L]^{\mathrm{T}}[A_b^{13}]+[B_{b\kappa}]^{\mathrm{T}}[B_{b1}^{13}]\right)[B_N^t]dA_e\right\rangle[S^e]^{\mathrm{T}}\\ +[S^e]^{\mathrm{T}}[S^e]\left\langle\int_{A_e}[B_N^{dt}]^{\mathrm{T}}\left([A_b^{13}][B_b^L]+[B_{b2}^{13}][B_{b\kappa}]\right)dA_e\right\rangle\end{bmatrix}[S^e]d\theta\,,$$

$$[K_{Nit}^{e}]=\int_{\theta_1}^{\theta_2}\begin{bmatrix}[S^e]^{\mathrm{T}}\left\langle\int_{A_e}\left([B_b^L]^{\mathrm{T}}[A_b^{13}]+[B_{b\kappa}]^{\mathrm{T}}[B_{b1}^{13}]\right)[B_{Ni}^t]dA_e\right\rangle[S^e]^{\mathrm{T}}\\ +[S^e]^{\mathrm{T}}[S^e]\left\langle\int_{A_e}[B_N^{dt}]^{\mathrm{T}}\left([A_b^{13}][B_b^L]+[B_{b2}^{13}][B_{b\kappa}]\right)dA_e\right\rangle\end{bmatrix}[S^e]d\theta\,,$$

$$[K_{NNt}^{e}]=\int_{\theta_1}^{\theta_2}\left[[S^e]^{\mathrm{T}}[S^e]\left\langle\int_{A_e}[B_N^{dt}]^{\mathrm{T}}[A_b^{13}][B_N^t]dA_e\right\rangle[S^e]^{\mathrm{T}}[S^e]\right]d\theta\,,$$

$$[K_{NNit}^{e}]=\int_{\theta_1}^{\theta_2}\left[[S^e]^{\mathrm{T}}[S^e]\left\langle\int_{A_e}[B_N^{dt}]^{\mathrm{T}}[A_b^{13}][B_{Ni}^t]dA_e\right\rangle[S^e]^{\mathrm{T}}[S^e]\right]d\theta\,,$$

$$\{P_{Lt}^{Te}\}=\int_{\theta_1}^{\theta_2}\left\langle[S^e]^{\mathrm{T}}\{P_L^{Te}\}\right\rangle d\theta\,,$$

$$\{P_{Nt}^{Te}\}=\int_{\theta_1}^{\theta_2}\left[[S^e]^{\mathrm{T}}[S^e]\left\langle\int_{A_e}[B_N^{dt}]^{\mathrm{T}}\{A_T\}dA_e\right\rangle\right]d\theta\,,$$

$$\{f_t^{Pe}\}=\int_{\theta_1}^{\theta_2}\left\langle[S^e]^{\mathrm{T}}\{P_M^e(\theta)\}\right\rangle d\theta\,,$$

$$[C_s^e]=k_d\int_{\theta_1}^{\theta_2}\left\langle[S^e]^{\mathrm{T}}\left\{P_L^{Ee}\right\}+[S^e]^{\mathrm{T}}[S^e]\int_{A_e}\left([B_N^{dt}]^{\mathrm{T}}\{A_{be}\}\right)dA_e\right\rangle[S_1^s]d\theta \qquad (3.26)$$

Since the response of the overall plate is assumed as periodic, the angle limits (i.e. θ_1 and θ_2) are considered for one cycle/period (i.e. 0 to 2π). Assembling the elemental equations (Eq. (3.24) and (3.25)) in the whole domain of the overall plate, the following global equation can be obtained,

$$[K_t]\{\Delta X\}-\sum_{q=1}^{R}[K_{Lqt}]\{\Delta X_q\}=\{f_{it}\}+\{f_t^T\}+\{f_t^P\}-(\omega_i+\Delta\omega)[C_s]\{w_{si}\}-\omega_i[C_s]\{\Delta w_s\}+\{f_w\}\Delta\omega \tag{3.27}$$

$$[K_{tq}]\{\Delta X\}-[K_{dtq}]\{\Delta X_q\}=\{f_{itq}\}+\{f_{wq}\}\Delta\omega\,,\ q=1,2,.....,R. \tag{3.28}$$

Making use of the expression of sensing-point displacement ($\{w_{si}\}$,$\{\Delta w_s\}$) in term of the global displacement vector ($\{X_i\}$,$\{\Delta X\}$) (Eq. 2.34), the simplified form of Eq. (3.27) can be written as,

$$[K_c]\{\Delta X\}-\sum_{q=1}^{R}[K_{Lqt}]\{\Delta X_q\}=\{f_c\}+\{f_t^T\}+\{f_t^P\}+\{f_{wc}\}\Delta\omega\,,$$

$$[K_c]=[K_t]+\omega_i[C],$$

$$\{f_c\}=\{f_{it}\}-\omega_i[C]\{X_i\},$$

$$\{f_{wc}\}=\{f_w\}-[C]\{X_i\},\ \ |C|=|C_s|\ |N_s| \tag{3.29}$$

Now, the governing equations of motion of the overall plate (Eqs. (3.28) and (3.29)) can be written within single expression as,

$$[K_{eq}]\{\Delta X_{eq}\}=\{f_{eq}\}+\{f_{eq}^w\}\Delta\omega \tag{3.30}$$

where,

$$|K_{eq}|=\begin{bmatrix} |K_c| & -|K_{L1t}| & -|K_{L2t}| & . & . & -|K_{LRt}| \\ |K_{t1}| & -|K_{dt1}| & |0| & . & . & |0| \\ |K_{t2}| & |0| & -|K_{dt1}| & . & . & |0| \\ . & . & . & . & . & . \\ . & . & . & . & . & . \\ |K_{tR}| & |0| & |0| & . & . & -|K_{dtR}| \end{bmatrix},$$

$$\{\Delta X_{eq}\}=\begin{Bmatrix} \{\Delta X\} \\ \{\Delta X_1\} \\ \{\Delta X_2\} \\ . \\ . \\ \{\Delta X_R\} \end{Bmatrix},\ \{f_{eq}^{\omega}\}=\begin{Bmatrix} \{f_{\omega c}\} \\ \{f_{\omega 1}\} \\ \{f_{\omega 2}\} \\ . \\ . \\ \{f_{\omega R}\} \end{Bmatrix}$$

$$\{f_{eq}\}=\begin{Bmatrix}\{f_c\}\\ \{f_{it1}\}\\ \{f_{it2}\}\\ .\\ .\\ \{f_{itR}\}\end{Bmatrix}+\begin{Bmatrix}\{f_t^T\}+\{f_t^P\}\\ \{0\}\\ \{0\}\\ .\\ .\\ \{0\}\end{Bmatrix} \tag{3.30a}$$

Equation (3.30) can also be expressed in the following form,

$$\{\Delta X_{eq}\}=\{f_1\}+\Delta\Phi\{f_2\}$$

$$\{f_1\}=[K_{eq}]^{-1}\{f_{eq}\},\ \{f_2\}=[K_{eq}]^{-1}\{f_{eq}^{\omega}\} \tag{3.31}$$

where, the relations $\Phi=\omega_i/\omega_0$ and $\Delta\Phi=\Delta\omega/\omega_0$ are introduced utilizing the fundamental frequency (ω_0) of vibration. For numerical evaluation of frequency responses of the overall FG plate, Eq. (3.31) is solved utilizing a solution methodology as presented in Section 2.3 in Chapter 2.

3.3 Numerical results and discussions

An FG plate integrated with a ACLD layer is considered as shown in Fig. 3.1. The geometrical properties of the FG plate are considered as: $a=b=400$ mm, $h=6$ mm. The constraining PFRC layer is considered to have a thickness (h_p) of, 250 μm. The piezoelectric fiber orientation angle (ψ) and the piezoelectric fiber volume fraction (v_f) in the PFRC actuator layer are considered as 0^o and 40%, respectively. Simply-supported boundary conditions of the overall FG plate are considered and a uniformly distributed transverse harmonic mechanical load is applied. The temperature dependent material properties of the metal and ceramic constituent materials of FG substrate plate are considered as given in Section 2.4 Chapter 2. For the viscoelastic layer, the thickness (h_v) of 1 mm is considered unless mentioned and its material properties in terms of the GHM parameters are considered as given in table below (Shi et al., 2004), ($G^{\infty}=3.877\times10^4$ N/m^2, $\rho=789.5$ kg/m^3).

Table 3.1 GHM parameters

$\alpha_1 =$	2.3263×10⁴	$\tilde{\omega}_1 =$	6.6169×10⁶	$\tilde{\xi}_1 =$	3.0787
$\alpha_2 =$	4.1977×10¹	$\tilde{\omega}_2 =$	3.2854×10⁴	$\tilde{\xi}_2 =$	1.4288×10²
$\alpha_3 =$	3.5174×10¹	$\tilde{\omega}_3 =$	4.7515×10⁴	$\tilde{\xi}_3 =$	6.1785×10²

Following the same procedure as illustrated for the analysis of previous smart FG plate (Chapter 2), the frequency responses of the overall smart FG plate are computed in terms of the parameter W^t while the corresponding equilibrium position of the overall plate is represented by the parameter W^s (Section 2.4). The damping in the overall plate caused by the ACLD layer is measured in terms of the parameter W^t_{peak} (Section 2.4). The maximum value of W^t is considered as less than h and three terms ($r = 1, 2, 3$) of the Fourier series are considered for the present solutions.

3.3.1 Validation of the present incremental finite element model

For verification of present nonlinear incremental finite element model, the linear and the nonlinear free vibration responses of the FG substrate plate are evaluated without ACLD layer ($h_p \approx 0$, $h_v \approx 0$, $V = 0$). It is observed that the computed fundamental natural frequency parameter (Ω) and the nonlinear frequency-amplitude relations do not deviate from the similar results for previous verification (Table 2.1 and Table 2.2). However, for verifying the implementation of GHM method, the forced linear frequency response of the overall plate are evaluated by modeling the material properties of the viscoelastic layer according to the complex stiffness method. In Figure

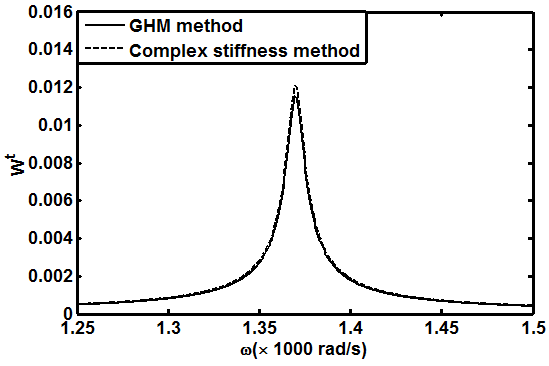

Fig. 3.2 Forced linear frequency responses of the overall FG plate (p = 10 N/m^2, k_d=30, $T_c = T_m$=300 K, n=1).

3.2, the obtained frequency response is compared with that when the GHM method is used for modeling the viscoelastic layer. It may be observed from Fig. 3.2 that the results using GHM method are in good agreement with those obtained using complex stiffness method thus verifying the implementation of GHM method in the present formulation.

3.3.2 Effect of control gain (k_d)

Figure 3.3 illustrates the nonlinear frequency response curves when the PFRC layer is either a passive constraining layer (PCLD, $k_d = 0$) or an active constraining layer (ACLD, $k_d \neq 0$). The same figure also shows the frequency response curve when the active PFRC actuator layer is directly attached to the substrate plate-surface. From the PCLD and ACLD responses, it may be observed that the active ($k_d \neq 0$) PFRC constraining layer significantly increases the damping in the overall FG plate compared to that when it is a passive ($k_d = 0$) constraining layer. This result implies a potential use of PFRC actuator as the active constraining layer for ACLD treatment for controlling the nonlinear vibration of FG plates in the frequency-domain. It may also be observed from Fig. 3.3 that the actuation-capability of active PFRC layer increases significantly when it acts as an active constraining layer instead of a simple actuator layer directly attached to the substrate plate-surface. So, Fig. 3.3 indicates to employ the PFRC actuator in the form of ACLD layer for effective control of vibration of FG plates.

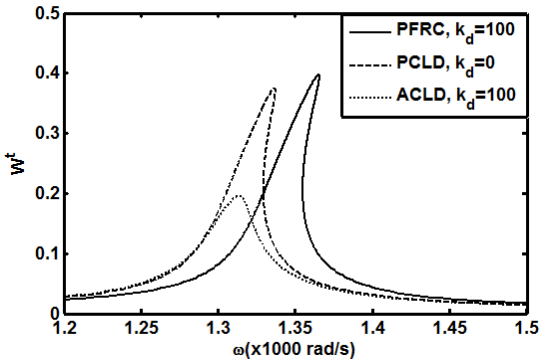

Fig. 3.3 Nonlinear frequency responses of the overall FG plate ($T_c = T_m$=300 K, n=2, p = 500 N/m^2).

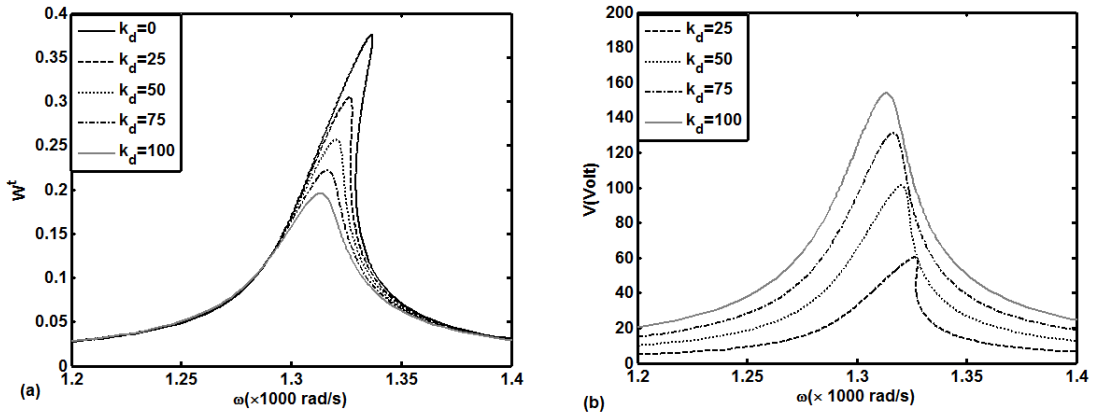

Fig. 3.4(a) Nonlinear frequency responses of the overall FG plate and (b) the corresponding variations of control voltage ($T_c = T_m = 300$ K, n=2, p = 500 N/m^2).

Figure 3.4(a) demonstrates the nonlinear frequency responses of the overall FG plate for different values of feedback control gain (k_d) when the mechanical load-amplitude (p) remains constant in the absence of thermal effect. The corresponding variations of required control voltage are also illustrated in Fig. 3.4(b). It may be observed from these figures that the damping in the overall plate can be increased by assigning a higher value of control gain (k_d). Although a higher value of control gain raises the maximum value of required control voltage across the thickness of the PFRC constraining layer, but it is within the reasonable range (Fig. 3.4(b)). In case of the direct integration of PFRC actuator layer over the surface of substrate plate, similar results in Fig. 2.6 show that the maximum value of control voltage remains almost constant for any value of control gain (k_d) (with a constant value of, p). However, it should be noted here that the value of control gain (k_d) would be assigned so that the corresponding voltage across the thickness of the PFRC actuator layer would not exceed its permissible value.

3.3.3 Effect of substrate FG plate-surface temperature (T_c)

Figures 3.5-3.8 illustrate the effect of ceramic-rich surface temperature (T_c) on the nonlinear vibration characteristics of the overall smart FG plate in the frequency-domain and also, on the corresponding damping caused by the ACLD layer. The overall plate

undergoes thermal bending deformations along the negative z-direction due to the bottom ceramic-rich surface temperature. Similar to the previous analysis (Chapter 2), this initial thermal bending deflection of the overall plate at a temperature remains almost constant during its vibration under an applied harmonic mechanical load of any frequency. So, the initial thermal bending deflection of the overall plate due to a ceramic-rich surface temperature of substrate plate may be considered as the equilibrium position of the overall plate during its vibration at any frequency. Figure 3.5 illustrates the initial thermal bending deflections of the FG plate integrated with ACLD layer for different bottom ceramic-rich surface temperatures of substrate plate. For the same temperatures, the corresponding linear and nonlinear frequency responses are demonstrated in Figs. 3.6(a)-(b). It could be noted here that the difficulty in the convergence of solutions arises due to the sharp turn of different solution components (harmonic terms). But, the peak-point deflection of every frequency response curve is distinctly obtained as shown in the results.

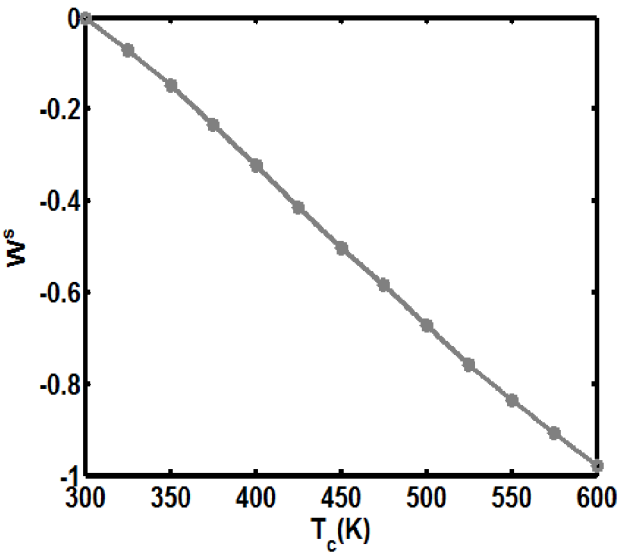

Fig. 3.5 Variations of thermal bending deflections of the overall FG plate with increasing bottom ceramic rich substrate-plate-surface temperature (T_c) (n =1, T_m =300 K, p = 500 N/m^2).

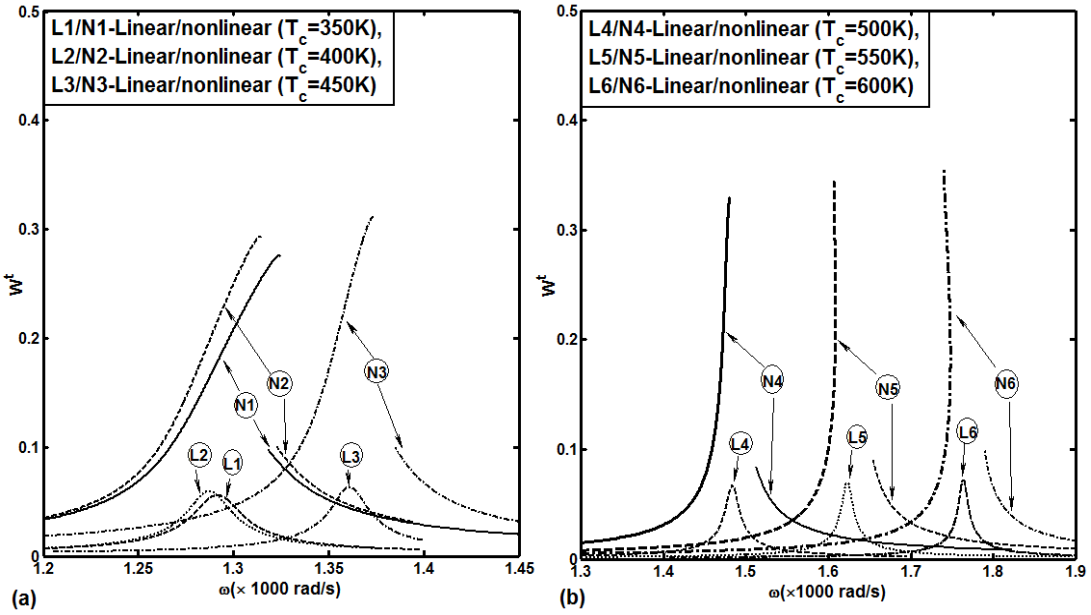

Fig. 3.6 Linear and nonlinear frequency responses of the overall FG plate for different ceramic rich substrate-plate-surface temperatures (n=1, k_d=50, T_m=300 K, p = 100 N/m^2 for linear responses and p = 500 N/m^2 for nonlinear responses).

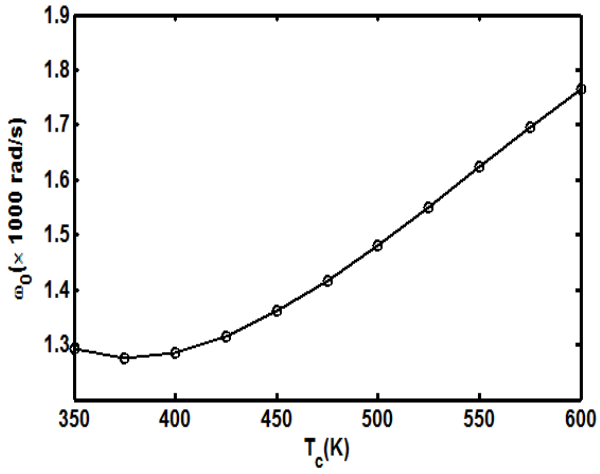

Fig. 3.7 Variation of fundamental frequency (ω_0) of the overall FG plate with the ceramic rich substrate-plate-surface temperature (T_c) (p = 100 N/m^2, n=1, T_m=300 K, k_d = 50).

Figures 3.6(a)-(b) illustrate the same observations as those are obtained from Figs. (2.8). In the present case (ACLD), the variation of fundamental frequency (ω_o) of the overall plate with temperature (T_c) is presented in Fig. 3.7. In comparison to Fig. 2.9, Fig. 3.7 shows that the limiting value of temperature (T_c) for alteration of nature of variation of fundamental frequency (ω_o) remains almost the same ($T_c = 375$ K) for both the cases (ACLD layer and PFRC layer). For the FG substrate plate integrated with ACLD layer, the difference between the frequencies ($\Delta\omega_{peak} = (\omega_{peak})_{nonlinear} - (\omega_{peak})_{linear}$) corresponding to the peak-points of linear and nonlinear frequency response curves for every temperature (T_c) is plotted in Fig. 3.8. A comparison of this results (Fig. 3.8) with similar results in Fig. 2.10 implies that the limiting temperature (T_c) corresponding to alteration of structural behavior of the overall smart FG plate does not depend on the type of smart layer (ACLD layer and PFRC layer).

Figure 3.9(a) shows the peak-point deflections (W^t_{peak}) of the nonlinear frequency responses (Fig. 3.6) for different temperatures (T_c). The corresponding values of required control voltage (V_{peak}) are also illustrated in Fig. 3.9(b). It may be observed from Fig. 3.9(a) that for constant values of control gain (k_d) and load-amplitude (p), the magnitude of W^t_{peak} increases with the increasing temperature (T_c). Thus, the increased initial thermal bending deflection at a higher temperature (T_c) causes lesser damping in the overall FG plate in expense of higher required control voltage (Fig. 3.9(b)) across the thickness of PFRC constraining layer. It may be noted by comparing the results in Fig. 3.9 with those in Fig.

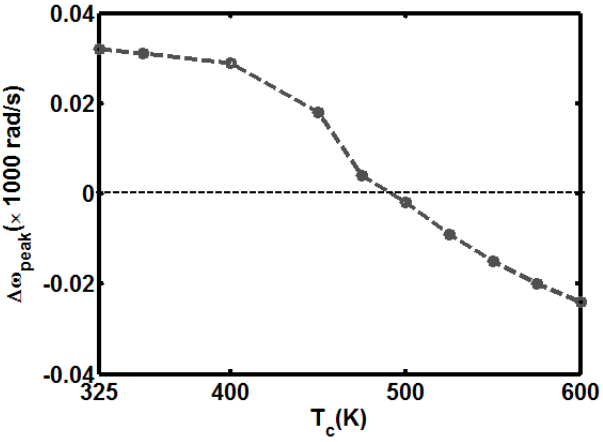

Fig. 3.8 Difference between the frequencies ($\Delta\omega_{peak}$) corresponding to the peak-points of linear and nonlinear frequency responses of the overall FG plate (Fig. 3.6) at each ceramic rich surface temperature (T_c) (n=1, k_d=50, T_m=300 K, p = 100 N/m^2 for linear responses and p = 500 N/m^2 for nonlinear responses).

2.11 that the nature of variation of the magnitude of W^t_{peak} within a range of temperature (T_c) differs when the ACLD layer is used instead of PFRC layer even though the nature of variation of corresponding control voltage remains almost the same.

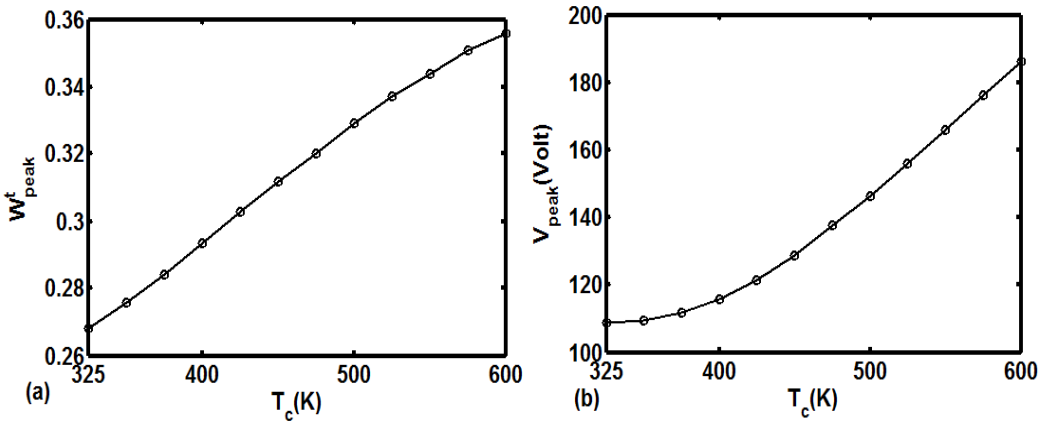

Fig. 3.9 Variations of (a) the peak-point deflection (W^t_{peak}) of frequency response curve and (b) the corresponding control voltage (V_{peak}) with the ceramic rich substrate-plate-surface temperature (T_c) (p = 500 N/m^2, k_d=50, n=1, T_m=300 K).

3.3.4 Effect of volume-fraction index (n) of substrate FG plate

Figure 3.10 illustrates the linear and the nonlinear frequency responses of the overall plate for different values of volume fraction index (n) of the FG substrate plate in the presence of a ceramic-rich surface temperature ($T_c = 600$ K). The equilibrium position of the overall plate corresponding to its linear/nonlinear frequency responses at each value of n is also shown in Fig. 3.11. The linear frequency responses in Fig. 3.10 imply the variation of fundamental frequency (ω_o) of the overall FG plate with the volume fraction index (n) that is also clearly presented in Fig. 3.12. This figure exhibits similar observations as those which obtained from the analysis of FG plates integrated with PFRC layer (Fig. 2.14). So, the nature of variation of fundamental frequency with volume fraction index (n) does not change due to the use of ACLD layer instead of PFRC layer (Figs. 3.12 and 2.14). The effect of volume fraction index (n) of the FG substrate plate on the performance of ACLD layer for controlling the nonlinear vibration of overall FG plate in the frequency-domain is illustrated in Fig. 3.13. For two different temperatures ($T_c = 300$ K and 600 K), Fig. 3.13(a)

shows the variation of the peak-point deflection (W^t_{peak}) of the nonlinear frequency response curve (Fig. 3.10) with the volume fraction index (n). The variation in the corresponding required control voltage (V_{peak}) is also presented in Fig. 3.13(b). It may be observed from Fig. 3.13 (a) that the damping in the overall plate caused by the ACLD layer is not much dependent on the volume fraction index (n) when the overall plate is at room temperature ($T_c = T_m = 300$ K). But for a higher temperature ($T_c > 300$ K, $T_m = 300$ K), the increased initial thermal bending deflection caused by the increase of n significantly affects the actuation-capability of ACLD layer. Recalling similar results in Figs. 2.16(a), it may be noted that the nature of variation of damping in the overall plate with the volume fraction index (n) changes as the PFRC layer is substituted by ACLD layer.

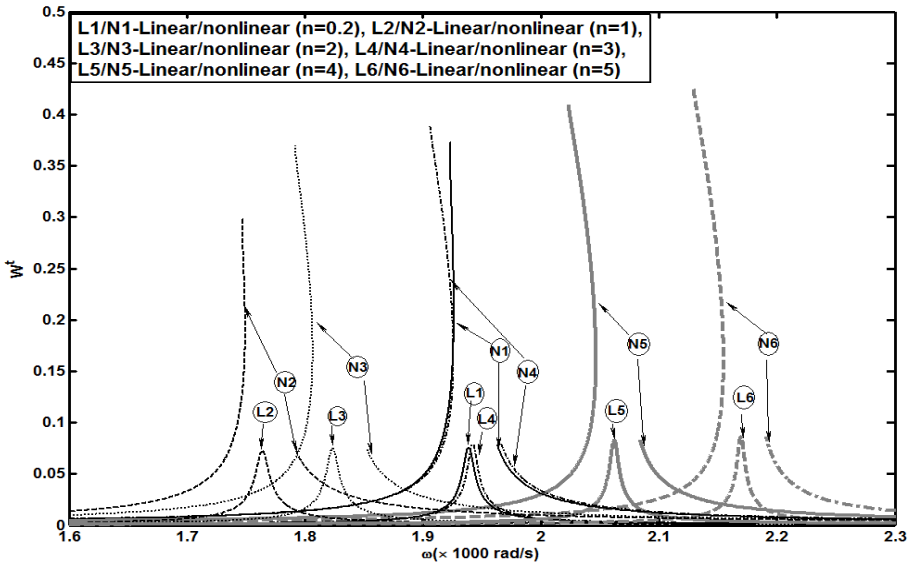

Fig. 3.10 Linear and nonlinear frequency responses of the overall FG plate for different values of volume fraction index (n) (k_d=50, T_m = 300 K, T_c = 600 K, p =100 N/m^2 for linear responses and p = 500 N/m^2 for nonlinear responses).

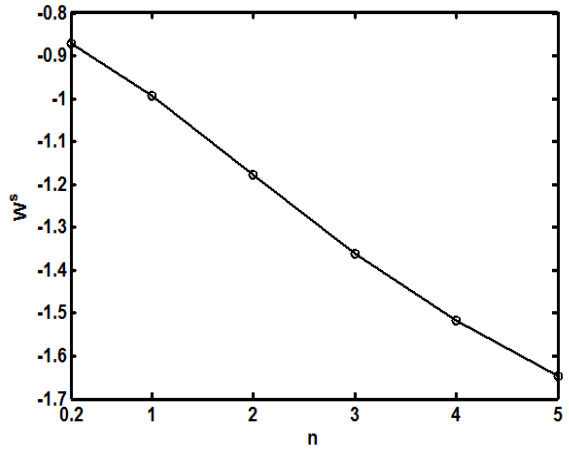

Fig. 3.11 Initial thermal bending deflections of the overall FG plate for different volume fraction index (n) of the FG substrate plate (T_c =600 K, T_m =300 K).

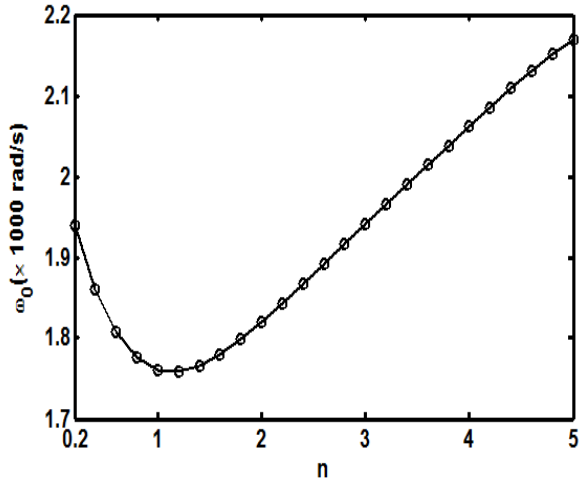

Fig. 3.12 Variation of linear fundamental frequency (ω_0) of overall FG plate with volume fraction index (n) of the FG substrate plate in the presence of a temperature gradient (T_c =600 K, T_m =300 K).

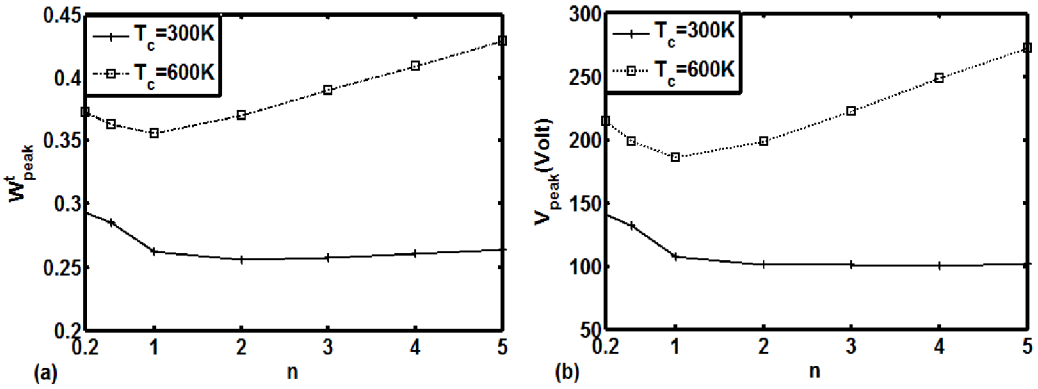

Fig. 3.13 Variations of (a) the peak point deflections (W^t_{peak}) of the nonlinear frequency response curve (Figure 3.10) and (b) the corresponding control voltage (V_{peak}) with the volume fraction index (n) of the FG substrate plate ($T_m = 300$ K, $k_d = 50$, $p = 500$ N/m^2).

3.3.5 Effect of viscoelastic layer-thickness (h_v)

Figure 3.14(a) illustrates the variation of the peak-point deflection (W^t_{peak}) of the nonlinear frequency response curve with the thickness (h_v) of the constrained viscoelastic layer for two different ceramic-rich surface temperatures ($T_c = 300$ K and 600 K). The variations in the corresponding feedback control voltage (V_{peak}) are also illustrated in Fig. 3.14(b). It may be observed from these figures that for constant values of control gain (k_d) and temperature (T_c), the peak-deflection (W^t_{peak}) and the corresponding required control voltage (V_{peak}) both significantly decrease with the increasing h_v up to about, $h_v = 2$ mm. Beyond this value of h_v, there are insignificant variations of W^t_{peak} and V_{peak}. Thus, the increase of damping in the overall plate is restricted to certain value of thickness of the constrained viscoelastic layer. It may also be observed from Fig. 3.14(a) that for a particular temperature (T_c), the damping in overall FG plate significantly increases with the increase of k_d when the value of h_v remains between 0.5 mm and 1.5 mm. This signifies an optimal thickness of the constrained viscoelastic layer for effectual utilizations of PFRC actuator layer as well as viscoelastic layer.

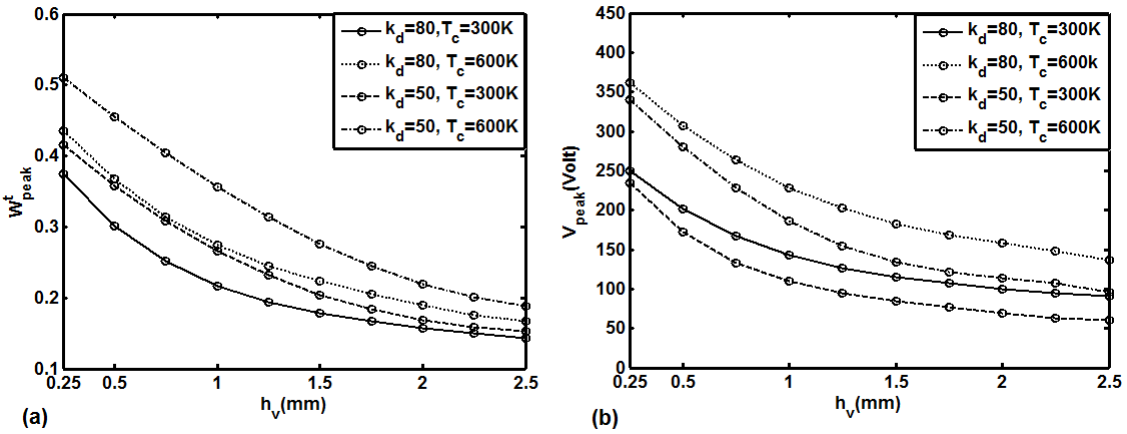

Fig. 3.14(a) Variations of peak-point deflection (W^t_{peak}) of nonlinear frequency response and (b) the corresponding required control voltage (V_{peak}) with the constrained viscoelastic layer

3.3.6 Effect of fiber volume fraction (v_f) in constraining PFRC layer

Figure 3.15 illustrates the frequency responses of the overall plate for different values of piezoelectric fiber volume fraction (v_f) of PFRC active constraining layer. It may be observed from this figure that for constant values of control gain (k_d) and load-amplitude (p), the damping in the overall plate caused by ACLD layer significantly varies with the piezoelectric fiber volume fraction (v_f) and the maximum damping in the overall plate is achieved for, $v_f = 0.8$. Since the same observation is also obtained from the previous analysis of FG plate integrated with PFRC layer (Fig. 2.2), one should consider 80% fiber

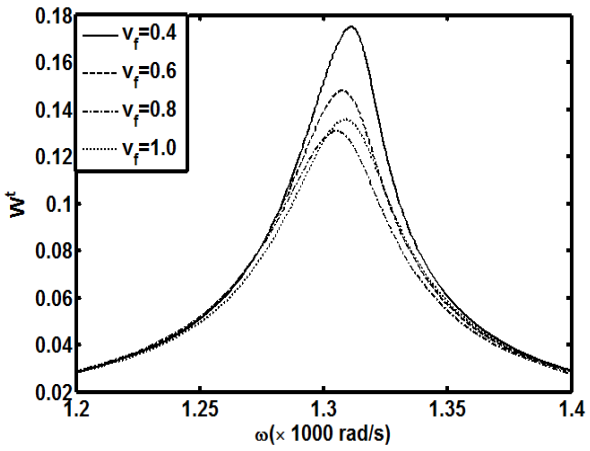

Fig. 3.15 Nonlinear frequency responses of the overall FG plate for different values of fiber volume fraction (v_f) in the PFRC constraining layers (p = 500 N/m^2, k_d=100, $T_c = T_m$=300 K, n=2).

volume fraction of PFRC for both cases (ACLD layer and PFRC actuator layer). But, practically it is considered at present as 40% because of the practical difficulties in achieving a PFRC with a very high (80%) fiber volume fraction.

3.3.7 Effect of fiber orientation angle (ψ) in constraining PFRC layer

For constant values of control gain (k_d) and load-amplitude (p), Fig. 3.16 demonstrates the variation of peak-point deflection (W^t_{peak}) of the frequency response curve for different values of piezoelectric fiber orientation angle (ψ) in the PFRC constraining layer. The lowest magnitude of W^t_{peak} in Fig. 3.16 indicates a particular fiber orientation angle ($\psi = \pm 45^o$) for effective use of PFRC constraining layer. Since the same observation has also been obtained from the previous analysis (Fig. 2.3), the piezoelectric fiber orientation angle (ψ) in the PFRC actuator layer would always be considered as, $\pm 45^o$. But practically, any value of ψ could be considered because of its (ψ) insignificant effect on W^t_{peak} (Figs. 3.16 and 2.3).

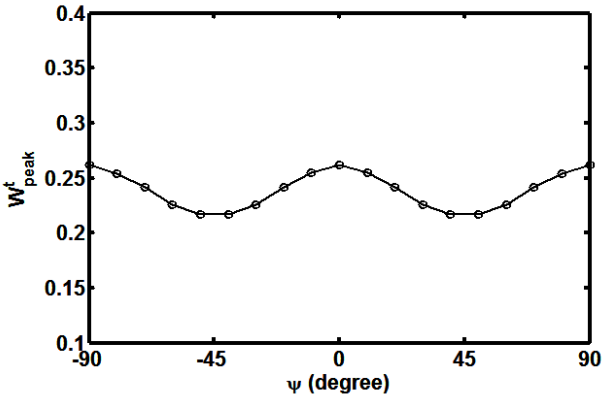

Fig. 3.16 Variation of peak-point deflection (W^t_{peak}) of controlled nonlinear frequency response curve with the fiber orientation angle (ψ) in the PFRC constraining layer (p =500 N/m^2, k_d =100, $T_c = T_m$ =300K, n =1).

3.3.8 Effect of substrate FG plate thickness (h)

Figures 3.17(a) and 3.17(b) illustrate the variations of the peak-point deflection (W^t_{peak}) of the nonlinear frequency response curve and the corresponding feedback control voltage (V_{peak}), respectively with the thickness (h) of substrate FG plate when the control-gain (k_d) and the load-amplitude (p) remain constant. It may be observed from these figures that for a particular temperature (T_c), both the peak-deflection (W^t_{peak}) and corresponding

control voltage (V_{peak}) decrease with the increasing thickness (h) of substrate FG plate. Because of the higher rate of decrease in the value of W^t_{peak} or V_{peak} in case of higher temperature (T_c), the responses for both the temperatures ($T_c = 600$ K and 300 K) merge at a higher value of, h. This may be due to the lesser magnitude of initial thermal bending deflection for thicker (more rigid) FG plate.

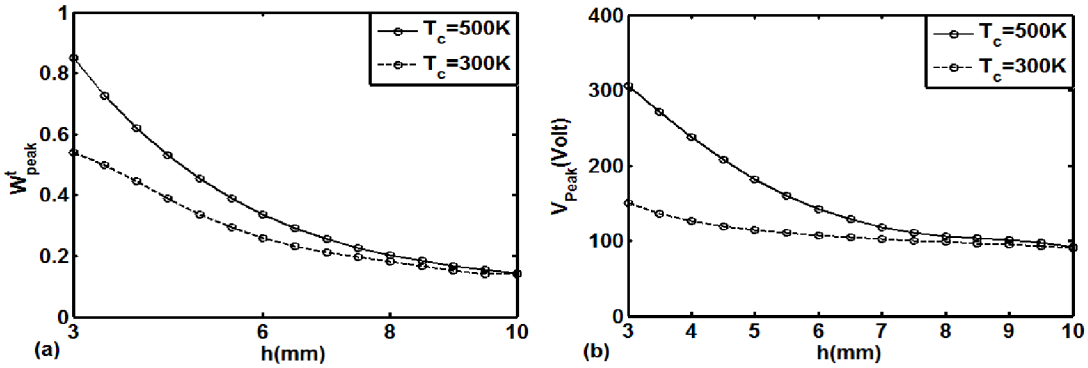

Fig. 3.17(a) Variations of (a) peak-point deflection (W^t_{peak}) of the nonlinear frequency response curve and (b) the corresponding feedback control voltage (V_{peak}) with the FG substrate-plate-thickness (h)(p =500 N/m^2, k_d=50, T_m=300 K, n=1).

3.4 Conclusions

In this chapter, an incremental nonlinear dynamic finite element model of FG plates integrated with an ACLD layer is developed. The present derivation is an extension of previous one (Section 2.2) due to the use of PFRC actuator layer as a constraining layer of ACLD treatment of vibration of overall FG plate. The analysis basically represents the effect of temperature on the nonlinear frequency responses of FG plates integrated with ACLD layer and also, on the corresponding actuation-capability of PFRC constraining layer. The PFRC constraining layer is activated by supplying external voltage according to negative velocity feedback control strategy. The kinematics of deformation of the overall plate is defined following the layer-wise FSDT and the geometric/kinematic nonlinearity of the same is considered according to the von Karman nonlinear strain-displacement relations. The GHM method is utilized for modeling the viscoelastic layer in the time-domain. Employing the Hamilton's principle, the incremental nonlinear finite element

equations of motion of the overall plate are first derived in the time-domain. Subsequently, those are expressed in the frequency-domain assuming the periodic motion of the overall plate according to the Fourier series. The incremental nonlinear finite element equations of motion in the frequency-domain are solved using a numerical solution methodology as presented in Section 2.3. The numerical illustrations in the present chapter reveal that the use of a viscoelastic material in the form of ACLD layer drastically improves the actuation-capability of PFRC actuator as compared to that when it (PFRC actuator) is directly attached to the substrate-plate surface. The analysis also reveals that the damping caused by ACLD layer is not remarkably dependent on the volume fraction index of FG substrate plate at room temperature. But, for higher temperatures, the same (damping) is affected significantly by the increase of volume fraction index of substrate plate. In the use of ACLD layer with PFRC constraining layer, the analysis suggests an optimal value of constrained viscoelastic layer for achieving effective damping in the overall smart FG plate. Except the issue of damping in the overall smart FG plate, other characteristics of linear/nonlinear frequency responses of heated smart FG plate do not vary significantly due to the use of ACLD layer instead of PFRC layer.

Chapter 4

SIZE AND LOCATION OF PFRC/ACLD PATCH FOR EFFECTIVE CONTROL OF NONLINEAR VIBRATION OF FG PLATS WITH A HEATED PLATE-SURFACE

This chapter presents the size and location of PFRC-actuator/ACLD patch over the surface of substrate FG plate for effective control of nonlinear vibration of the overall smart FG plate. A numerical procedure is proposed for determination of effective size and location of PFRC-actuator/ACLD patch. The numerical results illustrate these parameters (size and location) with and without consideration of thermal effect.

4.1 Introduction

The preceding chapters dealt with the performance of PFRC actuator/ACLD layer in control of nonlinear frequency responses of FG plates with a heated plate-surface. Since the PFRC is comprised of long, thin and brittle piezoelectric fibers, the breakage of fibers during its operation is a possible occurrence that eventually hampers the corresponding actuation-capability. So, such piezoelectric actuators are generally used in the form of patches instead of the form of layer. If the PFRC is used in the form of a patch, then the location of PFRC actuator/ACLD patch over the surface of the FG substrate plate and its (patch) size are important parameters for effective control of vibration of the overall FG plate. In the present chapter, these important parameters (size and location) are determined through the proposition of a numerical procedure in conjunction with the developed nonlinear finite element models of overall smart FG plates in the preceding chapters.

4.2 Numerical procedure for effective size and location of PFRC/ACLD patch

In order to find out the best location of the ACLD/PFRC patch over the top surface of FG substrate plate, the importance of the ACLD/PFRC material at every point on the

top surface of the FG substrate plate is numerically tested. The finite element descritization of the smart FG plate is done such that each element represents the size of PFRC patch and the centroid of each element is considered to be the location of the patches. First, an ACLD/PFRC layer is considered throughout the top surface of the substrate plate. Then, a differential patch of ACLD/PFRC surrounding a point under test is removed and the peak-point (W^t_{peak}) of nonlinear frequency response curve corresponding to this configuration of the overall plate is evaluated. The differential area of the ACLD/PFRC patch is taken as constant such that the total area of the rest of ACLD/PFRC layer remains the same for all test points. A number of test points on the top surface of the FG substrate plate are considered. Then, for constant values of control gain (k_d), load-amplitude (p) and temperature (T_c); the peak-point (W^t_{peak}) of nonlinear frequency response curve corresponding to each test point are evaluated and represented by the surface plot for the variation of W^t_{peak} as illustrated in Figs. 4.5-4.8. In the absence and the presence of temperature (T_c), Figs. 4.5

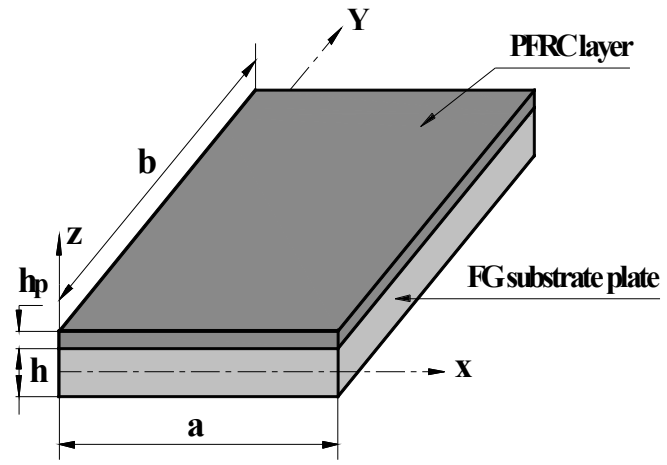

Fig. 4.1 Schematic diagram of FG plate integrated with a layer of PFRC.

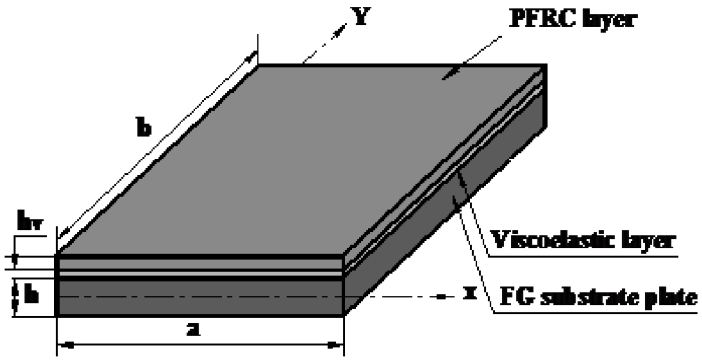

Fig. 4.2 Schematic diagram of FG plate integrated with a layer of ACLD treatment.

and 4.6, respectively illustrate the surface plots for the variation of W_{peak}^{t} in case of PFRC actuator layer attached to the top surface of the FG substrate pate. Figures 4.7 and 4.8 demonstrate the same for ACLD layer.

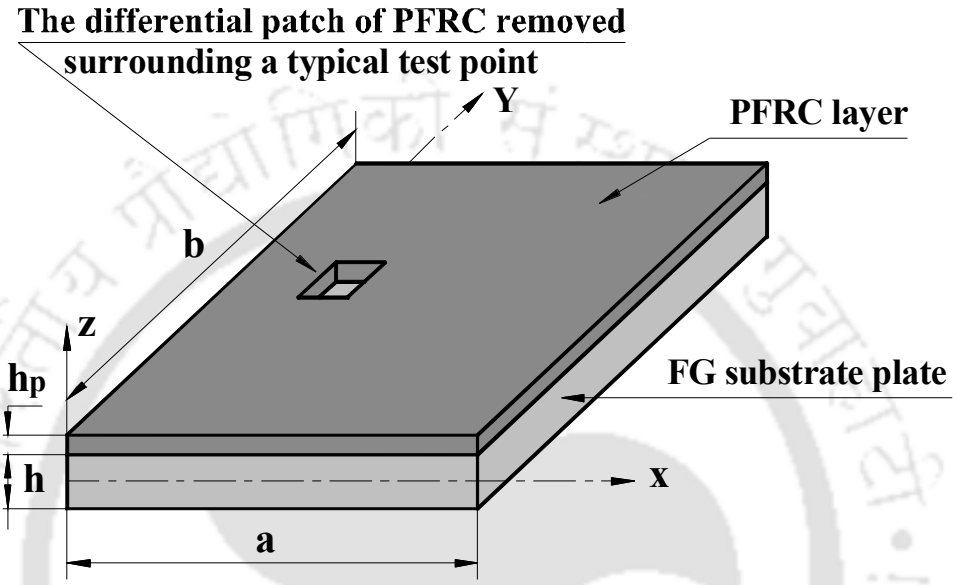

Fig. 4.3 Schematic diagram of a differential patch of PFRC removed surrounding a typical test point

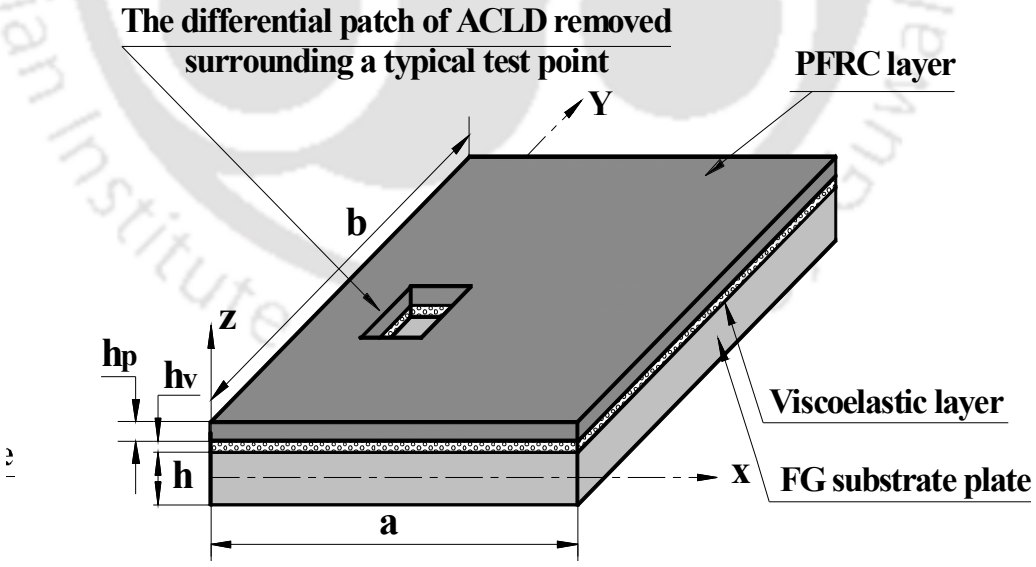

Fig. 4.4 Schematic diagram of a differential patch of ACLD removed surrounding a typical test point

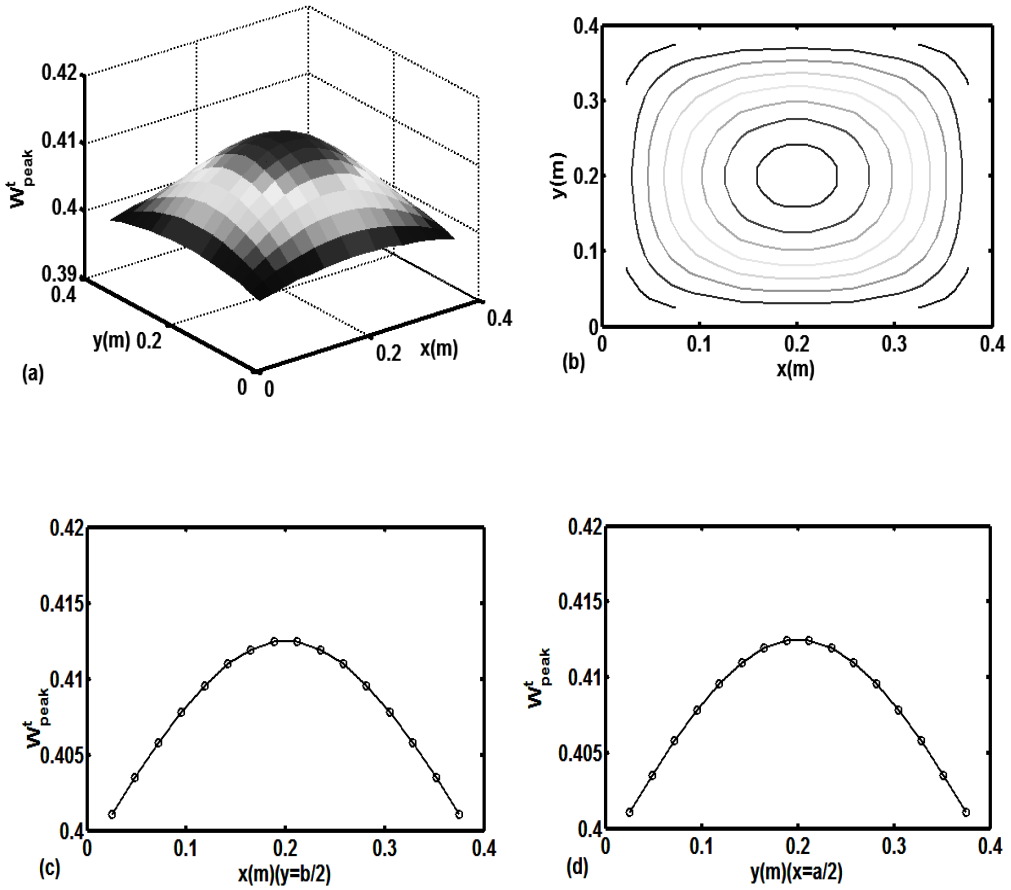

Fig.4.5(a) Surface plot for the variation of (W^t_{peak}) with the different test points on the top surface of FG substrate plate, (b) corresponding contour plot,(c)-(d) variations of (W^t_{peak}) with the different test points along x- direction ($y=b/2$) and y direction($x=a/2$) (p = 400 N/m^2, λ =1, k_d =100, $T_c = T_m$ =300K, n =2).

Since the removal of differential PFRC patch from an important location/point significantly affects the actuation-capability of PFRC layer, the corresponding W^t_{peak} would have more value. Thus, the surface plot for the variation of W^t_{peak} in Fig. 4.5(a) implies that the area surrounding the middle point on the top surface of substrate FG plate is the most important location of PFRC patch for effective control of vibration of the overall FG plate. This location is also elaborated in Fig. 4.5(b) by the corresponding

contour plot. Along with this best location of the PFRC patch, other important parameters like its dimensions along x and y directions (Fig. 4.1) can also be estimated from Figs. 4.5(c)-(d). Figures 4.5(c)-(d) represent the variations in the value of W^t_{peak} along x-direction (at $y = b/2$) and y-direction (at $x = a/2$), respectively.

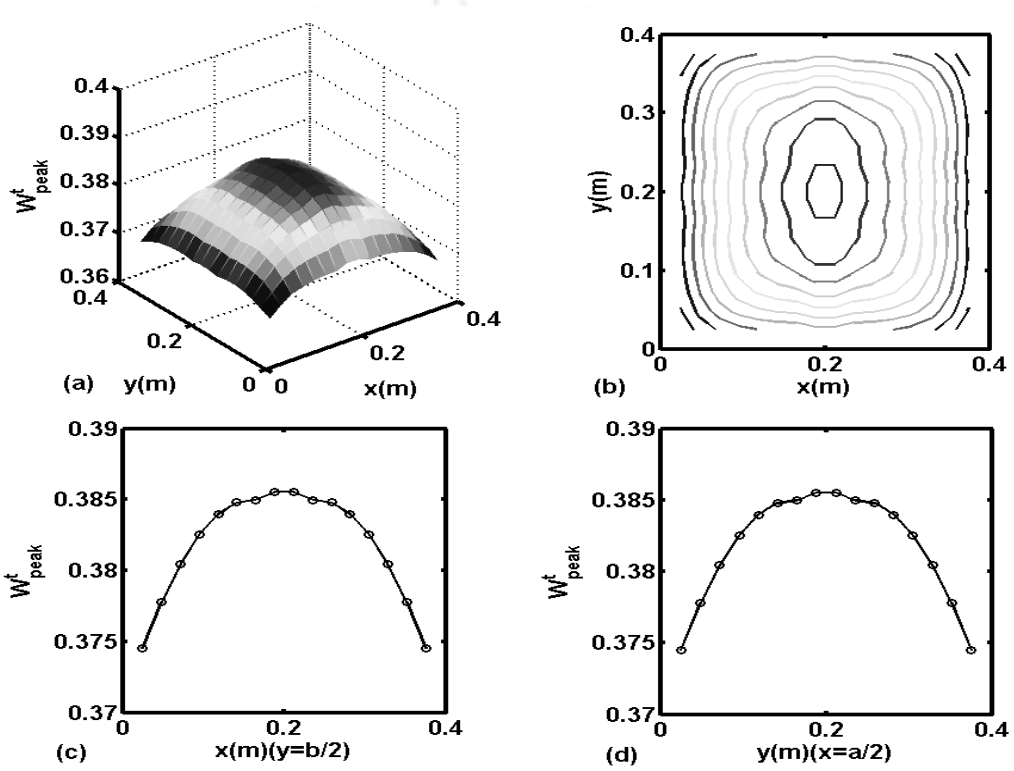

Fig. 4.6 (a) Surface plot for the variation of (W^t_{peak}) with the different test points on the top surface of FG substrate plate, (b) corresponding contour plot,(c)-(d) variations of W^t_{peak} with the different test points along x-direction ($y = b/2$) and $y-$ direction ($x = a/2$) (PFRC patch, p = 400 N/m^2, λ =1, k_d =100, T_m = 300 K, T_c = 500 K, n =1).

These figures show that the points at the middle zone ($x = a/2$, $y = b/2$) are almost equally important but the importance of the points towards the edges of the plate decreases at a greater rate. Thus, the dimensions of the PFRC patch along x and y

directions can be estimated within the area defined by, $x = 0.1$ m, $x = 0.3$ m, $y = 0.1$ m and $y = 0.3$ m (Figs. 4.5(c)-(d)). In the presence of a ceramic-rich surface temperature

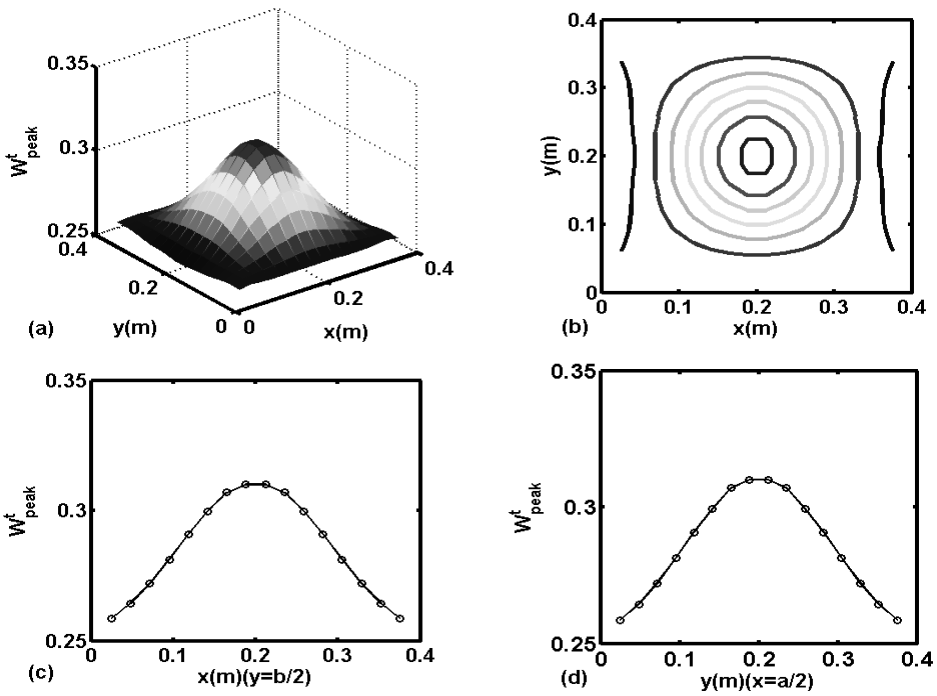

Fig. 4.7 (a) Surface plot for the variation of (W^t_{peak}) with the test points on the top surface of FG substrate plate, (b) corresponding contour plot,(c)-(d) variations of W^t_{peak} with the test points along x-direction ($y = b/2$) and $y-$ direction ($x = a/2$) (ACLD patch, p=500 N/m^2, k_d=50, $T_c = T_m$=300 K, n=1).

($T_c = 500$ K), the location of PFRC patch does not alter as it is indicated in Figs. 4.6(a)-(b). But, Figs. 4.6(c)-(d) show that the dimensions (size) of the patch along x and y directions would not be the same as those estimated in earlier case (Figs. 4.5(c)-(d)). In this case, a larger stretch of the patch along each of x and y-directions may be considered for estimating the effective size/dimensions of the patch. In case of the use of ACLD patch in the absence of temperature (T_c), Fig. 4.7(a) shows the surface plot of W^t_{peak} with test points (from which a differential ACLD patch is removed) and 4.7(b)

shows the corresponding contour plot. Figures 4.7(c)-(d) show the variation of W_{peak}^{t} along x and y directions, respectively indicating the sensitivity of ACLD location on the W_{peak}^{t}. Similarly in the presence of temperature (T_c),

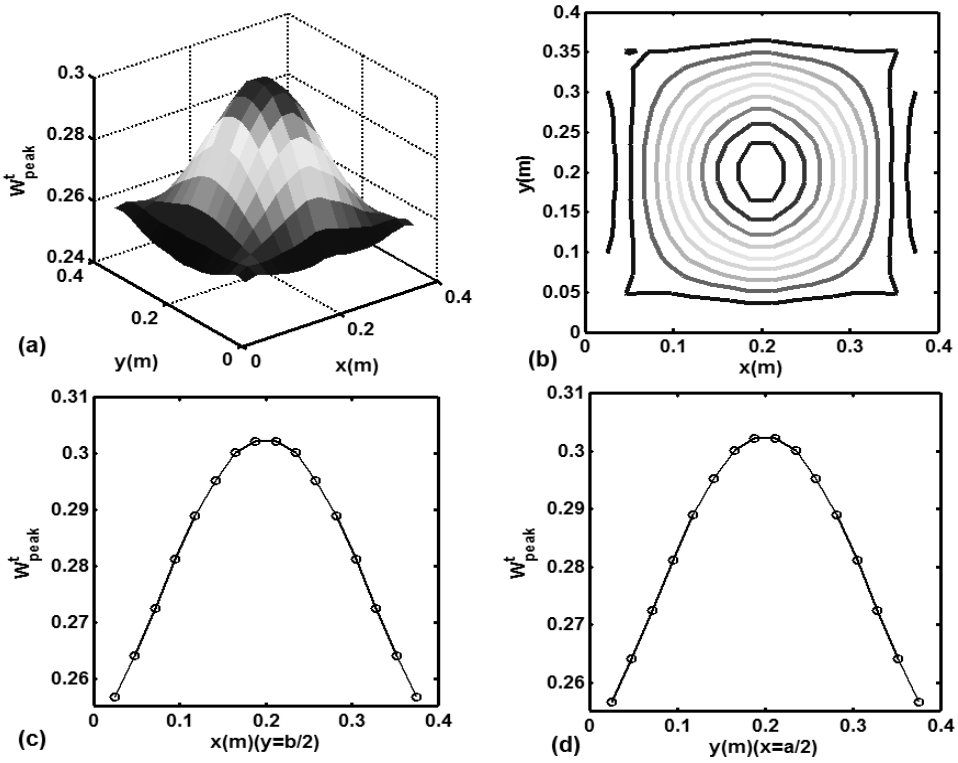

Fig. 4.8(a) Surface plot for the variation of (W_{peak}^{t}) with the test points on the top surface of FG substrate plate, (b) corresponding contour plot, (c)-(d) variations of W_{peak}^{t} with the test points along x-direction ($y=b/2$) and $y-$direction ($x=a/2$) (ACLD patch, p=400 N/m^2, k_d=50, T_m = 300 K, T_c =500 K, n=1).

Fig. 4.8(a) shows the surface plot of W_{peak}^{t} with test points and 4.8(b) shows the corresponding contour plot. Figures 4.8(c)-(d) show the variation of W_{peak}^{t} along x and y directions, respectively indicating the sensitivity of ACLD locations on the W_{peak}^{t}. Also, from Figs. 4.7(c)-(d) and 4.8(c)-(d), the same estimation for effective dimensions of

ACLD patch could be made as that is done for PFRC patch in the absence of temperature (T_c) (Figs. 4.5(c)-(d)). It should be noted that the above mentioned location and size of PFRC actuator/ACLD patch are determined for effective control of nonlinear vibration of FG plates corresponding to its fundamental mode of vibration. For other modes of vibration of the same, these effective parameters (size and location) may be different and can be determined following the same numerical procedure as described in the present work. However, in the present estimations of size and location of PFRC/ACLD patch over the surface of FG substrate plate for effective control of a particular mode of vibration of overall plate, none of the available optimization algorithms is utilized. So, the estimated size and location of PFRC/ACLD patch are called at present as "effective size and location of patch" instead of "optimal size and location of patch".

4.3 Conclusions

In this chapter, a numerical procedure is described for estimating size and location of PFRC/ACLD patch over the top surface of substrate FG plate for effective control of vibration of overall FG plate. This procedure is implemented in conjunction with the incremental nonlinear finite element models of the overall FG plate developed in the preceding chapters. For a particular mode of vibration of the overall FG plate, the numerical results reveal that the effective location of PFRC/ACLD patch over the top surface of FG substrate plate does not alter due to the presence of ceramic-rich surface temperature. But, the effective size of the same (patch) may alter in effect of the presence of temperature. An indicative change of effective size of PFRC patch due to the existence of temperature gradient across the thickness of substrate FG plate is observed while similar temperature gradient has no significant effect on the same (effective size) of ACLD patch.

Chapter 5

DESIGN OF LAMINATED COMPOSITE PLATES USING GRADED ORTHOTROPIC FIBER-REINFORCED COMPOSITE PLIES

This chapter deals with the design of graded fiber-reinforced composite laminates. A new lamination scheme is proposed through the design of a graded orthotropic fiber-reinforced composite lamina with varying fiber-volume fraction along the thickness direction. The main objective of the overall design is to eliminate the property mismatch at the inter-laminar surfaces of composite laminates. The numerical results are presented to substantiate the efficiency of the proposed lamination scheme.

5.1 Introduction

The laminated fiber-reinforced composite structures suffer from an obvious drawback of delamination under the high mechanical and/or thermal stresses mainly because of the mismatch of material properties in the thickness direction. For alleviating such a drawback without affecting orthotropic elastic properties of composite plies, a design of graded fiber-reinforced composite laminate has been presented in a recent study (Fu et al. 2010). In this study, the concept of FGM is utilized and the continuous variations of material properties as well as stresses across the thickness of composite laminate are achieved by means of low fiber volume fraction (FVF) at interlaminar surfaces of composite plies. But, this low FVF in all plies may hamper the laminate-rigidity that is not addressed in the same study. Also, another problem of stress-concentration for every in-plane normal stress arises at the top/bottom surface of the laminate that eventually raises the maximum value of the same stress. In order to achieve continuous variations of material properties across the thickness of a composite laminate without affecting orthotropic elastic properties of composite plies, laminate-rigidity and maximum values of stresses, a new lamination scheme is proposed in this study. The proposed lamination scheme is implemented through the design of a graded orthotropic fiber-reinforced

composite lamina with varying FVF across its (lamina) thickness. The proposed strategy of lamination utilizes graded as well as conventional orthotropic composite plies. The graded composite plies work mainly for eliminating the mismatch of material properties at the interlaminar surfaces of plies while the conventional plies strengthen the overall laminate. The new lamination scheme is demonstrated through the conversion of a conventional laminated composite plate (CLCP) into a conventional-graded laminated composite plate (CGLCP). A bending analysis of these plates (CLCP and CGLCP) is carried out for investigating the suitability of present conversion of a CLCP through the corresponding changes in laminate-rigidity, stress-mismatch at interlaminar surfaces, stress-concentration and maximum values of stresses in the laminate.

5.2 Present graded composite lamina

Figure 5.1(a) shows a unidirectional continuous fiber-reinforced composite lamina. The fibers within the lamina are oriented in parallel to x axis and a typical cross-section of the lamina in yz-plane is illustrated in Fig. 5.1(b). The thickness of the lamina is denoted by, h_c. The basic building block of this composite is a fiber-matrix pack that is in shape of a rectangular parallelepiped. A fiber-matrix pack is comprised of a continuous fiber embedded within the epoxy matrix and its longitudinal, lateral and transverse directions are in parallel to x, y and z axes, respectively. The axes of a fiber-matrix pack and its fiber lie on the same line in parallel to x axis while the cross-sections of both are considered in shape of square section. The fiber is supposed to be perfectly bonded with the matrix-phase and the linear elastic materials for both the phases are assumed. The side of the square cross-section of a fiber is denoted by a_f and that of the corresponding fiber-matrix pack is denoted by, a_c. The volume fractions of fiber and matrix phases within a fiber-matrix pack are designated by the symbols, v_f and v_m, respectively. A group of fiber-matrix packs having horizontally coplanar axes is designated as a layer of fiber-matrix packs and it (layer) is denoted by, ℓ-layer (Fig. 5.1(b)). Also, the axes of any

two vertically consecutive fibers/fiber-matrix packs lie on the same vertical plane (Fig. 5.1(b)).

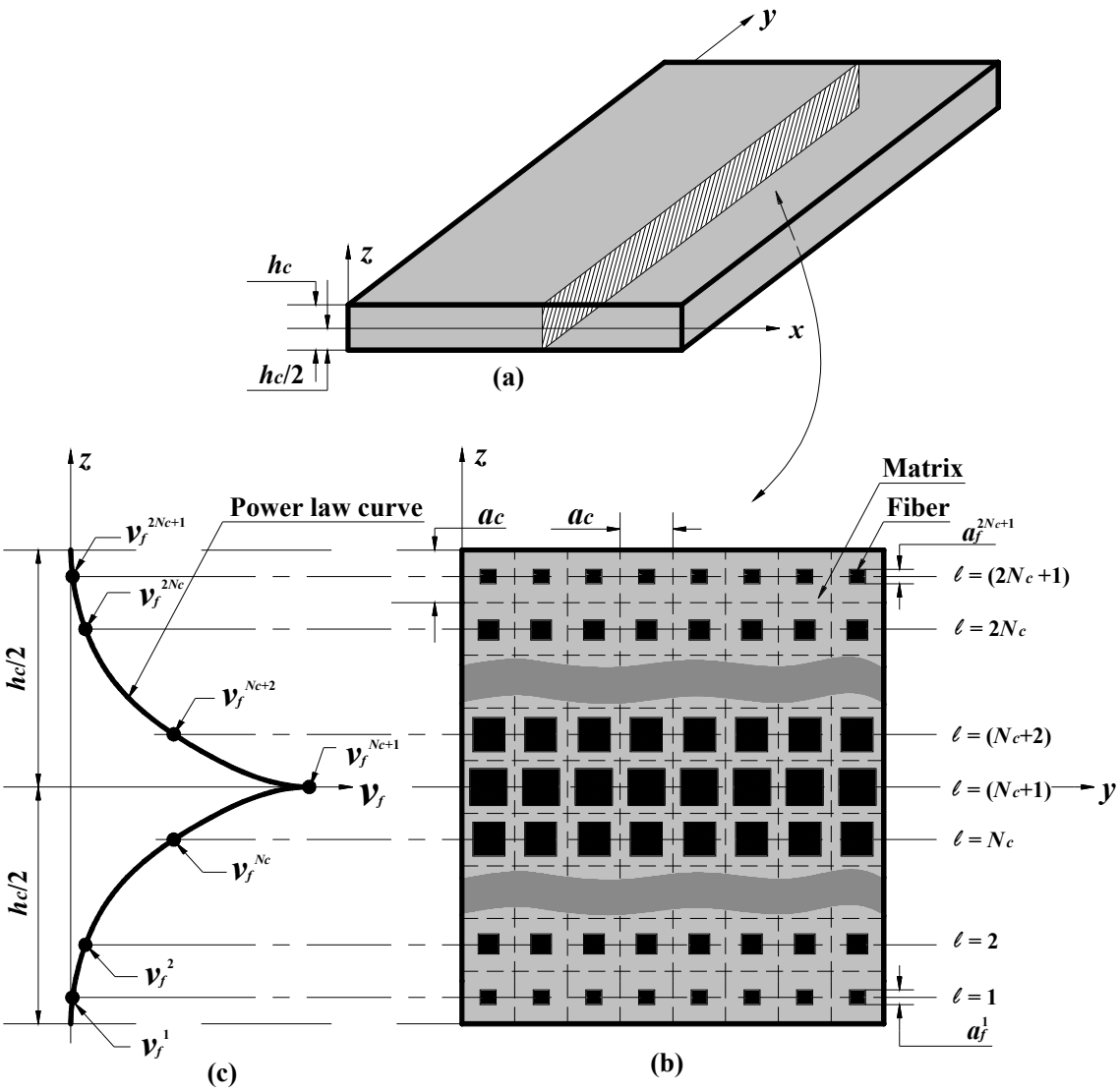

Fig. 5.1 Schematic diagram of (a) graded composite lamina, (b) a sectional view (yz -plane) and (c) variation of FVF according to power-law.

The composite lamina is considered to be composed of $(2N_c+1)$ number of layers in such a way that the same number of layers (N_c) are stacked above and below the middle layer $(\ell=(N_c+1))$. All fiber-matrix packs within a layer are of identical FVF

while the FVF varies among the layers. The variation of FVF among the layers is considered

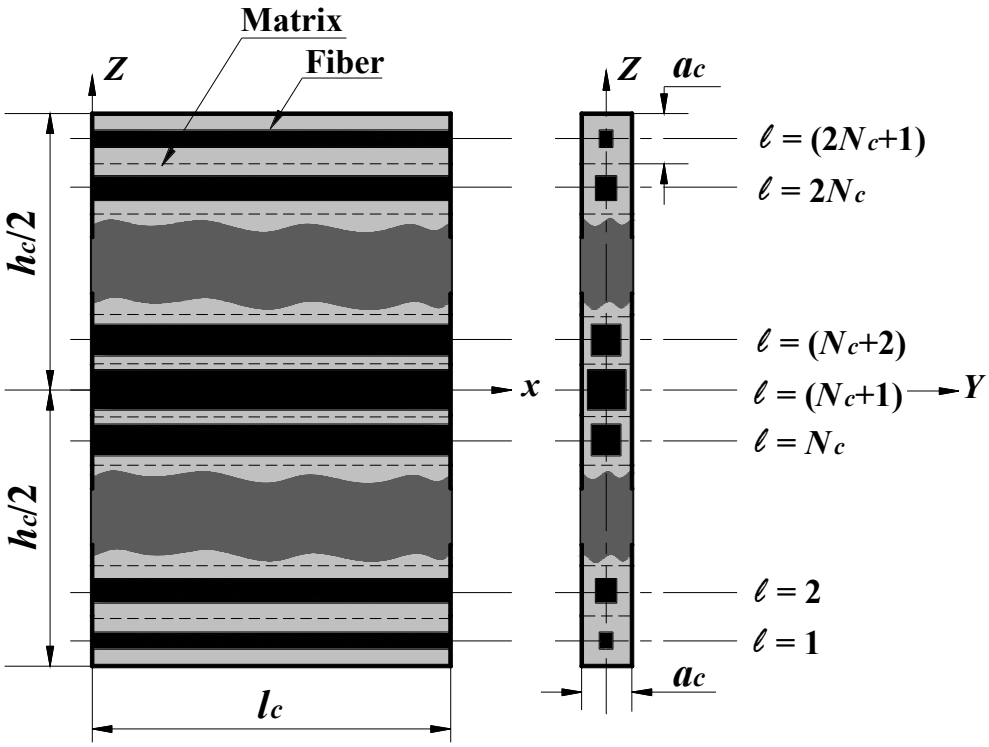

Fig. 5.2 Schematic diagram of RV of the graded unidirectional continuous fiber-reinforced composite lamina (Fig. 5.1).

according to a simple power-law. For the sake of simplicity in consideration of power-law, the maximum value of FVF is taken at the middle plane ($z=0$) of the lamina and it (FVF) symmetrically decreases to a minimum value along both ($+z$ and $-z$) directions from the middle plane according to the power-law (Fig. 5.1(c)). Although the use of power-law provides a continuous variation of FVF along the thickness direction (z), but the FVF of a layer is taken corresponding to a point on the power-law curve where the centre-line of that layer intersects (Figs. 5.1(b)-(c)). Since identical square cross-section (a_c) of all fiber-matrix packs within the composite lamina is considered, the variation of FVF among the layers is achieved by the layer-wise variation of fiber-cross-section. For instance, the side (a_f^ℓ) of square cross-section of fibers within a layer (ℓ-layer) with the FVF of v_f^ℓ ($\ell = 1,2,.....,(2N_c+1)$) is, $a_f^\ell = a_c\sqrt{v_f^\ell}$. However, according to this

constructional strategy, the fiber-matrix packs within the middle layer have maximum FVF while the same within the top/bottom layer have minimum FVF.

5.3 Graded effective elastic properties

Since every layer is comprised of identical fiber-matrix packs (Fig. 5.1(b)), a representative volume (RV) as shown in Fig. 5.2 may be chosen as an elemental volume for predicting the effective graded elastic properties of the composite lamina. A boundary face of RV is defined by its normal direction. So, its six boundary faces are denoted by, $+x$, $-x$, $+y$, $-y$, $+z$ and $-z$ planes. The effective graded elastic properties of the present composite lamina are estimated following a concept of homogeneous model of FG materials proposed by Reiter and Dvorak (1997, 1998). The original work of Reiter and Dvorak (1997, 1998) is for the particulate micro-structure of a two-phase graded material with single composition gradient. In this proposition (Reiter and Dvorak 1997, 1998), the medium of FG solid is modeled by stacking several parallel homogeneous layers along the direction of variation of composition gradient. The constituent volume fractions of layers are assigned following the single composition gradient of the FG solid. Then, the effective properties of every layer are determined using either Mori-Tanaka method or Self-consistent scheme depending on the location of that layer within the FG solid. However, following this proposition, every fiber-matrix pack of RV (Fig. 5.2) of present composite is assumed as a homogeneous layer while the layers within the RV are of different FVFs. In the present prediction of effective properties of every homogeneous layer, first volume-average elastic properties of RV are estimated. Subsequently, the effective properties of every homogeneous layer are extracted from the volume-average properties of RV. Since the layers are coupled within the RV, the prediction of effective properties of homogeneous layers from the volume-average properties of RV includes the effect of coupled interaction among the layers on their effective properties. It should be noted that the effective properties of homogeneous layers in the work of Reiter and Dvorak (1997, 1998) are estimated considering every layer as a discrete representative volume element (RVE). However, for the present graded fiber-reinforced composite, negligibly small effect of this coupled

interaction among the layers on their effective properties is observed as it is quantified in later section.

The volume-average stress ($\{\bar{\sigma}\}$) and strain ($\{\bar{\varepsilon}\}$) field quantities over the volume of RV can be expressed in terms of the similar field quantities ($\{\bar{\sigma}^{\ell}\}$, $\{\bar{\varepsilon}^{k}\}$) of layer-volumes as follows,

$$\{\bar{\sigma}\} = \sum_{\ell=1}^{(2N_c+1)} \upsilon^{\ell} \{\bar{\sigma}^{\ell}\},$$
$$\{\bar{\varepsilon}\} = \sum_{\ell=1}^{(2N_c+1)} \upsilon^{\ell} \{\bar{\varepsilon}^{\ell}\},$$
$$\upsilon^{\ell} = V^{\ell} / V \tag{5.1}$$

where, V^{ℓ} and V are the volumes of ℓ^{th} layer and RV, respectively. Similar relations can also be written for ℓ^{th} layer as follows,

$$\{\bar{\sigma}^{\ell}\} = \left(\upsilon_f^{\ell} \{\bar{\sigma}_f^{\ell}\} + \upsilon_m^{\ell} \{\bar{\sigma}_m^{\ell}\}\right),$$
$$\{\bar{\varepsilon}^{\ell}\} = \left(\upsilon_f^{\ell} \{\bar{\varepsilon}_f^{\ell}\} + \upsilon_m^{\ell} \{\bar{\varepsilon}_m^{\ell}\}\right),$$
$$\upsilon_f^{\ell} = V_f^{\ell} / V^{\ell},$$
$$\upsilon_m^{\ell} = V_m^{\ell} / V^{\ell} \tag{5.2}$$

where, V_f^{ℓ} and V_m^{ℓ} are the volumes of fiber and matrix phases in the ℓ^{th} layer; $\{\bar{\sigma}_f^{\ell}\} / \{\bar{\varepsilon}_f^{\ell}\}$ and $\{\bar{\sigma}_m^{\ell}\} / \{\bar{\varepsilon}_m^{\ell}\}$ are the volume-average stress/strain vectors for fiber and matrix phases of ℓ^{th} layer. Substituting Eq. (5.2) in Eq. (5.1), the following expression for the volume-average stress vector ($\{\bar{\sigma}\}$) of RV can be obtained,

$$\{\bar{\sigma}\} = \sum_{\ell=1}^{(2N_c+1)} \upsilon^{\ell} \left(\upsilon_f^{\ell} \{\bar{\sigma}_f^{\ell}\} + \upsilon_m^{\ell} \{\bar{\sigma}_m^{\ell}\}\right) \tag{5.3}$$

The constitutive relations for the fiber and matrix phases within a layer (ℓ) can be written as,

$$\{\bar{\sigma}_f^{\ell}\} = [C_f]\{\bar{\varepsilon}_f^{\ell}\},$$

$$\{\bar{\sigma}_m^{\ell}\} = [C_m]\{\bar{\varepsilon}_m^{\ell}\} \tag{5.4}$$

where, $[C_f]$ and $[C_m]$ are stiffness matrices for fiber and matrix phases, respectively. Substituting Eq. (5.4) in Eq. (5.3), the following expression of $\{\bar{\sigma}\}$ can be obtained,

$$\{\bar{\sigma}\} = \sum_{\ell=1}^{(2N_c+1)} \upsilon^{\ell}\left(\upsilon_f^{\ell}[C_f]\{\bar{\varepsilon}_f^{\ell}\} + \upsilon_m^{\ell}[C_m]\{\bar{\varepsilon}_m^{\ell}\}\right) \tag{5.5}$$

The volume-average strain vector ($\{\bar{\varepsilon}^{\ell}\}$) for ℓ^{th} layer is connected with that ($\{\bar{\varepsilon}\}$) of RV by,

$$\{\bar{\varepsilon}^{\ell}\} = [\bar{A}^{\ell}]\{\bar{\varepsilon}\},$$

$$\sum_{\ell=1}^{(2N_c+1)} \upsilon^{\ell}[\bar{A}^{\ell}] = [I] \tag{5.6}$$

where, $[\bar{A}^{\ell}]$ is the volume-average strain concentration matrix for ℓ^{th} layer and $[I]$ is the unity matrix. Similarly, the volume-average strain vectors ($\{\bar{\varepsilon}_f^{\ell}\}, \{\bar{\varepsilon}_m^{\ell}\}$) for fiber and matrix phases within a layer (ℓ) can be expressed in terms of the volume-average strain vector ($\{\bar{\varepsilon}\}$) of RV as,

$$\{\bar{\varepsilon}_f^{\ell}\} = [\bar{A}_f^{\ell}]\{\bar{\varepsilon}\},$$

$$\{\bar{\varepsilon}_m^{\ell}\} = [\bar{A}_m^{\ell}]\{\bar{\varepsilon}\},$$

$$\sum_{\ell=1}^{(2N_c+1)} \upsilon^{\ell}(\upsilon_f^{\ell}[\bar{A}_f^{\ell}] + \upsilon_m^{\ell}[\bar{A}_m^{\ell}]) = [I] \tag{5.7}$$

where, $[\bar{A}_f^{\ell}]$ and $[\bar{A}_m^{\ell}]$ are the volume-average strain concentration matrices of fiber and matrix phases in ℓ^{th} layer. Substituting Eq. (5.2) in Eq. (5.6) and then using Eq. (5.7), the following expression of the volume-average strain concentration matrix ($[\bar{A}^{\ell}]$) for ℓ^{th} layer can be obtained,

$$[\bar{A}^{\ell}] = \left(\upsilon_f^{\ell}[\bar{A}_f^{\ell}] + \upsilon_m^{\ell}[\bar{A}_m^{\ell}]\right) \tag{5.8}$$

Introducing Eq. (5.7) in Eq. (5.5) and then using Eq. (5.8), the following relation between the volume-average stress and strain vectors of RV can be obtained,

$$\{\bar{\sigma}\} = [\bar{C}]\{\bar{\varepsilon}\},$$
$$[\bar{C}] = \sum_{\ell=1}^{(2N_c+1)} \left[\upsilon^{\ell}\left\langle \upsilon_f^{\ell}\left([C_f]-[C_m]\right)[\bar{A}_f^{\ell}] + [C_m][\bar{A}^{\ell}]\right\rangle\right] \tag{5.9}$$

Equation (5.9) describes the volume-average elastic properties of RV. For the assumption of homogenized layers (ℓ), these average properties (Eq. (5.9)) would be the average of effective properties of all layers within the RV. For a homogeneous layer (ℓ) within the RV, the effective constitutive relation can be written as,

$$\{\bar{\sigma}^{\ell}\} = [\bar{C}^{\ell}]\{\bar{\varepsilon}^{\ell}\} \tag{5.10}$$

where, $[\bar{C}^{\ell}]$ is the effective stiffness matrix for the ℓ^{th} homogeneous layer. Now, since all homogeneous layers are coupled within the RV, Eq. (5.10) can be inserted into Eq. (5.1). Subsequently, using the relation given in Eq. (5.6), the following expression can be obtained,

$$\{\bar{\sigma}\} = \sum_{k=1}^{(2N_c+1)} (\upsilon^{\ell}[\bar{C}^{\ell}][\bar{A}^{\ell}])\{\bar{\varepsilon}\} \tag{5.11}$$

Comparing Eq. (5.9) with Eq. (5.11), the following expression for $[\bar{C}^{\ell}]$ can be obtained,

$$[\bar{C}^{\ell}] = \upsilon_f^{\ell}\left([C_f]-[C_m]\right)[\bar{A}_f^{\ell}][\bar{A}^{\ell}]^{-1} + [C_m] \tag{5.12}$$

Equation (5.12) represents the expression of effective elastic matrix ($[\bar{C}^{\ell}]$) of ℓ^{th} homogeneous layer within the RV. The strain concentration matrices ($[\bar{A}_f^{\ell}], [\bar{A}^{\ell}]$) are the key factors for evaluation of $[\bar{C}^{\ell}]$. Since these strain concentration matrices are defined with respect to the volume-average strain of RV, the effect of coupled interaction among

the layers within the RV on their (layers) effective properties is included. However, the strain concentration matrices ($[\overline{A}_f^{\ell}]$,$[\overline{A}^{\ell}]$) for different layers in RV may be evaluated using available micromechanics theories like Mori-Tanaka method, Self-consistent method etc. Although these micromechanics theories provide quick predictions of effective properties of the composite, but the same could also be evaluated numerically using finite element (FE) procedure that may provide more realistic predictions of effective properties of the composite (Odegard 2004). So, the FE procedure is followed in this work by deriving a three-dimensional FE model of RV as presented in the next section. According to the theorem of average strain for composite materials, the homogeneous displacement boundary conditions over the boundary surfaces of RV are applied in order to compute its (RV) volume-average strain ($\{\overline{\varepsilon}\}$) using the following expression,

$$\{\overline{\varepsilon}\} = \frac{1}{V}\left(\sum_{\ell=1}^{N_{Rv}} \int_{V_\ell} \{\varepsilon_\ell\}\, dV_\ell \right) \tag{5.13a}$$

where, N_{Rv} is the total number of elements within the FE model of RV; $\{\varepsilon_\ell\}$ is the strain vector at any point within the ℓ^{th} element; V_ℓ is the volume of ℓ^{th} element. Similar to Eq. 5.13(a), the volume-average strains of a layer (ℓ) and corresponding fiber counterpart can be computed from the FE model of RV using the following expressions,

$$\left\{\overline{\varepsilon}^{\ell}\right\} = \frac{1}{V^{\ell}}\left(\sum_{\ell=1}^{N^{\ell}} \int_{V_\ell} \{\varepsilon_\ell\}\, dV_\ell \right),$$

$$\left\{\overline{\varepsilon}_f^{\ell}\right\} = \frac{1}{V_f^{\ell}}\left(\sum_{\ell=1}^{N_f^{\ell}} \int_{V_\ell} \{\varepsilon_\ell\}\, dV_\ell \right) \tag{5.13b}$$

where, N^{ℓ} is the number of elements within the ℓ^{th} layer; N_f^{ℓ} is the number of elements within the fiber phase of ℓ^{th} layer. Six types of homogeneous displacement boundary conditions are considered as those are demonstrated in Table 5.1. Every type of these

boundary conditions provides one non-zero strain component of $\{\bar{\varepsilon}\}$ that yields the corresponding columns of $[\bar{A}^{\ell}]$ and $[\bar{A}_f^{\ell}]$ according to Eqs. (5.6) and (5.7), respectively. Thus, all columns of the concentration matrices ($[\bar{A}^{\ell}]$, $[\bar{A}_f^{k}]$) can be computed by applying the six types of boundary conditions (Table 5.1) separately on the FE model of RV. However, in order to estimate the effective elastic properties of homogeneous layers using the FE model of RV, there are basically four aforesaid expressions (Eqs. (5.6), (5.7), (5.12) and (5.13)) are to be utilized in association with the appropriate boundary conditions (Table 5.1).

Table 5.1 Boundary conditions for determining elements of $\{\bar{\varepsilon}\}$

Boundary conditions	Elements of $\{\bar{\varepsilon}\}$
$u\|_{-x}=0,\ u\|_{+x}=(\varepsilon_x^0\times\ell_c)\ ,\ v\|_{-y}=0,\ v\|_{y}=0,$ $w\|_{-z}=0,\ w\|_{+z}=0$	$\bar{\varepsilon}_x\approx\varepsilon_x^0, \bar{\varepsilon}_y=\bar{\varepsilon}_z=\bar{\gamma}_{yz}=\bar{\gamma}_{xz}=\bar{\gamma}_{xy}=0$
$u\|_{-x}=0,\ u\|_{+x}=0\ ,\ v\|_{-y}=0,\ v\|_{y}=(\varepsilon_y^0\times a_c),$ $w\|_{-z}=0,\ w\|_{z}=0$	$\bar{\varepsilon}_y\approx\varepsilon_y^0, \bar{\varepsilon}_x=\bar{\varepsilon}_z=\bar{\gamma}_{yz}=\bar{\gamma}_{xz}=\bar{\gamma}_{xy}=0$
$u\|_{-x}=0,\ u\|_{+x}=0,\ v\|_{-y}=0,\ v\|_{-y}=0,$ $w\|_{-z}=0,\ w\|_{+z}=(\varepsilon_z^0\times h_c)$	$\bar{\varepsilon}_z\approx\varepsilon_z^0, \bar{\varepsilon}_x=\bar{\varepsilon}_y=\bar{\gamma}_{yz}=\bar{\gamma}_{xz}=\bar{\gamma}_{xy}=0$
$v\|_{-z}=0,\ v\|_{z}=(\frac{1}{2}\gamma_{yz}^0\times h_c),\ w\|_{-y}=0,$ $w\|_{4}=(\frac{1}{2}\gamma_{yz}^0\times a_c)$	$\bar{\gamma}_{yz}\approx\gamma_{yz}^0, \bar{\varepsilon}_x=\bar{\varepsilon}_y=\bar{\varepsilon}_z=\bar{\gamma}_{xz}=\bar{\gamma}_{xy}=0$
$u\|_{-z}=0,\ u\|_{+z}=(\frac{1}{2}\gamma_{xz}^0\times h_c),\ w\|_{-x}=0,$ $w\|_{+x}=(\frac{1}{2}\gamma_{xz}^0\times\ell_c)$	$\bar{\gamma}_{xz}\approx\gamma_{xz}^0, \bar{\varepsilon}_x=\bar{\varepsilon}_y=\bar{\varepsilon}_z=\bar{\gamma}_{yz}=\bar{\gamma}_{xy}=0$
$u\|_{-y}=0,\ u\|_{y}=(\frac{1}{2}\gamma_{xy}^0\times a_c),\ v\|_{-x}=0,$ $v\|_{+x}=(\frac{1}{2}\gamma_{xy}^0\times\ell_c)$	$\bar{\gamma}_{xy}\approx\gamma_{xy}^0, \bar{\varepsilon}_x=\bar{\varepsilon}_y=\bar{\varepsilon}_z=\bar{\gamma}_{xz}=\bar{\gamma}_{yz}=0$

5.4 Finite element model of RV

The strain vector at any point within the RV can be written as,

$$\{\varepsilon\} = \{\varepsilon_x \quad \varepsilon_y \quad \varepsilon_z \quad \gamma_{yz} \quad \gamma_{xz} \quad \gamma_{xy}\}^{\mathrm{T}} \tag{5.14}$$

and the strain displacement relation is,

$$\varepsilon_x = \frac{\partial u}{\partial x}, \quad \varepsilon_y = \frac{\partial v}{\partial y},$$

$$\varepsilon_z = \frac{\partial w}{\partial z}, \quad \gamma_{xy} = \left(\frac{\partial u}{\partial y} + \frac{\partial v}{\partial x}\right),$$

$$\gamma_{xz} = \left(\frac{\partial u}{\partial z} + \frac{\partial w}{\partial x}\right), \quad \gamma_{yz} = \left(\frac{\partial v}{\partial z} + \frac{\partial w}{\partial y}\right) \tag{5.14a}$$

where, ε_x, ε_y and ε_z are the normal strains along x, y and z directions, respectively; γ_{xz} and γ_{yz} are the transverse shear strains in the xz and yz-planes, respectively; γ_{xy} is the in-plane shear strain in the xy plane.

$u(x,y,z)$, $v(x,y,z)$, $w(x,y,z)$ are the displacements at any point in the RV along x, y and z directions, respectively.

Similar to the strain vector (Eq. (5.14)), the stress vector at any point within the RV can be written as,

$$\{\sigma\} = \{\sigma_x \quad \sigma_y \quad \sigma_z \quad \tau_{yz} \quad \tau_{xz} \quad \tau_{xy}\}^{\mathrm{T}} \tag{5.15}$$

where, σ_x, σ_y and σ_z are the normal stresses along x, y and z directions, respectively; τ_{xz} and τ_{yz} are the transverse shear stresses in the xz and yz-planes, respectively; τ_{xy} is the in-plane shear stress in the xy-plane.

The displacement components (u, v and w) at any point within the RV can be expressed in the form of a displacement vector ($\{\tilde{d}\}$) as follows,

$$\left\{\tilde{d}\right\} = \{u \quad v \quad w\}^{\mathrm{T}} \tag{5.16}$$

Substituting Eq. (5.16) in Eq. (5.14), the strain vector ($\{\varepsilon\}$) at any point within the RV can be expressed as follows,

$$\{\varepsilon\} = [L]\{\tilde{d}\}$$

$$[L] = \begin{bmatrix} \frac{\partial}{\partial x} & 0 & 0 & 0 & \frac{\partial}{\partial z} & \frac{\partial}{\partial y} \\ 0 & \frac{\partial}{\partial y} & 0 & \frac{\partial}{\partial z} & 0 & \frac{\partial}{\partial x} \\ 0 & 0 & \frac{\partial}{\partial z} & \frac{\partial}{\partial y} & \frac{\partial}{\partial x} & 0 \end{bmatrix}^{\mathrm{T}} \tag{5.17}$$

The constitutive relations for fiber and matrix phases within the RV can be written as,

$$\{\sigma^s\} = [C^s]\{\varepsilon^s\}, \ s = 1,2 \tag{5.18}$$

where, the superscript s denotes fiber or matrix phase according to its value as 1 or 2, respectively; the matrix ($[C^s]$) is the stiffness matrix for fiber or matrix phase. The first variation of strain energy (δU) of RV can be expressed as,

$$\delta U = \sum_{s=1}^{2} \int_{V_s} \{\delta\varepsilon^s\}^{\mathrm{T}} \{\sigma^s\} dV_s \tag{5.19}$$

where, δ is an operator for first variation; V_s is the volume of fiber ($s=1$) or matrix ($s=2$) phase.

Using Eqs. (5.17)-(5.18) in Eq. (5.19), the first variation of strain energy (δU) can be written as,

$$\delta U = \sum_{s=1}^{2} \int_{V_s} \{\delta d\}^{\mathrm{T}} [L]^{\mathrm{T}} [C^s][L]\{d\} dV_s \tag{5.20}$$

For deriving FE model of RV, its volume is discretized using 27-node isoparametric hexahedral element. The displacement vector ($\{\tilde{d}\}$) for i^{th} node of an element can be expressed as,

$$\{\tilde{d}_i\} = \{u_i \quad v_i \quad w_i\}^{\mathrm{T}}, \ i = 1,2,3...,27 \tag{5.21}$$

The displacement vector at any point within a typical element can be written as,

$$\left\{\tilde{d}\right\} = \left[\tilde{N}\right]\left\{\tilde{d}^e\right\} \tag{5.22}$$

where, $[\tilde{N}]$ is the shape function matrix and $\{\tilde{d}^e\}$ is the elemental nodal displacement vector. Using Eq. (5.22) in Eq. (5.20), the simplified expression for the first variation of strain energy (δU^e) of a typical element can be written as,

$$\delta U^e = \left\{\delta\tilde{d}^e\right\}^{\mathrm{T}}\left[K^e\right]\left\{\tilde{d}^e\right\} \tag{5.23}$$

where,

$$\left[K^e\right] = \int_{V_s^e}\left(\left[\tilde{N}\right]^{\mathrm{T}}[L]^{\mathrm{T}}\left[C^s\right][L]\left[\tilde{N}\right]\right)dV_s^e \tag{5.23a}$$

where, V_s^e is the elemental volume within fiber (s = 1) or matrix (s = 2) phase volume. Upon assembling the elemental equations (Eq. (5.23)) into the global space, the global expression for the first variation of strain energy can be obtained as,

$$\delta U = \left\{\delta\tilde{X}\right\}^{\mathrm{T}}[K]\left\{\tilde{X}\right\} \tag{5.24}$$

where, $[K]$ is the global stiffness matrix; $\{\tilde{X}\}$ is the global nodal displacement vector. The specified nodal displacements over the boundary surfaces of RV could be incorporated in the expression of strain energy (Eq. (5.24)) following a simple procedure as demonstrated by Cook et al. (2003). For a specified nodal displacement (say, $\tilde{X}_j$ element of $\{\tilde{X}\}$), the first variation of the corresponding element ($\tilde{X}_j$) of the global nodal displacement vector ($\{\tilde{X}\}$) is equal to zero ($\delta\tilde{X}_j = 0$). So, the j^{th} row of $[K]$ is to be deleted and a column of $[K]$ with the same index (j) (say, $\{f_j\}$) is also to be removed for constituting the displacement load vector as follows,

$$\delta U = \left\{\delta\tilde{X}_r\right\}^{\mathrm{T}}\left(\left[K_r\right]\left\{\tilde{X}_r\right\} + \{f_j\}\tilde{X}_j\right) \tag{5.25}$$

In Eq. (5.25), $[K_r]$ and $\{\tilde{X}_r\}$ are the resulting global stiffness matrix and global nodal displacement vector after imposition of specified nodal displacement ($\tilde{X}_j$). Equation (5.25) can also be written in generalized form when a number of nodal displacements (N_d) are specified as,

$$\delta U = \left\{\delta \tilde{X}_r\right\}^{\mathrm{T}} \left([K_r] \left\{\tilde{X}_r\right\} - \{P\} \right) \tag{5.26}$$

where,

$$\{P\} = -\sum_{j=1}^{N_d} \{f_j\} \tilde{X}_j \tag{5.26a}$$

According to the principle of minimum potential energy ($\delta U = 0$), the following governing equations of equilibrium can be obtained as,

$$[K_r]\{\tilde{X}_r\} = \{P\} \tag{5.27}$$

For the specified displacement boundary conditions (Table 5.1) over the boundary surfaces of the RV, the corresponding displacement field can be obtained by the solution of Eq. (5.27). Utilizing this displacement field, the volume-average strain vectors of RV, layers and fiber phase of a layer can be computed using Eqs. (5.13a-b).

5.5 Finite element formulation for graded laminated composite plate

The main objective in the design of present graded fiber-reinforced composite lamina is to utilize it for reducing the mismatch of material properties and stresses at the inter-surfaces of plies in laminated composite structures. In order to substantiate this intent, a bending analysis of laminated composite plates comprised of presently designed graded composite plies is performed. Since a higher side-to-thickness ratio for laminated composite plates is considered in the present analysis, geometrically nonlinear bending analysis of the plates is carried out using FE procedure.

Figure 5.3 shows a laminated composite plate. The length, width and height of the plate are denoted by a, b and h, respectively. Unless otherwise mentioned, the plies are of uniform thickness. The middle plane of the plate is considered as the reference plane and a corner of this plane is the origin of the reference coordinate system ($oxyz$) (Fig. 5.3). Since a thin laminated plate is considered, the kinematics of deformation of the overall plate is defined according to the first order shear deformation theory (FSDT) as given in Eq. 2.8 with a shear correction factor as 5/6 (Reddy 2003) Equation 2.8 can be rewritten as,

$$u(x,y,z,t) = u_0(x,y,t) + z\theta_x(x,y,t),$$

$$v(x,y,z,t) = v_0(x,y,t) + z\theta_y(x,y,t),$$

$$w(x,y,z,t) = w_0(x,y,t) \tag{2.8}$$

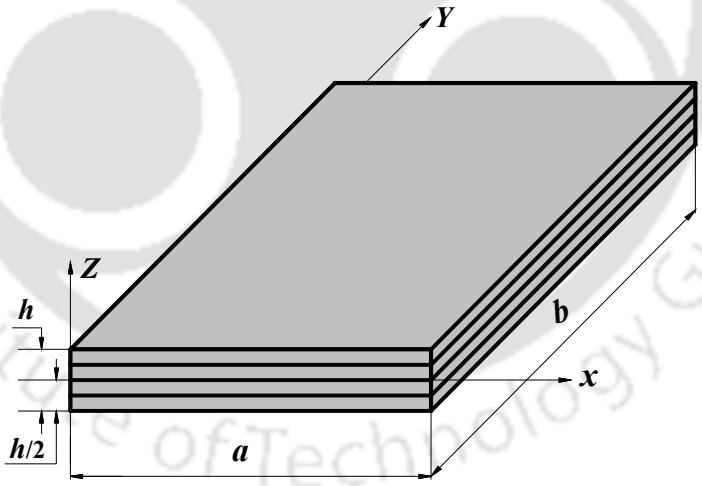

Fig. 5.3 Schematic diagram of a laminated graded composite plate.

According to this displacement field (FSDT) and von Karman nonlinear strain-displacement relations, the strain vectors and its first variation can be written as,

$$\{\varepsilon_b\} = ([L_b^L] + [L_N] + z[L_\kappa])\{d\}\,,\ \{\varepsilon_s\} = [L_s]\{d\}$$

$$\{\delta\varepsilon_b\} = ([L_b^L] + [L_N^d] + z[L_\kappa])\{\delta d\}\,,\ \{\delta\varepsilon_s\} = [L_s]\{\delta d\} \tag{5.28}$$

where,

$$[L_b^L] = \begin{bmatrix} \frac{\partial}{\partial x} & 0 & 0 & 0 & 0 \\ 0 & \frac{\partial}{\partial y} & 0 & 0 & 0 \\ \frac{\partial}{\partial y} & \frac{\partial}{\partial x} & 0 & 0 & 0 \end{bmatrix},$$

$$[L_N] = \begin{bmatrix} 0 & 0 & \frac{1}{2}\frac{\partial w}{\partial x}\frac{\partial}{\partial x} & 0 & 0 \\ 0 & 0 & \frac{1}{2}\frac{\partial w}{\partial y}\frac{\partial}{\partial y} & 0 & 0 \\ 0 & 0 & \frac{\partial w}{\partial x}\frac{\partial}{\partial y} & 0 & 0 \end{bmatrix},$$

$$[L_\kappa] = \begin{bmatrix} 0 & 0 & 0 & \frac{\partial}{\partial x} & 0 \\ 0 & 0 & 0 & 0 & \frac{\partial}{\partial y} \\ 0 & 0 & 0 & \frac{\partial}{\partial y} & \frac{\partial}{\partial x} \end{bmatrix},$$

$$[L_N^d] = \begin{bmatrix} 0 & 0 & \frac{\partial w}{\partial x}\frac{\partial}{\partial x} & 0 & 0 \\ 0 & 0 & \frac{\partial w}{\partial y}\frac{\partial}{\partial y} & 0 & 0 \\ 0 & 0 & \frac{\partial w}{\partial x}\frac{\partial}{\partial y} + \frac{\partial w}{\partial y}\frac{\partial}{\partial x} & 0 & 0 \end{bmatrix},$$

$$[L_s] = \begin{bmatrix} 0 & 0 & \frac{\partial}{\partial y} & 0 & 1 \\ 0 & 0 & \frac{\partial}{\partial x} & 1 & 0 \end{bmatrix} \tag{5.28a}$$

In Eq. (5.28), $\{d\}$ is the generalized displacement vector as given in Eq. (2.9) and repeated here as follows,

$$\{d\} = [u_0 \quad v_0 \quad w_0 \quad \theta_x \quad \theta_y]^{\mathrm{T}} \tag{2.9}$$

Since the material properties of graded composite plies vary along the thickness direction (z), their stiffness coefficients can be expressed as the functions of thickness-coordinate (z). Accordingly, the constitutive relations for a graded composite ply can be written as,

$$\{\sigma_b^k\} = [\bar{C}_b^k(z)]\{\varepsilon_b^k\},$$

$$\{\sigma_s^k\} = [\bar{C}_s^k(z)]\{\varepsilon_s^k\}, \qquad k = 1, 2, 3, \ldots\ldots N_p$$

where,

$$[\bar{C}_b^k(z)] = \begin{bmatrix} \bar{c}_{11}^k(z) & \bar{c}_{12}^k(z) & \bar{c}_{16}^k(z) \\ \bar{c}_{12}^k(z) & \bar{c}_{22}^k(z) & \bar{c}_{26}^k(z) \\ \bar{c}_{16}^k(z) & \bar{c}_{26}^k(z) & \bar{c}_{66}^k(z) \end{bmatrix},$$

$$[\bar{C}_s^k(z)] = \begin{bmatrix} \bar{c}_{44}^k(z) & \bar{c}_{45}^k(z) \\ \bar{c}_{45}^k(z) & \bar{c}_{55}^k(z) \end{bmatrix} \tag{5.29}$$

where, the superscript k denotes a particular ply within the laminate. N_p is the total number of plies. $[\bar{C}_b^k(z)]$ and $[\bar{C}_s^k(z)]$ are the transformed stiffness matrices of k^{th}-ply with respect to the reference coordinate system (xyz).

For an applied uniformly distributed transverse mechanical load of intensity, p, the first variation of the total potential energy (δT_p) of the laminated composite plate can be written as,

$$\delta T_p = \int_0^a \int_0^b \left[\sum_{k=1}^{N_p} \int_{h_k}^{h_{k+1}} \left(\{\delta\varepsilon_b^k\}^{\mathrm{T}} \{\sigma_b^k\} + \{\delta\varepsilon_s^k\}^{\mathrm{T}} \{\sigma_s^k\} \right) dz - (\delta\tilde{w}\, p) \right] dy dx \tag{5.30}$$

Substituting Eqs. (5.28)-(5.29) in Eq. (5.30), the following expression for δT_p can be obtained,

$$\delta T_p = \int_0^a \int_0^b \begin{bmatrix} \{\delta\tilde{d}\}^{\mathrm{T}} \left\langle ([L_{bL}]^{\mathrm{T}} + [L_N^d]^{\mathrm{T}})\,[A_b]([L_{bL}] + [L_N]) + [L_\kappa]^{\mathrm{T}}[B]([L_{bL}] + [L_N]) + \right. \\ \left. ([L_{bL}]^{\mathrm{T}} + [L_N^d]^{\mathrm{T}})[B][L_\kappa] + [L_\kappa]^{\mathrm{T}}[D][L_\kappa] + [L_s]^{\mathrm{T}}[A_s][L_s] \right\rangle \{\tilde{d}\} - \langle \delta\tilde{w}\, p \rangle \end{bmatrix} dydx \tag{5.31}$$

In Eq. (5.31), the rigidity matrices ($[A_b], [A_s], [B], [D]$) are given by,

$$[A_b] = \sum_{k=1}^{N_p} \int_{h_k}^{h_{k+1}} [\bar{C}_b^k(z)]dz,$$

$$[A_s] = \sum_{k=1}^{N_p} \int_{h_k}^{h_{k+1}} [\bar{C}_s^k(z)]dz,$$

$$[B] = \sum_{k=1}^{N_p} \int_{h_k}^{h_{k+1}} [\bar{C}_b^k(z)]z dz,$$

$$[D] = \sum_{k=1}^{N_p} \int_{h_k}^{h_{k+1}} [\bar{C}_b^k(z)]z^2 dz \tag{5.32}$$

where, h_k and h_{k+1} are the thickness (z)-coordinates of the bottom and top surfaces of k^{th} ply, respectively. For deriving FE model of the plate, the xy-plane of the plate is discreatized using 9-node isoparametric quadrilateral element. Correspondingly, the generalized displacement vector (Eq. (2.9)) within a typical element can be written according to Eq. (2.21) ($\{d\} = [N]\{d^e\}$). Employing the principle of minimum potential energy ($\delta T_p = 0$) after the substitution of Eq. (2.21) in Eq. (5.31), the equilibrium equations for a typical element can be obtained as,

$$\left([K_L^e] + [K_N^e]\right)\{d^e\} = \{P^e\} \tag{5.33}$$

where,

$$[K_L^e] = [K_{Lb}^e] + [K_{Ls}^e],$$

$$[K_{Ls}^e] = \int_{A_e} \left([B_s]^{\mathrm{T}}[A_s][B_s]\right) dA_e,$$

$$[K_{Lb}^e] = \int_{A_e} \left([B_b^L]^{\mathrm{T}} \left\langle [A_b][B_b^L] + [B][B_\kappa] \right\rangle + [B_\kappa]^{\mathrm{T}} \left\langle [B][B_b^L] + [D][B_\kappa] \right\rangle\right) dA_e,$$

$$[K_N^e] = \int_{A_e} \left(\left\langle [B_b^L]^{\mathrm{T}} [A_b] + [B_\kappa]^{\mathrm{T}} [B] \right\rangle [B_N] + [B_N^d]^{\mathrm{T}} \left\langle [A_b][B_b^L] + [B][B_\kappa] \right\rangle \right) dA_e ,$$

$$\{P^e\} = \int_{A_e} \left([N]^{\mathrm{T}} [0 \quad 0 \quad p \quad 0 \quad 0]^{\mathrm{T}} \right) dA_e$$

(5.33a)

In Eq. (5.33a), A_e is the area of a typical element in the xy-plane; $[K_L^e]$ and $[K_N^e]$ are the linear and nonlinear counterparts of the elemental stiffness matrix; $[K_{Lb}^e]$ and $[K_{Ls}^e]$ are the bending and shear counterparts of the linear elemental stiffness matrix ($[K_L^e]$); $\{P\}$ is the elemental nodal load vector. The forms of different strain-displacement matrices appearing in Eq. (5.33a) are similar to those given in Eq. (2.23) where the operator matrices ($[L_b^L]$, $[L_N]$, $[L_s]$, $[L_\kappa]$, $[L_N^d]$) are defined in Eq. (5.28a). In the present formulation, since the bending ($[K_{Lb}^e]$) and shear ($[K_{Ls}^e]$) counterparts of the linear stiffness matrix ($[K_L^e]$) are separately formulated, the selective integration can be implemented in a straight forward manner. Assembling the elemental equations (Eq. (5.33)) in the global space, the global nonlinear FE equations of equilibrium of the laminated composite plate under the uniformly distributed transverse mechanical load can be obtained as,

$$\left([K_L] + [K_N] \right) \{X\} = \{P\} \tag{5.34}$$

where, $[K_L]$ and $[K_N]$ are the linear and nonlinear counterparts of the global stiffness matrix; $\{P\}$ is the global nodal load vector; $\{X\}$ is the global nodal displacement vector.

5.6 Numerical results and discussions

In this section, first the effective elastic properties of the present graded fiber-reinforced composite lamina are evaluated using the present FE model of RV and appropriate boundary conditions (Table 5.1). Next, the geometrically nonlinear bending responses of laminated composite plates are evaluated for the use of presently designed graded composite plies. The merits and demerits in the use of graded composite ply within the

laminated composite plates are discussed. Finally, the demerits are eliminated through the proposition of a new lamination scheme utilizing presently designed graded composite ply as well as conventional composite ply.

5.6.1 Verification of present finite element model of RV

Since a similar graded fiber-reinforced composite lamina is not available in the literature, the present FE model of RV and boundary conditions (Table 5.1) are verified considering uniform FVF ($v_f = 0.6$) for all fiber-matrix packs/layers within the RV.

Table 5.2 Comparison of elastic constants obtained from present analysis for a lamina (AS4/3501-6 unidirectional continuous fiber reinforced composite, $v_f = 0.6$) with the similar published results

Elastic constants (GPa)	Present results	Analytical results (Sun and Chen 1990)	Analytical results (Chamis 1984)	Analytical results (Reley and Whitney 1966)	Experimental results (Daniel and Lee 1990)	Experimental results (Sun and Chen 1988)
E_1	142.60	142.9	142.9	142.9	142	139
E_2	9.51	9.20	9.79	9.78	10.30	9.85
G_{12}	5.92	5.50	6.53	5.80	7.60	5.25
G_{23}	3.05	___	3.01	___	3.8	___
ν_{12}	0.25	0.26	0.26	0.25	___	0.3
ν_{23}	0.38	___	0.42	___	___	___

The computed effective elastic coefficients are compared with similar elastic coefficients of an identical unidirectional fiber-reinforced composite analyzed by earlier researchers (Reley and Whitney 1966; Chamis 1984; Sun and Chen 1988, 1990; Daniel and Lee 1990). This comparison is illustrated in Table 5.2. It may be observed from Table 5.2 that the present results are in good agreement with the available analytical results (Reley and Whitney 1966; Chamis 1984; Sun and Chen 1990) and experimental results (Sun and Chen 1988; Daniel and Lee 1990). Thus, the accuracy of present FE model of RV and the

appropriateness of boundary conditions (Table 5.1) used in prediction of effective elastic coefficients of fiber-reinforced composites are verified.

5.6.2 Effective elastic properties of graded composite lamina

In the present composite lamina, the materials for the matrix and fiber phases are considered as Epoxy ($E=$ 3.5 GPa, $\nu=$ 0.35) and high modulus glass ($E=110$ GPa, $\nu=0.22$), respectively (Jones 1999). The continuous variation of FVF across the thickness of the composite lamina according to a simple power-law can be defined as,

$$v_f = v_f^m \left(1+(-1)^{\lambda} \times \left(\frac{2z}{h_c}\right)\right)^n \tag{5.35}$$

where, the maximum value of FVF (v_f^m) is considered at the middle plane ($z=0$) of the lamina and the minimum value of the same (v_f) is considered as zero at the top/bottom surface of the lamina; n is the power-law exponent ($0 \le n \le \infty$); λ is a positive integer.

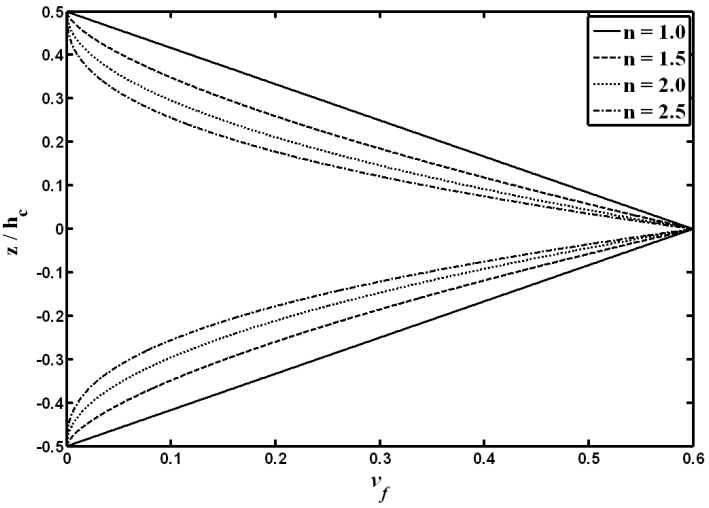

Fig. 5.4 Variations of FVF (v_f) across the thickness of composite lamina for different values of power-law exponent (n).

The variation of v_f along the thickness direction is symmetric with respect to the middle plane ($z=0$) of the lamina and this variation along the positive or the negative z-direction from the middle plane ($z=0$) can be obtained by even or odd value of λ, respectively. According to this power-law, the variations of FVF (v_f) for different values of power-law exponent (n) are illustrated in Fig. 5.4. The maximum FVF (v_f^m) at the middle plane ($z=0$) is considered as 0.6 for any value of n. So, the FVF of the middle layer ($\ell = (N_c+1)$, Fig. 5.4) remains constant as 0.6

for any value of n. Except the middle layer, the FVF of any layer decreases with the increase of the power-law exponent (n) (Fig. 5.4). In order to reduce the difference of the magnitudes of various elastic coefficients at the top/bottom surface of the composite

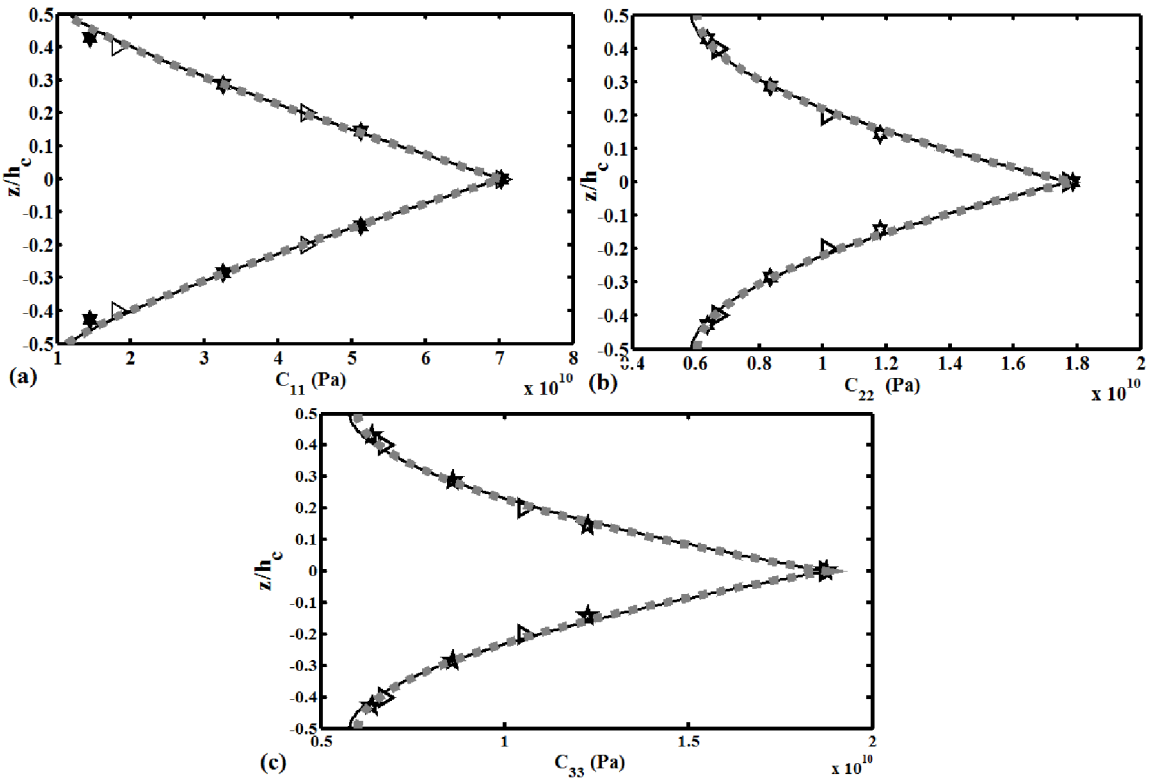

Fig. 5.5 Effective elastic coefficients $(c_{11}^{\ell}, c_{22}^{\ell}, c_{33}^{\ell})$ of different homogeneous layers in RV and the corresponding fitted curves ($N_t = 5$ or 7, $\triangleright : C_{ij}^{\ell}$ for $N_t = 5$, — $: C_{ij}^{\ell}$ -fitted curve for $N_t = 5$, ★ $: C_{ij}^{\ell}$ for $N_t = 7$, ▪▪ $: C_{ij}^{\ell}$ -fitted curve for $N_t = 7$).

lamina, lower value of FVF in the top ($\ell = (2N_c + 1)$)/bottom ($\ell = 1$) layer is desired. This requirement could be attained by considering higher value of n (Fig. 5.4). However, the value of n and the total number of layers within a specified thickness of composite lamina are important factors according to the practical design-aspects of the composite lamina. For a high value of n, the top/bottom layer ($\ell = 1$ or $(2N_c + 1)$) has very low value of FVF that may cause difficulties in fabrication of the graded composite lamina.

For a constant value of n, similar difficulties may arise when the number of layers increases within a specified thickness of the lamina. Although these aspects are to be taken care in practice, the present theoretical study is carried out considering the maximum value of n as 2.0 and the maximum number of layers $(2N_c+1)$ as 7 within a constant thickness (350 μm) of composite lamina.

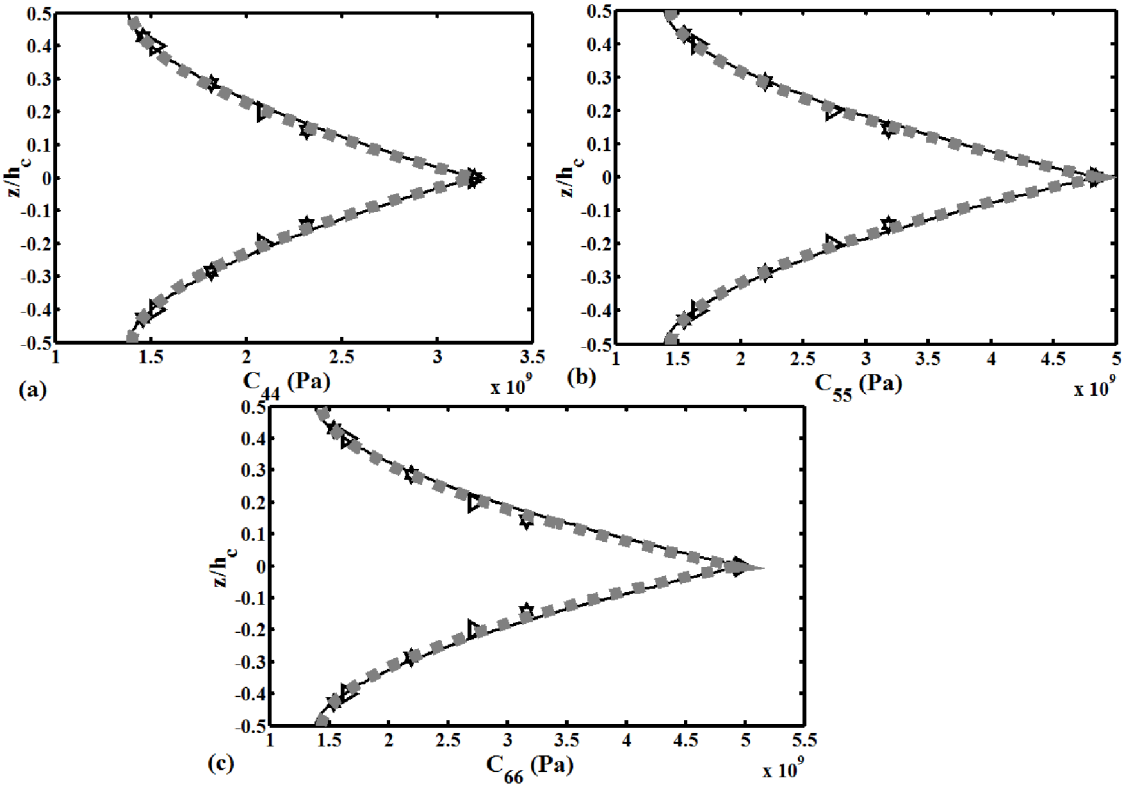

Fig. 5.6 Effective elastic coefficients $(c_{44}^{\ell}, c_{55}^{\ell}, c_{66}^{\ell})$ of different homogeneous layers in RV and the corresponding fitted curves ($N_t=5$ or 7, $\triangleright: C_{ij}^{\ell}$ for $N_t=5$, — $: C_{ij}^{\ell}$ -fitted curve for $N_t=5$, ★ $: C_{ij}^{\ell}$ for $N_t=7$, ▪▪▪ $: C_{ij}^{\ell}$ -fitted curve for $N_t=7$).

For a particular value of power-law exponent $(n=1)$, Figs. 5.5-5.7 illustrate the effective elastic coefficients (c_{ij}^{k}) of different homogeneous layers within the RV. The total number of layers is considered as either five $(N_t=5)$ or seven $(N_t=7)$ within a constant thickness of RV. In these figures (Figs. 5.5-5.7), the computed magnitude of a coefficient for a homogeneous layer is plotted corresponding to the z-coordinate of its

(layer) centre. For any of the two cases ($N_t = 5$ or 7), it may be observed from these figures that the nature of variation of a coefficient along the thickness (z) direction is similar to that of FVF. So, for the sake of simplicity in its (graded lamina) macroscopic applications, the continuous variation of every coefficient along the thickness (z) direction is assumed and it is modeled by a power-law as follows,

$$C_{ij}(z) = \left(C_{ij}^{max} - C_{ij}^{min}\right) \times \left\{1 + (-1)^{\lambda} \times \left(\frac{2z}{h_c}\right)\right\}^{n_c} + C_{ij}^{min} \qquad (5.36)$$

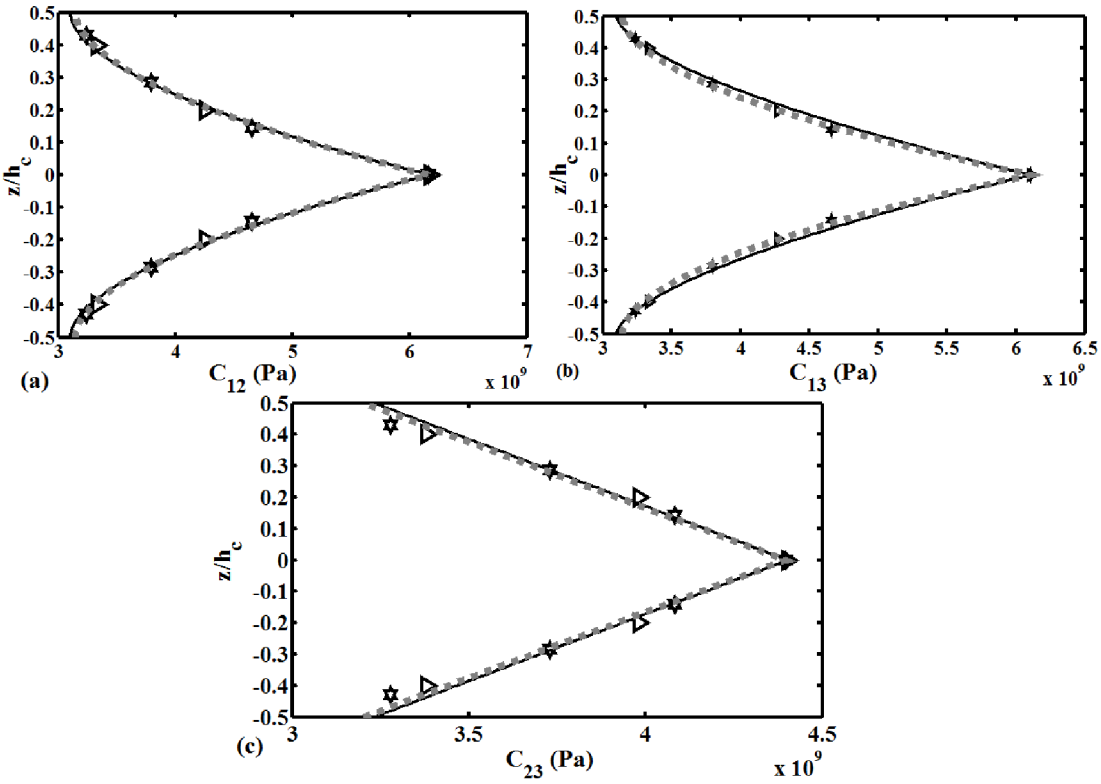

Fig. 5.7 Effective elastic coefficients $(c_{12}^{\ell}, c_{13}^{\ell}, c_{23}^{\ell})$ of different homogeneous layers in RV and the corresponding fitted curves ($N_t = 5$ or 7, $\triangleright : C_{ij}^{\ell}$ for $N_t = 5$, — $: C_{ij}^{\ell}$ -fitted curve for $N_t = 5$, ✸ $: C_{ij}^{\ell}$ for $N_t = 7$, ▪▪ $: C_{ij}^{\ell}$ -fitted curve for $N_t = 7$).

where, C_{ij}^{max} and C_{ij}^{min} are maximum and minimum values of a coefficient (C_{ij}), respectively. n_c is the power-law exponent that determines the shape of the fitted curve

through the computed magnitudes of a coefficient for different homogeneous layers of RV. According to the aforesaid power-law (Eq. (5.36)), the fitted curves for all coefficients are shown in the same figures (Figs. 5.5-5.7) and the corresponding parameters ($C_{ij}^{\max}, C_{ij}^{\min}, n_c$) are furnished in Table 5.3. For constant values of n and thickness (h) of RV, Figs. 5.5-5.7 demonstrate an important observation that the nature of variation of a coefficient does not depend on the total number (N_t) of layers within the RV. Therefore, the increased number of layers within a specified thickness of RV is required mainly for alleviating the flaw in the assumption of continuous variations of coefficients.

Table 5.3 $C_{ij}^{\max}, C_{ij}^{\min}$ and n_c corresponding to the fitted curves in Figs. 5.5-5.7 according to the power-law (Eq. (5.36))

C_{ij}	$C_{ij}^{\max}(\times 10\ GPa)$		$C_{ij}^{\min}(\times 10\ GPa)$		n_c	
	$N_t = 5$	$N_t = 7$	$N_t = 5$	$N_t = 7$	$N_t = 5$	$N_t = 7$
C_{11}	7.0304	7.0275	1.1642	1.1450	1.20	1.20
C_{22}	1.7723	1.7868	0.58576	0.60412	1.80	1.90
C_{33}	1.8725	1.8747	0.57722	0.60057	1.80	1.90
C_{44}	0.31938	0.31936	0.13838	0.14016	1.67	1.80
C_{55}	0.48418	0.48416	0.13922	0.14390	1.67	1.80
C_{66}	0.49643	0.49119	0.13879	0.14380	1.67	1.80
C_{12}	0.61747	0.61604	0.31027	0.31464	1.80	1.85
C_{13}	0.61945	0.61082	0.31017	0.31451	1.60	1.85
C_{23}	0.44026	0.43962	0.32318	0.32027	1.00	1.00

For different values of n, the variations of effective elastic coefficients across the thickness of RV ($N_t = 7$) are illustrated in Figs. 5.8-5.10. The magnitudes of the parameters ($C_{ij}^{\max}$, $C_{ij}^{\min}, n_c$) corresponding to the fitted curves (Figs. 5.8-5.10) are also

illustrated in Table 5.4. It may be observed from Figs. 5.8-5.10 that every coefficient (c_{ij}) has its maximum magnitude at the middle layer for any value of n. Moreover, this maximum magnitude does not vary with n because of the constant value of FVF at the middle layer. Except the middle layer, the magnitudes of effective coefficients (C_{ij}) of any layer decrease for the increase of power-law exponent (n).

However, Figs. 5.8-5.10 and Table 5.4 illustrate an important observation that the increasing value of n yields the reduction in the difference between the magnitudes of two coefficients like (C_{11} and C_{22}) or (C_{44} and C_{55}) or (C_{12} and C_{23}) at the top/bottom layer of RV. The magnitudes of these pairs of coefficients at the top/bottom layer of RV may also be almost equal ($C_{11} \approx C_{22}$, $C_{44} \approx C_{55}$, $C_{12} \approx C_{23}$) for certain value of n as it is 2.0 at present case ($C_{ij}^{\min}$, $n = 2.0$, Table 5.4). However, this reduced mismatch among the magnitudes of material constants at the top/bottom surface of graded composite lamina is a useful fact for accomplishing continuous variations of material properties and stresses across the thickness of composite laminates as it is shown in later section.

Table 5.4 $C_{ij}^{\max}$, $C_{ij}^{\min}$ and n_c corresponding to the fitted curves in Figs. 5.8-5.10 according to the power-law (Eq. (5.36))

C_{ij}	$C_{ij}^{\max}(\times 10\,GPa)$			$C_{ij}^{\min}(\times 10\,GPa)$			n_c		
	n = 1.0	n = 1.5	n = 2.0	n = 1.0	n = 1.5	n = 2.0	n = 1.0	n = 1.5	n = 2.0
C_{11}	7.0275	7.0300	7.0331	1.1450	0.66247	0.52100	1.20	1.55	1.90
C_{22}	1.7868	1.7756	1.7672	0.60412	0.56701	0.54300	1.90	2.5	3.40
C_{33}	1.8747	1.8728	1.8710	0.60057	0.56529	0.54400	1.90	2.50	3.40
C_{44}	0.31936	0.31937	0.31642	0.14016	0.13165	0.13050	1.80	2.25	2.90
C_{55}	0.48416	0.48422	0.48435	0.14390	0.13136	0.12900	1.80	2.40	3.10
C_{66}	0.49119	0.49628	0.50054	0.14380	0.13133	0.12900	1.80	2.40	3.25
C_{12}	0.61604	0.61751	0.61837	0.31461	0.30393	0.30138	1.85	2.30	3.25
C_{13}	0.61082	0.61053	0.61053	0.31451	0.30387	0.30117	1.85	2.30	3.20
C_{23}	0.43962	0.44016	0.44197	0.32027	0.30550	0.30132	1.0	1.23	1.60

In the foregoing estimation of effective elastic properties of present graded fiber-reinforced composite lamina, the homogeneous layers are considered to be coupled within the RV. The importance of this consideration (coupled layers) can be verified through a parallel estimation of effective properties of every homogeneous layer in RV by taking it (layer) as a discrete representative volume element (RVE). For every layer of RV ($N_t = 7$), Table 5.5 illustrates the magnitudes of effective elastic coefficients (C_{ij}) which are predicted either for coupled (C) layers or for decoupled/discrete (DC) layers. It may be observed from Table 5.5 that a little difference between these two considerations (C and DC) occurs for the inner layers ($\ell = 3, 4, 5$). Thus, this result suggests that any of the approaches (C/DC) could be followed in estimation of effective graded elastic properties of present graded fiber-reinforced composite.

Table 5.5 Magnitudes of effective elastic coefficients (C_{ij}) predicted either for coupled (C) layers or for decoupled/discrete (DC) layers ($N_t = 7$, $n = 1$)

C_{ij} (×10 GPa)		$k=1$	$k=2$	$k=3$	$k=4$	$k=5$	$k=6$	$k=7$
C_{11}	C	1.481	3.319	5.159	7.012	5.159	3.319	1.481
	DC	1.481	3.325	5.221	7.065	5.221	3.325	1.481
C_{22}	C	0.640	0.797	0.954	1.111	0.954	0.797	0.640
	DC	0.639	0.860	1.239	1.876	1.239	0.860	0.639
C_{33}	C	0.639	0.794	0.948	1.103	0.948	0.794	0.639
	DC	0.639	0.860	1.239	1.876	1.239	0.860	0.639
C_{44}	C	0.146	0.180	0.214	0.247	0.214	0.180	0.146
	DC	0.147	0.184	0.238	0.328	0.238	0.184	0.147
C_{55}	C	0.154	0.204	0.254	0.303	0.254	0.204	0.154
	DC	0.155	0.219	0.321	0.483	0.321	0.219	0.155
C_{66}	C	0.154	0.203	0.253	0.302	0.253	0.203	0.154
	DC	0.155	0.219	0.321	0.483	0.321	0.219	0.155
C_{12}	C	0.324	0.366	0.411	0.454	0.411	0.366	0.324
	DC	0.324	0.367	0.468	0.612	0.468	0.367	0.324
C_{13}	C	0.324	0.366	0.410	0.453	0.410	0.366	0.324
	DC	0.324	0.367	0.468	0.612	0.468	0.367	0.324
C_{23}	C	0.326	0.371	0.422	0.470	0.422	0.371	0.326
	DC	0.326	0.374	0.405	0.445	0.405	0.374	0.326

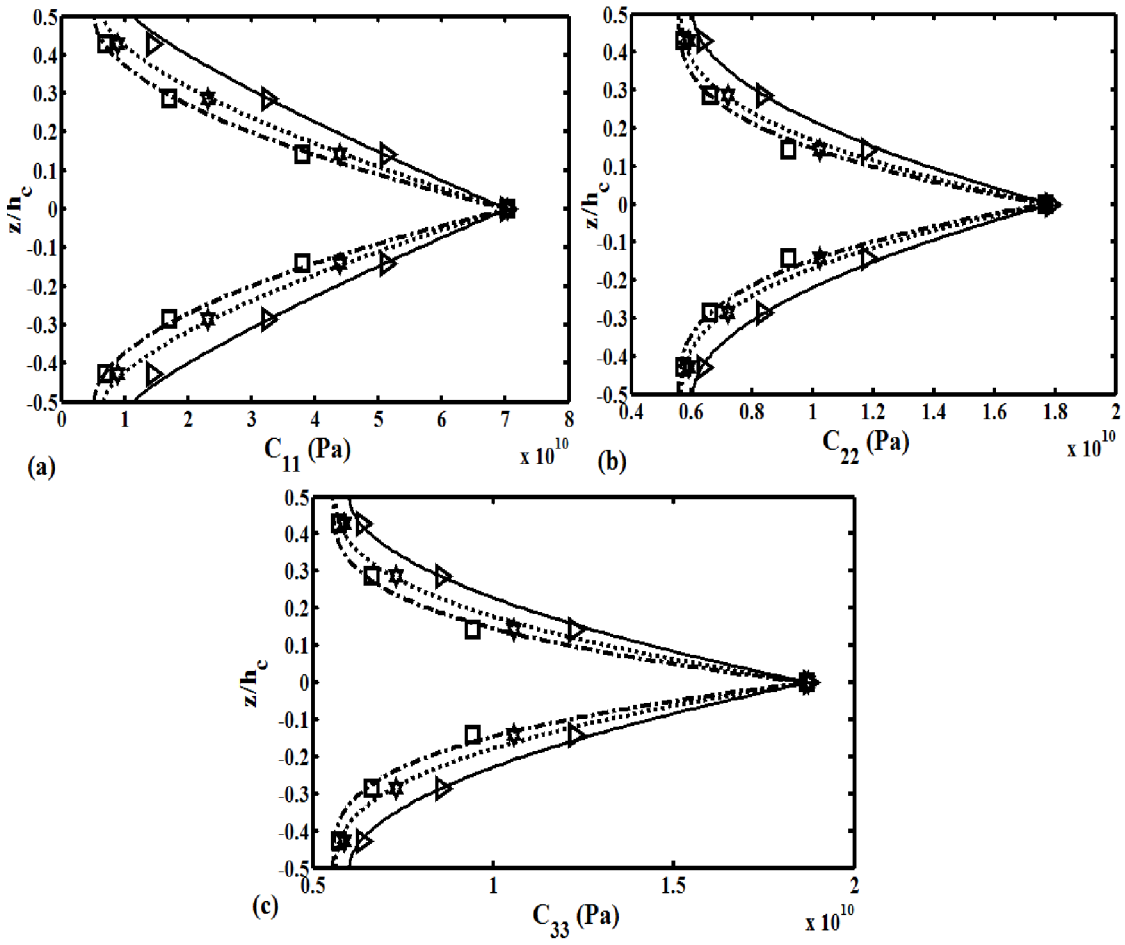

Fig. 5.8 Effective elastic coefficients $(c_{11}^{\ell}, c_{22}^{\ell}, c_{33}^{\ell})$ for different homogeneous layers in RV and the corresponding fitted curves for different values of power-law exponent (n) ($N_t = 7$, $v_f^m = 0.6$, ▷ :C_{ij}^{ℓ} for $n = 1.0$, —:C_{ij}^{ℓ}-fitted curve for $n = 1.0$, ✸ :C_{ij}^{ℓ} for $n = 1.5$, ...:C_{ij}^{ℓ} -fitted curve for $n = 1.5$, □:C_{ij}^{ℓ} for $n = 2.0$, - - -:C_{ij}^{ℓ}-fitted curve for $n = 2.0$).

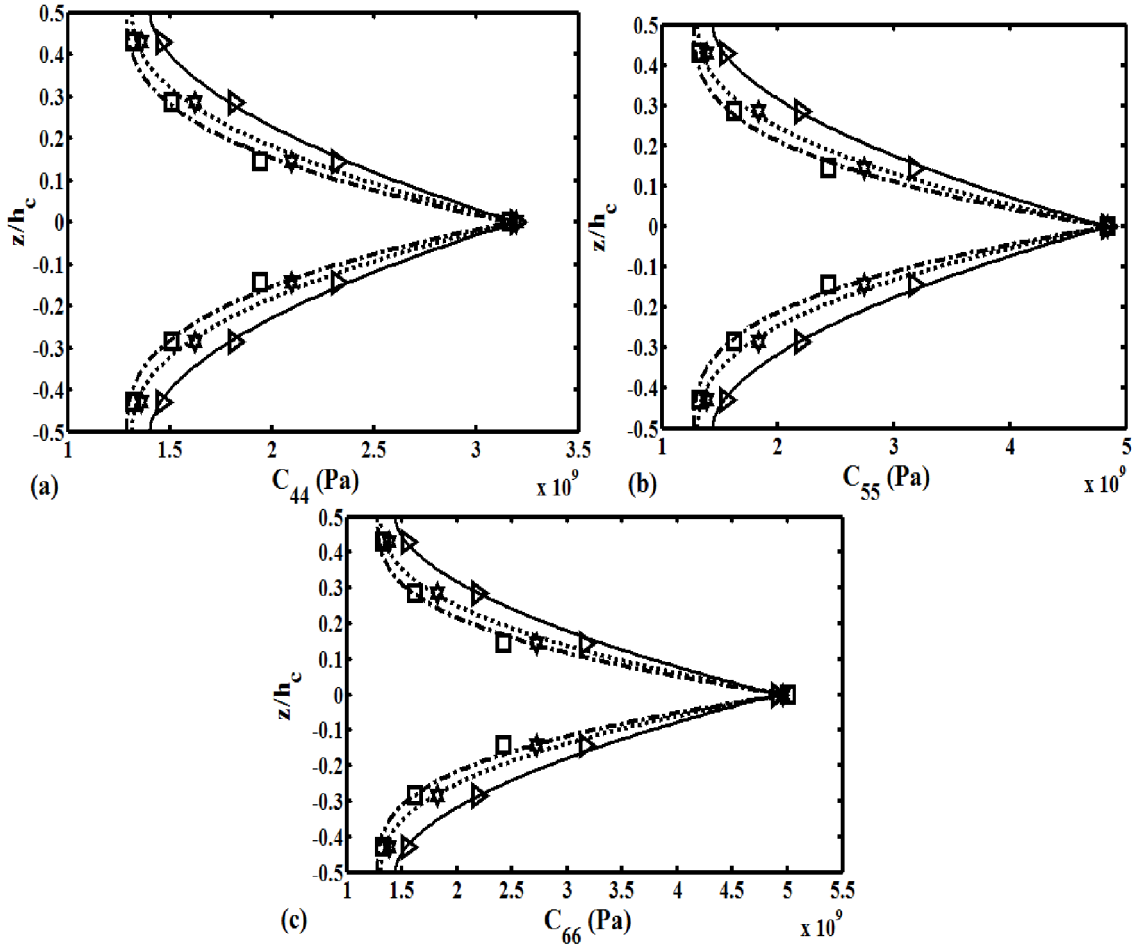

Fig. 5.9 Effective elastic coefficients $(c_{44}^{\ell}, c_{55}^{\ell}, c_{66}^{\ell})$ for different homogeneous layers in RV and the corresponding fitted curves for different values of power-law exponent (n) ($N_t = 7$, $v_f^m = 0.6$, ▷ : C_{ij}^{ℓ} for $n = 1.0$, —: C_{ij}^{ℓ}-fitted curve for $n = 1.0$, ★ : C_{ij}^{ℓ} for $n = 1.5$, ·····: C_{ij}^{ℓ} -fitted curve for $n = 1.5$, □: C_{ij}^{ℓ} for $n = 2.0$, - - -: C_{ij}^{ℓ}-fitted curve for $n = 2.0$).

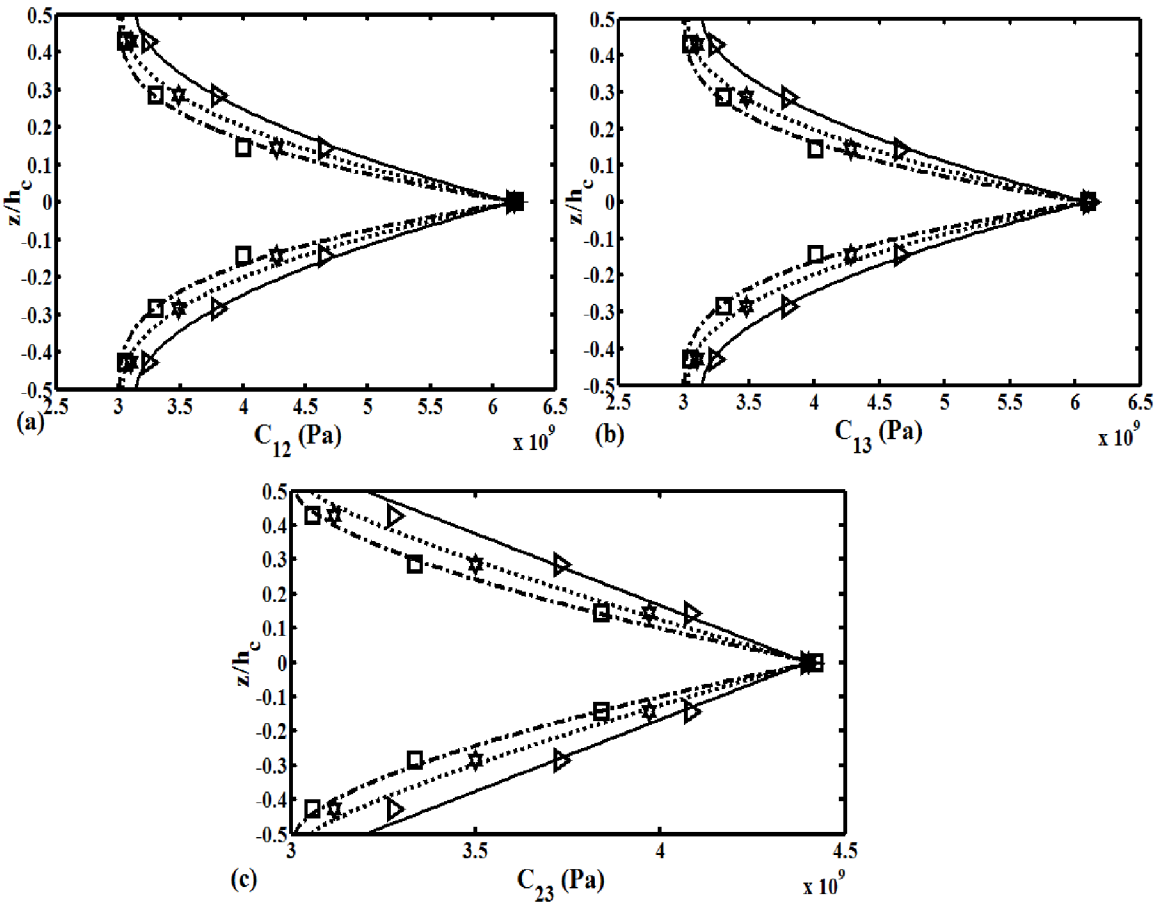

Fig. 5.10 Effective elastic coefficients $(c_{12}^{\ell}, c_{13}^{\ell}, c_{23}^{\ell})$ **for different homogeneous layers in RV and the corresponding fitted curves for different values of power-law exponent** (n) **(**$N_t = 7$, $v_f^m = 0.6$, $\triangleright$ **:**C_{ij}^{ℓ} **for** $n = 1.0$ **,** —**:**C_{ij}^{ℓ}**-fitted curve for** $n = 1.0$, ★ **:**C_{ij}^{ℓ} **for** $n = 1.5$, ·····**:**C_{ij}^{ℓ} **-fitted curve for** $n = 1.5$, □**:**C_{ij}^{ℓ} **for** $n = 2.0$, - - -**:**C_{ij}^{ℓ}**-fitted curve for** $n = 2.0$**).**

In the aforesaid graded fiber-reinforced composite lamina (Fig. 5.1), the variation of FVF is considered to be symmetric with respect to the middle plane ($z = 0$) of the lamina. The material properties at the top surface of the lamina are the same as those on the bottom surface of the same. This lamina (Fig. 5.11) has its minimum stiffness at its top/bottom surface while the maximum stiffness of the same is achieved at the middle plane ($z = 0$). However, similar graded lamina could also be designed for maximum stiffness at one of its top and bottom surfaces while the other surface of the same has minimum stiffness.

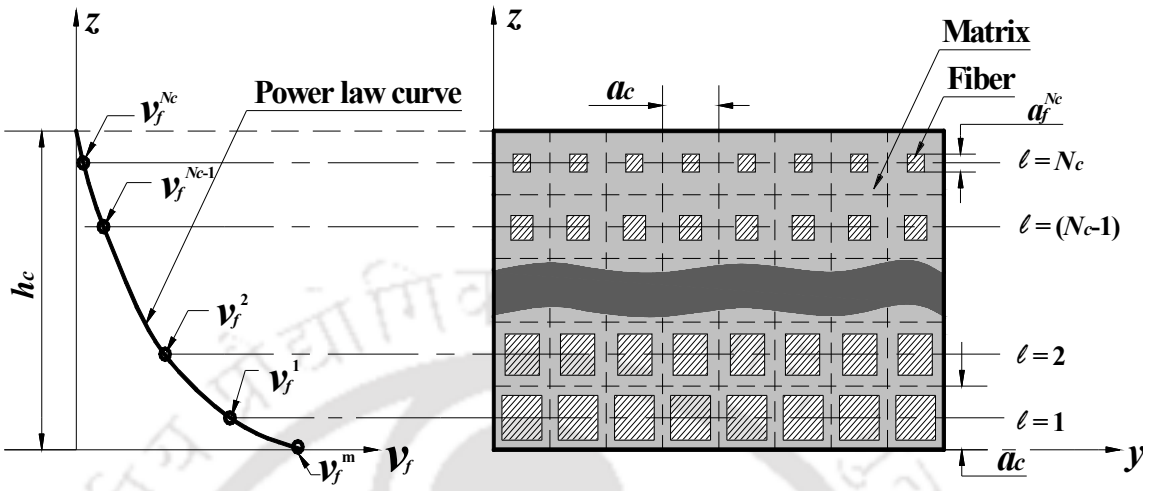

Fig. 5.11 Schematic diagrams of (a) graded fiber-reinforced composite lamina and (b) micro-structure of a typical yz-section of the graded fiber-reinforced composite lamina (V_f^m is the maximum value of FVF)

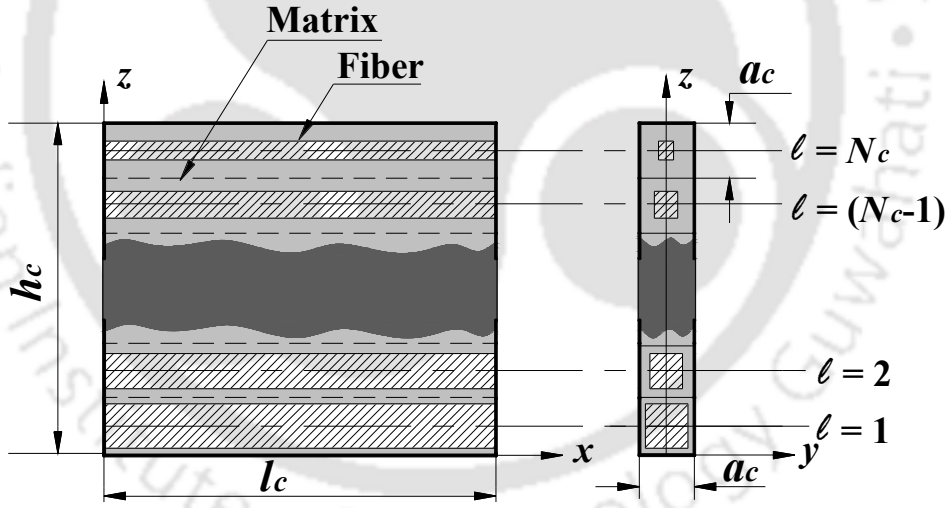

Fig. 5.12 Schematic diagram of representative volume (RV) of the graded fiber-reinforced composite.

Figure 5.11 shows such a lamina that is equivalent to the top half of the previous lamina (Fig. 5.1).The maximum FVF at the bottom surface of the lamina is considered as 0.6 while the minimum FVF is considered at the top surface of the same lamina as zero. Four layers ($N_t = 4$) are considered and the corresponding RV is shown in Fig. 5.12. Following the aforesaid procedure for evaluation of effective graded properties, the

variations of material properties of this lamina (Fig. 5.11) are illustrated in Fig. 5.13 and Table 5.6 considering two values of power-law exponent ($n =$ 1 and 2). Figure 5.13 and Table 5.6 show similar variations of elastic constants as those are illustrated for the top half of previous graded lamina (Fig. 5.1, Figs. 5.8-5.10, Table 5.4).

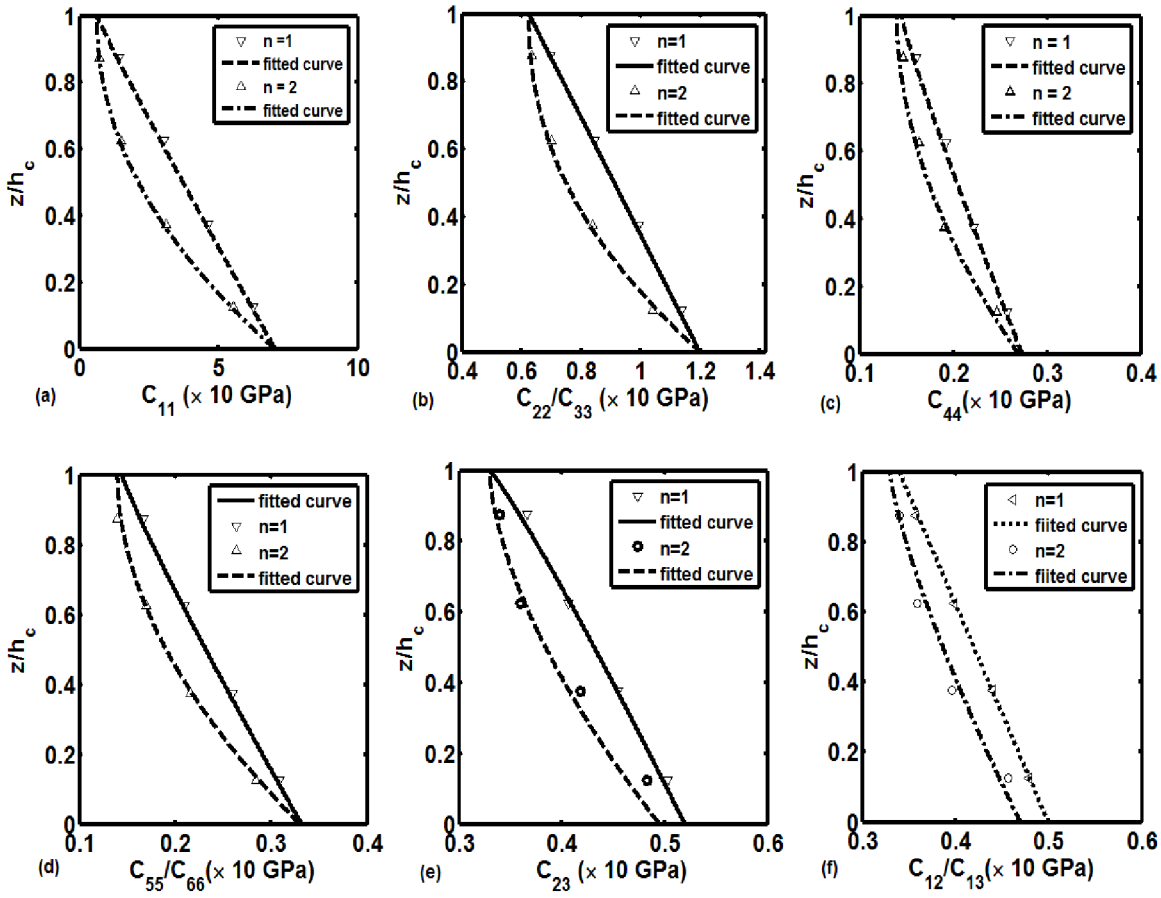

Fig. 5.13 Variations of elastic constants (C_{ij}) across the thickness of the graded composite lamina for different values of power-law exponent (n).

The consideration of uniform FVF ($\upsilon_f = 0.6$) in all fiber-matrix packs of RV (Figs. 5.2 and 5.12) yields a conventional unidirectional fiber-reinforced composite lamina. So, the present graded composite lamina is basically a modified form of conventional unidirectional fiber-reinforced composite lamina and this modification is carried out by varying the FVF across the thickness of the lamina. However, the magnitudes of elastic

coefficients of conventional composite lamina with FVF of 0.6 are illustrated in Table 5.7 and these magnitudes may be compared with the similar magnitudes (Figs. 5.8-5.10, Tables 5.4 and 5.6) for graded lamina. It may be observed from Tables 5.4, 5.6, 5.7 and Figs. 5.8-5.10, 5.13 that the average magnitude of any elastic coefficient decreases when the conventional lamina is converted into the graded fiber-reinforced composite lamina according to the present design. Thus, the overall stiffness of the graded composite lamina is lesser than that of the conventional composite lamina.

Table 5.6 Numerical values of $C_{ij}^{\max}$, $C_{ij}^{\min}$ and n_c

C_{ij}	$C_{ij}^{\max}(\times 10\ GPa)$		$C_{ij}^{\min}(\times 10\ GPa)$		n_c	
	$n=1$	$n=2$	$n=1$	$n=2$	$n=1$	$n=2$
C_{11}	7.04	7.02	0.65	0.65	1.05	2.1
C_{22}/C_{33}	1.20	1.25	0.626	0.62	1.0	2.2
C_{44}	0.274	0.27	0.1448	0.14	1.1	1.9
C_{55}/C_{66}	0.332	0.33	0.1449	0.15	1.1	2.2
C_{12}/C_{13}	0.501	0.48	0.338	0.32	1.0	1.6
C_{23}	0.527	0.495	0.337	0.34	0.9	1.6

Table 5.7 Elastic constant for the composite ply of uniform FVF of 0.6

$C_{ij}(\times 10\ GPa)$					
C_{11}	C_{22}/C_{33}	C_{44}	C_{55}/C_{66}	C_{12}/C_{13}	C_{23}
7.027	1.787	0.319	0.491	0.616	0.634

5.6.3 Graded laminated composite plates

The present graded fiber-reinforced composite lamina is designed with an objective of reduced mismatch of material properties and stresses at the interlaminar-surfaces in laminated composite structures. To substantiate this, presently two conventional laminated composite plates (CLCPs) are considered and their conventional plies are replaced by present graded plies (Fig. 5.1). In this conversion of a CLCP into a graded

laminated composite plate (GLCP), the stacking sequence and other geometrical properties of the laminated plate are not altered. Also, the numerical study for both plates (CLCP and GLCP) is carried out without altering the boundary conditions (simply-supported) and intensity of uniformly distributed transverse load. The FVF of the conventional composite plies is taken as 0.6 while the maximum FVF of the graded composite plies is considered as 0.6. The corresponding material properties of plies are,

Epoxy: $E = 3.5$ GPa, $\nu = 0.35$.

High modulus glass: $E = 110$ GPa, $\nu = 0.22$.

The linear/nonlinear bending responses of laminated plates (CLCP and GLCP) are evaluated using the present FE formulation for laminated composite plates and direct iteration method. The transverse deflections, loads and stresses are presented in terms of the following dimensionless parameters respectively,

$$W = w/h,$$

$$Q = \left(\frac{p}{E_f}\right) \times \left(\frac{a}{h}\right)^4,$$

$$\bar{\sigma}_x = \left(\frac{\sigma_x}{|p|}\right) \times \left(\frac{h}{a}\right)^3,$$

$$\bar{\sigma}_y = \left(\frac{\sigma_y}{|p|}\right) \times \left(\frac{h}{a}\right)^3 \tag{5.37}$$

where, E_f is the Young's modulus of fiber-phase material and the transverse deflection (w) is evaluated at the middle point of the plate.

5.6.3.1 Verification of FE model of laminated composite plate

The present FE formulation for bending analysis of laminated composite plates is verified through the computation of dimensionless transverse deflection (W) at the middle point of a simply-supported conventional symmetric cross-ply ($0^o/90^o/0^o$) laminated composite plate. The computed dimensionless transverse deflections for different applied mechanical loads (Q) are plotted in Fig. 5.14 together with the similar results for an identical plate analyzed by Liew et al. (2004). Figure 5.14 shows an excellent agreement of present results with the similar published results (Liew et al. 2004) thus verifying the accuracy of the present FE formulation for laminated composite plates.

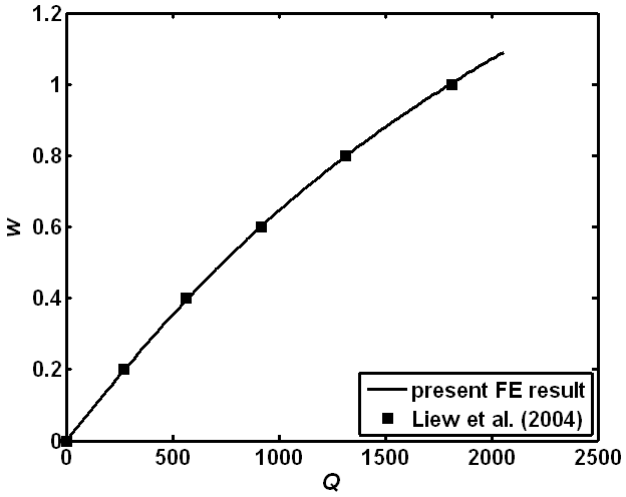

Fig. 5.14 Comparison of dimensionless transverse deflections (W) at the middle point of a simply-supported conventional symmetric cross-ply ($0^o/90^o/0^o$) laminated plate with the similar results for an identical plate analyzed by Liew et al. (2004).

5.6.3.2 Bending responses of GLCPs

Figure 5.15 illustrates the transverse deflection (W) vs. load (Q) curves for symmetric and asymmetric CLCPs/GLCPs. For any of the plates (symmetric/asymmetric), Fig. 5.15 shows lesser rigidity of GLCP as compared to that of corresponding CLCP. Moreover, the rigidity of GLCP decreases as its graded plies are made of higher power-law exponent (n). For liner and nonlinear bending deformations of symmetric CLCP/GLCP, two different mechanical loads (p = 10 N/m^2, 5 kN/m^2) are considered from Fig.

5.15(a). Corresponding to these mechanical loads, the distributions of dimensionless stresses ($\bar{\sigma}_x$, $\bar{\sigma}_y$) across the thickness of the symmetric GLCP/CLCP are demonstrated in Figs. 5.16(a)-(d). It may be observed from Figs. 5.16(a)-(d) that there is a significant stress-mismatch at the interface of 0° and 90° plies of CLCP. But, this stress-mismatch could significantly be reduced by the use of present graded composite plies. Also, this stress-mismatch could almost be eliminated using the graded plies of higher power-law exponent (n). Similar stress-distributions for asymmetric GLCP/CLCP are also presented in Fig. 5.17. In this case, the values of mechanical load (Q) corresponding to linear and nonlinear deformations of asymmetric GLCP/CLCP are chosen from Fig. 5.15(b). The results in Fig. 5.17 exhibit similar observations as those are obtained for symmetric plates (Fig. 5.16).

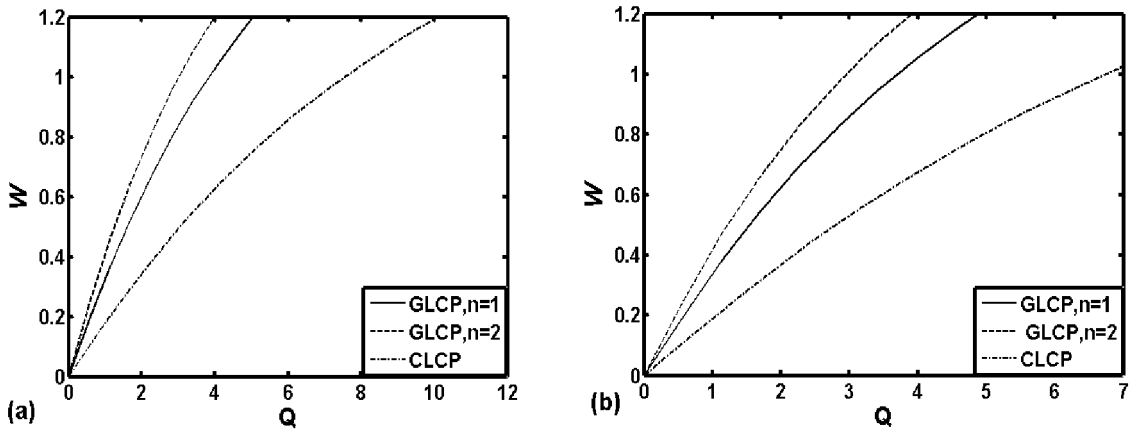

Fig. 5.15 Variations of dimensionless transverse deflection (W) at the middle point of (a) symmetric ($0^0/90^0/0^0$) and (b) asymmetric ($90^0/0^0/90^0/0^0$) cross-ply laminated composite plates with the dimensionless transverse mechanical load (Q).

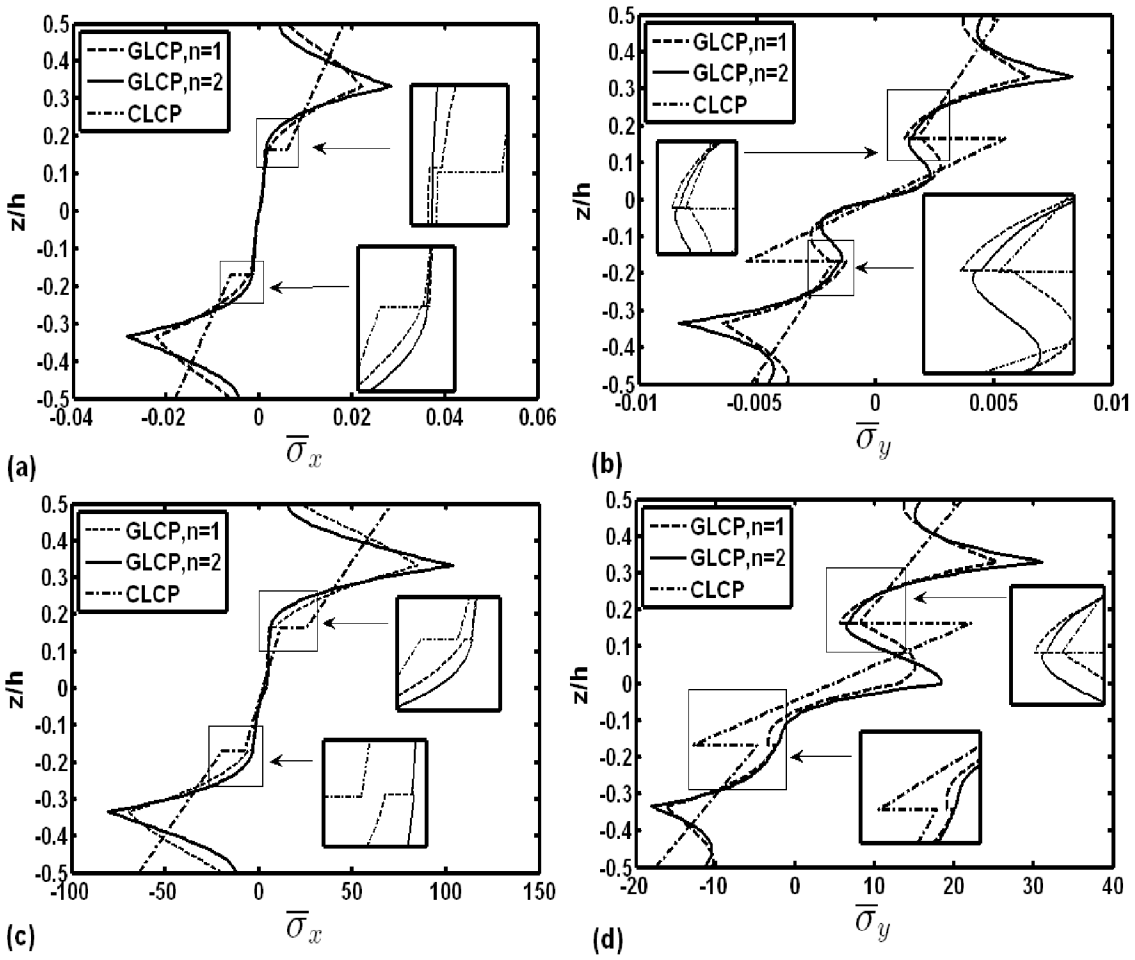

Fig. 5.16 Distributions of the dimensionless stresses $(\overline{\sigma}_x, \overline{\sigma}_y)$ across the thickness of the graded/conventional symmetric cross-ply $(0^0/90^0/0^0)$ laminated composite plate under the (a)-(b) linear (p = 10 N/m^2) and (c)-(d) nonlinear (p = 5 kN/m^2) bending deformations.

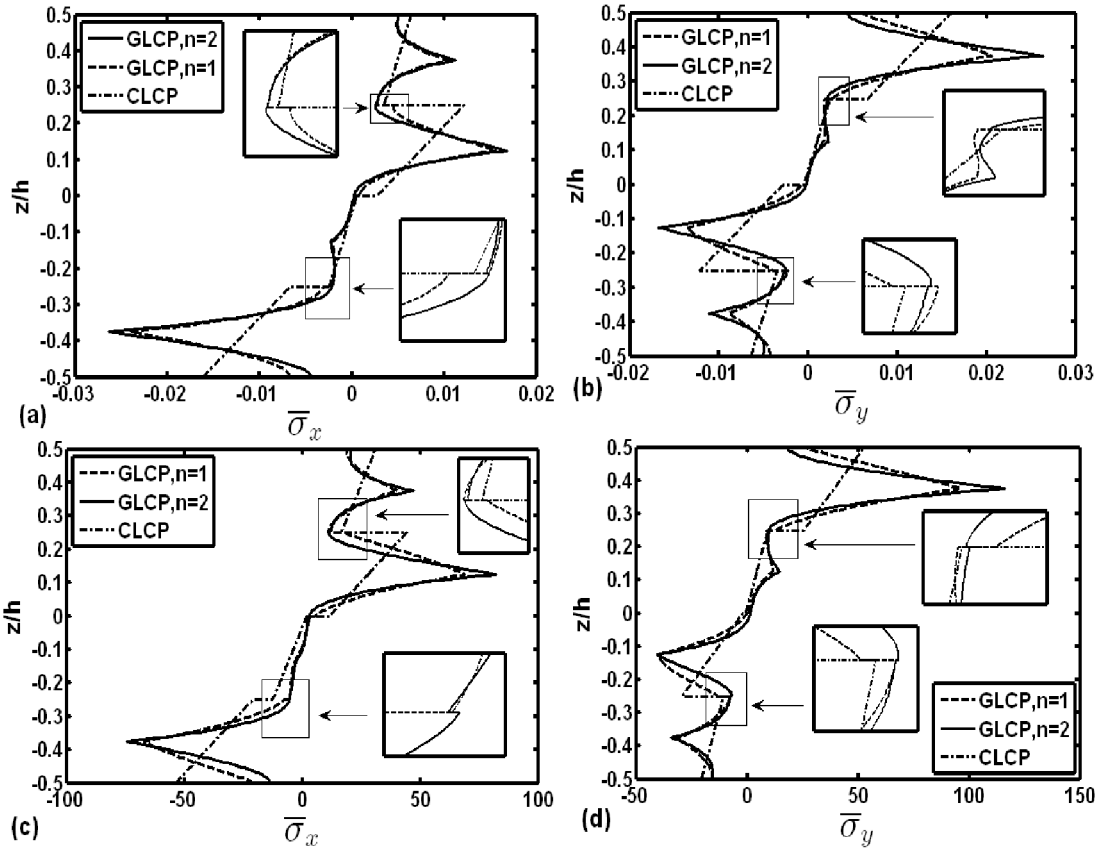

Fig. 5.17 Distributions of the dimensionless stresses $(\overline{\sigma}_x, \overline{\sigma}_y)$ across the thickness of the graded /conventional asymmetric cross-ply $(90^0/0^0/90^0/0^0)$ laminated composite plate under the (a)-(b) linear (p = 10 N/m^2) and (c)-(d) nonlinear (p = 5 kN/m^2) bending deformations.

5.6.4 Conventional-graded laminated composite plates

The continuous stresses in Figs. 5.16-5.17 indicate similar nature (continuous) of variations of material properties across the thickness of laminate. But, the discrepancies like the increase of maximum value of every stress (Figs. 5.16-5.17) and the decrease of laminate-rigidity (Figs. 5.15) arise in forming a GLCP through direct substitution of conventional plies of a CLCP. In order to eliminate these demerits retaining the merit of continuous variations of stresses/material properties, a new lamination scheme is proposed in the present study by utilizing graded as well as conventional composite

plies within the same laminate. These two (graded and conventional) different types of plies are utilized within a laminate in such a manner that the graded plies work mainly for achieving continuous variations of material properties while the conventional plies strengthen the laminate. Since this type of laminated plate is composed of graded as well as conventional laminas, it (laminated plate) is presently designated as conventional-graded laminated composite plate (CGLCP). However, in this strategy of lamination, a graded ply is considered to have maximum stiffness at one of its top and bottom surfaces while the other surface of the same has minimum stiffness. So, the graded ply illustrated in Fig. 5.11 is utilized.

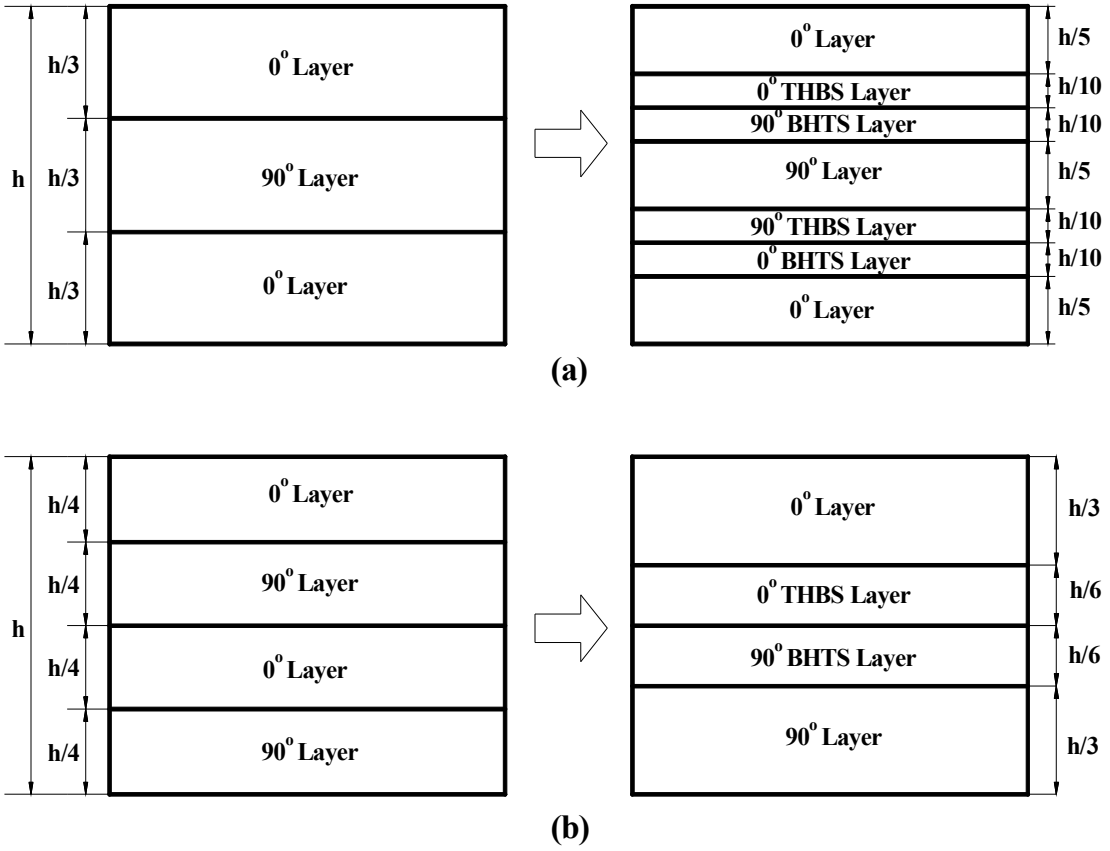

Fig. 5.18 Modified stacking sequences for conventional-graded composite plates (a) symmetric and (b) asymmetric laminated.

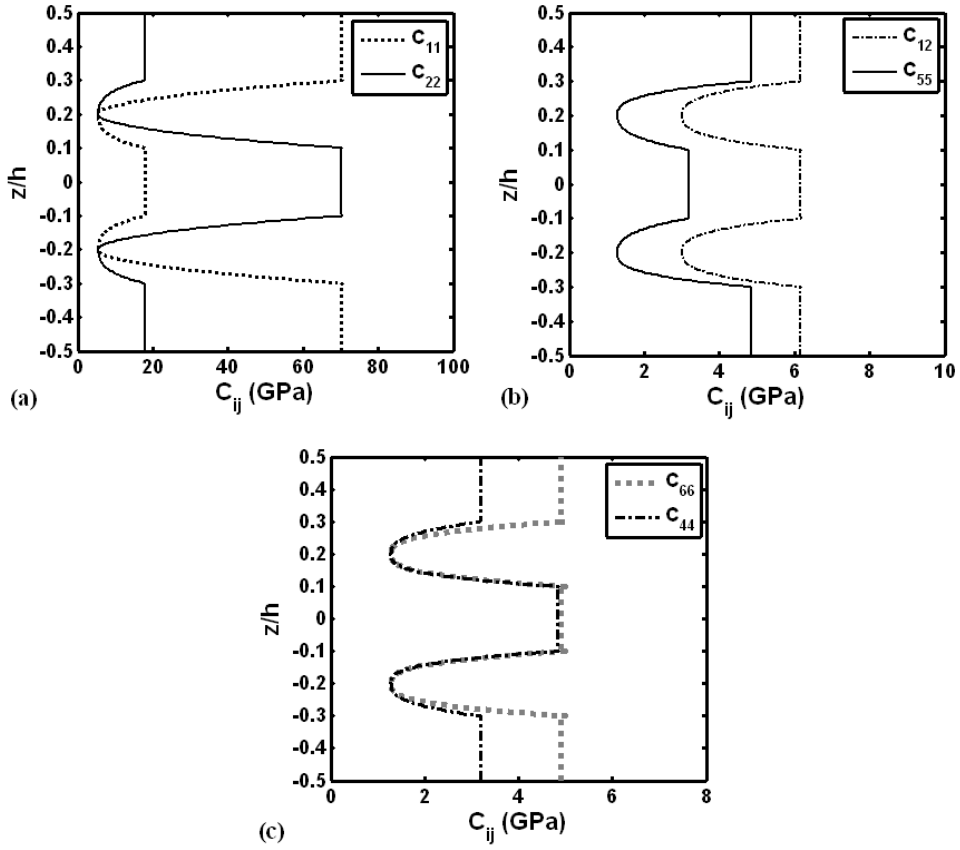

Fig. 5.19 Variations of elastic constants (C_{ij}) across the thickness of the symmetric conventional-graded laminated composite plate (CGLCP, $n = 2$).

It should be noted that this graded composite ply (Fig. 5.11) can be utilized in its two forms. The first one is for its stiffer top-surface and softer bottom-surface. The next one is just reverse of the first one. Corresponding to these two forms of the graded ply (Fig. 5.11), it is designated either as top-hard-bottom-soft (THBS) ply or as bottom-hard-top-soft (BHTS) ply. Utilizing these two forms of the graded ply, two conventional laminated composite plates of symmetric ($0^o/90^o/0^o$) and asymmetric ($90^o/0^o/90^o/0^o$) stacking sequences are modified as illustrated in Fig. 5.18. The total thickness of the laminate is not altered for this modification of stacking sequence and the thickness of THBS layer or BHTS layer is considered as half of that for the conventional composite-ply within the same laminate. It may be observed from Fig. 5.18 that a pair of THBS and

BHTS layers is used between two conventional layers in order to reduce the mismatch of material properties at their inter-surface. For symmetric laminate (Fig. 5.18(a)), a pair of THBS and BHTS layers is inserted at every inter-surface of 0^o and 90^o layers. If the same procedure is followed in case of asymmetric laminate (Fig. 5.18(b)), then three pairs of THBS and BHTS layers are required. But, as the stiffness of a THBS/BHTS layer is lesser than that of a conventional layer and a constant laminate-thickness is considered in this conversion, too many THBS/BHTS layers within a laminate may cause considerable reduction of its (laminate) rigidity. Thus, the stacking sequence of asymmetric conventional laminate is modified considering only one pair of THBS and BHTS layers as illustrated in Fig. 5.18(b).

For a particular value of power-law exponent ($n = 2$), the variations of different elastic coefficients (C_{ij}) across the thickness of laminates (CGLCPs) are demonstrated in Fig. 5.19. It may be observed from Fig. 5.19 that the elastic coefficients continuously vary across the thickness of the laminate (CGLCP). Also, the symmetric nature of variation of elastic properties of CLCP does not alter as it (CLCP) is converted to CGLCP. For the conversion of asymmetric ($90^o/0^o/90^o/0^o$) CLCP into a CGLCP, the corresponding variations of elastic coefficients (C_{ij}) across the thickness of CGLCP are illustrated in Fig. 5.20. This figure shows that the asymmetric CLCP remains as asymmetric laminate after its conversion into CGLCP.

Figure 5.21 illustrates the deflection (W) vs. load (Q) curves for symmetric and asymmetric CGLCPs (Figs. 5.18). Similar responses of corresponding symmetric and asymmetric CLCPs are also illustrated in the same figure. In comparison to the previous results (Fig. 5.15), it may be observed from Fig. 5.21 that the rigidity of the symmetric/asymmetric CGLCP is significantly increased towards the same of corresponding symmetric/asymmetric CLCP. This occurs because of the use of conventional plies. It may also be observed that there is no significant change in the rigidity of a CGLCP due to the change of the value of power-law exponent (n) because the stiffness of every graded ply in CGLCP is not a major issue in its (CGCLP) design.

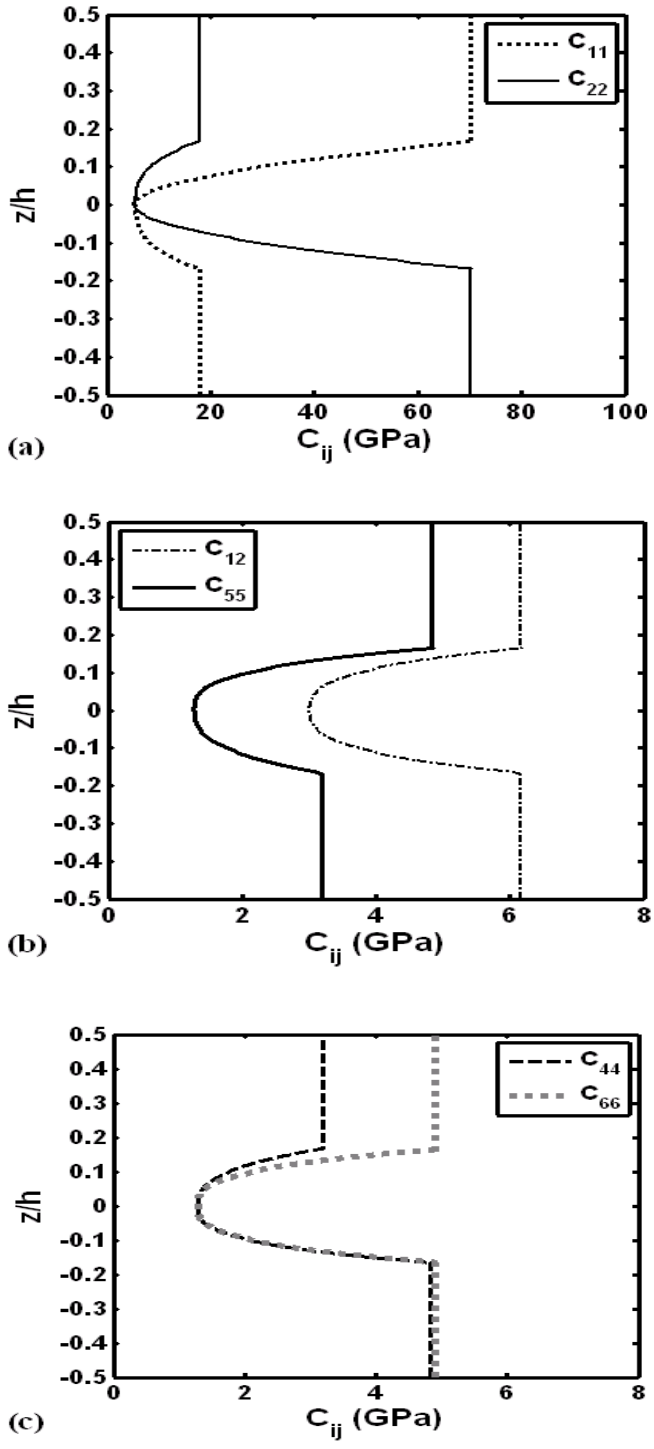

Fig. 5.20 Variations of elastic constants (C_{ij}) across the thickness of the asymmetric conventional-graded laminated composite plate (CGLCP, $n = 2$).

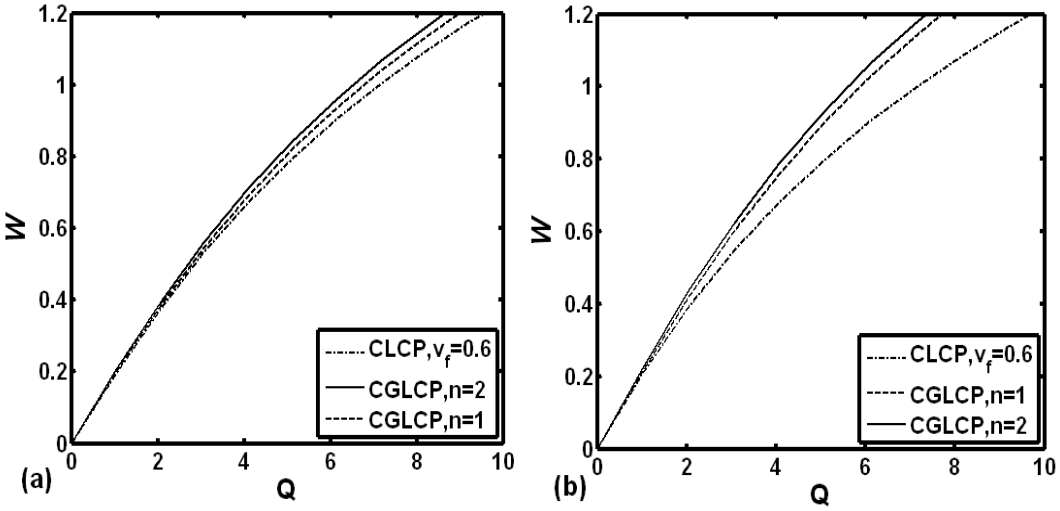

Fig. 5.21 Variations of dimensionless transverse deflection (W) at the middle point of (a) symmetric and (b) asymmetric cross-ply laminated composite plates with the dimensionless transverse mechanical load (Q).

For two different loads (p = 10 N/m^2, 5 kN/m^2) corresponding to linear and nonlinear bending deformations of symmetric CGLCP, the distributions of stresses $(\bar{\sigma}_x, \bar{\sigma}_y)$ across the thickness of the laminate are illustrated in Fig. 5.22. It may be observed from Fig. 5.22 that the stresses are almost continuously distributed across the thickness of the plate. It is also interesting to observe in comparison to Fig. 5.16 that the maximum value of every stress component does not alter for the conversion of a symmetric CLCP into a symmetric CGLCP. Similar to the previous results (Figs. 5.16), a higher value of power-law exponent (n) causes lesser stress-discontinuity at the interlaminar-surfaces in CGLCP. In the case of conversion of an asymmetric CLCP into an asymmetric CGLCP, the stress distributions are demonstrated in Fig. 5.23 that exhibits similar observations as those are obtained from the symmetric case (Fig. 5.22). The foregoing results (Figs. 5.19-5.23), show that the proposed lamination scheme provides continuous variations of material properties and stresses across the thickness of laminated plate. This advantage could be achieved with ample changes of laminate-

rigidity and maximum values of stresses in the laminate. In this conversion there is no appearance of stress-concentration.

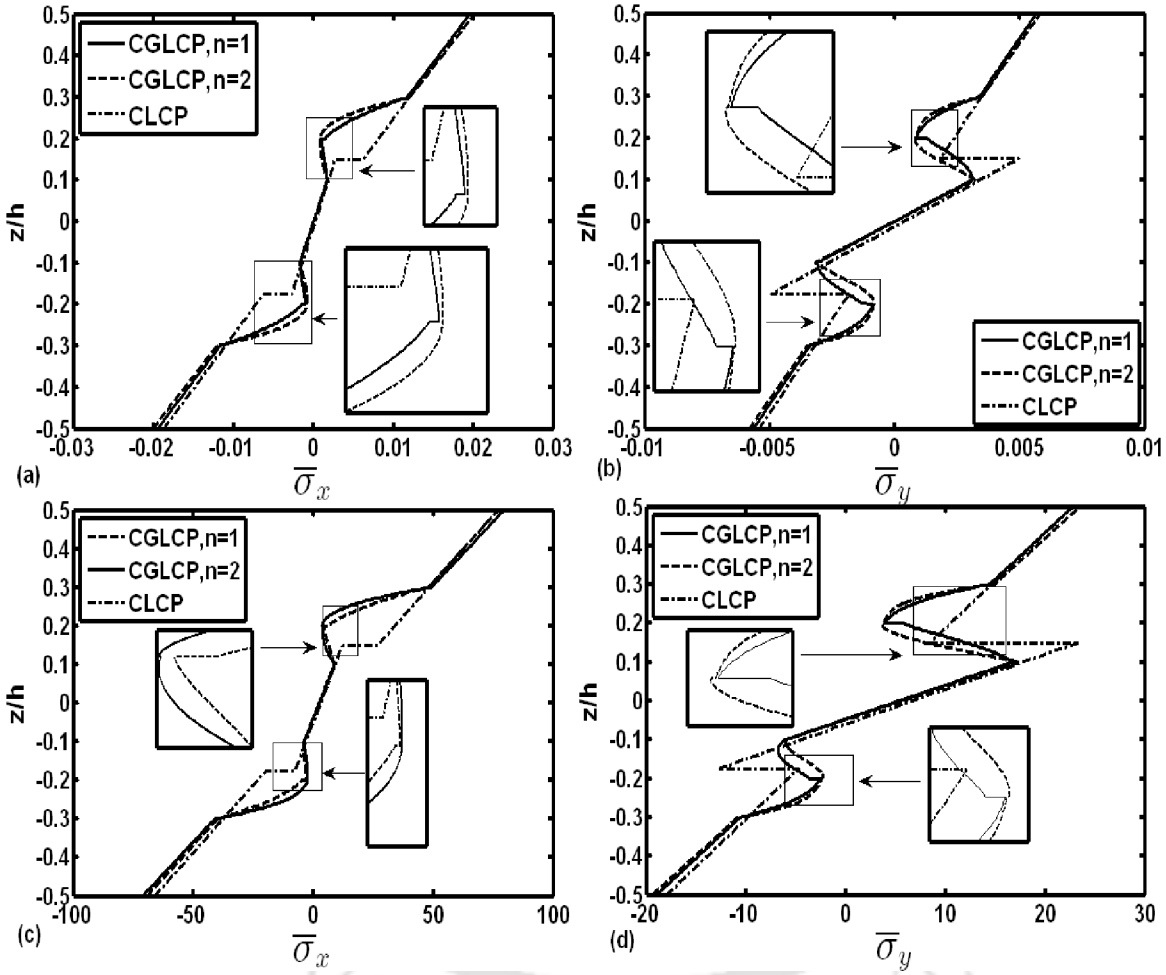

Fig. 5.22 Distributions of the dimensionless stresses $(\overline{\sigma}_x, \overline{\sigma}_y)$ across the thickness of the conventional-graded (Fig. 5.18(a))/conventional symmetric $(0^0/90^0/0^0)$ laminated composite plate under its (a)-(b) linear (p = 10 N/m^2) and (c)-(d) nonlinear (p = 5 kN/m^2) bending deformations.

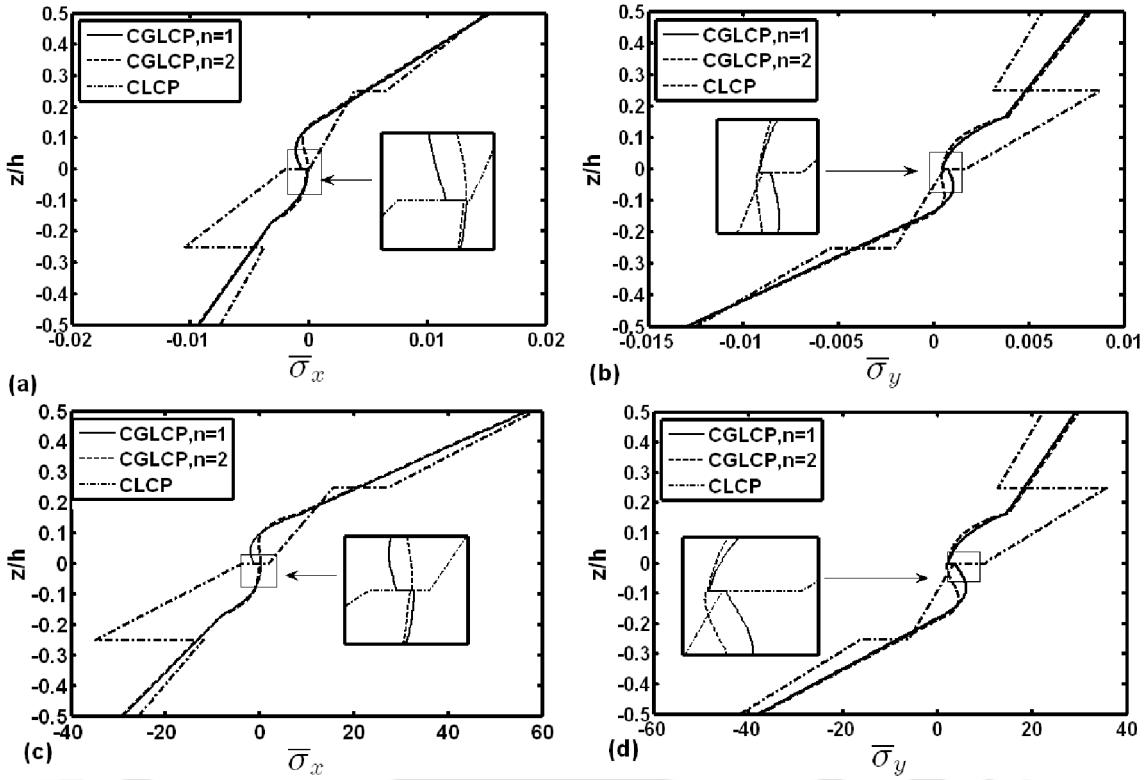

Fig. 5.23 Distributions of the dimensionless stresses $(\overline{\sigma}_x, \overline{\sigma}_y)$ across the thickness of the conventional-graded (Fig.5.18(b))/ conventional asymmetric cross-ply $(90^0/0^0/90^0/0^0)$ laminated composite plate under its (a)-(b) linear (p = 10 N/m^2) and (c)-(d) nonlinear (p = 5 kN/m^2) bending deformations.

5.7 Conclusions

In this chapter, a graded orthotropic fiber-reinforced composite lamina is designed and it is utilized for achieving continuous variations of material properties and stresses across the thickness of composite laminates through the proposition of a new lamination scheme. The graded composite lamina is basically a stack of horizontal layers of unidirectional continuous fiber-reinforced composite. Every layer is comprised of one row of horizontally coplanar continuous fibers embedded within epoxy matrix. The fibers in all layers are aligned in the plane of the lamina and orientated uniformly. The FVF varies among the layers following a simple power-law. All fibers within a layer have identical cross-sectional area while the same (area) varies layer-wise in order to

accomplish the variation of FVF among the layers. The volume-average elastic properties of the graded composite lamina are estimated using FE procedure. These average properties are then expressed as graded elastic properties in the direction of variation of FVF utilizing an available concept of homogenous layers in FG composites. The numerical analysis on the effective properties of graded composite lamina reveals identical nature of variation of every elastic coefficient as it (nature) is for the variation of corresponding FVF. It is observed that the number of composite layers within a specified thickness of lamina does not have much effect on the nature of variation of any effective elastic coefficient. The number of layers within a specified thickness of lamina is important only for physically achievable continuous variations of effective elastic coefficients.

The utilization of the present graded composite lamina within the laminated composite plates is demonstrated for the cases of two conventional laminated composite plates (CLCPs). A new lamination scheme is proposed for conversion of these CLCPs into conventional-graded laminated composite plates (CGLCPs) using graded as well as conventional composite plies. In this conversion, the prime intent of continuous variations of material properties across the thickness of composite laminate is achieved. The corresponding changes in the laminate-rigidity and maximum values of stresses in the laminate are substantiated through the numerical evaluation of bending responses of plates (CLCPs and CGLCPs). The numerical results for bending analysis of plates reveal ample changes of laminate-rigidity and maximum values of stresses while achieving the continuous variations of material properties and stresses across the thickness of laminate by means of aforesaid conversion/lamination scheme.

Chapter 6

NONLINEAR FREQUENCY RESPONSE ANALYSIS OF A SMART GRADED FIBER-REINFORCED COMPOSITE LAMINATED PLATE

In this chapter, dynamic characteristics of conventional- graded laminated composite plate (CGLCP) in the frequency domain is presented. In addition, a smart CGLCP having an ACLD layer and an active constraining layer of PFRC is also considered for studying the active damping of vibration of such graded laminated composite plates. Many of the equations already described in previous chapters have been referred and again repeated in this chapter for the convenience of the reader.

6.1 Introduction

In the preceding chapter, a design of graded fiber-reinforced composite laminated plate is demonstrated through the conversion of conventional laminated composite plate (CLCP) into conventional-graded laminated composite plate (CGLCP). The bending analysis (Chapter 5) of these laminated composite plates (CLCP and CGLCP) reveals ample changes of laminate-rigidity and maximum values of stresses in the laminate while achieving the advantage of continuous variations of material properties along the thickness direction. However, for general use of the proposed graded laminate (CGLCP) as a structural member, it is important to investigate the dynamic characteristics of such graded laminate and compare these with similar characteristics of corresponding conventional laminate (CLCP). Since the present work is performed towards the development of advanced laminated composite structures, an associated issue is the suppression of their vibration that is often carried out using piezoelectric actuators (Bailey and Hubbard 1985; Miller and Hubbard 1987; Crawley and Luis 1987) or the same in advanced form of ACLD (Baz 1993; Baz and Ro 1995; Ray and Baz 1999; Ray 2006). Presently, a layer of ACLD with an active constraining layer of PFRC (Mallik and Ray 2003) is considered and the changes in its (ACLD) actuation-capability due to the

use of CGLCP instead of CLCP are investigated by analyzing the frequency responses of the plates (CLCP and CGLCP) integrated with a layer of ACLD. The active damping in the overall smart laminated plate is achieved by supplying external voltage according to negative velocity feedback control strategy. First, an incremental finite element model of smart CGLCP is derived for its dynamic analysis in the frequency domain. Next, the numerical results are presented to illustrate the dynamic characteristics of a CLCP due to its conversion into a CGLCP. The corresponding changes in active damping caused by ACLD layer are also illustrated through the same numerical results.

6.2 Incremental finite element formulation

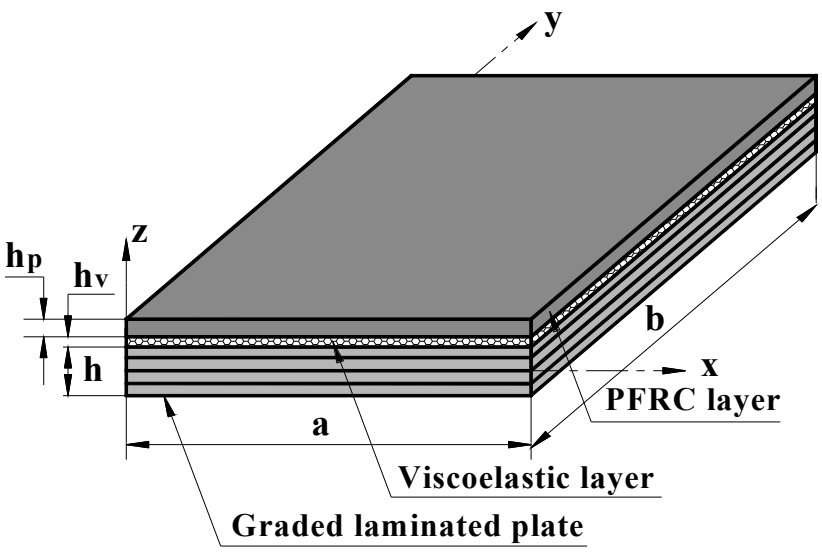

Fig. 6.1 Schematic diagram of a graded laminated composite plate integrated with ACLD layer.

Figure 6.1 shows a graded laminated composite plate integrated with a layer of ACLD. The constraining layer of ACLD is made of PFRC. The top and bottom surfaces of PFRC constraining layer are fully electrode-surfaces in order to activate this smart layer by supplying external voltage (V). The number of layers within the substrate graded laminated plate is denoted by, N_s. In addition, the $(N_s+1)^{th}$ and $(N_s+2)^{th}$ layers are the viscoelastic and PFRC layers, respectively. The middle plane of the substrate laminated plate is considered as the reference plane and the origin of the reference

coordinate system is located at one corner of the reference plane (Fig. 6.1). The boundaries of the overall plate are represented by, $x=0,a$ and $y=0,b$. The thickness of the substrate plate/viscoelastic layer/PFRC layer is denoted by, h / h_v / h_p. The alignment and orientation of piezoelectric fibers in the PFRC constraining layer are the same as those shown in Fig. 3.1. The state of strain and the state of stress at any point within the overall laminated composite plate are defined by Eq. (2.1) and Eq. (2.2) which are repeated here for the convenience of the reader,

$$\{\varepsilon_b\}=\{\varepsilon_x \quad \varepsilon_y \quad \varepsilon_{xy}\}^{\mathrm{T}}, \{\varepsilon_s\}=\{\varepsilon_{yz} \quad \varepsilon_{xz}\}^{\mathrm{T}} \tag{2.1}$$

$$\{\sigma_b\}=\{\sigma_x \quad \sigma_y \quad \sigma_{xy}\}^{\mathrm{T}}, \ \{\sigma_s\}=\{\sigma_{yz} \quad \sigma_{xz}\}^{\mathrm{T}} \tag{2.2}$$

For the analysis of FG plates, several shear deformation theories are addressed in the literature (Reddy 2003; Benachour et al. 2011; Bouiadjra et al. 2013; Larbi et al. 2013; Bouderba et al. 2013; Tounsi et al. 2013; Meziane et al. 2013; Zidi et al. 2014; Hebali et al. 2014; Belabed et al. 2014) to account parabolic distributions of transverse shear strains with/without transverse stretching. However, these shear deformation theories are important particularly for thick plates or even thin plates vibrating at higher modes (Benachour et al. 2011). Generally, the transverse shear strains are very small in thin plates and thus their analysis may be carried out considering classical plate theory (CPT) or first order shear deformation theory (FSDT) (Reddy 2003). Presently, a thin laminated plate (side-to-thickness ratio as 100) is considered and it is analyzed corresponding to its fundamental bending mode of vibration. Thus, the layer-wise FSDT as illustrated in Eq. (3.3) is considered for defining its (laminated plate) kinematics of deformation with a shear correction factor of 5/6 (Reddy 2003). The layer-wise FSDT as presented in Eq. (3.3) is again rewritten here,

$$\begin{aligned} u^k(x,y,z,t) &= u_0(x,y,t)+z_1^k\theta_x(x,y,t)+z_2^k\phi_x(x,y,t)+z_3^k\gamma_x(x,y,t)\ , \\ v^k(x,y,z,t) &= v_0(x,y,t)+z_1^k\theta_y(x,y,t)+z_2^k\phi_y(x,y,t)+z_3^k\gamma_y(x,y,t)\ , \\ w^k(x,y,z,t) &= w_0(x,y,t) \end{aligned} \tag{3.3}$$

where, the different z-co-ordinates (z_1^k, z_2^k, z_3^k) for the present laminated plate are as follows ,

$$z_1^k = z, z_2^k = z_3^k = 0 \text{ for } 1 \le k \le N_s,$$

$$z_1^k = h/2, z_2^k = (z - h/2), z_3^k = 0 \text{ for } k = (N_s + 1),$$

$$z_1^k = h/2, z_2^k = h_v, z_3^k = (z - h/2 - h_v) \text{ for } k = (N_s + 2) \quad (6.1)$$

Considering von Karman nonlinear strain-displacement relations and displacement field given by Eq. (3.3), the strain vectors ($\{\varepsilon_b^k\}$, $\{\varepsilon_s^k\}$) for k^{th} layer of the overall laminated plate can be expressed by Eq. (3.5) as follows,

$$\{\varepsilon_b^k\} = \{\varepsilon_{bL}\} + \{\varepsilon_{bN}\} + [z_b^k]\{\kappa_b\},$$

$$\{\varepsilon_s^k\} = \{\varepsilon_s\} + [z_s^k]\{\kappa_s\} \quad (3.5)$$

The generalized strain vectors and the z-co-ordinate matrices in Eq. (3.5) are given in Eq. (3.6).The constitutive relations for a layer ($1 \le k \le N_s$) within the laminated substrate plate can be written according to Eq. (5.29) as follows,

$$\{\sigma_b^k\} = [\bar{C}_b^k(z)]\{\varepsilon_b^k\},$$

$$\{\sigma_s^k\} = [\bar{C}_s^k(z)]\{\varepsilon_s^k\} \quad (5.29)$$

where, $k = 1, 2, 3, \ldots\ldots N_s$ for viscoelastic layer ($k = (N_s + 1)$) and PFRC layer ($k = (N_s + 2)$) are expressed in Eqs. (3.2) and (2.6) respectively. A thin PFRC constraining layer with top and bottom electrode-surfaces is considered. The voltage is supplied across the electrode-surfaces that yields the electric field components as $E_x \approx 0$, $E_y \approx 0$ and $E_z = -V/h_p$. For an applied uniformly distributed harmonic transverse mechanical load of intensity, $p(x, y, t)$, the first variations of the total potential energy (δT_p) and the total kinetic energy (δT_K) of the overall laminated composite plate at any time (t) can be written as (Tiersten 1969),

$$\delta T_p = \int_0^a \int_0^b \left[\sum_{k=1}^{(N_s+2)} \int_{h_k}^{h_{k+1}} \left(\left\{\delta\varepsilon_b^k\right\}^{\mathrm{T}} \{\sigma_b^k\} + \left\{\delta\varepsilon_s^k\right\}^{\mathrm{T}} \{\sigma_s^k\} \right) dz - \int_{h_k}^{h_{k+1}} \{\delta\bar{E}\}^{\mathrm{T}} \{D\}\,|_{k=(N_s+2)}\, dz - (\delta w)p \right] dy\,dx \quad (6.2)$$

$$\delta T_K = \int_0^a \int_0^b \left[\sum_{k=1}^{(N_s+2)} \int_{h_k}^{h_{k+1}} \left\langle [\delta\dot{u} \quad \delta\dot{v} \quad \delta\dot{w}] \rho^k [\dot{u} \quad \dot{v} \quad \dot{w}]^{\mathrm{T}} \right\rangle dz \right] dy dx = \int_0^a \int_0^b \left(\{\delta\dot{d}\}^{\mathrm{T}} [\bar{m}] \{\dot{d}\} \right) dy dx \qquad (6.3)$$

ρ^k is the mass density of the k^{th} -layer of the overall laminated plate. Similar to the previous incremental formulation in Chapter 3, a state of vibration of overall laminated composite plate is defined by Eqs. (2.18a) that can be rewritten as,

$$\{d\} = \{d_i\} + \{\Delta d\}, \ \omega = (\omega_i + \Delta\omega) \qquad (2.18a)$$

where, the explicit forms of displacement vector ($\{d_i\}$) and corresponding increment ($\{\Delta d\}$) are illustrated in Eq. 3.12 as follows,

$$\{d_i\} = [u_{0i} \quad v_{0i} \quad w_{0i} \quad \theta_{xi} \quad \phi_{xi} \quad \gamma_{xi} \quad \theta_{yi} \quad \phi_{yi} \quad \gamma_{yi}]^{\mathrm{T}},$$

$$\{\Delta d\} = [\Delta u_0 \quad \Delta v_0 \quad \Delta w_0 \quad \Delta\theta_x \quad \Delta\phi_x \quad \Delta\gamma_x \quad \Delta\theta_y \quad \Delta\phi_y \quad \Delta\gamma_y]^{\mathrm{T}} \qquad (3.12)$$

Accordingly, the incremental forms of generalized strain vectors ($\{\varepsilon_{bL}\}, \{\varepsilon_{bN}\}, \{\varepsilon_s\}, \{\kappa_b\}, \{\kappa_s\}$) within the strain vectors ($\{\varepsilon_b^k\}, \{\varepsilon_s^k\}$) can be represented by Eqs. (3.13) as follows,

$$\{\varepsilon_{bL}\} = \{\varepsilon_{bL}^i\} + \{\Delta\varepsilon_{bL}\},$$

$$\{\varepsilon_{bN}\} = \{\varepsilon_{bN}^i\} + \{\Delta\varepsilon_{bN}\},$$

$$\{\kappa_b\} = \{\kappa_b^i\} + \{\Delta\kappa_b\},$$

$$\{\varepsilon_s\} = \{\varepsilon_s^i\} + \{\Delta\varepsilon_s\},$$

$$\{\kappa_s\} = \{\kappa_s^i\} + \{\Delta\kappa_s\} \qquad (3.13)$$

where, $\{\varepsilon_{bL}^i\}$, $\{\varepsilon_{bN}^i\}$, $\{\kappa_b^i\}$, $\{\varepsilon_s^i\}$ and $\{\kappa_s^i\}$ are the strain vectors for the given sate of deformation $\{d_i\}$ while $\{\Delta\varepsilon_{bL}\}$, $\{\Delta\varepsilon_{bN}\}$, $\{\Delta\kappa_b\}$, $\{\Delta\kappa_s\}$ and $\{\Delta\varepsilon_s\}$ are the corresponding increments are illustrated in Eq. 3.14.

For deriving finite element model of the overall plate, the plane of the plate is discretized using 9-node quadrilateral isoparametric element and the displacement field within a typical element is defined by Eq. (2.21) which can be rewritten as,

$$\{d\} = [N]\{d^e\} \qquad (2.21)$$

Using Eqs. (5.29), (2.6), (3.2), (3.5), (2.18a), (3.13) in Eqs. (6.2) and then using Eq. (2.21), the following simplified expression for the first variation of total potential energy (δT_p^e) for a typical element can be obtained as,

$$\delta T_p^e = \delta\{\Delta d^e\}^{\mathrm{T}} \begin{bmatrix} [K_L^e]\{d_i^e\}+[K_L^e]\{\Delta d^e\}+[K_{Ni}^e]\{d_i^e\}+[K_N^e]\{\Delta d^e\}+[K_{NNi}^e]\{d_i^e\} \\ +[K_{NN}^e]\{\Delta d^e\}-\{P_L^{Ee}\}V-\{P_N^{Ee}\}V-\{P_M^e(t)\}+[K_v^e]G(t)\{d^e(0)\} \\ +[K_v^e]\int_0^t G(t-\tau)\left\langle \frac{\partial}{\partial\tau}\{d_i^e(\tau)\}+\frac{\partial}{\partial\tau}\{\Delta d^e(\tau)\}\right\rangle \partial\tau \end{bmatrix} \tag{6.4}$$

Thus, the different sub-matrices in Eq. (6.4) are defined by the same expressions as those are given in Eqs. (3.15a)-(3.16). However, the expressions of different rigidity matrices ($\boldsymbol{A}_b^{13}$, $\boldsymbol{A}_s^{13}$, $\boldsymbol{B}_{b1}^{13}$, $\boldsymbol{B}_{b2}^{13}$, $\boldsymbol{D}_b^{13}$, $\boldsymbol{B}_{s1}^{13}$, $\boldsymbol{B}_{s2}^{13}$, $\boldsymbol{D}_s^{13}$, $\boldsymbol{A}_s^2$, $\boldsymbol{B}_{s1}^2$, $\boldsymbol{B}_{s2}^2$, $\boldsymbol{D}_s^2$) and electro-elastic coupling vectors ($\boldsymbol{A}_{be}$, $\boldsymbol{B}_{be}$, $\boldsymbol{A}_{se}$, $\boldsymbol{B}_{se}$) are modified for the use of several layers ($1 \le k \le N_s$) instead of single layer ($k=1$) within the substrate plate as follows,

$$\boldsymbol{A}_b^{13} = \sum_{k=1,k\neq(N_s+1)}^{N_s+2} \int_{h_k}^{h_{k+1}} \bar{\boldsymbol{C}}_b^k dz,$$

$$\boldsymbol{A}_s^{13} = \sum_{k=1,k\neq(N_s+1)}^{N_s+2} \int_{h_k}^{h_{k+1}} \bar{\boldsymbol{C}}_s^k dz,$$

$$\boldsymbol{A}_s^2 = \int_{h_k}^{h_{k+1}} \boldsymbol{C}_s^k\,|_{k=(N_s+1)}\, dz,$$

$$\boldsymbol{B}_{b2}^{13} = \sum_{k=1,k\neq(N_s+1)}^{N_s+2} \int_{h_k}^{h_{k+1}} \bar{\boldsymbol{C}}_b^k \boldsymbol{z}_b^k dz,$$

$$\boldsymbol{B}_{b1}^{13} = \sum_{k=1,k\neq(N_s+1)}^{N_s+2} \int_{h_k}^{h_{k+1}} (\boldsymbol{z}_b^k)^{\mathrm{T}} \bar{\boldsymbol{C}}_b^k dz,$$

$$B_{s2}^{13} = \sum_{k=1,k\neq(N_s+1)}^{N_s+2} \int_{h_k}^{h_{k+1}} \bar{\boldsymbol{C}}_s^k \boldsymbol{z}_s^k dz,$$

$$B_{s2}^2 = \int_{h_k}^{h_{k+1}} \boldsymbol{C}_s^k \boldsymbol{z}_s^k\,|_{k=(N_s+1)}\, dz,$$

$$B_{s1}^{13} = \sum_{k=1,k\neq(N_s+1)}^{N_s+2} \int_{h_k}^{h_{k+1}} (z_s^k)^{\mathrm{T}} \bar{C}_s^k dz \ ,$$

$$\boldsymbol{D}_b^{13} = \sum_{k=1,k\neq(N_s+1)}^{N_s+2} \int_{h_k}^{h_{k+1}} (z_b^k)^{\mathrm{T}} \bar{C}_b^k z_b^k dz,$$

$$\boldsymbol{D}_s^2 = \int_{h_k}^{h_{k+1}} (z_s^k)^{\mathrm{T}} C_s^k z_s^k \,|_{k=(N_s+1)} \, dz$$

$$D_s^{13} = \sum_{k=1,k\neq(N_s+1)}^{N_s+2} \int_{h_k}^{h_{k+1}} (z_s^k)^{\mathrm{T}} \bar{C}_s^k z_s^k dz \ ,$$

$$\boldsymbol{B}_{be} = \int_{h_k}^{h_{k+1}} (z_b^k)^{\mathrm{T}} \bar{e}_b [0 \quad 0 \quad -1/h_p]^{\mathrm{T}} \,|_{k=(N_s+2)} \, dz \ ,$$

$$\boldsymbol{B}_{se} = \int_{h_k}^{h_{k+1}} (z_s^k)^{\mathrm{T}} \bar{e}_s [0 \quad 0 \quad -1/h_p]^{\mathrm{T}} \,|_{k=(N_s+2)} \, dz \ ,$$

$$\boldsymbol{B}_{s1}^2 = \int_{h_k}^{h_{k+1}} (z_s^k)^{\mathrm{T}} C_s^k \,|_{k=(N_s+1)} \, dz \ ,$$

$$\boldsymbol{A}_{be} = \int_{h_k}^{h_{k+1}} \bar{e}_b [0 \quad 0 \quad -1/h_p]^{\mathrm{T}} \,|_{k=(N_s+2)} \, dz \ ,$$

$$\boldsymbol{A}_{se} = \int_{h_k}^{h_{k+1}} \bar{e}_s [0 \quad 0 \quad -1/h_p]^{\mathrm{T}} \,|_{k=(N_s+2)} \, dz \qquad (6.5)$$

The first variation of kinetic energy δT_k^e of a typical element can be expressed in similar for δT_k^e given in Eq. (3.15) as follows,

$$\delta T_k^e = \int_0^a \int_0^b \left\langle \{\delta \dot{d}\}^{\mathrm{T}} [\bar{m}] \{\dot{d}\} \right\rangle dy dx \qquad (3.15)$$

where, the form of $[\bar{m}]$ is modified for several layers $(1 \le k \le N_s)$ within the laminated substrate plate as follows,

$$[\bar{m}] = \sum_{k=1}^{(N_s+2)} \int_{h_k}^{h_{k+1}} \left\langle \left([Z_{mt}]^{\mathrm{T}} + [Z_{mr}^k]^{\mathrm{T}} \right) \rho^k \left([Z_{mt}] + [Z_{mr}^k] \right) \right\rangle dz$$

$$\mathbf{Z}_{mt}=\begin{bmatrix}1&0&0&0&0&0&0&0&0\\0&1&0&0&0&0&0&0&0\\0&0&1&0&0&0&0&0&0\end{bmatrix},$$

$$Z^k_{mr}=\begin{bmatrix}0&0&0&z^k_1&z^k_2&z^k_3&0&0&0\\0&0&0&0&0&0&z^k_1&z^k_3&z^k_3\\0&0&0&0&0&0&0&0&0\end{bmatrix} \tag{6.6}$$

The governing elemental equations of motion are derived by substituting the expressions of first variations of elemental potential energy (δT^e_p, Eq. (6.4)) and kinetic energy(δT^e_k, Eq. (3.15)) in the expression (Eq. (2.16)) of Hamilton's principle as follows,

$$\begin{aligned}&[M^e]\{\ddot{d}^e_i\}+[M^e]\{\Delta\ddot{d}^e\}+[K^e_L]\{d^e_i\}+[K^e_L]\{\Delta d^e\}+[K^e_{Ni}]\{d^e_i\}+[K^e_N]\{\Delta d^e\}+[K^e_{NNi}]\{d^e_i\}\\&+[K^e_{NN}]\{\Delta d^e\}+[K^e_v]G(t)\{d^e(0)\}+[K^e_v]\int_0^t G(t-\tau)\left\langle\frac{\partial}{\partial\tau}\{d^e_i(\tau)\}+\frac{\partial}{\partial\tau}\{\Delta d^e(\tau)\}\right\rangle\partial\tau=\\&\{P^{Ee}_L\}\times V-\{P^{Ee}_N\}\times V-\left\{P^e_M(t)\right\}\end{aligned} \tag{6.7}$$

The constrained viscoelastic layer within ACLD layer is modeled in the time-domain using Golla-Hughes-McTavish (GHM) method (Golla and Hughes, 1985). According to the GHM method, the material modulus function is represented as a series of mini-oscillator terms in the Laplace domain that is illustrated earlier in (Eq. 3.18) and could be rewritten as,.

$$s\tilde{G}(s)=G^{\infty}\left[1+\sum_{q=1}^{R}\alpha_q\frac{s^2+2\tilde{\xi}_q\tilde{\omega}_q s}{s^2+2\tilde{\xi}_q\tilde{\omega}_q s+\tilde{\omega}_q^2}\right] \tag{3.18}$$

This material modulus function could be introduced in Eq. (6.7) following a procedure as presented in Section 3.2.1 and the resulting governing equations of motion of the overall laminated plate can be obtained in the same form as those are given in Eqs. (3.19)-(3.20) as follows,

$$\begin{aligned}&[M^e]\{\ddot{d}^e_i\}+[M^e]\{\Delta\ddot{d}^e\}+[K^e_{Lc}]\{d^e_i\}+[K^e_{Lc}]\{\Delta d^e\}+[K^e_{Ni}]\{d^e_i\}+[K^e_N]\{\Delta d^e\}+[K^e_{NNi}]\{d^e_i\}\\&+[K^e_{NN}]\{\Delta d^e\}-\sum_{q=1}^{R}[K^e_{Lq}]\left\langle\{z^e_{iq}\}+\{\Delta z^e_q\}\right\rangle=\{P^{Ee}_L\}\times V+\{P^{Ee}_N\}\times V+\left\{P^e_M\right\}\end{aligned} \tag{3.19}$$

$$\left\langle \{\ddot{z}_{iq}^e\} + \{\Delta\ddot{z}_q^e\} \right\rangle + 2\tilde{\xi}_q\tilde{\omega}_q \left\langle \{\dot{z}_{iq}^e\} + \{\Delta\dot{z}_q^e\} \right\rangle + \tilde{\omega}_q^2 \left\langle \{z_{iq}^e\} + \{\Delta z_q^e\} \right\rangle = \tilde{\omega}_q^2 \left\langle \{d_i^e\} + \{\Delta d^e\} \right\rangle \quad (3.20)$$

where, $q = (1,2,.....,R)$; $\{z_{iq}^e\}$ and $\{\Delta z_q^e\}$ are the elemental nodal auxiliary dissipation co-ordinate vector and the corresponding increment , respectively. The matrices ($|K_{Lc}^e|$, $|K_{Lq}^e|$) in Eq. (3.19) are given in Eq. (3.21),

$$[K_{Lc}^e] = \left\langle [K_L^e] + [K_v^e]\mathrm{G}^\infty (1 + \sum_{q=1}^{R} \alpha_q) \right\rangle, [K_{Lq}^e] = [K_v^e]\mathrm{G}^\infty \alpha_q \quad (3.21)$$

The steady state vibration of the overall smart laminated composite plate is assumed as a result of steady state excitation and it is actively controlled by supplying the external voltage across the thickness of PFRC constraining layer according to the velocity feedback control strategy (Eq. (2.28)) as follows,

$$V = -k_d \dot{w}_s = -k_d \left(\dot{w}_{si} + \Delta\dot{w}_s \right) \quad (2.28)$$

The steady state motion of the overall plate during its vibration could be modeled by harmonic balance method (HBM) in which the forms of solutions ($\{\Delta d^e\}$, $\{z_q^e\}$) are expressed in Eqs. (2.24) and (3.22),

$$\{d^e\} = \{a_0\} + \sum_{r=1}^{F} \left\langle \{a_r\}\cos(r\omega t) + \{b_r\}\sin(r\omega t) \right\rangle \quad (2.24)$$

$$\{z_q^e\} = \{a_{q0}\} + \sum_{r=1}^{F} \left\langle \{a_{qr}\}\cos(r\omega t) + \{b_{qr}\}\sin(r\omega t) \right\rangle \quad (3.22)$$

Using these forms of solutions, the resulting equations of motion after implementation of GHM method can be expressed in the frequency-domain. A similar conversion of equations of motion from time-domain to frequency-domain along with the present control strategy is presented in Sections 3.2.2 and 3.2.3. Following the same procedure, the global equations of motion in the frequency-domain can be expressed in a form as described by Eq. (3.27-3.28) which are reproduced as,

$$[K_t]\{\Delta X\} - \sum_{q=1}^{R} [K_{Lqt}]\{\Delta X_q\} = \{f_{it}\} + \{f_t^T\} + \{f_t^P\} - (\omega_i + \Delta\omega)[C_s]\{w_{si}\} - \omega_i[C_s]\{\Delta w_s\} + \{f_w\}\Delta\omega \quad (3.27)$$

$$[K_{tq}]\{\Delta X\} - [K_{dtq}]\{\Delta X_q\} = \{f_{itq}\} + \{f_{wq}\}\Delta\omega\,,\ q = 1,2,.....,R. \quad (3.28)$$

Now, expressing the displacements ($\{\Delta w_s\}, \{w_{si}\}$, Eq. (2.30)) at sensing point in terms of the global nodal displacement vectors ($\{X_i\}, \{\Delta X\}$) according to Eq. (2.34), ($\{w_{si}\} = [N_s]\{X_i\}$ and $\{\Delta w_s\} = [N_s]\{\Delta X\}$).

The final form of equations of motion can be represented as given in Eq. (3.30) that is rewritten as,

$$[K_{eq}]\{\Delta X_{eq}\} = \{f_{eq}\} + \{f_{eq}^{w}\}\Delta\omega \tag{3.30}$$

The methodology for solutions of this form of equations is described in Section 2.3 and it is also followed at present in evaluation of the nonlinear frequency responses of the graded laminated composite plate integrated with a ACLD layer.

6.3 Numerical results and discussions

The primary objective in the present design of a graded composite lamina (Fig. 5.1) and CGLCP (Fig. 5.18) is to achieve the continuous variations of material properties and stresses along the thickness direction. This is verified in Chapter 5 and it may be concluded that the detrimental effects of mismatch of material properties at the inter-laminar surfaces of laminated composite structures can be eliminated by the use of present graded composite lamina. However, for this modification of CLCP into CGLCP, the corresponding changes in the dynamic behavior of the structure is another important issue that is numerically evaluated in the present section considering the symmetric and asymmetric CGLCPs/CLCPs (Figs. (5.18(a)-(b))) integrated with a layer of ACLD. The geometrical properties of the overall laminated plate are considered as, $a = b = 0.4$ m, $h = 4$ mm, $h_p = 250$ μm, $h_v = 1$ mm. Unless otherwise mentioned, the piezoelectric fiber orientation angle (ψ) and the FVF in the PFRC constraining layer are considered as 0^{o} and 40%, respectively. The material properties of the PFRC corresponding to its 40% FVF are given in Section 2.4. The material properties of the viscoelastic layer in terms of the GHM parameters are given in Section 3.3 (Table 3.1) The simply supported boundary conditions ($v_0 = 0, w_0 = 0, \theta_y = 0, \phi_y = 0, \gamma_y = 0$ at $x = 0, a$ and $u_0 = 0$, $w_0 = 0$, $\theta_x = 0$, $\phi_x = 0$, $\gamma_x = 0$ at $y = 0, b$) over the boundaries of the overall laminated composite plate are considered. The overall plate is subjected to a uniformly

distributed transverse harmonic mechanical load as it is considered in the previous problem (Chapter 3). The responses at the middle point of the overall plate are evaluated for presenting the numerical results. Since the transient transverse displacement ($w(t)$) at the middle point of the overall plate is in combination of different harmonics, the maximum value of $w(t)$ within a period of vibration at a frequency is computed and presented as, $W = w(t)_{\max} / h$. Similar to the previous numerical analysis (Section 3.3), the maximum value of W is considered as less than h and three terms ($r = 1, 2, 3$) of Fourier series are considered for the solutions. Also, the maximum displacement (W_{peak}) of the frequency response corresponding to the fundamental mode of vibration of the overall laminated plate is taken as a parameter for measuring the active damping in the overall laminated plate cause by ACLD layer.

Table 6.1 Verification of fundamental natural frequency

Laminated plate	Dimension less fundamental natural frequency	
	present	(Reibero and Petyt 1999)
Laminate $(0^0 / 90^0 / 0^0)$	15.222	15.191
Laminate $(0^0 / 90^0 / 0^0 / 90^0)$	10.361	10.231

6.3.1 Verification of present finite element formulation

The present incremental finite element formulation is verified through the computation of linear and nonlinear free vibration responses of CLCPs without ACLD layer ($h_p \approx 0$, $h_v \approx 0$, $k_d = 0$). The computed dimensionless natural frequencies of symmetric and asymmetric CLCPs are illustrated in Table 6.1 together with the similar results available in the literature Reibero and Petyt (1999). The responses for nonlinear free vibration of a symmetric CLCP are tabulated in Table 6.2 together with the similar results for an identical plate analyzed in Han and Petyt (1997). It may be observed from these tables that the present results are in excellent agreement with the previously published results (Han and Petyt 1997; Reibero and Petyt 1999) thus verifying the present formulation.

Next, the implementation of GHM method is verified by modeling the stiffness of viscoelastic layer according to the conventional complex stiffness method.

Table 6.2 Comparison of nonlinear frequency ratio (ω/ω_0) for a fully clamped rectangular laminated composite plate with the similar results given by Han and Petyt (1997) (ω_0 is the fundamental natural frequency).

W	0.2	0.4	0.6	0.8	1.0	1.2
ω/ω_0 (Han and Petyt 1997)	1.0058	1.0232	1.0516	1.0903	1.1382	1.1941
ω/ω_0 (Present)	1.0056	1.0281	1.0493	1.0892	1.1363	1.1945

6.3.2 Free vibration response of CLCP/CGLCP

Figure 6.2 illustrates the linear frequency responses of overall asymmetric CLCP when the constrained viscoelastic layer is modeled using either GHM method or complex stiffness method. It may be observed from Fig. 6.2 that the result for GHM method is in good agreement with that for conventional complex stiffness method. This comparison verifies the implementation of GHM method in the present formulation of a laminated composite plate integrated with a layer of ACLD.

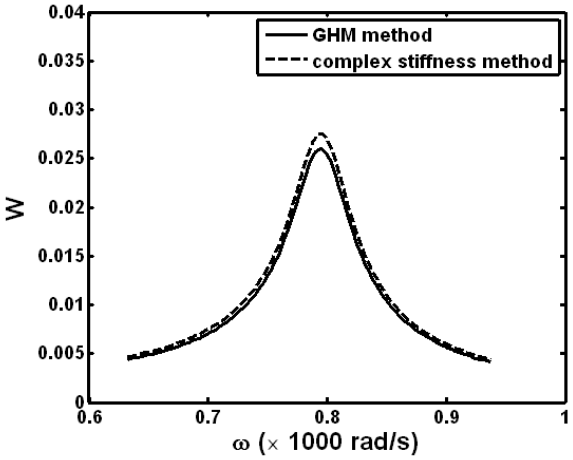

Fig. 6.2. Linear frequency responses of asymmetric overall CLCP when the constrained viscoelastic layer is modeled using either GHM method or complex stiffness method ($p = 50$ N/m², $k_d = 25$, Laminate: $(90^0/0^0/90^0/0^0)$.

Table 6.3 illustrates the dimensionless natural frequencies for first four bending modes of symmetric and asymmetric CGLCPs/CLCPs. It may be observed from this table that the natural frequency of any mode of vibration insignificantly varies with the value of power-law exponent (n). But, for any value of power-law exponent (n), the

natural frequency decreases when a CLCP is converted to a CGLCP. This may be mainly due to the fact that the decrease of average stiffness of the laminate for incorporation of graded plies. As a consequence, the decrease in average stiffness of the laminated plate depends on the number of graded plies and the corresponding thickness (of graded plies) utilized for conversion of CLCP into CGLCP. However, this difference in the frequency of free vibration does not change significantly when the laminated plates freely vibrates at a moderate amplitude as it is illustrated in Table 6.4 considering the nonlinear free vibration of a laminated plate (CLCP/CGLCP) near its fundamental frequency.

Table 6.3 Dimensionless natural frequencies ($\Omega = \omega a^2\sqrt{\rho/\left(E_m h^2\right)}$) for first four bending modes of symmetric and asymmetric CGLCPs/CLCPs (E_m is the Young's modulus of matrix-phase material).

Laminate		Dimensionless natural frequency (Ω)			
		Ω_1	Ω_2	Ω_3	Ω_4
Symmetric	GLCP (n = 1)	24.125	52.874	83.626	102.751
	GLCP (n = 2)	23.706	51.838	82.626	101.301
	CLCP	25.312	55.379	87.771	107.678
Asymmetric	GLCP (n = 1)	21.897	62.301	62.301	92.663
	GLCP (n = 2)	21.760	61.880	61.880	92.024
	CLCP	24.536	71.155	71.155	104.761

Table 6.4 Dimensionless frequencies ($\Omega = \omega a^2\sqrt{\rho/\left(E_m h^2\right)}$) for different amplitudes of free vibration of symmetric and asymmetric CGLCPs/CLCPs (ω is near the fundamental frequency).

Laminate		Dimensionless frequency (Ω)		
	W	0.2	0.4	0.6
Symmetric	GLCP (n = 1)	24.214	24.478	24.917
	GLCP (n = 2)	23.792	24.047	24.465
	CLCP	25.395	25.724	26.244
Asymmetric	GLCP (n = 1)	22.001	22.307	22.811
	GLCP (n = 2)	21.860	22.158	22.646
	CLCP	24.627	24.961	25.486

6.3.3 Effect of load- amplitude (p)

Figure 6.3(a) shows the controlled nonlinear frequency responses of symmetric CGLCP ($n=1$) and CLCP for different values of load-amplitude (p) with a constant value of feedback control gain (k_d). The corresponding variations of required control voltage

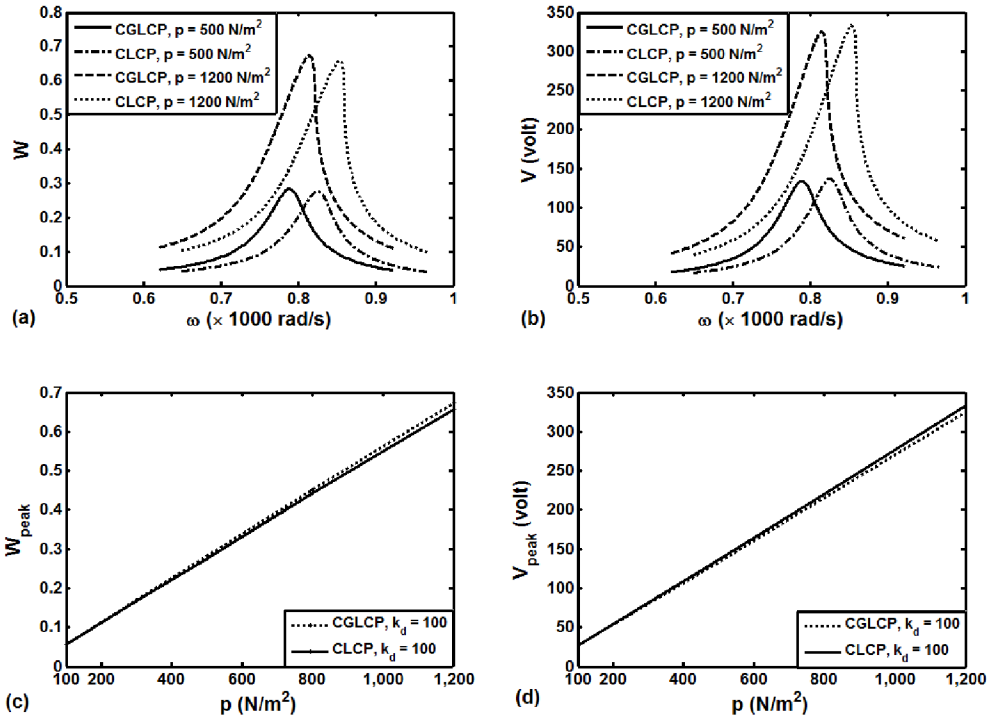

Fig. 6.3 (a) Nonlinear frequency responses of the overall symmetric CGLCP ($n=1$)/CLCP ($0^0/90^0/0^0$) and (b) the corresponding variations of control voltage ($k_d=100$); variations of (c) peak-amplitude (W_{peak}) of frequency response curve and (d) the corresponding control voltage (V_{peak}) with the load-amplitude (p).

across the thickness of the PFRC constraining layer of ACLD arrangement are also illustrated in Fig. 6.3(b). It may be observed from these figures that the frequency responses shift a little towards lower frequency when the substrate CLCP is replaced by CGLCP. This may be mainly due to the decrease in the stiffness of the overall plate as a CLCP is converted to CGLCP. But, there are no significant changes of peak-amplitude of vibration and the corresponding required control voltage for a particular value of load-amplitude. In order to exemplify this observation, the variations of peak-amplitude (W_{peak}) of frequency response curve and the corresponding control voltage (V_{peak}) with

the load-amplitude are illustrated in Figs. 6.3(c) and 6.3(d), respectively. Similar results in case of the conversion of an asymmetric CLCP to an asymmetric CGLCP are also demonstrated in Fig. 6.4. In this case of asymmetric laminated composite plates, changes of peak-amplitude and corresponding control voltage for the modification of CLCP into CGLCP are more than those of the previous case (Fig. 6.3). These changes of peak-amplitude and corresponding control voltage (Fig. 6.4) also increase as the load-amplitude increases or the overall plate encounters greater nonlinear deformation.

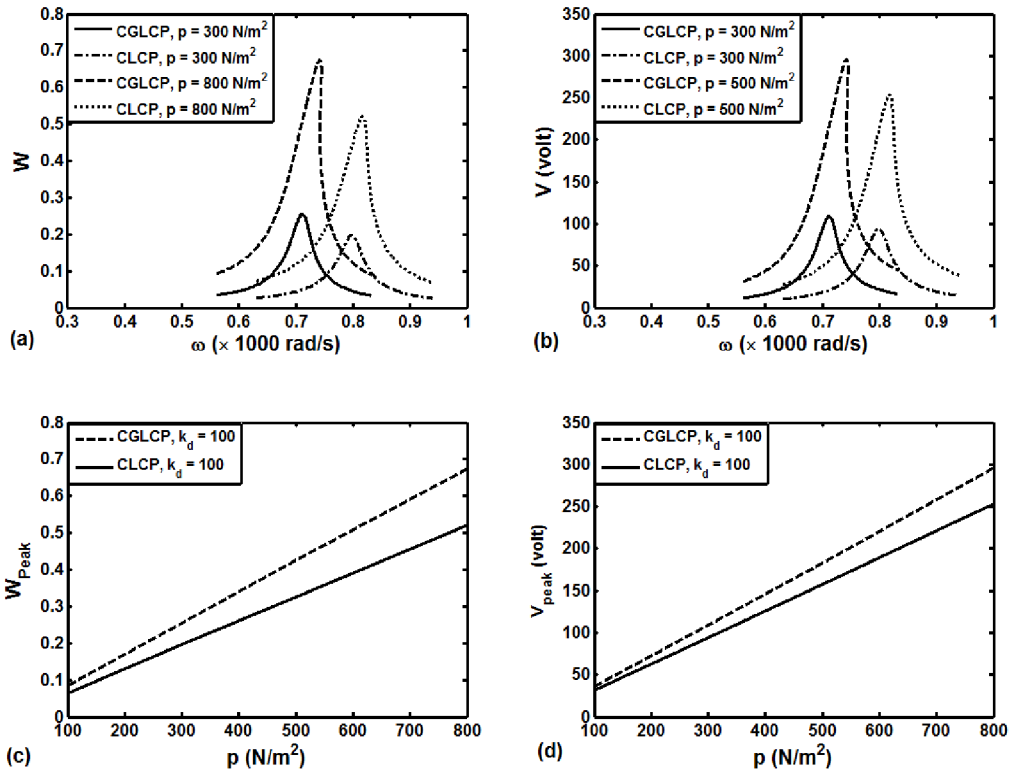

Fig. 6.4 (a) Nonlinear frequency responses of the overall asymmetric CGLCP (n = 1)/CLCP $(90^0/0^0/90^0/0^0)$ and (b) the corresponding variations of control voltage ($k_d = 100$); variations of (c) peak-amplitude (W_{peak}) of frequency response curve and (d) the corresponding control voltage (V_{peak}) with the load-amplitude (p).

In case of the symmetric laminates of a specified thickness (Fig. 5.18 (a)), the original conventional plies of CLCP are retained and the graded plies are used between the

conventional plies in the corresponding CGLCP. But, in asymmetric laminates of a specified thickness (Fig. 5.18(b)), the 2nd and 3rd conventional plies of CLCP are replaced by the graded plies for its modification into CGLCP. Thus, although the continuous stresses in the both (symmetric and asymmetric) CGLCPs are achieved (Figs. 5.22-5.23), but the modified stacking sequence for CGLCP within a constant thickness of laminate is an important issue for close dynamic response of CGLCP to that of corresponding CLCP.

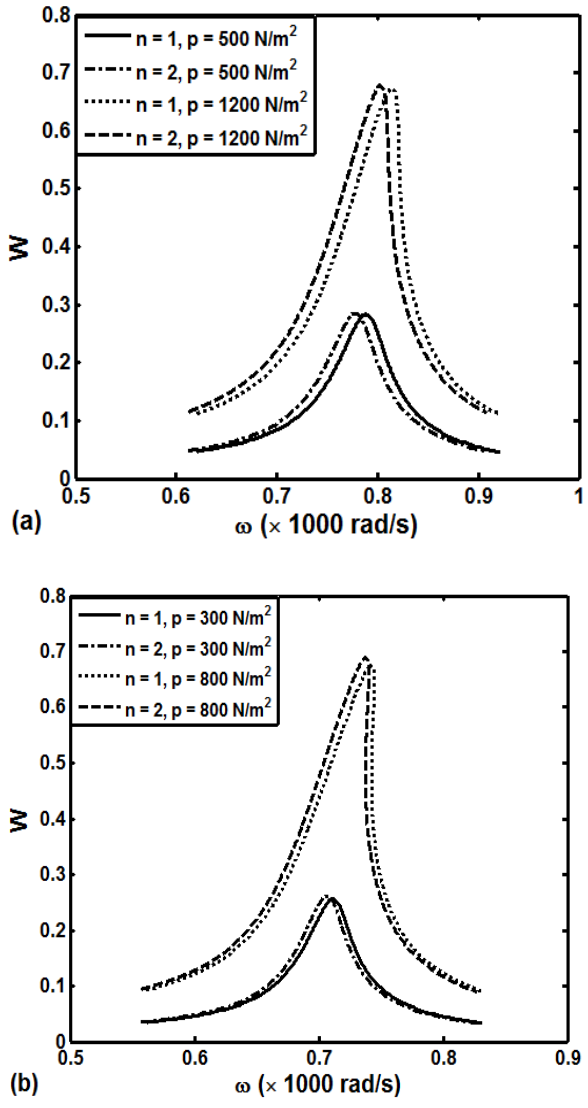

Fig. 6.5 Nonlinear frequency responses of the overall (a) symmetric and (b) asymmetric CGLCPs for different values of power-law exponent (n)($k_d = 100$).

6.3.4 Effect of power law exponent (n)

The change in frequency response of symmetric/asymmetric CLCP for its modification into symmetric/asymmetric CGLCP is illustrated in Figs. 6.3-6.4 considering a particular value of power-law exponent ($n=1$) of the graded plies in CGLCP. Now, if the value of power-law exponent for graded plies in CGLCP is considered as either 1 or 2, then the corresponding frequency responses of symmetric and asymmetric CGLCPs are illustrated in Figs. 6.5(a) and (b), respectively. For a particular value of load-amplitude, it may be observed from Figs. 6.5(a)-(b) that there is no significant effect of power-law exponent (n) of graded plies within the symmetric/asymmetric CGLCP on its (CGLCP) frequency response.

6.3.5 Effect of control gain (k_d)

For a constant load-amplitude, the variation of peak-amplitude (W_{peak}) of frequency response curve of symmetric CLCP/CGLCP with the control gain (k_d) is demonstrated in Fig. 6.6(a). The variation of corresponding control voltage (V_{peak}) is also illustrated in Fig. 6.6(b). Similar results for asymmetric CLCP/CGLCP are also shown in Figs. 6.6(c)-(d). It may be observed from these figures that the ACLD layer can induce a significant damping in the CGLCP/CLCP in expense of reasonable applied voltage. The nature of variation of peak-amplitude with control gain (k_d) does not differ as a CLCP is modified into a CGLCP. But, for a particular value of control gain (k_d), the damping in the CGLCP is less than that (damping) in the corresponding CLCP.

6.3.6 Effect of viscoelastic-layer thickness (h_v) in ACLD arrangement

Figures 6.7(a) and (b) illustrate the variations of peak-amplitude of frequency response curve with the thickness (h_v) of the constrained viscoelastic layer for overall symmetric and asymmetric CLCPs/CGLCPs, respectively. The load-amplitude for a particular type (symmetric or asymmetric) of laminate remains constant. It may be observed from these

figures that the nature of variation of peak-amplitude with the thickness of viscoelastic layer remains the same as a CLCP is converted into a CGLCP.

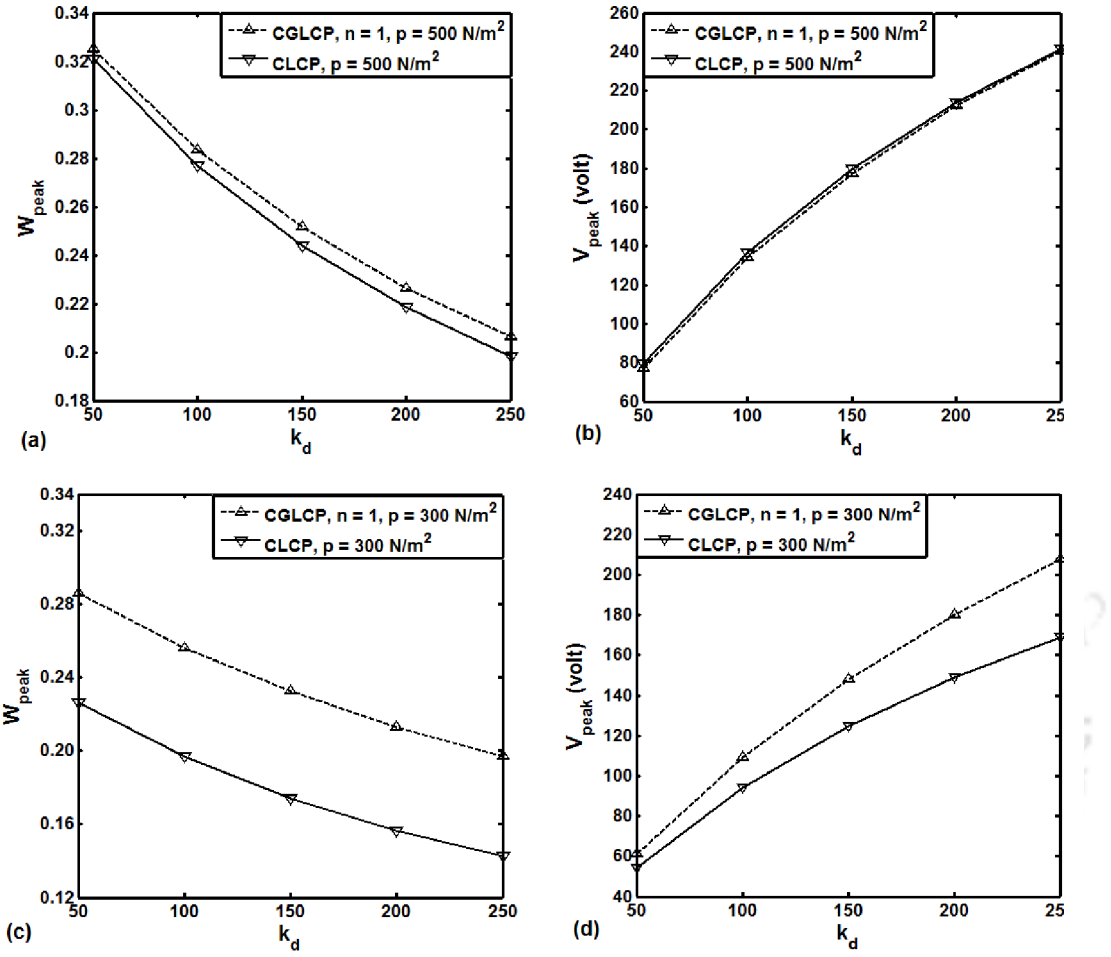

Fig. 6.6 Variations of peak-amplitude (W_{peak}) of frequency response curve and the corresponding control voltage (V_{peak}) with the control gain (k_d); (a)-(b) symmetric CGLCP/CLCP, (c)-(d) asymmetric C GLCP/CLCP.

It may also be observed from the same figures that for any value of control gain (k_d), the damping in the overall symmetric/asymmetric laminate (CLCP/CGLCP) significantly increases up to certain value of the increasing thickness of constrained viscoelastic layer (Fig. 6.7). Also, there is no effective utilization of active constraining layer (PFRC) at a higher thickness of the constrained viscoelastic layer. However, for any of the laminates, the variations of peak-amplitude for two different values of control gain (k_d) show that the active constraining layer (PFRC) effectively increases the damping in the overall

laminate for an increase of control gain (k_d) when the constrained viscoelastic layer is of small thickness. Thus, for effective use of the active constraining layer (PFRC), a small thickness of the viscoelastic layer is to be assigned.

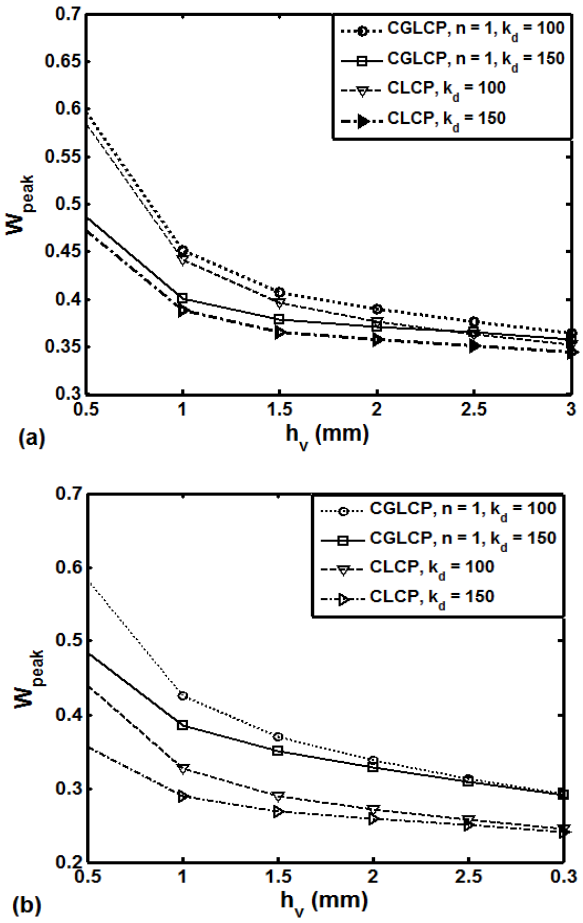

Fig. 6.7 Variation of peak-amplitude (W_{peak}) of frequency response curve with the thickness of the constrained viscoelastic layer, (a) symmetric CGLCP/CLCP, (b) asymmetric CGLCP/CLCP.

6.3.7 Effect of fiber-orientation angle (ψ) in PFRC layer

The variations of peak-amplitude of frequency response curve with the piezoelectric fiber orientation angle (ψ) in the PFRC constraining layer of ACLD layer are illustrated in Figs. 6.8(a) and (b) for symmetric and asymmetric CLCP/CGLCP, respectively. For symmetric laminates (CLCP and the corresponding CGLCP), it may be observed from Fig. 6.8(a) that the maximum actuation-capability of ACLD layer occurs when the

piezoelectric fibers in PFRC layer are oriented at an angle of $\pm 45^{o}$. But, the same (ψ) changes to $\pm 90^{o}$ for asymmetric laminates (CLCP and the corresponding CGLCP) (Fig. 6.8(b)). It may also be observed from Fig. 6.8 that the nature of variation of peak-amplitude with ψ does not alter as a CLCP is converted to CGLCP. But, the significant change in the magnitude of peak-amplitude may occur especially at the angle (ψ) of maximum actuation-capability of ACLD layer.

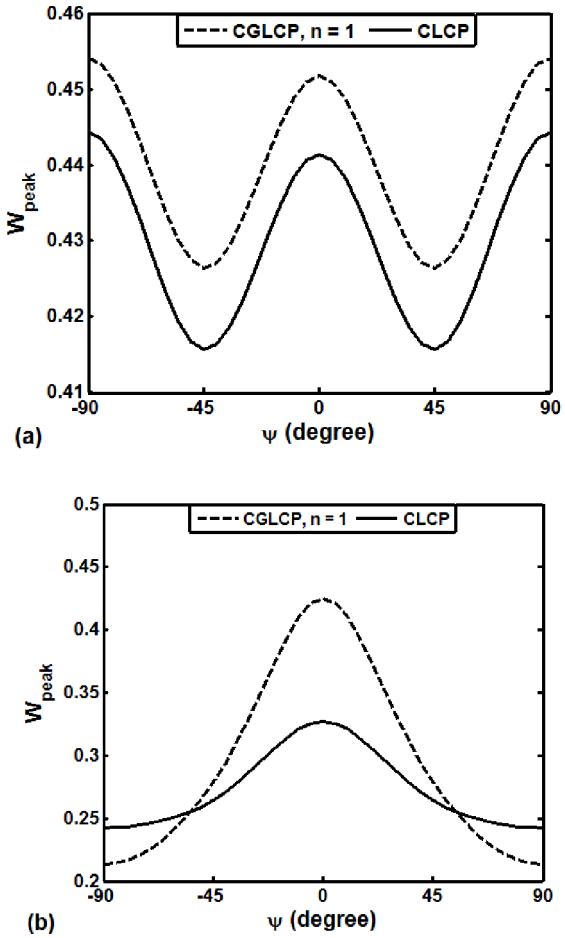

Fig. 6.8 Variation of peak-amplitude (W_{peak}) of frequency response curve with the piezoelectric fiber orientation angle (ψ) of PFRC constraining layer; (a) symmetric CGLCP/CLCP, (b) asymmetric CGLCP/CLCP ($k_d = 100$, $p = 800$ N/m²).

6.4 Conclusions

In order to achieve continuous variations of material properties across the thickness of a CLCP, a new lamination scheme is proposed in Chapter 5 that is basically the

conversion of a CLCP into a CGLCP utilizing graded as well as conventional composite plies. For this conversion, the corresponding changes in the dynamic characteristics are demonstrated in the present chapter through the analysis of nonlinear frequency responses of CLCP/CGLCP integrated with an ACLD layer. The constraining layer of ACLD layer is made of PFRC. For achieving active damping in the overall laminated plate, the external voltage across the thickness of PFRC constraining layer is supplied according to a negative velocity feedback control strategy. The frequency response analysis of overall CLCP/CGLCP is carried out through an incremental finite element formulation based on the first order shear deformation theory (FSDT) and von Karman nonlinear strain-displacement relations. Employing the Hamilton's principle, the incremental finite element equations of motion of the overall laminated plate are first derived in the time-domain and then these are expressed in the frequency-domain assuming periodic vibration of the same (overall plate). The numerical results for free vibration of the overall laminated plate (CLCP/CGLCP) in the frequency-domain reveal a decrease of every natural frequency when a CLCP is modified into a CGLCP. But, this decrease does not alter significantly when the plates vibrate freely at moderate amplitude. The numerical illustrations also reveal that the modified stacking sequence for CGLCP within a constant thickness of laminate is an important issue for close response of CGLCP to that of the corresponding CLCP. The same issue is also important for the changes in actuation-capability of ACLD layer and corresponding required control voltage even though the nature of controlled response does not alter for the modification of conventional laminate (CLCP). It is observed that the value of power-law exponent used for micro-structure of (Fig.5.12) graded composite ply does not have much effect on the responses of CGLCP.

Chapter 7

CONCLUSIONS

Based on the numerical results and discussions of problems addressed in the present thesis, important conclusions inferred have been summarized in this chapter. Conclusions are presented in two parts viz. general conclusions and specific conclusions.

Some of the general conclusions drawn from the present work are as follows:

7.1 General conclusions

1. An incremental three dimensional finite element model of the isotropic FG plates integrated with a PFRC-actuator layer is developed for their geometrically nonlinear frequency-response analysis in the presence of temperature gradient across the thickness of substrate FG plate.
2. An arc-length extrapolation technique (Lau et al. 1990) is implemented for the numerical solutions along with the proposition of a new strategy for selecting the arc-length in each incremental step.
3. The developed FE model along with arc-length extrapolation technique has been used to study the effect of temperature on the vibration characteristics of smart FG plate in frequency-domain.
4. As a novel development, an incremental three dimensional FE formulation for geometrically nonlinear frequency-response analysis of heated isotropic FG plates integrated with an ACLD layer is proposed.
5. Performance of the PFRC actuator layer in active control of vibration of smart FG plate has been studied and the effects of different important parameters relevant to PFRC have been understood.
6. Numerical results reveal that temperature gradient across the thickness of FG plate has a pronounced effect on the performance of a PFRC/ACLD in control of smart FG plate.
7. Sensitivity of size and location of PFRC/ACLD patches on control performance has been studied and, optimal size and location has been recommended.

8. A new design of graded fiber-reinforced composite lamina is proposed and the effective elastic properties of such lamina are determined.
9. Efficacy of such graded lamina in mitigating the high inter-laminar stresses has been demonstrated by performing numerical stress analysis of laminates made of such laminas.
10. Performance of graded laminates are compared with that of conventional laminates to demonstrate the superiority of the proposed graded laminate.

7.2 Specific conclusions

The following specific conclusions are drawn from the work carried out in this thesis.

1. It is observed that the PFRC-actuator layer can induce more damping in the overall smart isotropic FG plate when it is attached to the metal-rich surface of substrate FG plate instead of its (smart layer) attachment to the ceramic-rich surface of the same substrate plate.
2. A piezoelectric fiber orientation angle in the PFRC-actuator layer has negligibly small effect on the controlled frequency responses of the overall smart isotropic FG plate.
3. Initial thermal bending deflection of the overall smart FG plates, due to temperature gradient across the thickness of the substrate isotropic FG plate remains almost constant during vibration under a harmonic excitation of any frequency.
4. It is observed that fundamental frequency of vibration of FG plate initially decreases as the temperature gradient increases. But beyond a certain value of temperature, fundamental frequency starts to increase due to the significant effect of thermal bending of the overall FG plate.
5. The increase of initial thermal bending deflection may also cause softening structural behavior of the overall FG plate although it (overall plate) usually exhibits hardening structural behavior.

6. In the case of a constant temperature gradient, fundamental frequency of a FG plate deceases as metal volume fraction increases but beyond a certain value of metal volume fraction, fundamental frequency of the same increases.
7. It is observed that the initial temperature gradient and hence the initial thermal bending deflection significantly affects the control performance of a smart FG plate having PFRC actuator layer.
8. At a high temperature gradient, the initial thermal bending deflection causes a significant increase in the control voltage requirement to achieve effective damping of vibration of smart FG plate.
9. Requirement of such high voltage limits the use of PFRC actuators in terms of exceeding the limit of externally applied voltage.
10. It is observed that the active damping in the overall smart FG plate may increase with the increase of temperature when it (overall plate) alters its hardening structural behavior to softening one at a high temperature. But, since this occurs at high frequency of vibration of the overall plate, the corresponding required control voltage according to velocity feedback control strategy reaches to too high value that may be impractical for the use of PFRC-actuator layer.
11. The dynamic analysis of isotropic FG plates integrated with ACLD layer reveals that the active damping in the overall plate significantly increases when PFRC-actuator layer is used in the form of ACLD layer instead of its (PFRC) direct attachment to the host-plate-surface. However, the dynamic characteristics of the overall smart isotropic FG plate remain almost the same if the PFRC-actuator layer is substituted by the ACLD layer. The only change appears in the active damping within the overall FG plate.
12. It is observed that a higher thickness of viscoelastic layer in ACLD arrangement causes ineffective utilization of corresponding active constraining layer (PFRC) for inducing active damping in the overall smart FG plate. A small thickness of

viscoelastic layer is to be considered in view of the effective use of both the layers (viscoelastic and PFRC layers) in ACLD arrangement.

13. It is observed for a particular mode of vibration of the overall smart FG plate that the effective location of the PFRC-actuator/ACLD patch on the surface of substrate FG plate is independent of temperature gradient across the thickness of substrate plate. But, its (patch) effective size may vary for different temperature gradients.
14. The numerical analysis of effective properties of graded orthotropic fiber-reinforced composite lamina reveals that the nature of variation of any elastic coefficient is similar to the corresponding nature of variation of FVF along the thickness direction.
15. For a particular functional (power-law) variation of FVF, the nature of variation of any elastic coefficient is not dependent on the number of layers of coplanar unidirectional fibers across a constant thickness of the lamina. The number of such layers of coplanar fibers within a specified thickness of lamina is important only for the variations of elastic coefficients in a continuous manner.
16. The bending analysis of both the plates (CLCP and CGLCP) reveals ample changes of laminate-rigidity and maximum values of stresses within the laminate while achieving the advantage of continuous variations of material properties along the thickness direction.
17. The nonlinear frequency response analysis of both the laminated composite plates (CLCP and CGLCP) integrated with an ACLD layer reveals that the dynamic characteristics of a CLCP may be close to those of the corresponding CGLCP. But, this similarity primarily depends on the way of utilization of graded orthotropic composite ply in the implementation of proposed lamination scheme. This observation also holds for the active damping within the overall smart laminated composite plate caused by ACLD layer.
18. From the frequency response analysis of CGLCP integrated with an ACLD layer, it is observed that the value of power-law exponent corresponding to the variation of FVF of graded composite ply does not have much effect on the dynamic behavior of

the overall smart CGLCP in the frequency domain. This observation implies to consider a value of power-law exponent of graded composite ply based on the static analysis of CGLCP.

7.3 Scope for future work

Although the objectives of this thesis have been fulfilled by the contributions presented in the preceding chapters of this dissertation, further research may still be pursued for the development of high performing smart graded structures. Some of the future works which may be readily undertaken in line with the present work are as follows,

Although the objectives of this thesis have been fulfilled by the contributions presented in the preceding chapters of this dissertation, further research may still be pursued for the development of high performing smart graded structures. Some of the future works which may be readily undertaken in line with the present work are as follows,

(a) Development of analytical model for geometrically nonlinear analysis of smart isotropic FG plate/shell under the harmonic excitation in the presence of temperature gradient across the thickness of host FG plate. Although this study is presently carried out using FE procedure, but the same could be performed analytically that is still unavailable in the literature. The main difficulty in the development of analytical model is the consideration of mode-shapes under thermal environment. The thermal environment imposes time-invariant thermal deformation of the smart plate and the mode-shapes of vibration would be coupled with this thermal deformation. A simple approach is to consider mode-shapes of vibration and the time-invariant thermal mode of deformation separately in the solution. But, one may not get accurate results in this approach that needs further investigation.

(b) Design of graded orthotropic fiber-reinforced composite lamina with varying length of fibers along the thickness direction. In the present design of graded fiber-reinforced composite, the variation of fiber-volume fraction is achieved through the

variation of cross sectional area of fibers. But there may be practical difficulty in sustaining the fibers of too small cross sectional area under large deformation. This difficulty may be alleviated through the variation of length of fibers along the thickness direction instead of the cross sectional area. This arrangement provides greater flexibility of the lamina and there will be no chance of fiber-failure. But, the practical difficulty arises in fabrication of such lamina due to the presence of short as well as continuous fibers with a specified strategy of their arrangement. However, this work could be performed for further theoretical development of graded fiber-reinforced composite lamina.

(c) The experimental verifications of the theoretical models developed in this thesis are also an important scope for further research work. In the present theoretical development of smart FG plates, a significant control-power of 1-3 piezoelectric composite actuators is observed. Certain new dynamic characteristics of the heated isotropic FG plates are also found. In order to verify these theoretical findings, the corresponding experiential studies are inevitable issues which are the subsequent studies.

References

Aboudi J, Pindera MJ, Arnold SM. A coupled higher-order theory for functionally graded composites with partial homogenization. Composites Engineering 1995; 33:931-966.

Aboudi J, Pindera MJ, Arnold SM. Higher-order theory for functionally graded materials. Composites: Part B 1999;30:777-832.

Agarwal BN, Treanor KE. Shape Control of a Beam Using Piezoelectric Actuators. Smart Materials and Structures 1999; 8: 729-740.

Akbarzadeh AH, Abbasi M, Hosseini Zad SK, Eslami MR. Dynamic analysis of functionally graded plates using the hybrid Fourier-Laplace transform under thermo mechanical loading. Meccanica 2011; 46:1373–1392.

Alibeigloo A, Nouri V, Static analysis of functionally graded cylindrical shell with piezoelectric actuator using differential quadrature method. Composite Structures 2010, 92(8):1175–1185.

Alibeigloo A. Exact solution for thermo-elastic response of functionally graded rectangular plates. Composite Structures 2010; 92:113–121.

Alijani F, Nejad FB, Amabili M. Thermal effects on nonlinear vibrations of functionally graded rectangular plates. *EOCN Italy 2011*, July 24-29.

Allahverdizadeh, Naei MH, NikkhahBahrami M. Nonlinear free and forced vibration analysis of thin circular functionally graded plates. Journal of Sound and Vibration 2008; 310: 966-984.

Altay G, Kmeci MCD. Variational principles and vibrations of a functionally graded plate. Computers and Structures 2005; 83:1340–1354.

Aragh BS, Yas MH. Three-dimensional free vibration of functionally graded fiber orientation and volume fraction cylindrical panels. Materials and Design 2010; 31: 4543-4552.

Aragh BS, Yas MH. Three-dimensional free vibration analysis of four-parameter continuous grading fiber reinforced cylindrical panels resting on Pasternaak foundations. Archive of Applied Mechanics 201; 81:1759-1779.

Azvine B, Tomlinson GR, Wynne RJ. Use of active constrained-layer damping for controlling resonant vibrations. Smart Materials and Structures 1995; 4:1-6.

Bailey T, Hubbard JE, Distributed piezoelectric polymer active vibration control of a cantilever beam. Journal of Guidance, Control, and Dynamics 1985; 8:605–611.

Balamurugan V, Narayanan S. Shell Finite Element for Smart Piezoelectric Composite Plate/Shell Structures and Its Application to the Study of Active Vibration Control. Finite Elements in Analysis and Design 2001; 37:713-738.

Balamurugan V, Manikandan B, Narayanan S. A Higher Order Finite Element Modeling of Piezolaminated Smart Composite Plates and its Application to Active Vibration Control. International Journal of Computational Methods 2007; 4:141-162.

Batra RC, Jin J. Natural frequencies of functionally graded anisotropic rectangular plate. Journal of Sound and Vibration 2005; 282:509-516.

Batra RC, Liang XQ, Yang JS. The Vibration of Simply Supported Rectangular Elastic Plate Due to Piezoelectric Actuators. International Journal of Solids and Structures 1996; 33:1597-1618.

Baz, A, Poh, S. Performance of an active control system with piezoelectric actuators. Journal of Sound and Vibration 1988; 126(2):327-343.

Baz A, Poh S. Experimental Implementation of the Modified Independent Modal Space Control Method. Journal of Sound and Vibration 1990; 139:133-149.

Baz A, Poh S, Optimal Vibration Control with Modal Positive Position Feedback. Optimal Control Applications and Methods 1996; 17:141-149.

Baz A, Ro, J. Optimum Design and Control of Active Constrained Layer Damping. ASME Journal of Vibrations and Acoustics 1995a); 117B: 135-144.

Baz A, Ro J, Vibration control of plates with active constrained layer damping. SPIE 1995b; 2445:393-409.

Baz A. Ro J. Vibration Control of Plates with Active Constrained Layer Damping. Smart Materials and Structures 1996; 5:272-280.

Baz, A. Active constrained layer damping, DAMPING'93 Conference, San Francisco, CA 1993, IBB 1-23.

Baz A, Poh S, Feder J. Independent Modal Space Control with Positive Position Feedback. ASME Journal of Dynamic Systems, Measurement and Control 1992; 114:96-103.

Bedjilili Y, Tounsi A., Berrabah HM., Mechab I., Adda BEA, Benaissa S. Natural frequencies of composite beams with a variable fiber volume fraction including rotary inertia and shear deformation. Applied Mathematics and Mechanics 2009;

30:717-726.

Behjat B, Khoshravan MR. Geometrically nonlinear static and free vibration analysis of functionally graded piezoelectric plates. Composite Structures 2012; 94:874-882.

Belabed Z, Houari MSA, Tounsi A, Mahmoud SR, Bég OA. An efficient and simple higher order shear and normal deformation theory for functionally graded material (FGM) plates. Composites: Part B 2014; 60:274-283.

Benachour A, Tahar HD, Atmane HA, Tounsi A, Ahmed MS. A four variable refined plate theory for free vibrations of functionally graded plates with arbitrary gradient. Composites: Part B 2011; 42:1386-1394.

Benatta MA, Mechab I, Tounsi A, Adda BEA. Static analysis of functionally graded short beams including warping and shear deformation effects. Computational Materials Science 2008; 44:765-773.

Bent AA, Hagood NW, Rodgers JP. Anisotropic Actuation with Piezoelectric Fiber Composites. Journal of Intelligent Material Systems and Structures 1995; 6:338-349.

Bent AA, Hagood NW. Piezoelectric Fiber Composites with Interdigitated Electrodes. Journal of Intelligent Material Systems and Structures 1997; 8:903-919.

Birman V. Active Control of Composite Plates Using Piezoelectric Stiffeners. International Journal for Mechanical Sciences 1993; 35:387-396.

Bouderba B, Houari MSA, Tounsi A. Thermomechanical bending response of FGM thick plates resting on Winkler-Pasternak elastic foundations. Steel and Composite Structures 2013; 14(1):85-104.

Bouiadjra RB, Adda BEA, Tounsi A. Nonlinear thermal buckling behavior of functionally graded plates using an efficient sinusoidal shear deformation theory. Structural Engineering and Mechanics 2013; 48(4):547-567.

Bouremana M, Tounsi A, Kaci A, Mechab I. Controlling thermal deformation by using composite materials having variable fiber volume fraction. Materials and Design 2009; 30:2532–2253.

Bruke SE, Hubbard J. Active Vibration Control of a Simply Supported Beam Using a Spatially Distributed Actuator. IEEE Control System Magazine 1987; 27:25-30.

Chamis CC. Simplified composite micro-mechanics equations of hygral, thermal and mechanical properties. SAMPE Quarterly 1984;14-23.

Chan HLW, Unsworth J. Simple Model for Piezoelectric Ceramic/Polymer 1-3 Composites Used in Ultrasonic Transducer Applications. IEEE Transactions on

Ultrasonics, Ferroelectrics and Frequency Control 1989; 36:434-441.

Chantalakhana C, Stanway R. Active constrained layer damping of clamped-clamped plate vibration. Journal of Sound and Vibration 2001; 241(5):755-777.

Chaudhury Z, Rogers CA. Enhancing Induced Strain Actuator Authority through Attachment to Structural Elements. AIAA Journal 1993; 31:1287-1292.

Chen CQ, Shen YP, Wang XM. Exact Solution of Orthotropic Cylindrical Shell with Piezoelectric Layers under Cylindrical Bending. International Journal of Solids and Structures 1996; 33:4481-4494.

Chen CS. Nonlinear vibration of a shear deformable functionally graded plates. Composite Structures 2005; 68:295-302.

Chen CS, Tan AS. Imperfection sensitivity in the nonlinear vibration of initially stresses functionally graded plates. Composite Structures 2007; 78: 529-536.

Chen CS, Chen TJ, Chen RD. Nonlinear vibration of initially stressed functionally graded plates. Thin-Walled Structures 2006; 44:844–851.

Chen WQ, Ding HJ, Hogzhou. On the free vibration of a functionally graded piezoelectric rectangular plate. Acta Mechanica 2002; 207-216.

Cheung YK, Chen SH, Lau SL. Application of the incremental harmonic balance method to cubic nonlinearity systems. Journal of Sound and Vibration 1990; 140(2): 273-286.

Chi SH, Chung YL. Mechanical behavior of functionally graded material plates under transverse load—Part I: Analysis. International Journal of Solids and Structures 2006; 43:3657–3674.

Chi SH, Chung YL. Mechanical behavior of functionally graded material plates under transverse load—Part II: Numerical results. International Journal of Solids and Structures 2006; 43:3675–3691.

Chiarappa DJ, Claysmith CR. Deformable Mirror Surface Control, Journal of Guidance and Control 1981; 4:27-34.

Cho HK, Rowlands RE. Optimizing Fiber Direction in Perforated Orthotropic Media to Reduce Stress Concentration. Journal of Composite Materials 2009; 43: 1177–1122.

Cho M, Oh J. Higher Order Zig-Zag Theory for Fully Coupled Thermo-Electric-Mechanical Smart Composite Plates. International Journal of Solids and Structures 2004; 41:1331-1356.

Christensen RM. Theory of viscoelasticity: An Introduction, 2nd edition, Academic Press. New York. 1982.

Clark RL, Flemming MR, Fuller CR. Piezoelectric Actuators for Distributed Excitation of Thin Plates: A Comparison between Theory and Experiment. ASME Journal of Vibration and Acoustics 1993; 115:332-339.

Cooley WG. Applications of functionally graded materials in aircraft structures. *Thesis*, 2005, AFIT/GAE/ENY/05-04.

Cotoni V, Masson P, Côté F, A Finite Element for Piezoelectric Multilayered Plates: Combined Higher-Order and Piecewise Linear C^o Formulation. Journal of Intelligent Material Systems and Structures 2006; 17:155-166.

Crawley EF, Lazarus KB. Induced Strain Actuation of Isotropic and Anisotropic Plates. AIAA Journal 1991; 29:944-951.

Crawley EF, Luis JD. Use of piezoelectric actuators as elements of intelligent structures. AIAA Journal 1987, 25:1373–1385.

Crawley EF. Intelligent Structures for Aerospace: A Technology Overview and Assessment. AIAA Journal 1994; 32:1689-1699.

Crawley EF, De Luis JD, Hagood NW, Anderson EH. Development of Piezoelectric Technology for Applications in Control of Intelligent Structures. Proceedings of American Control Conference 1988.

Daniel IM, Lee. JW. Progressive transverse cracking of cross-ply composites laminates", Journal of Composite Materials 1990; 24:1225-1243.

Devasia S, Tesfay M, Paden B, Bayo EAJ. Piezoelectric Actuator Design for Vibration Suppression: Placement and Sizing. Journal of Guidance, Control and Dynamics 1993;16:859-864.

Di Scioscio F, Gasbarri P, Marianetti C, Toglia C. Control of Vibrations of the International Space Station with Piezoelectric Actuators. International Astronautical Federation-56th International Astronautical Congress 2005; 6:3712-3728.

Dimitriads EK, Fuller CR. Active Control of Sound Transmission through Elastic Plates Using Piezoelectric Actuators. AIAA Journal 1991b; 29:1771-1777.

Dimitriads EK, Fuller CR, Rogers CA. Piezoelectric Actuators for Distributed Vibration Excitation of Thin Plates. ASME Journal of Vibration and Acoustics 1991a; 113:100-107.

Dong S, Tong L. Vibration Control of Plates Using Discretely Distributed Piezoelectric Quasi-Modal Actuators/Sensors. AIAA Journal 2001; 39:1766-1772.

Dvorak G, Zuiker J. The effective properties of functionally graded composites I. Extension of the Mori-Tanaka method to linearly varying fields. Composites in Engineering 1994; 4:19-35.

Ebrahimi F, Rastgoo A. An analytical study on the free vibration of smart circular thin FGM plate based on classical plate theory. Thin-Walled Structures 2008; 46:1402–1408.

Ebrahimi F, Rastgoo A. Temperature Effects on Nonlinear Vibration of FGM Plates Coupled with Piezoelectric Actuators", *Journal of solid Mechanics 2009;* 1:271-288.

Ebrahimi F, Rastgoo A. Nonlinear vibration of smart circular functionally graded plates coupled with piezoelectric layers. International Journal of Material Design 2009; 5:157-65.

Ebrahimi F, Rastgoo A, Kargarnovin MH. Analytical investigation on axisymmetric free vibrations of moderately thick circular functionally graded plate integrated with piezoelectric layers. Journal of Mechanical Science and Technology 2008; 22:1058-1072.

EL-Abbasi N, Meguid SA. Finite element modeling of the thermoelastic behavior of functionally graded plates and shells. International Journal of Computational Engineering Science 2000; 1(1):151-165.

Fakhari V, Ohadi A, Yousefian P. Nonlinear free and forced vibration behavior of functionally graded plate with piezoelectric layers in thermal environment. Composite Structures 2011; 93:2310-2321.

Fereidoon A, Asghardokht Seyedmahalle M, Mohyeddin A. Bending analysis of thin functionally graded plates using generalized differential quadrature method. Archives of Applied Mechanics 2011; 81:1523–1539.

Ferreira AJM, Batra RC, Roque CMC, Qian LF, Martins PALS. Static analysis of functionally graded plates using third-order shear deformation theory and a meshless method. Composite Structures 2005; 69:449–457.

Fieldman E, Aboudi J. Buckling analysis of Functionally graded plates subjected to uniaxial loading. Composite Structures 1997; 38:29-36.

Forward RL. Electronic Damping of Orthogonal Bending Modes in a Cylindrical Mast-Experiment. Journal of Spacecraft and Rocket 1981; 18:11-17.

Fu Y, Zhang P, Yang F. Interlaminar stress distribution of composite laminated plates with functionally graded fiber volume fraction. Materials and Design 2010;

31:2904-2915.

Fuller CR, Hansen CH, Synder SD. Active Control of Structurally Radiated Noise Using Piezoceramic Actuators. Proceedings of the Inter-Noise, Long Beach, C.A. 1989; 509-512.

Fuller CR, Synder SD, Hansen CH, Silcox RJ. Active Control of Interior Noise in Model Aircraft Fuselages Using Piezoceramic Actuators. AIAA Journal 1992; 30:2613-2617.

Gabbert U, Nestorović-Trajkov T, Köppe H. Finite Element-Based Overall Design of Controlled Smart Structures. Structural Control and Health Monitoring 2006;13:1052-1067.

Ghasemi-Nejhad MN, Porjalali S, Uyema M, Yousefpour A, Finite Element Method for Active Vibration Suppression of Smart Composite Structures Using Piezoelectric Materials. Journal of Thermoplastic Composite Materials 2006;19:309-352.

Ghosal A, Chattopadhyay A, Schulz MJ, Thornburgh R, Waldron K. Experimental Investigation of Damage Detection in Composite Material Structures Using a Laser Vibrometer and Piezoelectric Actuators. Journal of Intelligent Material Systems and Structures 2003; 14:521-537.

Giannopoulos G, Vantomme J. A Fully Thermoelectromechanically Coupled FE Analysis for the Dynamic Behavior of Smart Plates Using Discrete-Layer Kinematics. Proceedings of SPIE-The International Society for Optical Engineering 2005; 5757: 420-431.

Giannopoulos G, Vantomme JA, Thermal-electrical-mechanical Coupled FE Formulation Using Discrete Layer Kinematics for the Dynamic Analysis of Smart Plates. Smart Materials and Structures 2006; 15:1846-1857.

Giurgiutiu V, Zagrai A, Bao J. Damage Identification in Aging Aircraft Structures with Piezoelectric Wafer Active Sensors. Journal of Intelligent Material Systems and Structures 2004; 15:673-687.

Golla DF, Hughes TC. Dynamics of viscoelastic structures-A time domain, finite element formulation. ASME Journal of Applied Mechanics 1985; 52(4): 897-906.

Görnandt, A. and Gabbert, U., 2002, "Finite Element Analysis of Thermopiezoelectric Smart Structures", *Acta Mechanica*, Vol. 154, pp. 129-140.

Gu Y, Clark RL, Fuller CR. Experiments on Active Control of Plate Vibration Using Piezoelectric Actuators and Polyvinylidyne Fluoride (PVDF) Modal Sensors. Journal of Vibrations and Acoustics 1994; 116:303-308.

Gupta VK, Seshu P, Kurien Issac K, Shevgaonkar RK. Optimal Steering of a Paraboloid

Antenna Using Piezoelectric Actuators. Smart Materials and Structures 2007; 16:67-75.

Ha SK, Keilers C, Chang FK, Finite Element Analysis of Composite Structures Containing Distributed Piezoelectric Sensors and Actuators. AIAA Journal 1992, 30:772-780.

Hamed ES, Negm HM. Finite Element Model for Smart Beams with Piezoelectric Actuators and/or Sensors. Journal of Engineering and Applied Science 2004; 51:575-592.

Han W, Petyt M. Geometrically nonlinear vibration analysis of thin rectangular plates using the hierarchical finite element method-II: 1st mode of laminated plates and higher modes of isotropic and laminated plates. Computers and Structures 1997; 63(2):309-318.

Han SC, Lee WH, Park WT. Non-linear analysis of laminated composite and sigmoid functionally graded anisotropic structures using a higher-order shear deformable natural Lagrangian shell element. Composite structures 2009; 89; 8-19.

Hanagud S, Obal M W, Calise AJ. Optimal Vibration Control by the Use of Piezoceramic Sensors and Actuators. Journal of Guidance, Control and Dynamics 1992; 15:1199-1206.

Hao YX, Zhang W, Yang J, Li SY. Nonlinear dynamic response of a simply supported rectangular functionally graded material plate under the time-dependent thermal mechanical loads. Journal of Mechanical Science and Technology 2011; 25:1637-1646.

He LH. Axisymmetric Response of Circular Plates with Piezoelectric Layers: An Exact Solution. International Journal of Mechanical Sciences 1998; 40:1265-1279.

Hebali H, Tounsi A, Houari MSA, Bessaim A, Bedia EAA. New quasi-3D hyperbolic shear deformation theory for the static and free vibration analysis of functionally graded plates. Journal of Engineering Mechanics 2014; 140:374-383.

Hellweg HB,Crisfield MA, A New arc length method for handling sharp snap-backs. Computers and Structures 1995; 66:705-709.

Heyliger P. Exact Solutions for Simply Supported Laminated Piezoelectric Plates. ASME Journal of Applied Mechanics 1997; 64:299-306.

Heyliger P, Saravanos DA. Exact free-vibration analysis of laminated plates with embedded piezoelectric layers. The Journal of the Acoustical Society of America 1995; 98:1547-1557.

Huang XL, Shen HS. Nonlinear vibration and dynamic response of functionally graded

plates in thermal environments. International Journal of Solids and Structures 2004; 41:2403-2427.

Hwang WC, Park HC. Finite Element Modeling of Piezoelectric Sensors and Actuators", AIAA Journal 1993; 31:930-937.

Illaire H, Kropp W. Quantification of damping mechanisms of active constrained layer damping treatments. Journal of Sound and Vibration 2005; 281: 189-217.

Im S, Atluri SN. Effects of a Piezoactuator on a Finitely Deformed Beam Subjected to General Loading. AIAA Journal 1989; 27:1801-1807.

Inman DJ, Yang Y. Finite element analysis and experimental study on dynamic properties of a composite beam with viscoelastic damping. Journal of Sound and Vibration 2013; 332(23):6617-91.

Jafari Mehrabadi S, Kargarnovin H, Najafizadeh MM. Free vibration analysis of functionally graded coupled circular plate with piezoelectric layers. Journal of Mechanical Science and Technology 2009;23:2008-2021.

Johnson TJ, Brown RL, Adams DE, Schiefer M. Distributed Structural Health Monitoring with a Smart Sensor Array. Mechanical System and Signal Processing 2004;18:555-572.

Kargarnovin MH, Hashemi M. Buckling Analysis of Multilayered Functionally Graded Composite Cylindrical Shells. Applied Mechanics and Materials 2012; 108:74-79.

Kashtalyan M. Three-dimensional elasticity solution for bending of functionally graded rectangular plates. European Journal of Mechanics A/Solids 2004; 23: 853–864.

Ke LL, -Jie Yang, Kitipornchai S. An analytical study on the nonlinear vibration of functionally graded beams. Meccanica 2010; 45:743-745.

Koizumi M. Concept of FGM. Ceramic Transactions 1993; 34:3–10.

Koko TS, Orisamolu IR, Smith MJ, Akpan UO. Active Control Methodology for Thermal Distortion Management of Smart Composite Structures. Proceedings of SPIE- The International Society for Optical Engineering 1998; 3323:8-19.

Kubiak T. Dynamic buckling of thin-walled composite plates with varying width-wise material properties. International Journal of Solids and Structures 2005; 42: 5555–5567.

Kumar A, Chakraborty D. Effective properties of thermo-electro-mechanically coupled piezoelectric fiber reinforced composites. Materials and Design, doi:0.1016/J.matdes.2008.06.009.

Kumar N, Singh SP. Vibration control of curved panel using smart damping. Mechanical Systems and Signal Processing 2012; 30:232-247.

Kumari P, Nath JK, Dumir PC, Kapuria, S. 2D Exact Solutions for Flat Hybrid Piezoelectric and Magnetoelastic Angle-ply Panels under Harmonic Load. Smart Materials and Structures 2007; 16:1651-1661.

Kuo SY, Shiau LC. Buckling and vibration of composite laminated plates with variable fiber spacing. Composite Structures 2009; 90:196-200.

Kusculuoglu ZK, Royston TJ. Finite Element Formulation for Composite Plates with Piezoceramic Layers for Optimal Vibration Control Applications. Smart Materials and Structures 2005; 14:1139-1153.

Lanhe W. Thermal buckling of a simply supported moderately thick rectangular FGM plate. Composite Structures 2004; 64: 211–218.

Larbi LO, Kaci A, Houari MSA, Tounsi A. An efficient shear deformation beam theory based on neutral surface position for bending and free vibration of functionally graded beams. Mechanics Based Design of Structures and Machines 2013; 41:421-433.

Lee CK, Moon FC. Modal Sensors/Actuators. ASME Journal of Applied Mechanics 1990; 57:434-441.

Lee CK, Chiang WW, Sulivan O. Piezoelectric Modal Sensor/Actuator Pairs for Critical Active Damping Vibration Control. Journal of Acoustical Society of America 1991; 90:374-384.

Lee HJ, Saravonos DA. A Mixed Multi-Field Finite Element Formulation for Thermopiezoelectric Composite Shells. International Journal of Solids and Structures 2000; 37:4949-4967.

Leissa AW, Martin AF. Vibration and buckling of rectangular composite plates with variable fiber spacing. Composite Structures 1990; 14:339-357.

Li Q, Iu VP, Kou KP. Three-dimensional vibration analysis of functionally graded material plates in thermal environment. Journal of Sound and Vibration 2009; 324: 733–750.

Liew KM, He XQ, Meguid SA. Optimal control of functionally graded smart plates using genetic algorithms. Computational Mechanics 2004; 33:245-253.

Liew KM, He XQ, Ray T. On the use of computational intelligence in the optimal shape control of functionally graded smart plates. Computational Methods in Applied

Mechanical Engineering 2004;193: 4475–4492.

Liew KM, He XQ, Ng TY, Kitipornchai, S. Finite element peizothermoelasticity analysis and the active control of FGM plates with integrated piezoelectric sensors and actuators. Computational Mechanics 2003; 31:350-355.

Liew KM, Sivashanker S, He XQ, Ng TY. The modelling and design of smart structures using functionally graded materials and piezoelectrical sensor/actuator patches. *Smart Material and Structures* 2003; 12: 647-665.

Liew KM, Yang J, Kitipornchai S. Post buckling of piezoelectric FGM plates subject to thermoelectro mechanical loading. International Journal of Solids and Structures 2003; 40(15):3869-3892.

Lim YL, Vardhan VV, Vardhan VK. Closed loop Finite element modeling of ACLD damping in time domain analysis", Smart Material and Structures 2002;11:89-97.

Lin RR, Palazzolo AB, Kascak AF. Montague GT. Electromechanical Simulation and Testing of Actively Controlled Rotordynamic Systems with Piezoelectric Actuators. ASME Journal of Engineering for Gas Turbine and Power 1993; 115: 325-335.

Liu M, Chang F. K. The Manufacture of Composite Structures with a Built in Network of Piezoceramics. Composite Science and Technology 2002; 62:919-939.

Luo Q, Tong L. Exact Dynamic Solutions to Piezoelectric Smart Beams Including Peel Stresses, Part II: Numerical Results, Comparison and Approximate Solution. International Journal of Solids and Structures 2003; 40:4813-4836.

Mallik N, Ray MC. Effective Coefficients of Piezoelectric Fiber Reinforced Composites. AIAA Journal 2003; 41:704-710.

Mannini A, Gaudenzi P. Multi-Layer Higher-Order Finite Elements for the Analysis of Free-Edge Stresses in Piezoelectric Actuated Laminates. Composite Structures 2004; 63:263-270.

Markworth AJ, Ramesh KS, Parks Jr WP. Review Modelling studies applied to Functionally graded materials. Journal of Materials Science 1995; 38:2183-2193.

Maiti DK, PK Sinha Analysis of Smart Laminated Composites Employing piezo Embedded Super Element. Procedia Engineering 2011; 14: 3268–3276.

Martin AF, Leissa AW. Application of the Ritz method to plane elasticity problems for composite sheets with variable fiber spacing. International Journal of Numerical Methods in Engineering 1990; 28:1813-1825.

Matsunaga H, Stress analysis of functionally graded plates subjected to thermal and mechanical loadings. Composite Structures 2009; 87:344–357.

Meftah SA, Yeghnem R, Tounsi, A. Adda BEA. Lateral stiffness and vibration characteristics of composite plated RC shear walls with variable fiber spacing, Materials and Design 2008; 29:1955-1964.

Meftah SA, Yeghnem R, Tounsi A, Adda BEA. Seismic behavior of RC coupled shear walls repaired with CFRP laminates having variable fibers spacing. Construction and Building Materials 2007; 21:1661-1671.

Meziane MAA, Abdelaziz HH, Tounsi A. An efficient and simple refined theory for buckling and free vibration of exponentially graded sandwich plates under various boundary conditions. Journal of Sandwich Structures and Materials 2014; 16(3):293- 318.

Miller SE, Hubbard JE. Observability of a Bernoulli-Euler Beam Using PVF_2 as a Distributed Sensor. Draper report 1987, MIT.

Mohammad T, Singh BN. Large amplitude free and flexural vibration analysis of shear deformable FGM plates using nonlinear finite element method. Finite Elements in Analysis and Design 2011; 47:394-401.

Mook G, Pohl J, Michel F. Non-Destructive Characterization of Smart CFRP Structures. Smart Materials and Structures 2003; 12:997-1004.

Narayanan S, Balamurugan V. Finite Element Modeling of Piezolaminated Smart Structures for Active Vibration Control with Distributed Sensors and Actuators. Journal of Sound and Vibration 2003; 262:529-562.

Newnham RE, Skinner DP, Cross LE. Connectivity and Piezoelectric-Pyroelectric Composites. Materials Research Bulletin 1978; 13:525-536.

Nguyen Q, Tong L. Shape Control of Smart Composite Plate with Non-Rectangular Piezoelectric Actuators. Composite Structures 2004; 66:207-214.

Nguyen Q, Tong L. Voltage and Evolutionary Piezoelectric Actuator Design Optimization for Static Shape Control of Smart Plate Structures. Materials and Design 2007; 28:387-399.

Nguyen-Xuan H, Tran LV, Thai CH, Kulasegaram S, Bordas SPA. Isogeometric analysis of functionally graded plates using a refined plate theory. Composites: Part B 2014; 64:222-234.

Noda N. Thermal stresses in functionally graded materials. Journal of Thermal Stresses

1999, 22:477–512.

Ootao Y, Tanigawa Y. Control of the transient thermoelastic displacement of Functionally graded rectangular plate bonded to a piezoelectric plate due to nonuniform heating. ActaMechanica 2001; 148:17-33.

Oyekoya OO, Mba DU, El-Zafrany AM. Buckling and vibration analysis of functionally graded composite structures using the finite element method. Composite Structures 2009; 89:132-142.

Panda S, Ray MC. Active constrained layer damping of geometrically nonlinear vibrations of functionally graded plates using piezoelectric fiber-reinforced composites. Smart Materials and Structures 2008; 17:1-15.

Panda S, Ray MC. Nonlinear finite element analysis of functionally graded plates integrated with patches of piezoelectric fiber reinforced composite. Finite element analysis in Design 2008; 44:493-504.

Panda S, Ray MC. Active control of geometrically nonlinear vibrations of functionally graded laminated composite plates using piezoelectric fiber reinforced composite. Journal of Sound and Vibration 2009, 325(1-2):186-205.

Park CH, Baz A. Vibration control of bending modes of plates using active constrained layer. Journal of Sound and Vibration 1999; 227(4):711-734.

Park JS, Kim JH. Thermal postbuckling and vibration analyses of functionally graded plates. Journal of Sound and Vibration 2006; 289:77–93.

Pompe W, Worch H, Epple M, Friess W, Gelinsky M, Greil P, Hempel U, Scharnweber D, Schulte K. Functionally graded materials for biomedical applications. Materials Science and Engineering 2003; 362(A):40-60.

Praveen GV, Reddy JN. Nonlinear transient thermo elastic analysis of functionally graded ceramic metal plates. International Journal of Solids and Structures 1998; 35:4457-4467.

Rao SS, Sunar M. Analysis of Distributed Thermopiezoelastic Sensors and Actuators in Advanced Intelligent Structures. AIAA Journal 1993, 31:1280-1286.

Ray MC, Baz A. Optimization of energy dissipation of active constrained layer damping treatments. Journal of Sound and Vibration 1997; 208(3):391-406.

Ray MC, Reddy JN. Performance of piezoelectric for piezoelectric fiber reinforced composites for active structural-acoustic control of laminated composite plates. IEEE Transactions on Ultrasonics, Ferroelectrics and frequency Control 2004;

51(11): 1477-1490.

Ray MC, Sachade HM. Exact Solutions for the Functionally Graded Plates Integrated with a Layer of Piezoelectric Fiber Reinforced Composites. Journal of Applied Mechanics 2006; 73:622–632.

Ray MC. Optimal Control of Laminated Plates with Piezoelectric Sensor and Actuator Layers. AIAA Journal 1998;12:2204-2208.

Ray MC. Optimal Control of Laminated Shells with Piezoelectric Sensor and Actuator Layers. AIAA Journal 2003; 41:1151-1157.

Ray MC. Hybrid Damping of smart, Functionally graded plates using piezoelectric fiber reinforced composites. IEEE Transactions on Ultrasonics, Ferroelectrics and frequency Control 2006; 58(11):2152-2165.

Ray MC, Batra RC. Smart constrained layer damping of functionally graded shells using vertically/obliquely inclined 1-3 piezocomposite under thermal environment. Smart Materials and Structures 2008, 17:

Ray MC, Bhattacharya R, Samanta B. Exact solutions for static analysis of intelligent structures", AIAA Journal 1993; 31(9):1684-1691.

Ray MC, Bhattacharya R, Samantha B. Exact Solutions for Dynamic Analysis of Composite Plates with Distributed Piezoelectric Layers. Computers and Structures 1998; 66:737-743.

Ray MC, Mallik N. Finite element analysis of smart structures containing piezoelectric fiber-reinforced composite actuator. AIAA Journal 2004; 42(7):1398-1405.

Ray MC, Mallik N. Performance of smart damping treatment using piezoelectric fiber-reinforced composites. AIAA Journal 2005; 43(1):184-193.

Reddy JN. Analysis of Functionally graded plates. International Journal of Material Design 2000; 47:663-84.

Reddy JN. Mechanics of Laminated Composite Plates and Shells: Theory and Analysis, 2nd ed. Boca Raton (Florida, USA): CRC Press; 2003.

Reddy BA, Ray MC. Optimal Control of Smart functionally graded plates using piezoelectric fiber reinforced composites. Journal of Vibration and Control 2007; 13:795-814.

Reddy JN, Cheng ZQ. Three dimensional thermomechanical deformations of functionally graded plates. European Journal of Mechanics A/Solids 2001; 20: 841–

855.

Reibero P, Petyt M. Nonlinear vibration analysis of plates by hierarchical finite element and continuation methods. International Journal of Mechanical Sciences 1999; 41(4-5):437-459.

Reiter T, Dvorak GJ. Micromechanical models for graded composite materials. Journal of Mechanics and Physics of Solids 1997; 45:1281-1302.

Reiter T, Dvorak GJ. Micromechanical models for graded composite materials: II. Thermomechanical loading. Journal of Mechanics and Physics of Solids 1998, 46:1655-1673.

Reley MB, Whitney JM. Elastic properties of fiber reinforced composite materials. AIAA Journal 1966; 4:1537-1542.

Robbins Jr DH, Reddy JN. An Efficient Computational Model for the Stress Analysis of Smart Plate Structures. Smart Materials and Structures 1996; 5: 353-360.

Robbins DH, Reddy JN. Analysis of Piezoelectrically Actuated Beam Using a Layerwise Displacement Theory. Computers and Structures 1991; 41:265-279.

Samantha B, Ray MC, Bhattacharya R. Finite Element Model for Active Control of Intelligent Structures. AIAA Journal 1996; 34:1885-1893.

Sarangi SK, Ray MC. Smart control of nonlinear vibrations of doubly curved functionally graded laminated composite shells under a thermal environment using 1-3 piezoelectric composites. International Journal of Mechanical and Material design 2013; 9:253-280.

Sastry CVS, Mahapatra DR, Gopalakrishnan S, Ramamurthy TS. Distributed Sensing of Static and Dynamic Fracture in Self-Sensing Piezoelectric Composite: Finite Element Simulation. Journal of Intelligent Materials Systems and Structures 2004; 15:339-354.

Sateesh B, Maiti DK. Closed-Loop Active Vibration Control of A Typical Nose Landing Gear With Torsional MR Fluid Based Damper. Structural Engineering and Mechanics 2009; 31 (1): 39-56.

Sh. Hosseini-Hashemi, Rokni Damavandi Taher H, Akhavan H, Omidi M. Free vibration of functionally graded rectangular plates using first-order shear deformation plate theory. Applied Mathematical Modelling 2010; 34:1276–1291.

Shakeri Ml, Mirzaeifar R. Static and Dynamic Analysis of Thick Functionally Graded Plates with Piezoelectric Layers Using Layerwise Finite Element Model. Mechanics of Advanced Materials and Structure 2009; 16:561-575.

Shen HS. Nonlinear bending analysis of functionally graded plates subjected to transverse loads and in thermal environments. International Journal of Mechanical Sciences 2002; 44(3): 561-584.

Shen HS. Postbuckling of FGM plates with piezoelectric actuators under thermo-electro-mechanical loadings. International Journal of Solids and Structures 2005; 42:6101–6121.

Shen IY. Bending -vibration control of composite and isotropic plates through intelligent constrained-layer damping treatments. Smart Materials and Structures 1994; 3:59-70.

Shen IY. Active Constrained Layer Damping Treatments for Shell Structures: A Deep-Shell Theory, Some Intutive Results and an Energy Analysis. Smart Materials and Structures 1997; 6:89-101.

Sheng L, Zhao D. Numerical simulation of active control of structural vibration and acoustic control of fluid loaded composite plate. Journal of Sound and Vibration 2004; 272:109-124.

Shi Y, Hua H, Sol H. The finite element analysis and experimental study of beams with active constrained layer damping treatment. Journal of Sound and Vibration 2004; 278(1-2):343-363.

Shiau LC. Chue YH. Free-edge stress reduction through fiber volume fraction variation. Composite Structures 1991; 19:145-165.

Shiau LC, Lee GC. Stress concentration around holes in composite laminates with variable fiber spacing. Composite Structures 1993; 24:107-115.

Shiyekar SM, Kant T. An electromechanical higher order model for piezoelectric functionally graded plates. International Journal of Mechanical Material Design 2010; 6:163–174.

Smith WA, Auld BA. Modeling 1-3 Composites Piezoelectrics: Thickness Mode Oscillations. IEEE Transactions on Ultrasonics, Ferroelectrics and Frequency Control 1991; 38:40-47.

Song O, Librescu L, Rogers CA. Application of Adaptive Technology to Static Aeroelastic Control of Wing Structures. AIAA Journal 1992; 30:2882-2889.

Steven AL, Steven G, Don Leo. Active Structural Acoustic Control of a Launch Vehicle Fairing Using Monolithic Piezoceramic Actuators. Journal of Intelligent Material Systems and Structures 2001; 12:795-806.

Stöbener U, Gaul, L. Modal Vibration Control for PVDF Coated Plates. Journal of Intelligent Material Systems and Structures 2000; 11:283-293.

Sun CT, Chen JL. Failure of quasi-isotropic composites laminates with free edges. Journal of Reinforced Plastics and Composites 1988; 7:515-557.

Sun CT, Chen JL. A micromechanical model for plastic behavior of fibrous composite. Composites Science and Technology 1990; 40:115-129.

Sun D, Tong L, Wang D. Modal Actuator/Sensor by Modulating Thickness of Piezoelectric Layers for Smart Plates. AIAA Journal 2002; 40:1676-1679.

Sundararajan N, Prakash T, Ganapathi M. Nonlinear free flexural vibrations of functionally graded rectangular and skew plates under thermal environments. Finite elements in analysis and Design 2005; 42:152-168.

Sung Yi, Sze KY. A finite element formulation for composite laminates with smart constrained layer damping. Advances in Engineering Software 2000; 31: 520-537.

Suresh kumar R, Ray MC. Active control of geometrically nonlinear vibrations of doubly curved smart sandwich shells using 1-3 piezoelectric composites, Composite Structures 2013; 105:173-187.

Sze KY, Yao LQ. Modeling Smart Structures with Segmented Piezoelectric Sensors and Actuators. Journal of Sound and Vibration 2000; 235:495-520.

Tahouneh V, Yas MH, Tourang H, Kabirian M. Semi-analytical solution for three-dimensional vibration of thick continuous grading fiber reinforced (CGFR) annular plates on Pasternak elastic foundations with arbitrary boundary conditions on their circular edges. Meccanica 2013; 48:1313-1336.

Tauchert TR. Piezothermoelastic Behavior of a Laminated Plate. Journal of Thermal Stresses 1992; 15:25-37.

Taya M, Almajid AH, Hadnut S. Analysis of out of plane displacement and stress field in a piezo composite plate within functionally graded structure. International Journal of Solids and Structures 2001; 38:.3377–3391.

Thornburgh RP, Chattopadhyay A, Ghosal A. Transient Vibration of Smart Structures Using a Coupled Piezoelectric Mechanical Theory. Journal of Sound and Vibration 2004, 274:53-72.

Tian X, Shen Y. Finite Element Analysis of Thermoelastic Behavior of Piezoelectric Structures Under Finite Deformation. Acta Mechanica Solida Sinica 2002; 15:312-322.

Tiersten HF. Linear piezoelectric plate vibrations. New York: Plenum Press; 1969.

Tornabene F, Viola FA, Inman DJ. 2D differential quadrature solution for vibration analysis of functionally graded conical, cylindrical and annular plate structures. Journal of Sound and Vibration 2009; 328(3):259-290.

Tounsi A, Houari MSA, Benyoucef S, Bedia EAA. A refined trigonometric shear deformation theory for thermoelastic bending of functionally graded sandwich plates. Aerospace Science and Technology 2013; 24:209-220.

Tsunglinwu, kshukla K, Huang JH. Nonlinear static and dynamic analysis of functionally graded rectangular plate. International Journal of Applied Mechanics 2006; 11:679-698.

Tzou HS, Gadre M. Theoretical Analysis of a Multilayered Thin Shell Coupled with Piezoelectric Shell Actuators for Distributed Vibration Controls. Journal of Sound and Vibration 1989; 132:433-450.

Tzou HS, Gadre M. Active Vibration Isolation and Excitation by Piezoelectric Slab with Constant Feedback Gains. Journal of Sound and Vibration 1990; 136:477-490.

Tzou HS, Panditha S. A Multipurpose Dynamic and Tactile Sensor for Robot Manipulators. Journal of Robotic System 1987; 4:719-741.

Tzou HS, Tseng CI. Distributed Piezoelectric Sensor/Actuator Design for Dynamic Measurement/Control of Distributed Parameter Systems: A Piezoelectric Finite Element Approach. Journal of Sound and Vibration 1990; 138:17-34.

Tzou HS, Tseng CI. Distributed Modal Identification and Vibration Control of Continua: Piezoelectric Finite Element Formulation and Analysis. ASME Journal of Dynamic Systems. Measurement and Control 1991; 113:500-505.

Tzou HS. Distributed Modal Identification and Vibration Control of Continua: Theory and Applications. ASME Journal of Dynamic Systems, Measurement and Control 1991; 113:494-499.

Upadhyay AK, Shukla KK. Geometrically nonlinear static and dynamic response of functionally graded skew plates. Communications in Nonlinear Science and Numerical Communication 2013; 18:2252-2279.

Van Nostrand W, Knowles G, Inman D. Finite element modelling for active constrained layer damping. Proc. of Smart Structures and Materials Conference on Passive

damping 1994; 2193:126-137.

Varadan VV, Kim J, Varadan VK. Optimal Placement of Piezoelectric Actuators for Active Noise Control", AIAA Journal 1997; 35:526-533.

Varadan VV, Lim YH, Varadan VK. Closed Loop Finite Element Modeling of Active/Passive Damping in Structural Vibration Control. Smart Materials and Structures 1996; 5:685-694.

Vel SS, Batra RC. Exact Solution for Rectangular Sandwich Plates with Embedded Piezoelectric Shear Actuators. AIAA Journal 2001; 39:1363-1373.

Vel SS, Batra RC. Three-dimensional exact solution for the vibration of functionally graded rectangular plates. Journal of Sound and Vibration 2004;. 272: 703–730.

Von Groll G., Ewins DJ. The harmonic balance method with arc-length continuation in rotor/stator applications. Journal of Sound and Vibration 2001;124: 223-233.

Wang BL, Noda N. Design of a smart functionally graded thermopiezoelectric composite structure. Smart Material and Structures 2001; 10:189 doi:10.1088/0964-1726/10/2/303.

Wang BT, Rogers CA. Laminate Plate Theory for Spatially Distributed Induced Strain Actuators. Journal of Composite Material 1991; 25:433-452.

Wetherhold RC, Seelman S, Wang J. The use of functionally graded materials to eliminate or control thermal deformations. Composites Science and Technology 1996; 56:1099-1104.

Wilkie WK, Bryant RG, High JW, Fox RL, Hellbaum RF, Jalink A, Little BD, Mirick PH. NASA-Langley research centre macro fiber composite actuator: technical Overview 2000.

Wolfe D, Singh J. Functionally gradient ceramic/metallic coatings for gas turbine components by high energy beams for high temperature applications. Journal of Materials Science 1998; 33(14):3677-3692.

Woo J, Meguid SA, Ong LS. Nonlinear free vibration behavior of functionally graded plates. Journal of Sound and Vibration 2006; 289:595-611.

Woo J, Meguid SA. Nonlinear analysis of functionally graded plates and shallow shell. International Journal of Solids and Structures 2001; 38:7409-7421.

Xia, X. K. and Shen, H. S., 2009,"Nonlinear vibration and dynamic response of FGM plates with piezoelectric fiber reinforced composite actuators", *Composite Structure*, Vol. 90, pp. 254-62.

Xiang HJ, Shi ZF. Static analysis for functionally graded piezoelectric actuators or sensors under a combined electro-thermal load. European Journal of Mechanics and Solids 2009; 28:338-346.

Yang J, Kitipornchai S, Liew K M. Nonlinear analysis of thermoelectromechanical behaviour of shear deformable FGM plates with piezoelectric actuators. International Journal for Numerical Methods in Engineering 2004; 59(12):1605-32.

Yang J, Shen HS. Dynamic response of initially stressed functionally graded rectangular thin plates. Composite Structures 2001; 37:497-508.

Yang J, Shen HS. Vibration characteristics and Transient response of shear deformable functionally graded plates in thermal environments. Journal of Sound and vibration 2002; 255:579-602.

Yang J, Shen HS. Nonlinear analysis of functionally graded plates under transverse and in-plane loads. International Journal of Nonlinear Mechanics 2003; 38(4):467-482.

Yang J, Kitipornchai S, Liew KM. Large amplitude vibration of thermo-electro-mechanically stressed FGM laminated plates. Computational Methods in Applied Mechanical. Engineering 2003; 192: 3861–3885.

Yang YY. Time dependent analysis of Functionally Graded materials. International Journal of Solids and Structures 1999; 37:7593-7608.

Yas MH, Aragh BS. Free vibration analysis of continuous grading fiber reinforced plates on elastic foundation. International Journal of Engineering Science 2010; 48(12):1881-1895.

Yas MH, Aragh BS. Elasticity solution for free vibration analysis of four-parameter functionally graded fiber orientation cylindrical panels using differential quadrature method. European Journal of Mechanics - A/Solids 2011; 30:631–638.

Yellin JM, Shen I Y. A Self-Sensing Active Constrained Layer Damping Treatment for a Euler-Bernoulli Beam. Smart Materials and Structures 1996; 5:628-637.

Yiqi M, FuYiming. Nonlinear dynamic response and active vibration control for piezoelectric functionally graded plate. Journal of Sound and Vibration 2010; 329: 2015–2028.

Yousefi-Koma A, Mehrabian AR. A novel technique for optimal placement of piezoelectric actuators on smart structures. Journal of the Franklin Institute 2011; 348:12-23.

Zayas JR, Paquette J, Werlink RJ. Evaluation of NASA PZT Sensor/Actuator for

Structural Health Monitoring of a Wind Turbine Blade. Collection of Technical Papers-45th AIAA Aerospace Science Meeting 2007; 18:12353-12363.

Zemčik R, Rolfes R, Rose M, Tessmer J. High-Performance Four-Node Shell Element with Piezoelectric Coupling for the Analysis of Smart Laminated Structures. International Journal for Numerical Methods in Engineering 2007; 70:934-961.

Zhang HY, Shen YP. Vibration Suppression of Laminated Plates with 1-3 Piezoelectric Fiber-reinforced Composite Layers Equipped with Interdigitated Electrodes. Composite Structures 2007; 79:220-228.

Zhang NH, Wang ML. Thermoviscoelastic deformations of functionally graded thin plates. European Journal of Mechanics A/Solids 2007; 26: 872–886.

Zhang W, Hao Y, Guo X, Chen L. Complicated nonlinear responses of a simply supported FGM rectangular plate under combined parametric and external excitations. Meccanica 2011; doi: 10.1007/s11012-011-9491-4.

Zhang X, Zhang J. The hybrid control of vibration of thin plate with active constrained damping layer. Applied Mathematics and Mechanics 1998; 19(12), 1192-1134.

Zhao Z, Lee YY, Liew K M. Mechanical and thermal buckling analysis of functionally graded plates. Composite Structures 2009; 90:161–171.

Zhong Z, Shang ET. Three-dimensional exact analysis of a simply supported functionally gradient piezoelectric plate. International Journal of Solids and Structures 2003; 40:5335–5352.

Zhou RC, Lai Z, Xue DY, Huang, JK, Mei, C. Suppression of Nonlinear Panel Flutter with Piezoelectric Actuators Using Finite Element Method. AIAA Journal 1995; 6:1098-1105.

Zidi M, Tounsi A, Houari MSA, Brdia EAA, Beg O A. Bending analysis of FGM plates under hygro-thermo-mechanical loading using a four variable refined plate theory. Aerospace Science and Technology 2014; 34:24-34.

LIST OF PUBLICATIONS

The work presented in this thesis has led to the following publications:

1. Aravinda Kumar M S, Panda S, Chakraborty D. Harmonically excited nonlinear vibration of heated functionally graded plates integrated with piezoelectric composite actuator. *Journal of Intelligent Material Systems and Structures* 2015; 26:931-951.
2. Aravinda Kumar M S, Panda S, Chakraborty D. Piezo-viscoelastically damped nonlinear frequency response of functionally graded plates with a heated plate-surface. *Journal of Vibration and Control* 2014; 1-24,(DOI: 10.1177/1077546314532672).
3. Aravinda Kumar M S, Panda S, Chakraborty D. Design and analysis of a smart graded fiber-reinforced composite laminated plate. *Composite Structures* 2015; 124:176-195.
4. Aravinda Kumar M S, Panda S, Kumar S, Chakraborty D. A design of laminated composite plates using graded orthotropic fiber-reinforced composite plies. 2015; Composites Part B : Engineering 2015; 79:476-493.